



**This electronic thesis or dissertation has been
downloaded from Explore Bristol Research,
<http://research-information.bristol.ac.uk>**

Author:

Li, Jingwen

Title:

**Self-assembly of model isotropic and anisotropic colloids and proteins
*a real space analysis***

General rights

Access to the thesis is subject to the Creative Commons Attribution - NonCommercial-No Derivatives 4.0 International Public License. A copy of this may be found at <https://creativecommons.org/licenses/by-nc-nd/4.0/legalcode>. This license sets out your rights and the restrictions that apply to your access to the thesis so it is important you read this before proceeding.

Take down policy

Some pages of this thesis may have been removed for copyright restrictions prior to having it been deposited in Explore Bristol Research. However, if you have discovered material within the thesis that you consider to be unlawful e.g. breaches of copyright (either yours or that of a third party) or any other law, including but not limited to those relating to patent, trademark, confidentiality, data protection, obscenity, defamation, libel, then please contact collections-metadata@bristol.ac.uk and include the following information in your message:

- Your contact details
- Bibliographic details for the item, including a URL
- An outline nature of the complaint

Your claim will be investigated and, where appropriate, the item in question will be removed from public view as soon as possible.

Self-Assembly of Model Isotropic and Anisotropic Colloids and Proteins: a Real Space Analysis

By

JINGWEN LI



School of Physics
UNIVERSITY OF BRISTOL

A dissertation submitted to the University of Bristol in accordance
with the requirements of the degree of DOCTOR OF PHILOSOPHY in
the Faculty of Physics.

MARCH 2023

Word count: 41372

ABSTRACT

Self-assembly is a promising approach for generating complex functional microstructures with numerous technological applications. However, the understanding of the underlying mechanisms and the conditions required to achieve specific structures remain rudimentary, limiting its further utilisation. In this thesis, we investigated several self-building systems with varying interactions between constituent particles for a better knowledge of the self-assembly.

The first system involved using PMMA particles that are sterically stabilised to mimic hard spheres. Hard spheres exhibit a thermodynamic phase transition, from fluid to crystal phases, as a function of the packing fraction. However, a remarkable disagreement of experimental and simulation homogeneous nucleation rates by more than 10 orders of magnitude is observed in less supercooled region. We attempted to address this discrepancy by developing a novel confocal microscope image processing technique which allows crystallite identification of colloids with much smaller than typical size scale required for particle-resolved imaging, and thus enables the observation of much rare events, namely the formation of nuclei near the freezing volume fraction. We further examined our results by using larger PMMA with particle tracking methods locating the colloids. Unfortunately, we found no clear dependence of nucleation rate on the particle packing fraction, consistent with the previous experimental works. Hence this discrepancy remains a puzzle.

Bi-continuous protein gels with depletion attractions induced by polymer addition is the main topic of the second section. The phase behaviour of individual protein species were firstly studied. Various strategies were then employed, including surface modification of protein molecules and adjustment of adding sequence, to achieve the target structures. Expected binary gel networks were only accessible with specific polymer-protein size ratio. Notably, this study represents the first realization of binary protein gels in which the proteins preserve their intrinsic properties through the depletion interaction.

The third system is composed of rod-like particles and polymers to investigate the possibility of recovering the higher-dimensional ($d \rightarrow \infty$) hard sphere glass transition, based on the assumption that the behaviour of the system is represented by the numbers of interactions and the fact that both hard spheres in high d and hard rods with high aspect ratio interact with many neighbours. We developed a reproducible procedure for the dispersion of sepiolite clay particles, B20, and then prepared the mixture of rods and polymers at different volume fractions. With a small size ratio, $q = 0.2$ and the consequent short-range attraction, we tested a localised phase diagram at low rod volume fractions. During gelation, the dynamics, characterised by the structural relaxation time from the fitting of $c(t)$, exhibited a remarkable increase, while the network structure, indicated by $g(r)$, remained similar to its initial configuration. Our findings suggest that this loss of ergodicity in our rod-polymer mixture is similar to the dynamical arrest in the hard sphere high-dimensional case. Therefore, this simple experimental system provides a potential approach to interpreting higher-dimensional hard sphere vitrification.

ACKNOWLEDGEMENTS

I would like to express my deepest gratitude to all the people who have helped me throughout this long process. Without their support, I would not have been able to achieve my goals.

Firstly, I would like to acknowledge China Scholarship Council and University of Bristol for joint funding my PhD.

I would like to extend my deepest appreciation to my supervisor Prof. Paddy Royall for his invaluable guidance and wisdom. His knowledge, expertise and hard work have been instrumental in shaping my growth and development. Especially, he illuminated the pathway that I was eligible to start a PhD project when I was trapped in self-doubt...

I would also like to express my heartfelt gratitude to Adrian Barnes, who takes the responsibilities as a supervisor since Paddy left UoB and have played an essential role in my study. He provided important assistance. Additionally, many thanks to Jeroen van Duijneveldt for giving advice on my project and allowing me to use the chemicals and run experiments in his lab.

I am also deeply indebted to my group members for their constant help even until now. They have been a source of inspiration and motivation, pushing me to keep going even when the going gets tough. Their presence in my life has made it all the more enriching and enjoyable. In particular, I would like to thank Ioatzin, she provides incredible help all the time, from experiments to my mental health, and is always super kind. Thank Yushi for sharing codes for analysis and simulations as well as helping me correct my poor codes, and also inspiring me by his endless energy and enthusiasm. Thank Levke for kindly giving many suggestions on experiments and warm encouragement.

Last but not least, I would thank my family for their unwavering love and support. They have always been there for me, providing a safe environment that allows me to take psychotherapy. They have been my rock, offering me strength and guidance through every obstacle I encountered.

Once again, many thanks to all the wonderful people who have helped me along the way. I am truly grateful for their kindness and generosity.

AUTHOR'S DECLARATION

I declare that the work in this dissertation was carried out in accordance with the requirements of the University's Regulations and Code of Practice for Research Degree Programmes and that it has not been submitted for any other academic award. Except where indicated by specific reference in the text, the work is the candidate's own work. Work done in collaboration with, or with the assistance of, others, is indicated as such. Any views expressed in the dissertation are those of the author.

SIGNED: DATE:

TABLE OF CONTENTS

	Page
List of Tables	xi
List of Figures	xiii
1 Introduction	1
1.1 Colloids	1
1.1.1 Colloids as model system	1
1.1.2 Self-assembly	2
1.2 Hard spheres	3
1.2.1 Hard sphere crystallisation	3
1.2.2 Nucleation rate discrepancy	4
1.3 Colloidal interactions	7
1.3.1 Van der Waals Attraction Forces	7
1.3.2 Electrostatic interactions	8
1.3.3 Steric stabilisation	10
1.3.4 Polymers	10
1.3.5 Possible explanations for hard sphere nucleation rate discrepancy	15
1.4 Proteins as colloids	17
1.5 Rod-like colloids	19
1.5.1 Phase diagram and optical properties of liquid crystal	19
1.5.2 Rod-polymer mixtures	21
1.6 Predicting phase separation: the reduced second virial coefficient	22
2 Experimental and processing techniques	25
2.1 Imaging techniques	25
2.1.1 Scanning electron microscopy	25
2.1.2 Transmission electron microscopy	26
2.1.3 Confocal microscopy	27
2.1.4 Polariser	28
2.2 PMMA system	29

TABLE OF CONTENTS

2.2.1	Reaching density matching	30
2.2.2	Diluting samples to a given packing fraction	30
2.2.3	Glass capillaries	31
2.3	Rod system	33
2.3.1	Sepiolite clay	33
2.3.2	SAP polymer	34
2.4	Protein system	35
2.4.1	Expression of eGFP and mCherry	35
2.4.2	Purification of eGFP and mCherry	36
2.4.3	Concentration of proteins	37
2.4.4	Protein charge	37
2.4.5	Cationisation and anionisation	38
2.5	Image processing	39
2.5.1	Sampling density	39
2.5.2	Convolution and deconvolution	40
2.6	Structural characterisation	41
2.6.1	Radial Distribution Function	41
2.6.2	Topological cluster classification	42
3	Measuring Hard Sphere Nucleation Rates in Real Space	45
3.1	Introduction	45
3.2	Experimental System	47
3.3	Identifying crystal nuclei through image processing	49
3.3.1	Image parameters	49
3.3.2	Fourier transform	50
3.3.3	Cross-correlation	55
3.3.4	Particle tracking	57
3.4	Small PMMA — particles of $\sigma = 392$ nm	59
3.4.1	Understanding the volume fraction	59
3.4.2	Phase diagram	61
3.4.3	Discussion on the change of coexistence region	62
3.4.4	Nucleation barriers	64
3.5	Intermediate PMMA particles in the mixture of cis-decalin and tetralin	66
3.6	Large PMMA — L-PMMA	68
3.6.1	Phase diagram of L-PMMA	68
3.6.2	Tracking quality	71
3.6.3	Radial distribution function	73
3.6.4	Topological cluster classification	74
3.6.5	Nucleation barriers of L-PMMA	75

3.7	Conclusion	77
4	Binary Protein Gelation via Depletion Interaction	79
4.1	Introduction	80
4.1.1	Binary gel networks	80
4.1.2	Treating proteins as colloids	82
4.2	Experimental System	83
4.2.1	Characteristics of proteins	83
4.2.2	Protein Expression and Purification	84
4.2.3	Cationisation and anionisation of Proteins	85
4.2.4	Protein-Protein Interactions	86
4.2.5	Sample Preparation	87
4.3	Results	87
4.3.1	Phase diagram of eGFP plus PEG620 in deionised water	88
4.3.2	Investigating phase behaviour in different conditions	90
4.3.3	Binary Gel of eGFP and mCherry	93
4.3.4	Phase Behaviour of BSA in the presence of non-adsorbing PEG	94
4.3.5	Comparison with colloid–polymer mixtures	96
4.3.6	Phase behaviour of eGFP + BSA	99
4.4	Conclusion	102
5	Gelation of Colloidal Rod-Polymer Mixtures: Mean-field-like Arrest in 3D	105
5.1	Introduction	105
5.2	Experimental System	107
5.2.1	Preparation of stock suspensions	107
5.2.2	Particle characterisation	108
5.2.3	Phase diagram characterisation	110
5.2.4	Sample setup for confocal microscope	111
5.3	Results	112
5.3.1	Long-term phase behaviour	112
5.3.2	Phase behaviour neglecting gravity	115
5.4	Conclusion	121
6	Conclusion and future work	123
6.1	Hard sphere nucleation rates	123
6.2	Binary protein gels via depletion interaction	124
6.3	Gelation of Colloidal Rod-Polymer Mixtures: Mean-field-like Arrest in 3D	125
	Bibliography	127

LIST OF TABLES

TABLE	Page
3.1 The parameters of Yukawa potential for PMMA particles at $\sigma = 392$ nm.	60
3.2 The nucleation barrier heights for PMMA particles at $\sigma = 392$ nm.	65
3.3 The Yukawa parameters for the L-PMMA particles	71
4.1 Protein systems	88
4.2 Calculations of Yukawa potential for eGFP at different ionic strength	90
5.1 Rod mass fractions m and the calculated $\phi_{R_{\text{bare}}}$, $\phi_{R_{\text{eff}}}$, f_{nem} values.	110
5.2 Characteristic lengths ξ obtained by fitting $h(r)$ at $\phi_R = 0.00415$	120

LIST OF FIGURES

FIGURE	Page
1.1 Self-assembly systems	2
1.2 Sketch of the classical nucleation theory	5
1.3 The nucleation rate densities	6
1.4 DLVO dependence on the ionic strength	9
1.5 Sketch of the steric stabilisation	10
1.6 Illustration of polymer concentrations	12
1.7 Schematic picture of depletion interaction	12
1.8 Illustration of reservoir volume of spherical colloids	13
1.9 Illustration of reservoir volume of rod-like colloids	14
1.10 Theoretical phase diagram of globular proteins.	18
1.11 Sketch of the liquid crystal phases	20
1.12 Schlieren textures of nematic phase	21
2.1 Schematic picture of SEM and TEM	26
2.2 Schematic picture of confocal microscope	27
2.3 Schematic picture of polariser	28
2.4 Photos of sintering layers	32
2.5 Schematic diagram of sepiolite	33
2.6 Chemical formula of SAP230	34
2.7 Preparation of eGFP and mCherry	35
2.8 Scheme of cationisation and anionisation	38
2.9 TCC clusters	42
3.1 Representative confocal images used in this work	50
3.2 Scheme of fast Fourier transform processing	51
3.3 Identifying FT peaks	52
3.4 The effect of the ring threshold	53
3.5 FFT examples	55
3.6 The scheme for convolution	56
3.7 The scheme of nplocate algorithm	58

LIST OF FIGURES

3.8	The crystallinities of 392 nm PMMA	62
3.9	The size distribution of 392 nm PMMA	64
3.10	The nucleation barriers of 392 nm PMMA	65
3.11	The comparison of nucleation barrier heights of 392 nm PMMA and literatures	66
3.12	The crystallinities of 613 nm PMMA	67
3.13	The crystallinities of 1800 nm PMMA particles	69
3.14	The estimation of L-PMMA electrostatic interactions	70
3.15	A typical confocal image for particle tracking	71
3.16	The $g(r)$ and Percus–Yevick approximation of L-PMMA	73
3.17	The comparison of TCC analysis	74
3.18	Nuclei results of L-PMMA	76
3.19	The barrier heights	76
4.1	Examples of different binary gel systems	81
4.2	Possible binary gel structures	82
4.3	Protein structures	84
4.4	Phase diagram of eGFP + PEG620 in deionised water	89
4.5	Phase diagrams in different conditions	91
4.6	Confocal images of the binary structure of eGFP and mCherry.	94
4.7	Phase diagram of fluorescent labelled BSA in 25 mM HEPES plus 100 mM NaCl at pH 7.0	96
4.8	Phase states of colloid–polymer mixtures at $q = 0.40$ and 0.57	97
4.9	Phase diagrams in B_2 format	99
4.10	Binary gels of eGFP + BSA	100
4.11	Phase diagram of eGFP + PEG2000 in 25 mM HEPES plus 100 mM NaCl at pH 7.0 .	101
5.1	Size information of sepiolite clay B20	108
5.2	Isotropic-Nematic phase transition	109
5.3	Illustration of the scanned region	112
5.4	Polariser photos of B20 samples	113
5.5	Confocal images of B20 samples near the estimated phase boundary	114
5.6	3D reconstruction of B20 confocal image stacks	115
5.7	Phase diagrams of rods and PS with $L/D = 30$ and $q \approx 1$	116
5.8	A photo of B20 samples at $\phi_R = 0.0169$ with the increasing ϕ_P	116
5.9	Phase diagram of rods and PS with $L/D = 30$ and $q = 0.2$	118
5.10	$c(t)$ and $g(r)$ during phase transition	122

INTRODUCTION

1.1 Colloids

1.1.1 Colloids as model system

Colloids are the central theme in this thesis. We therefore first explain what they are. The word “colloid” refers to the heterogeneous mixture composed of insoluble particles dispersed in a continuous medium. It also denotes these dispersed particles themselves. Colloids have a diameter of approximately 1 nm to a few μm in any direction, implying that their size scale is much larger than the constituent particles of the medium, and thus the medium may be roughly treated as the background. A colloidal dispersion is intermediate between the suspensions in which complete sedimentation eventually occurs due to much larger particles, and solutions containing solute surrounded by solvent molecules, which are homogeneous and will never precipitate [86, 130].

The dynamics of the colloidal particles in a suspension is determined by Brownian motion, arising from the continuous collisions due to the thermal molecular motion of the medium, on the premise that the gravity is safely neglected. This requires colloids to have a much smaller diameter than the sedimentation length l_s , given by $l_s = k_B T / \Delta m g$ where k_B is the Boltzmann constant, T is the absolute temperature, Δm is the mass difference between the particle and the medium in the same volume (buoyant mass), and g is the gravitational acceleration.

Colloids can function as experimental model systems to investigate atomic or molecular phase behaviour, stemming from the fact that the thermal motions of the former is manifested by the Brownian motion. The understanding of similarities between colloids and basic particles has a long history. Einstein firstly recognised that colloids exhibit highly similar thermodynamics as atoms in statistics [83], for example, the Van’t Hoff equation [313] which reveals that the osmotic

pressure of a dilute suspension equals the pressure of a dilute gas of the same temperature and density. Perrin [227] examined the equilibrium density profile of resin colloids in a gravitational field, and found that it follows the Boltzmann distribution, obtaining a result that is known as the barometric distribution. Interestingly, gas molecules also follow the same law, providing evidence for the colloid to atom analogy. The thorough identification of this analogy was further developed by Onsager [213, 214], and McMillan and Mayer [195]. They proposed that the colloids can be considered as interacting through an averaged potential in which the osmotic pressure performs in a way similar to that of the total pressure of a gas system. Based on this analogy, colloidal particles have been used to study various self-assembly phenomena such as fluid, crystal [183, 241], glass [338] and phase coexistence [235].

1.1.2 Self-assembly

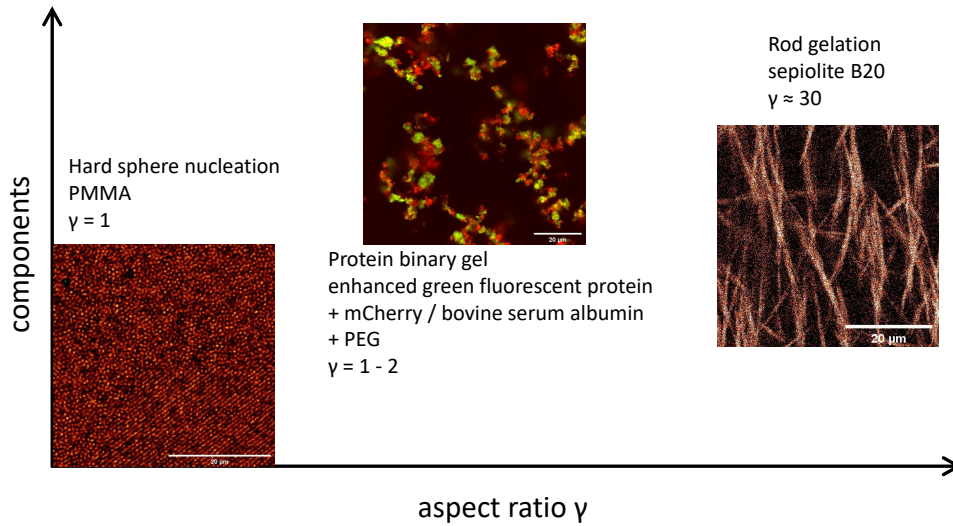


Figure 1.1: The systems investigated in this work. All the images are imaged by confocal microscopy. The complexity increases from left to right. (a) Hard sphere system consisting of monodispersed PMMA particles for nucleation rates (chapter 3). PMMA are regarded as weakly charged colloids. (b) Protein gelation via depletion interactions, in which several protein species are treated as colloids with different shapes (spheres or spherocylinders, see chapter 4). Polyethylene glycol (PEG) function as depletants. (c) Hard rod gelation via depletion interactions. The colloidal rods (sepiolite clay B20) have a high aspect ratio of around 30. Polystyrene (PS) are selected as depletants (chapter 5). Scale bars denote 20 μm .

Self-assembly is the spontaneous aggregation by which the specific patterns or structures forms by disordered and individual components, arising from the specific interactions between the components in their environment [135, 225]. This phenomenon exists throughout nature, from molecules to planets [323]. Tibbit proposed several principles for this architectural construction:

firstly, the constituent components need to be simple particles with programmable elements, such as amino acids in proteins. Secondly, the interaction is able to activate the assembling process. Finally, the system has a degree of resistance to errors and redundancy to produce desired architectures [303]. The work dedicated to the functional particles with distinct sizes and shapes for self-assembly and the approaches to realising various self-building activities is fast growing [225, 293, 334]. However, a complete understanding of the self-assembly mechanisms, as well as the methods of good process manipulation and imaging, remains rudimentary.

The most obvious building blocks of self-assembly systems are atoms and molecules, though we still lack effective approaches to precisely tuning the interactions due to their scale. Alternatively, colloidal particles, as mentioned above, can serve as atomic or molecular model systems. Their sizes (nanometres to microns) allow real-time and space imaging through various microscopy techniques, providing detailed information on the assembly process and the structures formed. Among different phase behaviour, the hard sphere phase transition becomes the benchmark. Pusey and van Meegen introduced a model system using polymethylmethacrylate (PMMA) colloidal particles to reproduce the hard sphere phase transition [241]. After that, more detailed research into hard sphere crystallisation was performed by means of light scattering techniques (see Sec. 1.2.2). However, a spectacular discrepancy still exists between the experimental and the simulation nucleation rates. We attempt to resolve this discrepancy by confocal microscopy in chapter 3.

Apart from the similarities to atomic and molecular systems, colloidal particles are able to mimic diverse conditions, as their interactions can be manipulated by the particle shape, dispersed medium, temperature, by particle surface modification, or by additives such as ions or polymers. Colloids may experience van der Waals attractions, electrostatic interactions and steric repulsion. Especially, the understanding of the depletion interaction, an attraction induced by the addition of non-absorbing polymers, has gradually developed since the 1950s [9, 10, 178, 321]. The phase behaviour of the mixture of such polymer species and proteins or rod-like colloids is at the core of chapters 4 and 5.

1.2 Hard spheres

1.2.1 Hard sphere crystallisation

Colloidal systems can be complex due to multiple components that vary in size and material. To obtain a deeper knowledge of these systems, model systems are commonly used. Ideally, they consist of monodisperse colloidal particles of identical size and material. The hard sphere model is one of the simplest models, widely studied for atoms and spherical molecules experiencing a particularly strong repulsive force at a short separation. The particles in such hard sphere model are defined as impenetrable spheres, which do not interact with each other when independent, yet the repulsion goes to infinity when they are going to overlap. The pairwise interaction potential

of the hard spheres is expressed as

$$(1.1) \quad u_{HS}(r) = \begin{cases} \infty, & r < \sigma \\ 0, & r \geq \sigma \end{cases}$$

where σ is the diameter of the hard spheres. This model provides a generic method to study the physical phenomena of perfect hard spheres. It can also be used to estimate the phase behaviours of systems with strong repulsion at short range [82]. Furthermore, many models collapse into a hard sphere model through mapping an effective hard sphere diameter σ_{eff} onto σ by matching the known characteristic properties, *e.g.* the freezing volume fraction and assuming the experimental data are related to the σ_{eff} [182, 258]. This model facilitates the investigation of key colloidal phenomena, allowing further insights into the behaviour of more complex systems.

The phase state of hard spheres is only determined by its volume fraction ϕ , where ϕ is calculated by the size σ and the number density n of the particles:

$$(1.2) \quad \phi = \frac{1}{6}\pi\sigma^3 n.$$

This system exhibits a first order fluid-crystal phase transition in equilibrium between the freezing volume fraction ϕ_f and melting volume fraction ϕ_m , which are equal to 0.494 and 0.545, respectively, as measured by Hoover *et al.* [134]. At a volume fraction under ϕ_f , the particles form a full fluid. In the coexistence region, the equilibrium crystallinity grows as a function of ϕ , until $\phi > \phi_m$ then the system is fully crystalline. Face centred cubic (FCC) structures are dominant from $\phi = 0.545$ to $\phi = 0.740$ as they have the highest entropy [192]. Yet when ϕ is higher than ~ 0.58 , hard spheres can experience vitrification if they prevent crystallisation [219], indicated by very slow dynamics.

1.2.2 Nucleation rate discrepancy

The classical nucleation theory (CNT) is the most widely used theoretical explanation to qualitatively understand the kinetics of nucleation [154]. CNT splits the Gibbs free energy of the formation of a spherical nucleus with the radius r into two terms, according to the following equation:

$$(1.3) \quad \Delta G = \frac{4}{3}\pi r^3 \rho_s \Delta\mu + 4\pi r^2 \gamma,$$

where ρ_s is the number density of the nuclei, $\Delta\mu$ is the difference in chemical potential between the solid and the surrounding fluid, and γ is the free energy density of the interface. The former term of the equation is the bulk term proportional to the nucleus volume, representing the energy decrease upon solid formation. It is always negative as the crystal has less free energy than the fluid in the supercooled region. The latter term, meanwhile, is the interfacial term which is always positive and proportional to r^2 , indicating the energy needed for creating a new surface.

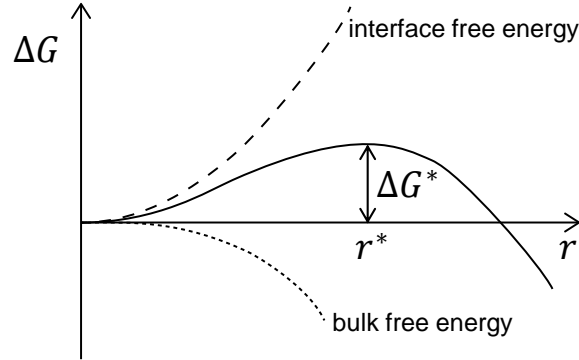


Figure 1.2: The schematic representation of the classical nucleation theory. The maximum global free energy is known as the nucleation barrier height ΔG^* , at which the nuclei size is defined as the critical size r^* .

When r is small, the second term dominates and thus ΔG increases. Only for the r larger than the critical size leads to a decrease of ΔG , which allows the spontaneous nucleation. This critical size is calculated by the height (maximum) of free energy ΔG , where the probability of the nucleus formation is minimum:

$$(1.4) \quad r^* = \frac{2\gamma}{\rho_s |\Delta\mu|}.$$

And the nucleation barrier height is given by

$$(1.5) \quad \Delta G^* = \frac{16\pi}{3} \frac{\gamma^3}{(\rho_s |\Delta\mu|)^2}.$$

The nuclei of critical size are metastable, and the attachment of the extra particles drops the free energy, making these nuclei more stable. The nucleation rate density I , showing the number of nuclei per unit time and per unit volume, is expressed by

$$(1.6) \quad I = A \exp \left[-\frac{\Delta G^*}{k_B T} \right],$$

where $A = \rho_f f_c^+ Z$ is the kinetic prefactor. Here ρ_f is the particle number density of the fluid, f_c^+ is the attachment coefficient representing the adding rate of molecules to the critical nuclei of the size n_c , and $Z = \sqrt{|\Delta G'|/(6\pi k_B T n_c)}$ denoting the Zeldovich factor, which describes the probability that critical nuclei continue to grow rather than melt. f_c^+ can be estimated by considering the rate of the particle transition and the number of particles around the nuclei surfaces. The first term is proportional to D_0/λ^2 (D_0 : diffusion coefficient, λ : typical distance for diffusion in the system), while the second term is proportional to the particle surface area, or $n_c^{2/3}$. Therefore, the attachment coefficient is obtained by

$$(1.7) \quad f_c^+ = \frac{24D_0 n_c^{2/3}}{\lambda^2}.$$

In real cases, fitting experimental data to CNT form is commonly used to obtain γ and λ [17, 272].

Most experimental data of the nucleation rate were measured through Small Angle Light Scattering (SALS) and Bragg Scattering (BS) (see Fig. 1.3), which both belong to scattering techniques. They are able to detect the mean radius of the nuclei $\bar{r}(t)$ at a given time point t and the crystallinity $\eta(t)$ of the whole specimen at the same time. The nucleation rate density is calculated as $I = \eta(t)/\frac{4}{3}\pi\bar{r}(t)^3 t$. Light scattering techniques allow characterisation of relatively small colloidal particles, *i.e.* $\sigma \leq 400\text{nm}$. Meanwhile, particle-resolved imaging techniques, such as confocal microscopy, have become more popular in recent years as they enable the identification of the particle positions which provide detailed information about the cluster structures for the crystallisation mechanisms [107, 146, 155].

Different studies may give different nucleation rates. This is because they scaled the results to relative rates by their own experimental parameters, such as the particle diameter and the solvent viscosity. Therefore, a uniform (reduced) dimensionless rate is needed for comparing various systems. It can be obtained by

$$(1.8) \quad I' = \frac{I\sigma^5}{D_s},$$

in which the scaling term $\frac{\sigma^5}{D_s}$ has the units of m^3s , neutralising the units of the nucleation rate density I with $\text{m}^{-3}\text{s}^{-1}$. D_s denotes the long time self-diffusion coefficient.

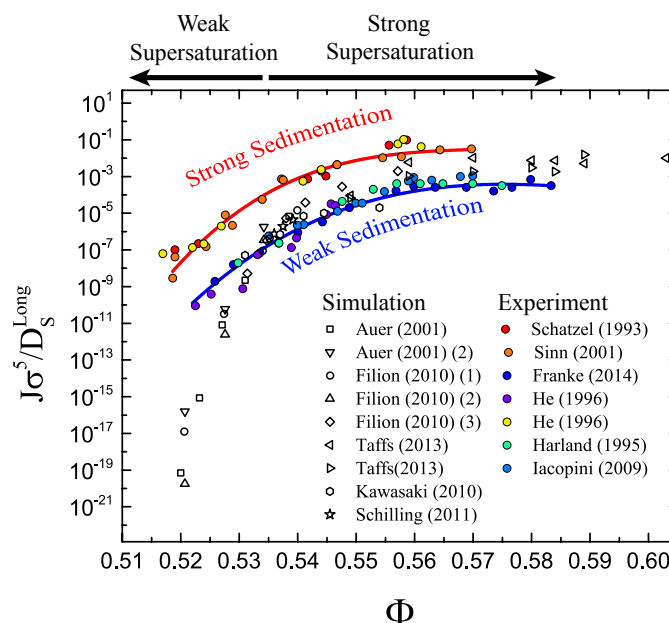


Figure 1.3: The literature results of the nucleation rate density scaled to uniform dimensionless unit. Open points are simulation data while coloured points represent experimental data with the polydispersity less than 0.055. The experimental data are sorted into two regions due to the different Peclet number, Pe , as pointed out by Russo *et.al* [263]. The upper region has Pe around 0.3 and the lower is of Pe around 0.01. Reprinted from Nicholas Wood [331].

Figure 1.3 shows the literature results of scaled hard sphere nucleation rate densities. These data split into three groups. The first is the group of top coloured points representing experimental data. They all used PMMA particles with $\sigma \sim 1 \mu\text{m}$ in a solvent mixture of tetralin and decalin [126, 267, 285]. The second batch of the experimental rates is the lower coloured ones, in which Harland *et al.* [124] and He *et al.* [126] also examined PMMA dispersed in tetralin and decalin, with the diameter $\sigma = 400$ and 430 nm, respectively. Iacopini *et al.* [139] and Franke [102] both studied micro gels of polystyrene of a diameter around 830 nm yet with different cross-link densities at $1/10$ and $1/30$, respectively. From the colloidal size, these systems seem indistinguishable. However, as was pointed out by Russo *et al.* [263], they actually have distinct Peclet numbers Pe . Pe is a dimensionless value, defined as the ratio of the gravitational to the diffusive rate of the particles, effectively normalising the colloidal sedimentation. When $Pe \gg 1$, sedimentation dominates the crystallisation process, whilst diffusion dominates when $Pe \ll 1$. The upper region in Fig. 1.3 is of Pe around 0.3 , and the lower region has Pe around 0.01 . Finally, the open symbols mean simulation data. Auer and Frenkel investigated the effect of polydispersity, and they report the results of hard sphere nucleation rate densities with a polydispersity from 0 [12] to 0.05 , 0.085 , 0.095 and 0.010 [13]. While other simulations focused on monodisperse particles. Filion *et al.* [94, 95] used several simulation techniques: forward flux sampling (triangle), molecular dynamics (diamond) and umbrella sampling (circle), as presented in Fig. 1.3. Schilling *et al.* [269] also used molecular dynamics as well as Monte Carlo simulation. These simulations reveal that the nucleation rate density grows rapidly with increasing hard sphere packing fraction in less supercooled region, say $\phi < 0.53$, whereas experimental rate density shows a much weaker dependence on ϕ at the same range. The discrepancy, at the lowest experimentally accessible packing fraction $\phi \approx 0.52$, exceeds 10 orders of magnitude. The possible reasons for this will be discussed after explaining the colloidal interactions.

1.3 Colloidal interactions

Ideal hard sphere dispersions do not exist in reality. However, it is possible to approach hard sphere dispersions through tuning the interactions between colloids. In colloidal systems, an unstable colloidal suspension tends to form aggregates as the attractive forces become dominant than the repulsive forces. The attraction mainly comes from the intrinsic van der Waals force, while different repulsions, including the electrostatic interaction and the steric repulsion, are often introduced to stabilise colloidal particles.

1.3.1 Van der Waals Attraction Forces

Van der Waals interactions occur between all particles, from the atomic to macroscopic scales. It originates from the transient oscillation of the electron cloud: the fluctuating electron density generates an electric field which induces a charge re-distribution of the neighbour particle,

thus the interactions between the dipoles form. They are short-range and steeply decrease as a function of r^6 where r is the centre-to-centre distance of two particles. Van der Waals forces have three contributions. For London (dispersion) forces, an instantaneous dipole polarises another natural molecule. Debye forces arise from the interactions between a permanent dipole and its polarised neighbour. Finally, in the case of Keesom forces, two inherent polarised molecules interact [130, 137]. The van der Waals potential of identical spherical particles was calculated by Hamaker as the following equation [142]

$$(1.9) \quad u_{vdW} = -\frac{A_H}{12} \left[\frac{\sigma^2}{r^2 - \sigma^2} + \frac{\sigma^2}{r^2} + 2 \ln \frac{r^2 - \sigma^2}{r^2} \right],$$

where A_H is the Hamaker constant and σ is the particle diameter. In a colloidal suspension, the value of the A_H is expressed by the refractive indices n and the dielectric constant ϵ as [142]

$$(1.10) \quad A_H = \frac{3}{4} k_B T \left(\frac{\epsilon_p - \epsilon_s}{\epsilon_p + \epsilon_s} \right)^2 + \frac{3h\nu}{16\sqrt{2}} \frac{(n_p^2 - n_s^2)^2}{(n_p^2 + n_s^2)^{\frac{3}{2}}},$$

where the subscript “p” and “s” denote particle and solvent, respectively, h is the Planck constant and ν is the frequency of fluctuation. In many cases, the van der Waals attractions can be minimised through preparing the dielectric constant or refractive index matching. However, these matchings are not always accessible for specific experimental conditions, thus the colloidal particles may form irreversible aggregation. To avoid undesired clusters, counteracting forces are needed. Electrostatic repulsion as well as steric stabilisation is commonly performed to stabilise particles in suspensions [137, 282].

1.3.2 Electrostatic interactions

It is widely accepted that a degree of charging is always induced during the dispersion of the colloidal particles into liquid mediums, by existing surface ionic groups, or the absorption of ions from the liquid, or both [258]. Ions of the opposite charge as the particles, known as counterions, form a layer enclosing the particles to balance the surface charge. This layer is defined as the electric double layer, with its thickness given by the Debye screening length $1/\kappa$. κ is determined by the dielectric constant and the ionic strength of the system, as

$$(1.11) \quad \kappa = \sqrt{4\pi\lambda_B\rho_{ion}},$$

where λ_B is the Bjerrum length describing the separation at which the interaction potential between two charged particles is equal to $k_B T$. It is calculated by $\lambda_B = \beta e^2 / (4\pi\epsilon_0\epsilon_r)$, in which $\beta = 1/k_B T$ is the thermal energy scale, e is the elementary charge, ϵ_0 is the permittivity of free space and ϵ_r is the relative dielectric constant of the solvent [170, 325]. The Debye screening length indicates the range of the electrostatic interactions. Far from the double layer the positively and negatively charged species achieve a fixed averaged value. In contrast, a repulsive potential is induced when two double layers overlap. The repulsion, as a function of the interparticle distance

for non-aqueous media and a consequent low ion concentration, is approximated by solving the Debye-Hückel equations in a linear Poisson-Boltzmann treatment which are of Yukawa form [252, 257]:

$$(1.12) \quad u_Y(r) = \epsilon_Y \frac{\exp[-\kappa(r - \sigma)]}{r/\sigma},$$

where ϵ_Y is the contact potential, calculated by

$$(1.13) \quad \epsilon_Y = k_B T \frac{Z^2}{(1 + \kappa\sigma/2)} \frac{\lambda_B}{\sigma},$$

in which Z is the particle charge scaled by the elementary charge e .

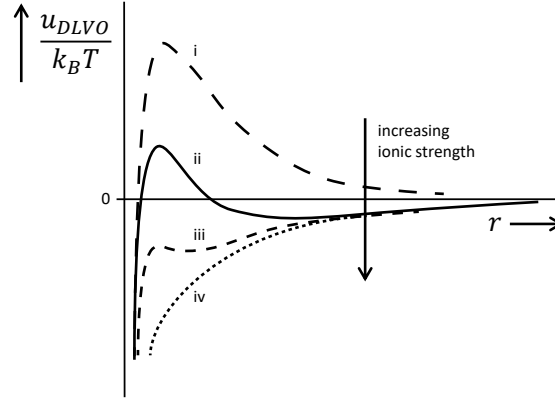


Figure 1.4: Illustration of DLVO potential dependence on the ionic strength. The ionic strength increases from i to iv .

The theory for the total interaction between charged colloidal particles was developed by Derjaguin and Landau [73], and Verwey and Overbeek [317], independently. It is now known as the DLVO potential, simply given by

$$(1.14) \quad u_{DLVO} = u_{vdW} + u_Y.$$

A schematic plot of the DLVO potential is represented in Fig. 1.4. Since the u_{DLVO} is the sum of u_{vdW} and u_Y , it is manipulated by the ionic strength, usually through adding salt, at a given van der Waals potential and colloid size. At a high ionic strength, the van der Waals attraction dominates, leading to particle aggregation. With less salt, a local maximum and a shallow secondary minimum appear, as indicated by Fig. 1.4(ii). The local maximum is at a distance comparable to the Debye screening length $1/\kappa$ which may suppress the particles irreversibly dropping into the deep attractive well (the primary minimum) at very short separations, while the aggregations due to the secondary minimum can be broken by decreasing the salt concentration or shaking. Finally, at low salt levels, the inter-particle interactions are repulsive, and a stable suspension is expected [174, 262].

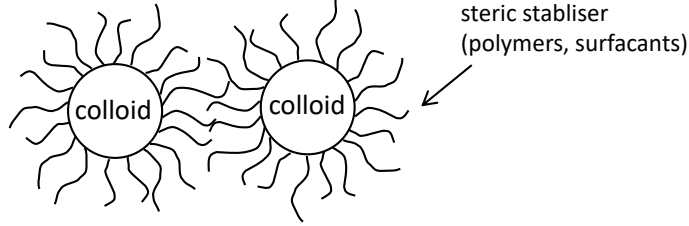


Figure 1.5: Sketch of the steric stabilisation.

1.3.3 Steric stabilisation

Steric stabilisation is another effective method to prevent particle aggregations [96]. Polymers can be absorbed or be chemically bound to the particle surfaces, which gives rise to a significant repulsive potential, as shown in Fig. 1.5. When two particles approach into the range of the attached polymers, the chains compress or interpenetrate, leading to a growing local polymer density. The repulsion is then generated by the lower polymer configurational entropy [294]. The working range of the steric layer is tuned by the length of polymer chains, thus the van der Waals attraction can be safely neglected if it is shorter than the steric repulsion [295, 325].

Especially, for polymethylmethacrylate (PMMA) particles grafted with poly-12-hydroxystearic acid (PHSA) used in our experiments, the steric stabilisation is well described by [42, 167, 258]

$$(1.15) \quad u_{\text{steric}}(r) = \epsilon(\sigma_h/r)^n.$$

where ϵ is the strength of the repulsion, σ_h is the diameter at which the hard-core potential becomes infinite, in other words, the separation at which the PHSA chains are fully interdigitated, r is the colloidal separation, and n is the repulsive index. Bryant *et al.* [42] also revealed that larger particles become harder and thus behave more like hard spheres with a given length of the steric layer.

1.3.4 Polymers

1.3.4.1 Polymer chains in solution

A polymer molecule is a chain of repeating sub-units, known as monomers. In the solid state, polymers are compact with little free space (voids) in either amorphous or semi-crystalline structure. On the contrary, they separate and are surrounded by the solvent molecules in a dilute solution. The polymer molecules constantly alter their 3D conformation in the solution, and the simplest model to describe them is the ideal chain, which treats a linear flexible chain with N bonds of length b as a random walk: it is placed in a cubic lattice where the move direction is limited to lattice axes and the step length is equal to b . From this model the characteristic radius, named as radius of gyration R_g , can be obtained[301].

However, two factors contribute to non-ideal chains in the real situation. The first is the excluded volume. Any monomers cannot overlap with another, neither their constituent parts.

Considering a dilute solution where each polymer molecule is independent, the unavailable volume for a monomer is the actual volume of other monomers plus the enclosed layers with a thickness of its size (the distance from its centre to the touching edge). A well-studied model including the excluded volume is the self-avoiding walk (SAW), preventing the revisiting of the same places in the lattice that have been visited. This model leads to a larger R_g . In general, the fitting of the SAW simulation gives the relationship of R_g and chain length, as the following equation [301]

$$(1.16) \quad R_g = 0.42N^{0.59}b.$$

The second noticeable factor is the effect of the solvent. The “good solvent” dissolves a given polymer well with lower free energy of the mixture, and vice versa. In the good solvent the monomers interact with the solvent molecules in preference to other monomers, inducing a repulsion between polymers and the expansion of the polymer coils, whilst in the poor solvent the inter-polymer interactions are energetically favourable, and the chains shrink. Flory–Huggins solution theory is a lattice model approximating thermodynamic properties for dissolving a polymer into a solvent. It assumes that every site of the lattice is occupied by either a polymer segment or a solvent molecule. The equation of the change of the Gibbs free energy during dissolving is then given by [97]

$$(1.17) \quad \Delta G = k_B T (n_s \ln \phi_s + n_p \ln \phi_p + n_s \phi_p \chi_{sp}),$$

where n_s and ϕ_s are solvent mole number and volume fraction, n_p and ϕ_p are polymer mole number and volume fraction, and χ , known as χ parameter, is defined by the energy change and the coordination number of the lattice Z by

$$(1.18) \quad \chi = Z[\epsilon_{sp} - (\epsilon_{ss} + \epsilon_{pp})/2]/k_B T,$$

where the meaning of ϵ is represented by its subscript, *i.e.* ϵ_{sp} means the solvent-polymer (sp) contact interaction. The symbol of χ indicates the favourable interactions: if χ is positive, polymers prefer to interact with each other, while a negative χ facilitates the polymer-solvent interactions. In particular, the value of χ is used as a criterion for identifying the polymer conformation. The solvent with $\chi = 0.5$ is defined as a “theta solvent (θ solvent)” where the excess chemical potential as well as enthalpy change of mixing is zero, and the polymer chains behave like ideal chains. In general, for a given polymer, if $\chi < 0.5$ then the solvent can be regarded as a good solvent [34, 35].

1.3.4.2 Overlap concentration

In a dilute solution with a good solvent, each polymer coil swells and roughly occupies a spherical space of a radius equal to R_g . They do not overlap as discussed before that the polymer-solvent interactions are more favourable. However, upon increasing the polymer concentration, they

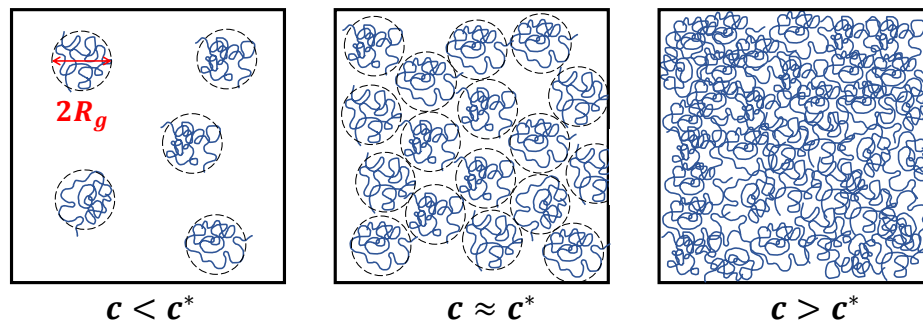


Figure 1.6: Illustration of polymer configurations with increasing concentration. $c < c^*$: dilute solution; $c \approx c^*$: near the overlap concentration; $c > c^*$: semi-dilute solution.

finally touch each other. The overlap concentration c^* , describing the state point at which the polymers fully fill the solution in their original shape without overlapping, is calculated as

$$(1.19) \quad c^* = \frac{3}{4\pi R_g^3} \times \frac{M_w}{N_A},$$

where M_w is the polymer molecular weight, and N_A is the Avogadro's constant. Fig. 1.6 shows the shape of polymer coils in different concentrations c . When c is smaller than c^* , the solution is a dilute solution where polymers are separate. When $c > c^*$ the solution is semi-dilute. Polymers are allowed to overlap in this condition, and the excluded volume gradually decreases to zero as a function of c [301, 340].

1.3.4.3 Depletion interaction

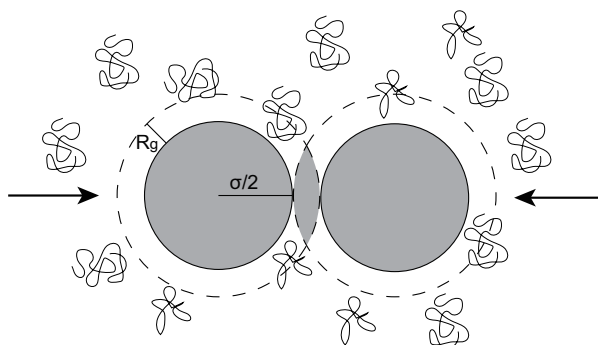


Figure 1.7: Illustration of the occurring of depletion interaction with spherical colloids plus non-absorbing polymers. The depletion layers are showed by the dashed lines. For overlapping depletion layers (grey area in the middle) the particles undergo anisotropic osmotic pressure as the polymers cannot enter the in-between space. The induced attraction is indicated by the arrows.

In colloidal suspensions, an inter-particle attraction can be induced by the addition of non-absorbing polymers. This is known as the depletion interaction, becoming first clear in 1954 by the

study of Asakura and Oosawa [9, 10], Both theoretical and experimental work of colloid-polymer mixture was carried out by Vincent [178] and Vrij [321]. Consider the most simple system, in which both colloids and polymers are spherical: a schematic picture is shown in Fig. 1.7. Here colloids are hard, which means they cannot overlap with each other, neither colloids and polymers. Thus, a homogeneous layer with a thickness of R_g (polymer radius of gyration) enclosing a particle — known as the depletion layer, indicated by short dashes in Fig. 1.7 — forms, which also excludes other polymers in the system. When two colloidal particles approach each other, the depletion layers overlap, generating a small space in-between (grey area) where polymers cannot enter, leading to the unbalance of osmotic pressure on particles. The effect of this is equivalent to an attraction between the colloids. Although the sketch depicts the case of colloidal spheres, the colloids can be any shape, and the corresponding Asakura Oosawa (AO) depletion potential is uniformly calculated by

$$(1.20) \quad W_{AO}(s) = \begin{cases} \infty, & s < 0 \\ -PV_{\text{overlap}}(s), & 0 < r < 2R_g \\ 0, & 2R_g < r \end{cases}$$

where s is the separation between two particles, $P = n_B k_B T$ is the osmotic pressure arising from the polymers with the polymer bulk number density n_P , and V_{overlap} is the total volume of overlapped depletion layers.

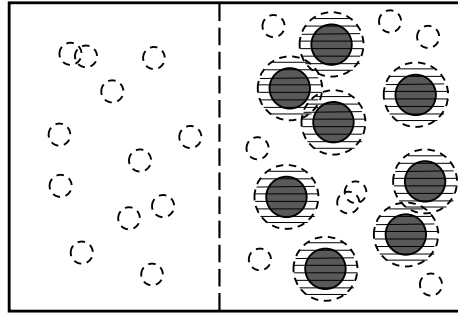


Figure 1.8: Illustration of the reservoir volume fraction. The reservoir (left) is in the osmotic pressure equilibrium with the right system comprised of hard spheres and depletants (dashed circles). The unshaded regions at right are available volume fraction for polymers. The hypothetical semi-membrane is indicated by the vertical dashes in-between.

Spherical colloids For a given shape of colloidal particles, the AO potential and the consequent phase behaviour is determined by the polymer-colloid size ratio $q = 2R_g/\sigma$ and the polymer reservoir volume fraction ϕ_P^R . The concept of a polymer reservoir can be explained by the free volume theory (FVT), which is widely used to simulate depletion phase behaviour. This theory considers the equilibrium of osmotic pressure between a colloid-polymer mixture and a polymer-only system. The polymers are simplified as penetrable hard spheres (phs). As shown in Fig. 1.8,

the whole container is separated by a semi-membrane which allows transit of phs and solvent but not of colloids. Treating the solvent as background, the reservoir (left) only consisting of phs attains osmotic equilibrium with the mixture of phs and colloids (right). Now the available free volumes for phs on the two sides are equal: it is the space not occupied by the particles and depletion layers, where the layers may overlap depending on the colloidal concentration. The reservoir volume fraction is then defined as the ratio of total phs volume to the volume of reservoir. The experimental volume fraction is related to reservoir volume fraction by $\phi_{exp} = \alpha \phi_{res}$, where α can be calculated by the free volume approximation [174]:

$$\begin{aligned}
 \alpha &= (1 - \phi) \exp \left[-A \left(\frac{\phi}{1 - \phi} \right) - B \left(\frac{\phi}{1 - \phi} \right)^2 - C \left(\frac{\phi}{1 - \phi} \right)^3 \right], \\
 A &= 3q + 3q^2 + q^3, \\
 B &= \frac{9}{2}q^2 + 3q^3, \\
 C &= 3q^3,
 \end{aligned}
 \tag{1.21}$$

where ϕ is the colloid volume fraction, q is the size ratio of phs to colloids.

With the known polymer reservoir volume fraction, the depletion potential of spherical colloids can be calculated as [174]:

$$\beta u_{AO}(r) = \begin{cases} \infty, & r < \sigma \\ -\phi_P^R \frac{(1+q)^3}{q^3} \left[1 - \frac{3r}{2(1+q)\sigma} + \frac{r^3}{2(1+q)^3\sigma^3} \right], & \sigma \leq r < \sigma + 2R_g \\ 0. & \sigma + 2R_g < r \end{cases}
 \tag{1.22}$$

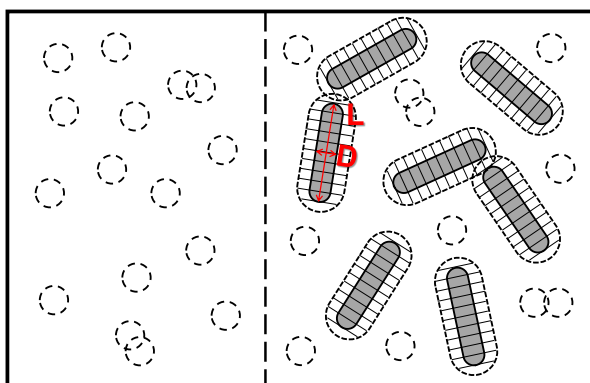


Figure 1.9: Illustration of the reservoir polymer volume fraction in the case of rods. The reservoir (left) is in the osmotic pressure equilibrium with the right system comprised of hard rod-like colloids and polymers, with a hypothetical semi-membrane in between (vertical dashes) that only allows pass of polymers (dashed circles). The available free volume for polymers at right is the unshaded regions.

Rod-like colloids Another common colloidal shape used in the model depletion systems is spherocylinder. The rod-like particles are characterised by an extra parameter, the aspect ratio

$\gamma = L/D$, where L and D are the length and the diameter of the rods, respectively. Here L uses the length of the entire colloid, as shown by the red arrow in Fig. 1.9. The size ratio is defined as $q = 2R_g/D$ in the rod-polymer mixture. Similarly, the fraction of available volume for depletants, α , can also be calculated by the free volume theory to obtain the reservoir volume fraction [174]:

$$\begin{aligned}
 \alpha &= (1 - \phi_R) \exp \left[-A \left(\frac{\phi_R}{1 - \phi_R} \right) - B \left(\frac{\phi_R}{1 - \phi_R} \right)^2 - C \left(\frac{\phi_R}{1 - \phi_R} \right)^3 \right], \\
 A &= \frac{6\gamma}{3\gamma - 1} q + \frac{3(\gamma + 1)}{3\gamma - 1} q^2 + \frac{2}{3\gamma - 1} q^3, \\
 B &= \frac{1}{2} \left(\frac{6\gamma}{3\gamma - 1} \right)^2 q^2 + \left(\frac{6}{3\gamma - 1} + \frac{6(\gamma - 1)^2}{(3\gamma - 1)^2} \right) q^3, \\
 C &= \frac{2}{3\gamma - 1} \left(\frac{12\gamma(2\gamma - 1)}{(3\gamma - 1)^2} + \frac{12\gamma(\gamma - 1)^2}{(3\gamma - 1)^2} \right) q^3.
 \end{aligned}
 \tag{1.23}$$

The AO potential of rod-like colloids varies depending on the size ratio q . Full expressions can be found from Lekkerkerker and Tuinier [174].

1.3.5 Possible explanations for hard sphere nucleation rate discrepancy

With the knowledge of colloidal interactions, we re-examine the experimental systems for the possible reasons for the hard sphere nucleation rate discrepancy. Most previous experimental work used sterically stabilised PMMA particles. Unlike perfect hard spheres in the simulations, the properties of PMMA and the solvent may affect the nucleation rates. We propose three potential explanations here. Firstly, the simulations of the homogeneous crystallisation do not count the colloid sedimentation. The movement of particles is clearly affected by the gravity with imperfect density matching, and this influence becomes stronger when using larger particles for imaging purposes. Many experimental studies took PMMA particles of $\sigma \sim 1\text{--}2\ \mu\text{m}$ [124, 267, 285]. Russo *et al.* [263] performed Brownian dynamics simulations with the Weeks–Andersen–Chandler (WCA) potential, which is a short-ranged repulsion model for nearly hard sphere cases. They found that the density difference significantly increases the nucleation rates to the similar scale of the experimental data, that is to say, the nucleation process accelerated by the sedimentation can fully explain the discrepancy. This is due to the heterogeneous density distribution along the gravity direction (density profile). For a sample with the average volume fraction $\phi_{ave} = 0.52$, the final volume fraction at the bottom is more than 0.54, and the volume fraction difference between the bottom and the top can exceed 0.1. Crystallisation then strongly prefers to occur in these high concentrated regions, and the measured rate is approximately equivalent to that of $\phi = 0.55\text{--}0.56$. Moreover, Ketzetzi *et al.* [155] studied PMMA particles of a hydrodynamic radius $r = 0.97\ \mu\text{m}$ through confocal microscopy. They supported the conclusion that sedimentation enhanced the crystallisation rate, but contradicted the simulations of Russo *et al.* in that the enhancement arose from the difference in local packing fraction. Instead, they found that the nucleation barrier had little correlation with the local packing fraction, and the barriers are almost the same along

the sample. Therefore, the role of sedimentation in the nucleation of hard sphere-like colloids remains unclear.

In order to eliminate the sedimentation, density matching is necessary. The key point is that the refractive index and density match are unable to be satisfied simultaneously in any known solvent. Light scattering techniques allows small colloids, say < 500 nm, thus the mixture of cis-decalin and tetralin is widely used which provides good refractive index matching with a final density ~ 0.93 g/cm³, calculated from He *et al.* [126] giving a mass fraction of $m_{\text{tetralin}} : m_{\text{decalin}} = 46 : 54$, while the density of PMMA is 1.196 [252]. We therefore expect that a single particle sediments less than 0.8 mm per day, and the effects of sedimentation can be safely neglected. However, for long-term observations or larger colloids, *i.e.* $\sigma > 1$ μm for tracking purposes, this density mismatching results in significant sedimentation which has been proved to remarkably enhance the nucleation rates by Brownian dynamics simulations [263] and experiments [155]. On the other hand, cycloheptyl bromide (CHB) is selected to prepare well density matched solvent in accompany with cis-decalin. This change does not only ignore the refractive index matching, but also results in high levels of electrostatic charging, giving the second possible reason: the softness.

PMMA exhibit a degree of softness from two sources. They have intrinsic softness of steric stabilisation arising from the grafted PHSA polymer chains, since the PHSA chains can be compressed. As discussed in Sec. 1.3.3, larger particles become harder with a given thickness of steric layer, yet for smaller ones it needs to be considered. Moreover, in the low dielectric constant solvents ($\epsilon_r = 2.2$ for cis-decalin [328] and $\epsilon_r = 7.9$ for CHB [128]) induce a significant degree of charging by the rule of thumb $Z\lambda_B/\sigma \approx 6$ [258], as well as leading to an almost unscreened Debye length as the ionic strength can be down to 10^{-10} M in the density matched mixture of cis-decalin and CHB [339]. In order to suppress the electrostatics, tetrabutyl ammonium bromide (TBAB) salt is added, though it has limited solubility in CHB. The maximum concentration of the salt is around 260 nM [175, 257], leading to a Debye length of around 100 nm. Given the length scales of the softness, the smaller particles seem to be affected more, as the ratio of the effective to the core diameter is inversely proportional to particle size at a given thickness of the soft layer. However, the experimental data in Fig. 1.3 shows that smaller ones agree better with the simulation results. Auer *et al.* [18] numerically investigated the effect of the PHSA stabilisation through comparing their freezing volume fraction with that reported by Pusey and van Megen [241], and found that individual steric repulsion was not able to fully explain the shift of the freezing packing fraction as they obtained a polymer length 2-3 times longer than that experimentally measured before, thus a further longer ranged repulsion term was needed. They then turned to weakly charged particles with the interaction represented by a Yukawa potential, as given by Equ. 1.12. This additional electrostatic repulsion helped the system better agree with the experimental ϕ_f , but only gave an upward shift of the nucleation rate densities by less than 2 orders of magnitude.

Finally, polydispersity δ also alters crystallisation, and has been studied as a possible reason for the rate gap. Simulation work shows that polydispersity shifts the coexistence region, but to an inverse direction. Fasolo *et al.* showed that the ϕ_f increased by about 0.02 for a δ of around 0.05, and the system might exhibit complex phase behaviours, such as fractionations into different solid phases [90]. Pusey *et al.* found that higher polydispersity ($\delta > 10\%$) suppressed the crystallization [240]. However, experimental data shows weak correlations between the δ and the nucleation rates. The upper group in Fig. 1.3 contains the results of Sinn *et al.* with $\delta = 0.025$ [285], Schatzel *et al.* [267] and He *et al.* [126] both with $\delta = 0.05$. whilst the lower group consists of Harland *et al.* with $\delta = 0.05$ [124], He *et al.* with $\delta = 0.07$ [126], Iacopini *et al.* with $\delta = 0.065$ [139] and Franke with $\delta = 0.055$ [102]. Given the polydispersity of the systems above, we find that particles with larger δ actually agree with the simulation better. Thus this property fails to resolve the discrepancy.

1.4 Proteins as colloids

One step up in complexity of the model systems, is from the nonfunctional colloids, *e.g.* silica or PMMA particles which are commonly used in hard sphere models, to functional particles. Hierarchically designed microstructures can be achieved by controlling the inter-particle interactions. If the constituent particles have specific properties, including physical, chemical and biological functions, the formed network may retain corresponding properties. With this in mind, the assembly of novel materials and applications via careful manipulation of the interactions has obtained significant progress in various fields [114], where proteins draw attention since they present various functions and properties, *e.g.* fluorescence, conductivity and light-harvesting [38, 43], giving promising prospects for constructing functional networks, and consequently offering unprecedented opportunities for the development of innovative biomaterials [186, 320].

Proteins themselves perform an essential role in all the cellular activities. They are large bio-macromolecules consisting of long chains of amino acids which are connected by peptide bonds. Each protein has its unique sequence of amino acids. Once formed, polypeptides will fold to a particular 3D configuration stabilised through several interactions, such as van der Waals attractions, electrostatic interactions, hydrogen bonds, covalent bonds and hydro-philic/phobic interactions. This spatial configuration determines the expressed properties of the protein [27].

Compared with isotropic colloids, protein molecules exhibit a much higher level of complexity because of their 3D conformation and their amino acid constitution, as different amino acids present various chemical properties and polarities, giving proteins shape, charge, and functional anisotropy. They also have a pH-related heterogenous charge distribution over their surface. Especially, each protein has a characteristic pH, named isoelectric point (pI), at which their net charge becomes neutral. Proteins can become more positive or negative due to the gain or loss of H^+ , at pHs lower or higher than their pI, respectively [85]. In general, a protein can be

affected by the electrostatic interaction, the van der Waals attraction, the depletion interaction, the counter-ion interaction, the hydrophobicity or hydrophilicity, and the hydrogen bonding in a dispersion [136, 144, 347]. This complexity leads to challenges for a full understanding of protein self-assembly. Therefore, a possible approach is to treat globular protein molecules as coarse-grained models, in particular, “patchy particles”, for studying phase behaviour. This model assumes a molecule is a hard sphere with attractive patches on its surface. Indeed, globular proteins under experimental conditions present similar phase transitions compared with the numerical estimation predicted by the patchy model [179, 193, 243]. An advantage of this method is that the attractive force is controllable in the protein solutions. Firstly, the electrostatic repulsion induced by the overlap of electric double layers can be tuned by pH and ionic strength, which further affects the overall interactions. Secondly, the patches can be decorated by protein surface modification, including cat-/an-ionisation and bonding other functional groups. Finally, some trivalent salts have been proved to drive protein assembly and consequent formation of crystals and gels [345].

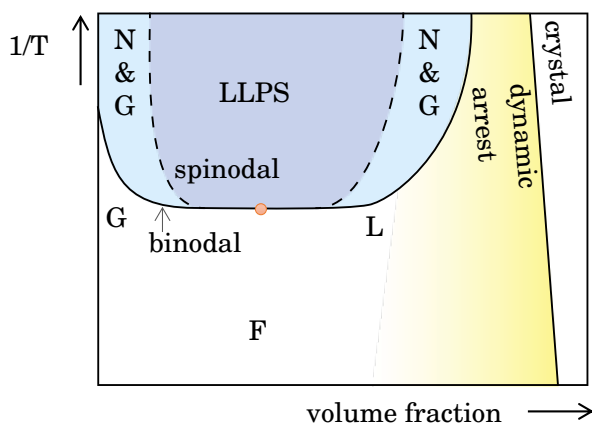


Figure 1.10: A schematic phase diagram of globular proteins. The proteins are treated as colloids with short-ranged attractions. “G”, “L” and “F” mean gas, liquid and fluid. “N & G” denotes nucleation and growth. The spinodal line is the dashes. The critical point is indicated by the orange circle [194, 260].

If further simplifying the globular proteins, they can be treated as hard spherical colloids with isotropic interactions. In recent years, further understanding of protein phase behaviour, such as the mechanism of crystallisation, has been made on the basis of their phase diagrams. It has been proved that the phase behaviour of colloids under an attraction highly depends on the value and the range of the attractive force [5]. For example, a metastable liquid-liquid phase separation appears with spherical colloids experiencing sufficiently short-ranged attraction, *i.e.* within $\sim 1/4$ of the hard core radius [341]. Likewise, one of the most important observations is that a liquid-liquid thermodynamically metastable state occurs below the temperature corresponding to the fluid-solid coexistence phase boundary in the case of globular proteins with

short-ranged attractions [41, 174]. Fig. 1.10 presents a typical phase diagram of such globular protein suspensions [79, 194]. Two important regions can be distinguished by the binodal and spinodal curves. Between these two lines, the solution is supersaturated and metastable with respect to small fluctuations, though the phase separation may occur by the formation of protein nuclei, which continue to develop before the system achieve equilibrium. Meanwhile, inside the spinodal curve, the spontaneous demixing occurs via through the spinodal decomposition in the absence of nucleation. Due to the small size of the protein molecules (usually a few nanometres), the phase separation is experimentally manifested as a liquid-liquid phase separation (LLPS) between a denser and a more diluted region. In other words, LLPS can represent any phase separation behaviour below the binodal curve in the biochemical field [80, 174, 194]. Note that “gas-liquid coexistence” is more frequently used in physics, and it is equivalent to the LLPS, both denoting the state in which two phases of different density, namely particle-poor and particle-rich domains, coexist. In order to further compare with protein experiments, we use LLPS throughout this work.

Moreover, the colloidal arrested states, such as gels and glasses, can occur inside the spinodal line [341]. Similarly, gels are likely to form through spinodal decomposition in protein solutions, as the same mechanism in colloidal systems [49]. The dynamically arrested phases, *i.e.* gels or glasses, can be achieved with quenches into LLPS region and/or high protein concentrations. Thus, manipulation of protein interactions around this metastable LLPS area becomes essential to investigate protein crystallisation, or kinetically trapped (gel or glass) states [106, 231, 233, 330]. The pathways into different states can be tuned by altering the attractive interactions, for example, depletion interactions induced by the addition of non-adsorbing polymers such as polyethylene glycol (PEG), since an increase in the polymer volume fraction is equivalent to a decrease in temperature in Fig. 1.10. The gelation driven by the depletion interactions is the main topic of Chapter 4.

However, in real cases, protein molecules still present anisotropic surface conditions including charge and amino acid groups as well as shape heterogeneity when compared with common colloidal particles. Considering the multi-involved interactions and the possible denaturation of the proteins (the process that proteins lose their folding structure and thus their inherent biological activities and functions) arising from pH, temperature and the additional salts, experimental conditions need to be carefully examined for each species used.

1.5 Rod-like colloids

1.5.1 Phase diagram and optical properties of liquid crystal

Another step up in complexity of the model systems is to use non-spherical colloids. In-depth investigations have been carried out on hard sphere suspensions. Meanwhile, anisometric particles have drawn increased attention in recent years [201, 206, 212]. A notable subset of these

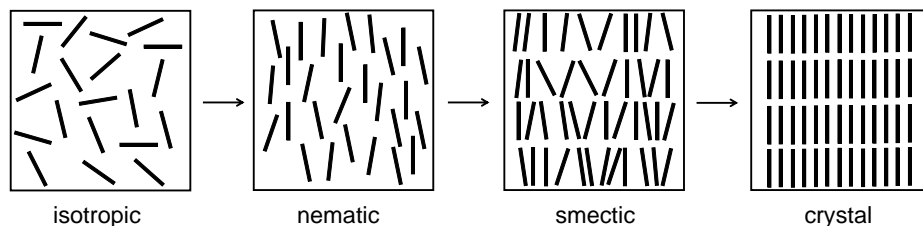


Figure 1.11: Schematic pictures of phases which may be obtained through concentrating a dilute dispersion of hard rods.

materials comprises clay minerals, either naturally-occurring or synthetic. They are characterised by their disc-like or rod-like shapes, and exhibit interesting phase behaviours in dispersions, such as liquid crystals [212]. Liquid crystals are an interesting class of materials with properties between isotropic liquid and solid crystal. For example, they are able to flow in a liquid style, but also exhibit symmetries intermediate between those of ordinary liquids and crystalline solids. The formation of liquid crystals requires anisometric constituent molecules or particles, such as a rod-like shape [288]. There are mainly three types of liquid crystals: thermotropic, lyotropic and metallotropic liquid crystals. The thermotropic type undergoes phase transitions as a function of temperature. Lyotropic types involve dispersing components into a solvent, namely colloidal liquid crystals. It exhibits different phase states in response to both temperature and particle concentration. In this work we only studied one lyotropic liquid crystal, sepiolite clay B20, at $\sim 20^\circ\text{C}$ and thus the effects arising from the temperature change can be ignored. Finally, the metallotropic liquid crystal refers to the material consisting of inorganic ions bound to long chain surfactants [191]. There are several kinds of liquid crystal phases which possess different symmetries. Fig. 1.11 shows the phase states as a function of hard rod volume fraction with the aspect ratio > 3.5 [174]. The isotropic phase has the homogeneity in any direction, and has no long-range order; the nematic phase exhibits the orientational order as it breaks the rotational symmetry; the smectic phase further shows the translational periodicity, in which layers form and can slide over another (rows in Fig. 1.11(c)); the crystal phase has both discrete translational and rotational symmetries. In this work we only studied the first two types, namely isotropic and nematic phases. The addition of non-absorbing polymers as depletants significantly alters the isotropic–nematic phase transition, as will be discussed in chapter 5.

The isotropic phase and typical liquid crystals can be differentiated by the birefringence. Birefringence is the optical property indicating different refractive indices determined by the direction of the polarisation and propagation of incident light. In a nematic phase, the horizontal refractive index (n_h) and the vertical refractive index (n_v) are different. Polarised incident light will be split into two rays with the same frequency but distinct phases, and these two rays travel at different velocities based on the thickness of the liquid crystal and the anisotropic refractive indices. The birefringence provides an effective method to distinguish the isotropic and nematic phases. When observed between a crossed polariser, the nematic phase alters the polarisation

of the incident beam, then the beam can partially pass the second crossed polariser as it is no more vertical to the second one. The flow and the retardation of the nematic phase generate characteristic dark and bright regions, known as “Schlieren texture”, as shown in Fig. 1.12. In contrast, the isotropic phase is unable to change the polarisation of the beams as it has identical refractive indices in any directions, thus the beam is blocked and only dark regions show (see Sec. 2.1.4 for a detailed explanation of polariser).



Figure 1.12: The Schlieren textures of the nematic phase of sepiolite clay B20 suspensions in the glass cuvettes through a crossed polariser. The rod volume fraction increases from left to right.

1.5.2 Rod-polymer mixtures

Various rod-like colloids have been used to explore lyotropic liquid crystals, starting from inorganic particles V_2O_5 [353] and biological molecules tobacco mosaic virus [23], to mineral materials such as smectite and sepiolite [91, 168], inspired by Onsager [214] who found that for hard rod systems, the phase transition between the isotropic and the nematic phase is determined by entropy. Moreover, the aim to separate and extract viruses has promoted rudimentary investigations into the mixture of non-absorbing polymers and hard rod-like particles [56, 169]. Although it had been demonstrated that the sediment of viruses could be induced by the addition of polymers, no detailed studies of the model systems of rod plus polymer had been carried out until the 1990s. Hard rod-like particles, characterised by their diameter D and length L , exhibit distinct phase behaviour from those of spherical particles at low concentrations with the polymers due to their aspect ratio [174]. This phenomenon has been studied theoretically by treating rods and polymers as spherocylinders and as penetrable hard spheres, respectively [36, 266]. Lekkerkerker *et al.* [174] used free volume theory to obtain the phase diagrams for several aspect ratios (L/D) and size ratios $q = \sigma/D$, where σ is the diameter of the penetrable hard spheres. Generally, there are four kinds of phase states. Firstly, rods with small L/D plus relatively large polymers (large q) generate a triple point where a nematic and two isotropic phases appear where the latter two phases have different density, equivalent to “colloidal gas” and “colloidal liquid”. Secondly, the isotropic-nematic phase coexistence appears at intermediate rod and polymer concentrations. Thirdly, an isotropic and two nematic phases occur for relatively long rods and

small size ratio. Finally, the coexistence of two nematic phases is observed for rod-like particles and small depletants.

However, in real cases, not only isotropic or nematic phases are observed. At relatively high polymer concentrations, which are equivalent to sufficiently strong depletion attractions, gel phases are likely to form due to dynamic arrest. Many experimental results have reported the gelation of a diverse range of particles. Wilkins *et al.* [324] studied an experimental mixture of rod-like polyamides and polymers through atomic force microscopy (AFM) and confocal light scanning microscopy (CLSM). The system used particles of an aspect ratio $L/D = 54$ and a size ratio $q = 0.11$ at low volume fractions $\phi_{rods} = 0.0005 - 0.01$. The polymers effectively alter the structures of rod clusters. The rods form a percolating network even at low polymer concentrations down to $c/c^* = 0.014$ where c^* is the polymer overlap concentration. Increasing c leads to homogeneous structural transitions of rods. At higher c/c^* , the rods prefer to form bundles in which multiple rod molecules align. These bundle structures change a little with further increase of c/c^* . Buitenhuis *et al.* [45] performed experiments on a mineral, boehmite, plus polystyrene (PS), with an aspect ratio around 6.5 and a size ratio around 1.2. They found a coexistence between a very dilute liquid phase and a gel phase which persisted for one hour, when the PS concentration exceeded 30 g/L with different boehmite volume fractions. Biological materials such as viruses or proteins can also be used as rod-like particles. For example, Adams *et al.* [1] observed the gelation of the tobacco mosaic virus (TMV) plus polyethylene oxide (PEG). TMV is a rigid spherocylinder protein surrounded by double stranded RNA, giving an aspect ratio of ≈ 17 . PEG of different molecular weights up to 600000 was able to induce a gel phase from the dilute isotropic phase.

1.6 Predicting phase separation: the reduced second virial coefficient

As discussed in Sec. 1.4, both colloids and proteins exhibit a metastable liquid-liquid phase separation due to short-ranged attractions, which has been demonstrated by both simulations and experiments [49, 194, 330]. The critical point of such LLPS can be well described by the reduced second virial coefficient, B_2^* . B_2^* is defined as the ratio of B_2 to B_2^{HS} , where B_2 is the second virial coefficient, and $B_2^{HS} = \frac{2}{3}\pi\sigma^3$ is the second virial coefficient of a hard sphere of a diameter σ . The second virial coefficient B_2 with a known isotropic potential $u(r)$ is given by [319]:

$$(1.24) \quad B_2 = 2\pi \int_0^\infty \left[1 - \exp\left(-\frac{u(r)}{k_B T}\right) \right] r^2 dr$$

A negative B_2 indicates an attraction, and vice versa. For a given colloidal size, the consequent B_2^* enables the prediction of the interaction strength needed for a phase separation. Vliegthart *et al.* [319] found that for distinct systems with short-ranged attractions, the values of the reduced second virial coefficient, B_2^* , at the critical point are highly similar, *i.e.*, $B_2^* \approx -1.5$.

Furthermore, B_2^* enables the measurement of the effective range of the attraction, which enables a further prediction whether a system exhibits a stable LLPS, or only a fluid-solid coexistence, as sufficiently short-ranged attraction results in the vanishing of this LLPS [118, 140, 198]. Noro and Frenkel [207] plotted the critical points of various systems, including the square well potential, the Lennard-Jones potential and the Yukawa potential, in the $(T^* - R)$ plane, where T^* means the reduced temperature which can be obtained from B_2^* , and R is a dimensionless representation of the range of the attraction calculated by subtracting 1 from the ratio of particle distance to particle diameter, $R = r/\sigma - 1$. They found that, firstly, the T^* is linearly proportional to the R . Secondly, the minimum R required for a stable LLPS is around 0.13 - 0.15 in spite of different attractions. Although their analysis only focused on the phase behaviour *around the critical point*, the findings might be generalised to out-of-critical regions as they were inferred from the extended law of corresponding states. Moreover, Asherie *et al.* [11] used a combined computational and analytic expression of some phenomenological characteristics to investigate the colloidal phase diagram, and obtained a rough boundary of $R \approx 0.25$. George and Wilson found that B_2^* values of protein crystallisation lie in a narrow range [111]. These result suggest that B_2^* can serve as a uniform criterion when comparing different systems.

EXPERIMENTAL AND PROCESSING TECHNIQUES

Various characterisation, experimental and processing techniques were used in this work to construct self-assembly systems composed of different constituent particles, namely PMMA, sepiolite clays and protein molecules, as well as to investigate the formation mechanisms and the microstructures. Scanning electron microscopy and transmission electron microscopy determined the size and shape of PMMA and clays, respectively. The majority of experimental work was imaged by the confocal microscopy. Then the preparation techniques for each model system were separately described. Finally, the specific image processing methods for PMMA systems were explained.

2.1 Imaging techniques

2.1.1 Scanning electron microscopy

The scanning electron microscopy (SEM) is a type of electron microscopy, which is a valuable technique to achieve high-resolution images with the help of a focused beam of electrons. The most important components of a typical SEM are shown in Fig. 2.1(a). An electron beam of specific energy range is emitted from the thermionic electron gun, then it is focused by a series of condenser lenses under vacuum. The focused beam passes through the deflection coils and the final lens, which deflects the beam in (x, y) plane allowing a raster scanning over a rectangular area. Once the primary electrons interact with the sample, the energy exchange generates various types of signals depending on the interacted object, *e.g.* nucleus or electrons of the atom. Those signals include the reflection of primary electrons, emission of secondary electrons and the emission of X-rays and visible lights, each of which can be recognised by specialised detectors. In SEM the secondary electrons are captured by an Everhart–Thornley detector based on their low

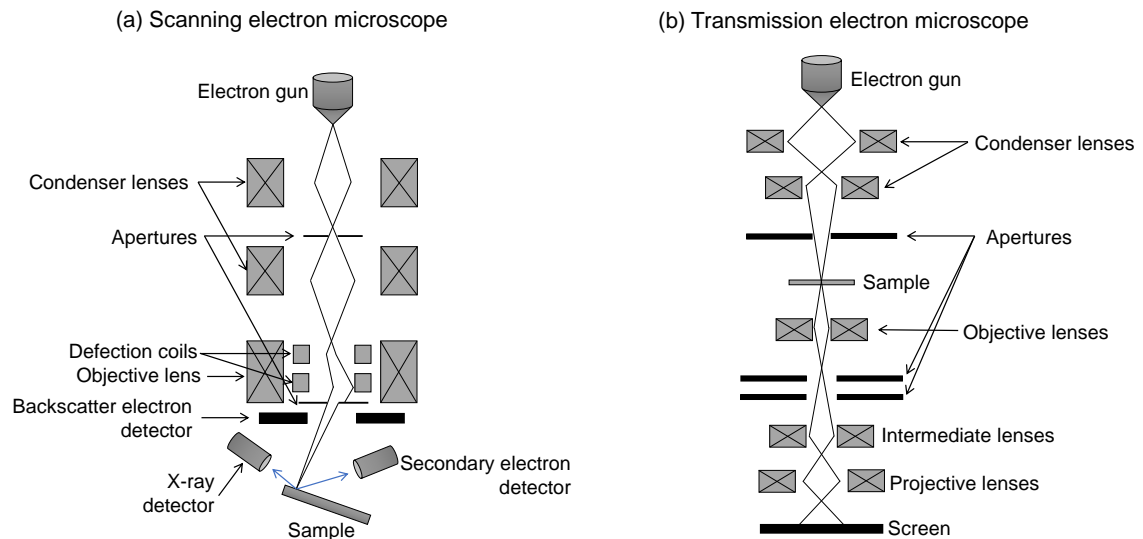


Figure 2.1: Schematic representation of the standard scanning electron microscope and transmission electron microscope.

energy ($< 50\text{eV}$) [87]. They are subsequently amplified and transformed to brightness intensities to form an image on a monitor, in which each pixel corresponds to a position of the beam on the sample. In addition, SEM enables the imaging of 3-dimensional information (topography), as it tunes the generation of secondary by the combination of the shadow contrast by incomplete detection of emitted electrons, the enhanced signal at sharp borders and the incidence angle of the primary electrons. SEM is not an optical imaging technique, thus it can achieve an extremely high resolution, *i.e.* falling to a few nanometres, since the wavelength and the consequent diffraction of electrons is much smaller than optical lights [153]. It has a few slight disadvantages, for example, the specimen needs to support the high vacuum environment, and be conductive and dry. Usually, the conductivity is resolved by coating a thin golden layer [53, 66, 203].

2.1.2 Transmission electron microscopy

The transmission electron microscopy (TEM) also uses an electron beam to interact with the specimen. A schematic diagram of a standard TEM is shown in Fig. 2.1(b). The electron beam is emitted from the thermionic electron gun, with further being focused by the condenser lens in vacuum to the desired size and location on the sample. Instead of another lens, they directly reach and pass through the thin sample. The transmitted electron beam is then focused through a set of functional lenses onto a fluorescent screen, to generate the final 2-dimensional image. The image is determined by the different contrast due to the scattering of the incident beam. The electrons pass through the empty region of the sample, creating fluorescent signals on the screen. On the contrary, the materials scatter the electrons in different levels depends on their inherent properties, which leads to a loss of the quantities of electrons reaching the screen, and

consequently various spot intensities. Therefore, the image shown by the fluorescent screen is a negative of the real specimen. TEM requires the similar conditions to SEM: a dry sample in high vacuum environment, sometimes coated by metallic nanoparticles. In addition, it requires the sample to be very thin, often less than 150 nm, to allow the transmission of the electrons. Nevertheless, it accesses a higher resolution of around 0.2 nm than that of a typical SEM [220, 245, 350].

2.1.3 Confocal microscopy

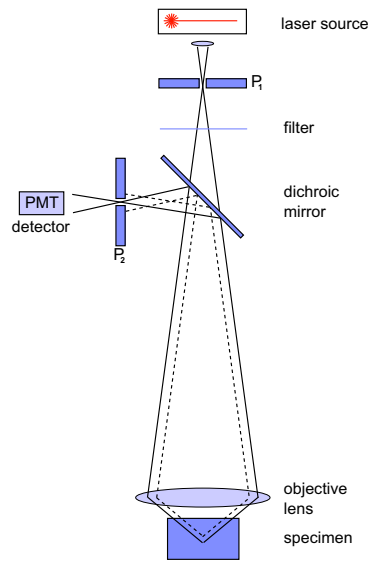


Figure 2.2: Schematic diagram of the confocal microscope. Reprinted from Royall [253].

Confocal microscopy, most frequently confocal laser scanning microscopy (CLSM), is an optical microscopy taking the advantage of the fluorescence. The initial concept of confocal microscopy was proposed in 1957, attempting to remove the light of out-of-focus planes in traditional fluorescent microscopy [199, 224]. A schematic representation of the modern confocal microscope is shown in Fig. 2.2. This configuration is epi-illumination, indicating both the excited and emitted light travelling through the same objective lens. A laser beam is reflected by a dichroic mirror which splits and retains the specific wavelength to excite the fluorophores. Then the beam is focused to the sample by the objective lens. The emitted fluorescent light from the focal plane of the sample is then focused by the same objective lens, and passes through the pinhole which is placed on a conjugated, or confocal, plane to the focal plane. Thus the light generated from out-of-focus planes is eliminated by the pinhole, increasing the resolution of the microscope. Finally, a photomultiplier tube (PMT) detector collects and amplifies the signal to generate a corresponding pixel on the screen. A key advantage of confocal microscopy is, it enables 3D imaging, which is impossible in widefield microscopy due to the out-of-focus sources, as a consequence of its raster scanning and the pinhole. The focused point is flooded with excitation

light evenly, and the fluorophores are excited simultaneously to form a spatial response. If the sample is scanned in z direction, a 3D image may be constructed. Even when scanning (x , y) planes, 3D results can be achieved by imaging consecutive focal planes and stacking. Furthermore, depending on the dyes in the sample, and the number of available detectors, multiple wavelengths can be excited and imaged simultaneously. Maximum resolution of confocal microscopy is obtained with the proper pinhole size which minimises the diffraction rings. A smaller pinhole aperture improves the optical properties, but decreases the emitted photons collected in the unit time and demands longer exposure which may cause bleaching. Theoretically, the optimal lateral and axial resolutions that a confocal microscope can achieve, are around 180 nm and 500 nm, respectively [100, 268].

2.1.4 Polariser

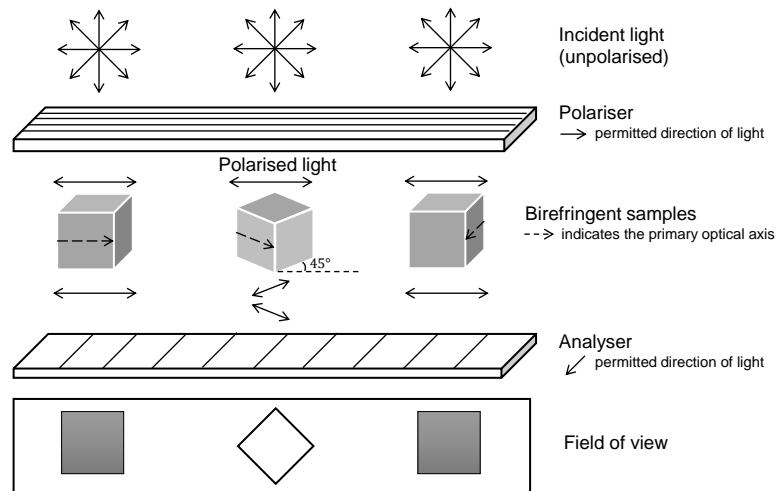


Figure 2.3: Schematic diagram of the working principle of the crossed polariser, in which the primary optical axis of the three samples form increasing angle with the polarised light: (a) 0° , (b) 45° , (c) 90° . Replotted from Zhang [348].

A polariser is an effective optical technique to distinguish anisotropic and isotropic states, providing the information about the composition and structure of the sample. The polariser filters the light beam, only allowing the transmission of a specific polarisation. Isotropic materials, *e.g.* liquids, exhibit uniform optical properties in any direction. They do not change the polarisation state of passing light. On the other hand, anisotropic materials, have changing optical properties depending both on the vibrational plane coordinates and the light propagation direction. In particular, birefringent samples, such as liquid crystals, are defined as having only two different refractive indices. If a material has the same refractive index along two axes, assuming to be x and y axes, while the left axis, in this case is z direction, is distinct, then the z axis is determined as the primary optic axis. Any light rays travel with equal velocity along this axis regardless of

their polarisation level. A scheme of a typical crossed polariser is shown in Fig. 2.3. The most important components are a pair of crossed optical filters placing above and below the specimen. The incident light is polarised by the first filter, then the birefringent sample splits the light into two beams whose amplitude and intensity depend on the orientation angle between the permitted vibrational directions of the sample and the polariser. If any optical axis is out of alignment with the polarised light, the split beams can partially pass through the second filter (analyser) which is set being vertical to the first filter, and the passed light generates an image. Whereas, the light retains the polarisation during transmission if one of the optical axes is parallel to the light, and then it is blocked by the analyser, resulting in dark regions on the imaging plane.

2.2 PMMA system

In 1986, Pusey and van Megen [241] investigated a colloidal system of sterically stabilised polymethylmethacrylate (PMMA) particles, which exhibited nearly-hard-sphere phase behaviours in equilibrium. Their research became the benchmark for the hard sphere phase behaviour taking PMMA colloids as models [7, 107, 234, 237]. Based on these works, we use a model system of PMMA dispersed into the mixture of cis-decalin and cyclohexyl bromide (CHB) closely approaching both the density and refractive index matching. The details of adjusting to density matching will be described in the next section. In particular, the refractive index matching minimise the Van der Waals attractions (see Sec. 1.3.1) [60, 149]. However, these low dielectric constant solvents ($\epsilon_r = 2.2$ for cis-decalin [328] and $\epsilon_r = 7.9$ for CHB [128]) induce a noticeable degree of charging [258]. The charge on the colloid is almost unscreened, but can be improved by the addition of tetrabutyl ammonium bromide (TBAB) salt [339]. The reported solubility of TBAB in this mixture is only around 260 nM [175, 257], leading to a Debye screening length of around 100 nm. This is substantially less than that of unscreened conditions. Nevertheless, it needs to be carefully considered when work with small PMMA particles, *i.e.* $\sigma < 1 \mu\text{m}$, as they are in the same length scale. Even for larger colloids, which are essential for particle-resolved imaging and particle tracking purposes, of the size $\sigma \geq 1 \mu\text{m}$, the effective diameters will increase due to the electric double layer.

The PMMA performed nucleation barrier analysis in this work are of two sizes, $\sigma = 392 \text{ nm}$, brought from Dr. A.B.Schofield in University of Edinburgh, and $\sigma = 1.8 \mu\text{m}$, previously synthesised by my colleague Beatriz Iozzin Ríos de Anda, Levke Ortlieb and Nicholas Wood, for different purposes which will be detailed in the result sections in chapter 3. They are all sterically stabilised through grafting poly(12- hydroxystearic acid) (PHSA) polymer chains onto their surfaces in a length scale of around 10 - 20 nm [42]. Both steric stabilisation and charge contribute to the softness of PMMA colloidal particles with respect to perfect hard spheres.

2.2.1 Reaching density matching

PMMA particles were stored in pure cis-decalin. Meanwhile, A stock solution of CHB was prepared by adding 1 mmol TBAB into 10mL CHB. This amount exceeds the solubility of TBAB. In order to achieve a supersaturated solution, the solution was left in a water bath at 40°C until full dissolution of the salt, represented by no visible crystallite in the eppendorf.

Generally, the sample preparation was based on the fact that mono-disperse hard spheres have a random close packing $\phi = 0.64$ [20, 30, 165]. It consisted of two steps: density matching and diluting to a given volume fraction. For the density matching, the particles dispersed in pure cis-decalin were centrifuged at a relative centrifugal force $\approx 10^4 g$ using a centrifuge (5804 R) for 6 minutes, to form a sediment with $\phi = 0.64$. After discarding the supernatant, the weight of the sediment was obtained by subtracting the weight of the container. The volume of PMMA and cis-decalin was calculated by taking the density of $0.36\rho_{\text{cis-decalin}} + 0.64\rho_{\text{PMMA}}$. CHB with TBAB was added in a volume of twice the calculated cis-decalin volume to give a reasonable base for the following density matching. The suspension was re-dispersed on a vortex stirrer (IKA, Germany) at 3000 rpm for 5 min, and then centrifuged at $10^4 g$ RCF for 15 min. The density of the solvent was characterised by the movement of PMMA. If the particles sedimented to the bottom, this indicated that the solvent is lighter, and extra CHB was needed. On the contrary, if the particles creamed on the top, the solvent was too dense in this case, and cis-decalin was added. This centrifuging - examining the position of the particles - adding corresponding solvent procedure repeated, until no noticeable sign of sedimentation or flotation were observed. The density matching was further checked by running the centrifuging for 30 min, and the addition of solvent followed the same rules as before if particle movement occurred.

The degree of matching was estimated by the sediment velocity v given in the equation

$$(2.1) \quad v = \frac{2}{9} \frac{\rho_{\text{PMMA}} - \rho_{\text{solvent}}}{\mu} r \omega^2 R_{\text{PMMA}}^2$$

where μ is the dynamic viscosity of the solvent, $\omega = 2\pi \times \text{RPM}/60$ is the centrifuge rotor speed, r is the distance from the centre of the rotor, and R_{PMMA} is the radius of PMMA particles [247]. Taking the worst assumption that any colloidal movement less than 10 mm would not be visible, this matching process led to a density error less than 0.00005 of ρ_{PMMA} for $\sigma = 1.8 \mu\text{m}$ PMMA and less than 0.001 for 392 nm PMMA, and the consequent volume fraction error < 0.000034 and < 0.0007 , respectively, at a desired volume fraction $\phi_{\text{desired}} = 0.30$.

2.2.2 Diluting samples to a given packing fraction

The suspension of PMMA was firstly performed the density matching described in Sec. 2.2.1, then was centrifuged in a temperature-controlled centrifuge (5804 R) with a relative centrifugal force $\approx 10^4 g$ at 40°C. The rising temperature broke the matched density by decreasing the solvent density, leading to a sediment at the bottom. The entire sedimentation took between 100 - 120 min according to the volume of the initial particles, and was identified through the

colourless supernatant by eyes. The supernatant, density matching at experimental condition (20°C), was transferred and stored in another clean, empty container for the following process. The sedimented pellet also had a random close packing of $\phi = 0.64$. After removing the supernatant, the weight of the pellet m_{pellet} was obtained by subtracting the weight of the container. The solvent had the same density as PMMA, so the volume of PMMA V_{PMMA} was easily given by $V_{\text{PMMA}} = m_{\text{pellet}} * 0.64 / \rho_{\text{PMMA}}$. With the known V_{PMMA} , the previous stored supernatant was re-introduced to dilute the pellet to the desired volume fraction. Our experiment requires high accuracy of the diluting volume as the nucleation rate is extremely sensitive to the change of colloidal volume fraction at less deeply supercooled region (See Fig. 1.3). However, the solvent has a different viscosity and surface tension from water, so that the common air displacement pipettes have errors when carrying the solvent, as they are calibrated by weighing water. Therefore, the quantity of the required density matched solvent for a given volume fraction was calculated in the form of weight

$$(2.2) \quad m_{\text{addSolvent}} = \frac{m_{\text{PMMA}}}{\phi_{\text{desired}}} - m_{\text{pellet}}$$

In practice this preparation process had a few sources of systematic and random errors. The error from density mismatching has been discussed at the end of Sec. 2.2.1, and was neglected considering its much smaller effect on the volume fraction. Another possible error came from the residue particles dried to the wall or near the lid of the container due to the solvent evaporation, especially with heating. Similarly, the solvent could remain clinging to the walls, which was undermined by repeating centrifugation and removing the supernatant.

Apart from the preparation procedure, PMMA itself has various densities depending on the synthesis process [162], which might affect the volume fraction. However, if the density was well-matched, the calculation of additional solvent is based on the ratio of volume fraction. In this process no density information was required as given in Equ. 2.2, since the ratio of volume was equivalent to that of weight at the same density. This means we did not need to examine the PMMA density for an accurate desired volume fraction.

2.2.3 Glass capillaries

The glass capillaries used in this work were bought from VitroCom. There were two types: rectangle capillaries of a size $0.10 \times 1.00 \times 50.0$ mm and wall thickness $0.070 \pm 10\%$ mm; square capillaries of a size $0.50 \times 0.50 \times 50.0$ mm and wall thickness $0.10 \pm 10\%$ mm. Either of them were suitable for studies irrelevant to the crystallisation. However, it has been shown that the presence of a smooth, hard wall (interface) significantly decreases the hard sphere nucleation barrier height [15, 152], leading to heterogeneous nucleation and dramatic acceleration of the whole nucleation rate. This is predicted by the Gibbs free energy of a nucleus near a wall. The nucleus is able to grow along the wall without a spherical shape. According to the classical nucleation theory, it has smaller surface area than the same volume nuclei spontaneously formed

in the bulk fluid, and consequent surface tension and free energy barrier [128, 274]. In order to explore the hard sphere homogeneous nucleation rate, we performed a sintering process which has been well-studied to be an effective method to suppress heterogeneous crystallisation, by coating a layer of polydispersed particles having a diameter 4 - 10 times larger than those of the colloidal particles [107, 351]. Square capillaries were selected for sintering, as the height of rectangle capillaries could not satisfy the demand of imaging a stack in a reasonably wide range along z direction, as well as being far away from the walls ($> 30 \mu\text{m}$). We prepared sintered capillaries coated by $1.2 \mu\text{m}$ (polydispersity 40.6%) particles for 392 nm PMMA and the mixture of monodispersed 4 and $5 \mu\text{m}$ particles for $1.8 \mu\text{m}$ PMMA. Generally, the coating particles were dispersed in hexane, which is an ideal solvent since it evaporates quickly. The capillaries were fully filled with the dispersion, then left horizontal to dry for 1 h. A thin sheet of the particles could be observed after drying. The capillaries were then placed into a constant temperature oven at 120°C for 90 min, with carefully remaining the bottom wall parallel to the ground all the time when moving the capillaries. The heating melted the particles a little, enabling them to adhere to their neighbours and the wall. This filling - drying - heating process repeated four times for each wall, and more times when necessary until the entire inner surface was covered. The sintering state was examined using an optical microscope (Leica DMI3000B), as shown in Fig. 2.4.

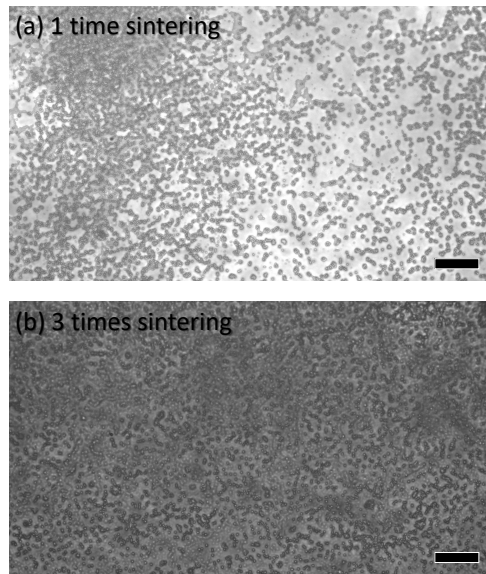


Figure 2.4: The photos of optical microscopy showing the sintering layers of polydispersed $1.2 \mu\text{m}$ PMMA particles. The brightness of the photo is inversely proportional to the thickness of the layer. In particular, the lighter grey regions in the left of (a) are not covered by PMMA, and need to perform sintering process for more times. Irregular patterns indicate the incomplete melting of the particles. Scale bars denote $10 \mu\text{m}$.

The preparation of samples in capillaries was simply performed by filling the corresponding suspension into the capillaries, then sealing the ends using glues. Different glues were selected depending on the purposes. If we needed to view the samples as soon as possible, commonly for

eliminating the effect of gravity, we used a two-component epoxy glue which hardens within 1 min when two parts are mixed. Alternatively, a UV glue (Norland 63) was used, which cures upon the exposure to ultraviolet light. Under our experimental UV light power it usually took 5 min. The UV glue had a better sealing property, remaining the samples for a few months. Therefore, we only used the epoxy glue when necessary.

2.3 Rod system

2.3.1 Sepiolite clay

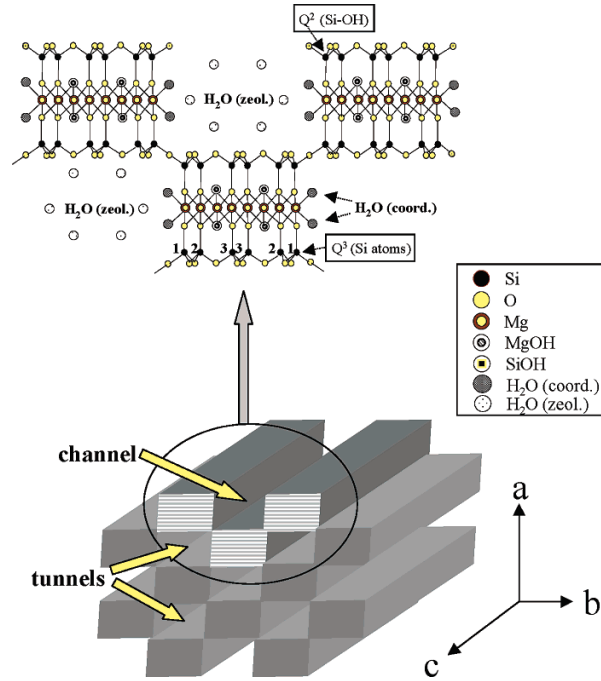


Figure 2.5: Schematic diagram of the sepiolite mineral. Reprinted from Kuang *et al.* [164].

Sepiolite clay with a chemical formula $Si_{12}Mg_8O_{30}(OH)_4(OH_2)_4 \cdot 8H_2O$ is a natural clay mineral of a rod-like shape [104, 302]. They belong to the phyllosilicates [311]. The basic units of the sepiolite are a 1:2 chain-layer structure consisted of one discontinuous magnesium oxygen octahedra sheet and two continuous silicon oxygen tetrahedra sheets [28], as shown in Fig. 2.5. The oxygen atoms in the tetrahedra connect the octahedra, leading to large surface areas and plenty of rectangular zeolitic channels of 1.06×0.37 nm elongated along c direction. These channels contain two types of water: coordinated H_2O located at the end of the octahedral in b direction; weakly bound zeolitic H_2O associated to oxygen atoms or coordinated H_2O in the channel structure via hydrogen bonding [284]. Due to the chain-layer morphology and the discontinuity, silanol groups are allowed to present at the ends of the external channels [164, 261]. These Si-OH groups and structural OH_2 molecules provides the possible hydrogen bondings to

other functional groups.

Sepiolite clay particles can be used as separated colloids or bundles, In this work we took the former. Sepiolite does not swell, remaining a stable structure even at high salt concentrations. In addition, they can be modified with different organic groups via active sides to improve the dispersion in various solvents. Another significant property is, guest molecules can be captured into the channels of sepiolite. For our imaging purpose through confocal microscopy, we needed to encapsulate dye molecules. Indigo dye has been found to be able to replace the zeolitic H₂O molecules by heating the mixture of clays and dyes [113, 244]. Moreover, Yasarawan and van Duijneveldt designed the procedure to obtain fluorescent sepiolite particles via introducing acridine orange dye into the sepiolite channels using a thermal treatment [337].

In this work, sepiolite particles clays, B20, were purchased from Tolsa (Spain), in a state of loose light grey powder. They consist of sepiolite type clays with surfactants ion exchanged onto the clay fibre surfaces. Although the manufacturer did not provide detailed information of the surfactant, it is likely to be either a single or dichain quaternary ammonium surfactant [348]. The length of individual clay particles ranges from 0.1 - 5 μ m. The rectangular cross section has a size of 10 - 30 nm in width and 5 - 10 nm in height [264, 265]. The dye labelling process and the size distribution after centrifugation (for a smaller polydispersity) will be detailed in rod results chapter 5.

2.3.2 SAP polymer

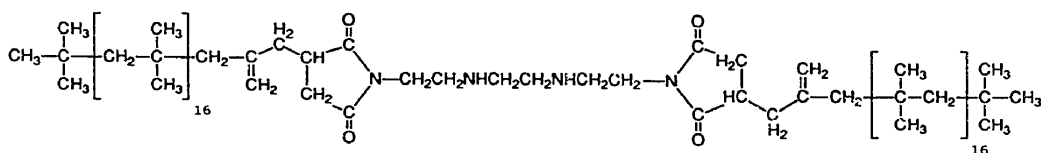


Figure 2.6: The chemical formula of SAP230. Reprinted from Buining *et al.* [44].

Buining *et al.* [44] first reported a method to sterically stabilise boehmite rod-like particles in the dispersion, by grafting a modified poly(isobutene) with the commercial name SAP230. In this work, SAP230 polymer was purchased from Infineum UK limited. It is a viscous brown liquid. The idealised chemical structure is shown in Fig. 2.6, extracted from references. SAP230 has been used for steric stabilisation in engine oil to reduce the formation of deposits which damage the petrol engines [348]. It also performs as a stabiliser in model systems of silica spherical particles [222, 289] and boehmite rods [44]. Following the procedure developed by Zexin Zhang [348], we used SAP230 for sterically stabilising the sepiolite B20 particles. Zhang demonstrated that successful grafting of SAP led to a significant decrease in the suspension viscosity, which was also observed in our preparation.

2.4 Protein system

In this work, three proteins were used, in which enhanced green fluorescent protein (eGFP) and mCherry are natural fluorescent proteins, while BSA is non-fluorescent. Both eGFP and mCherry were produced through protein expression (meaning production in biochemistry), with significant assistance from my colleague, Beatriz Itoatzin Ríos de Anda. Natural BSA was purchased from Sigma-Aldrich, in a state of lyophilised powder. Here lyophilisation is a water removal technique which is usually done by freezing the material, then increasing the temperature and/or reducing the pressure to sublimate the water.

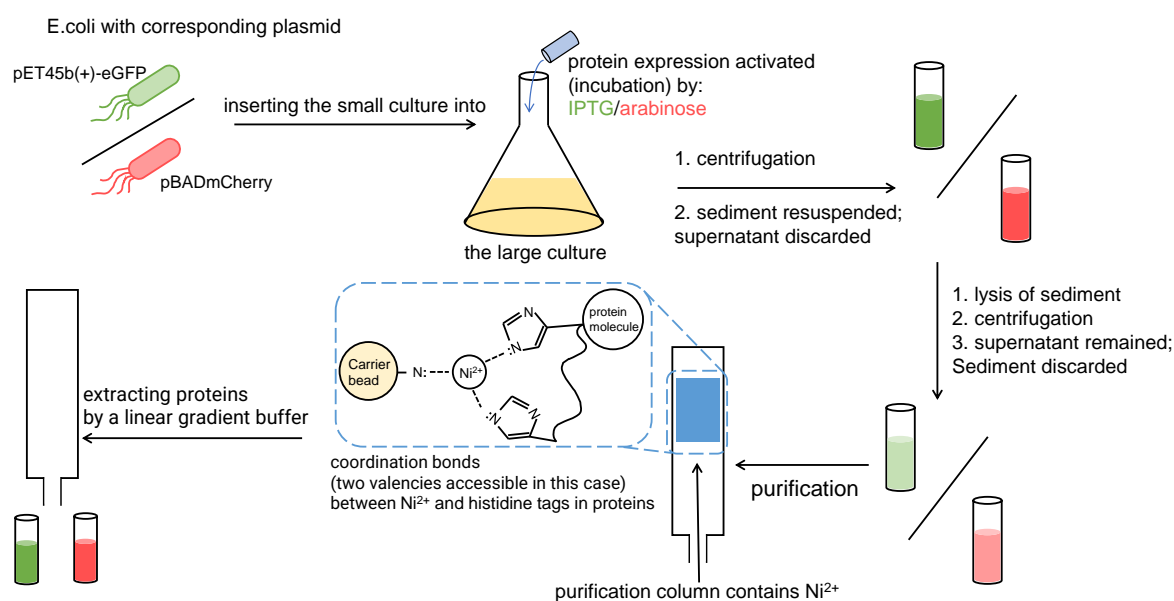


Figure 2.7: The preparation of eGFP and mCherry, involving expression and purification. Replotted from Ríos [248].

2.4.1 Expression of eGFP and mCherry

Generally, the expressions of eGFP and mCherry followed a very similar protocol, while different materials were used for each species. The expression performed was bacterial expression, by the transformation of the corresponding plasmid to *Escherichia coli* (*E. coli*) BL21 (DE3) cells. Plasmids are DNA molecules that can be artificially replicated. They act as delivery vehicles (“vectors”) to introduce a foreign genetic sequence into a bacterium to produce specific proteins [273]. We utilised pET45b(+)-eGFP for eGFP and pBADmCherry for mCherry, respectively. pET45b(+)-eGFP contains the DNA for eGFP expression, a histidine tag and a T7lac operator which function will be explained later, while pBADmCherry contains the DNA for mCherry expression and a histidine tag, but an arabinose promoter instead of the operator.

First, a small culture was built by inoculating 20 mL of lysogeny broth (LB), the plasmid-

inserted *E. coli* BL21 (DE3) and 10 $\mu\text{g/mL}$ antibiotic carbenicillin. The culture was allowed to develop for 16 h at 180 rpm and 37°C. A large culture was prepared by injecting the small culture into 1 L LB with 50 $\mu\text{g/mL}$ carbenicillin under the same condition as before. The bacterial density was quantified by the optical density (OD) which indicates the turbidity relevant to the cell growth. For eGFP, the $OD_{600\text{nm}}$ was monitored until it entered the range of 0.5 - 0.6. The expression of eGFP was activated by the addition of 1 mM Isopropyl β -D-1-thiogalactopyranoside (IPTG) into the large culture. This material is more likely to connect to the lac repressor, an enzyme preventing the transcription of the lac operon contained in the plasmid. Hence the generic information in the lac operon is able to transcript eGFP with IPTG suppressing the lac repressor [25, 208]. The introduction was waited for 1 h. Then the temperature was reduced to 30°C, to both facilitate eGFP expression and inhibit bacteria growth. After incubation for 16h, the culture was centrifuged at 4500 g for 15 min at 4°C. The supernatant was discarded, and the sediment was re-dispersed into a lysis buffer of pH = 8.0 with 20 mM imidazole, 50mM potassium phosphate and 300 mM NaCl, and stored at -20°C [248].

As shown in Fig. 2.7, the expression of mCherry had very similar procedures as those of eGFP. *E. coli* BL21 (DE3) cells transformed with pBADmCherry plasmid grew in the same culture. In the intermediate step, the desired range of $OD_{600\text{nm}}$ was 0.6 - 0.8. The next distinction appeared where mCherry expression was induced by adding arabinose with a final concentration of 0.2% in the LB. The arabinose, intrinsically inactive, contains the arabinose promoter *ara* p_{BAD} as well as its regulatory protein AraC. However, when added into the culture, the AraC prefers to bind to the sugar, consequently liberates the DNA, which facilitates the mCherry expression under p_{BAD} [270]. The rest of the protocol was the same as that of eGFP.

2.4.2 Purification of eGFP and mCherry

We used immobilised-metal affinity chromatography (IMAC) for protein purification, a technique taking advantage of the affinity of transition metal (Ni^{2+} in our case) to the nitrogen atoms of the histidine tags in the proteins [32]. The purification column is full of porous agarose structure, in which Ni^{2+} (chelates) forms coordination bonds with the chelating agent, nitriloacetic acid (NTA), still allowing another 2 ligands to bond to it. Here the $-\text{N}-$ of the imidazole in the histidine served as the ligands [32], as shown in Fig. 2.7 insert. Both two proteins employed the same method for the purification. The stock suspension at -20°C was defrosted, lysed by sonication of 30 s for 3 times (Fisherbrand Q500 Sonicator), and centrifuged (Pierce Protein Concentrator PES, 15K MWCO) for 30 min at 4°C. The supernatant was kept and filtered through a 0.22 μm syringe filter (Millipore) to the mentioned Ni-NTA column (filling materials: Pierce Ni-NTA magnetic agarose beads, column: Qiagen). The column had been soaked with the same lysis buffer used for stocking protein sediment. After the addition of the protein solution, the unbound protein molecules were removed by washing the column with the lysis buffer. Then the bound proteins were extracted with a linear gradient (0 - 100%) of a buffer at pH = 8.0 with 50 mM potassium

phosphate, 300 mM NaCl and 500 mM imidazole, which contains excess imidazole to replace the imidazole rings of the histidine tags from the Ni^{2+} , thus releases the proteins. The free proteins were then dialysed by the deionised water for 3 times with a 10K MWCo dialysis membrane [248]. The dialysed proteins were further concentrated, as detailed in the next section.

2.4.3 Concentration of proteins

Before concentration, the dialysed proteins were filtered through a $0.22\ \mu\text{m}$ round filter (Millipore) to remove possible aggregations and bacteria. The solution was then moved to the concentrator (Pierce Protein Concentrator PES) and centrifuged at 5000 rpm at 4°C . The centrifugation time depends on the initial and final volume. In our work the desired volume was around 1 mL.

The final concentration was obtained by measuring the absorbance. Fluorescent proteins were measured at corresponding excitation wavelength ($\lambda_{\text{eGFP}} = 488\ \text{nm}$ and $\lambda_{\text{mCherry}} = 587\ \text{nm}$), while BSA was measured at $\lambda_{\text{BSA}} = 280\ \text{nm}$. In order to achieve a more precise result, we performed the measurement for several dilutions (1/50, 1/100, 1/200) of the original concentrated stock solution. The concentration was calculated by the Beer-Lambert Law $A = \epsilon lc$, where A is the absorbance, ϵ is the molar extinction coefficient, l is the length of light path in the unit of cm and c is the protein concentration [24]. The values of the ϵ were taken as $\epsilon_{\text{eGFP}} = 56000/(\text{M}\cdot\text{cm})$ [150], $\epsilon_{\text{mCherry}} = 72000/(\text{M}\cdot\text{cm})$ [177] and $\epsilon_{\text{BSA}} = 66296/(\text{M}\cdot\text{cm})$ [112].

2.4.4 Protein charge

A single protein molecule can exhibit an anisotropic charge, represented as heterogeneous charge distribution and sign on the surface, due to the specific amino acid sequence and folding ways. The net charge is affected by pH value of its surrounding environment. The pH at which their net charge becomes electrically neutral is defined as the isoelectric point (pI). Above this pH, the proteins show a negative net charge, and vice versa. Therefore, buffer solutions are widely used to maintain a stable pH value and the consequently fixed protein net charge for convincing experiments. A typical buffer solution contains a weak acid HA and its conjugate base A^- in an aqueous solution. It has a resistance to the addition of strong acid or alkali (in a small amount), maintaining pH at a nearly constant value. When an acid is added to a buffer solution where the chemical equilibrium ($\text{HA} \rightleftharpoons \text{H}^+ + \text{A}^-$) exists, the concentration of hydrogen ions (H^+) rises, pushing the equilibrium shifting towards the left. Because of this, the increase of H^+ is less than the amount that the acid dissociated. A similar process occurs when the alkali is added, where the equilibrium will shift to the right [46, 287].

However, the surface charge of the proteins can not be directly measured even in a stable environment. Instead, it is calculated from several measurable properties. In general, we follow the procedure of the work of Roosen *et al.* [249]. Firstly, the electrophoretic mobility μ_e of 2 mg/mL protein, in solutions prepared under the same pH and temperature but a much lower salt concentration (commonly 10 mM NaCl) as the experimental samples, is measured with an

external electrical field by a Zetasizer (Nano ZS, Malvern, UK). The zeta potential, ζ , is related to the particle mobility by:

$$(2.3) \quad \zeta = \mu_e \frac{3\eta}{2\epsilon f(\kappa r)}$$

where η is the solution viscosity, ϵ is the dielectric permittivity, κ is the inverse Debye screening length, and r is the radius of proteins. The ionic strength used here has been updated to the value of the experimental conditions. The Henry function $f(\kappa r)$ is approximated by Oshima's relation [70, 211]:

$$(2.4) \quad f(\kappa r) = 1 + \frac{1}{2} \left[1 + \frac{2.5}{\kappa r [1 + 2 \exp(-\kappa r)]} \right]^{-3}$$

and the surface charge density σ can be calculated from a reduced zeta potential $\tilde{\zeta} = (e\zeta)/(2k_B T)$ as:

$$(2.5) \quad \sigma = \frac{2\epsilon\kappa k_B T}{e} \left[\sinh^2 \left(\frac{\tilde{\zeta}}{2} \right) + \frac{2}{\kappa r} \tanh^2 \left(\frac{\tilde{\zeta}}{4} \right) + \frac{8}{(\kappa a)^2} \ln \left(\cosh \left(\frac{\tilde{\zeta}}{4} \right) \right) \right]^{\frac{1}{2}}$$

The total surface charge of the protein in specific conditions is then obtained by $Q = A\sigma$, where A is the protein surface area.

2.4.5 Cationisation and anionisation

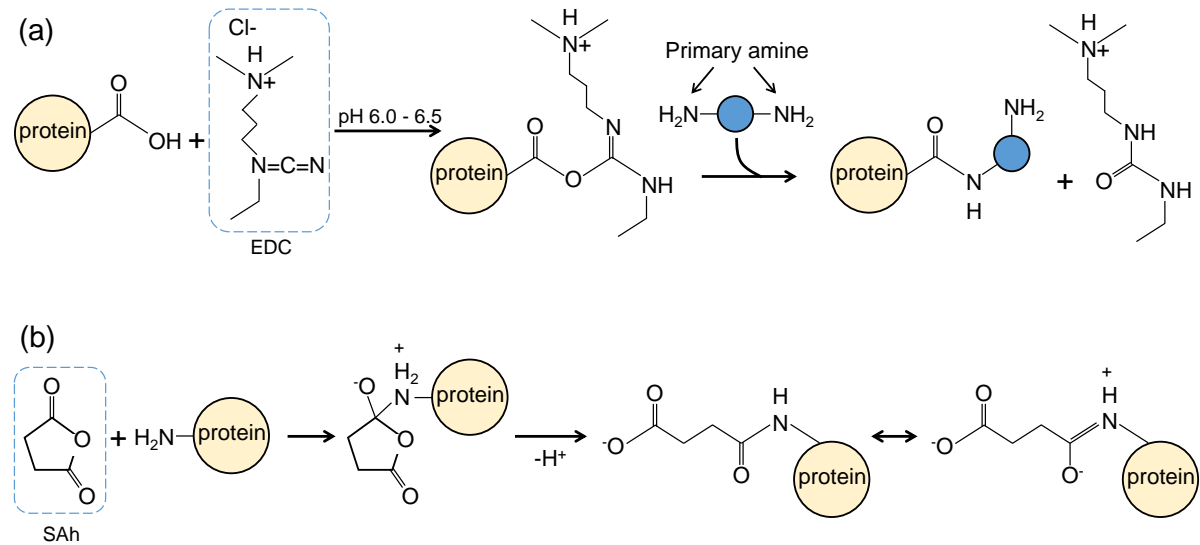


Figure 2.8: Schematic pictures of cationisation and anionisation process in this chapter. (a) Cationisation. The original $-\text{COOH}$ forms an amide bond. (b) Anionisation. The original $-\text{NH}_2$ forms an amide bond.

Both cationisation and anionisation are effective ways to adapt the surface charges of the proteins, without changing the protein spatial configuration. In the cationisation process, protein

molecules obtain more positive charges by chemical reactions of either replacing negative groups with cationic reactive agents, or linking positive groups, or both. A general scheme of the cationisation reaction activated by 1-ethyl-3-(3-dimethylaminopropyl) carbodiimide hydrochloride (EDC) is shown in Fig. 2.8(a). The exposed carboxylic acid groups ($-\text{COOH}$) on the protein surfaces can react with EDC, forming an intermediate product, O-acylisourea, which is an active ester and easily replaced by nucleophilic attack by a primary amino group [105, 204]. Thus, an amide bond forms, and the initial carboxylic group is substituted by the molecule linked with the primary amine. The net charge can be more positive if the bonded molecule has exposed amino groups, as indicated by the blue circle in Fig. 2.8(a). EDC is most efficient in an acidic environment and must be in buffers exclusive of irrelevant carboxyls and amines, which is the reason for choosing phosphate buffer solution. The phosphoric acid is a triprotic acid, indicating that it has 3 dissociation constants, thus it can provide a wide range of pH.

Meanwhile, as indicated by its name, anionisation involves the addition of negative charges. In this work we used succinic anhydride (SAh), a type of dicarboxylic acid anhydride. Upon nucleophilic attack in the alkaline conditions, the ring structure of the anhydride breaks, generating the acylated product with a newly formed carboxylate group replacing the original amino group (See Fig. 2.8(c)) [61, 127]. 0.1 M Na_2CO_3 buffer solution at pH = 8.0 were selected for this chemical reaction.

2.5 Image processing

2.5.1 Sampling density

In imaging processing, “sampling” refers to the process of switching a continuous signal into a numeric (discrete) sequence. The sampling density means the number of recorded pixels in 2D or voxels in 3D per unit distance, hence it is inversely proportional to the size of one pixel/voxel. This value is tuned by the *zoom* factor in the confocal microscopy, building the connection between the size in real space and the digital pixels/voxels. By increasing the sampling density, more detailed can be acquired. Although this method has a limit determined by the diffraction on the microscope lenses. Further increase beyond this limit does not provide more distinguishable details, but the waste of imaging speed and computer storage space. The ideal sampling density at which all the information is captured, can be calculated by the Nyquist–Shannon sampling theorem.

2.5.1.1 Nyquist theorem

The Nyquist–Shannon sampling theorem, named after H. Nyquist and C. Shannon [209, 210, 280], is an important theorem in signal processing. It builds the basic rule of allowing a discrete sequence to achieve all the information of a continuous signal with finite bandwidth. The Nyquist criterion states the following condition: A function $y(t)$ can be fully recovered by giving its values

at a series of points spaced $1/(2B)$ distance apart if the bandwidth of $y(t)$ is B [280]. The ideal sampling distance is therefore a distance less than $1/2B$. Applying a sampling distance longer than the Nyquist value, known as undersampling, gives rise to the lost of information as well as the aliasing [329]. On the contrary, smaller sampling distance, oversampling, is harmless except requiring longer imaging times and larger storage space. In the case of confocal microscopy, the Nyquist sampling distance is determined by the point spread function.

2.5.1.2 Point Spread Function

In optical systems, the acquired image experiences a degree of degradation of the real object due to the noise and the blurring. The noise is largely photon noise, an inherent property of the incident photon flux, and can be weakened through the average function of microscopes, which collects the sum of pixel intensities from multiple scans and uses the arithmetic mean as the final intensity. Meanwhile, the blurring is mainly caused by the diffraction. This three-dimensional diffraction response of an infinitely small point light source is known as the Point Spread Function (PSF). When light is emitted from a point object, the objective lens fails to focus the light to a same size point on the image plane. Instead, the concentric circles surrounding a bright central disk forms in the (x, y) plane, due to the convergence and interference of the light waves at the paraxial (perfect) focal point. While the image often exhibits an hourglass or ellipsoid shape when scanned over the z direction by a confocal microscope [146, 268]. It has been demonstrated that the PSF of the light microscopy can be well described by a three-dimensional Gaussian model [145, 327]. In this work we used a commercial software, Huygens professional [292], to model the PSF of our system with given parameters including the excitation and emission wavelength, the numerical aperture and the lens immersion refractive. Alternatively, one can measure the image of a fluorescent bead embedded in a homogeneous medium that approaches an essentially “point” object for many times to achieve a convincing mean PSF [58].

The acquired image of the confocal microscope is the sum of all the PSFs. That is to say, the observed object is cropped to smaller parts, and the final image is the collection of the generated PSF results of each part. This formation process can be represented by a convolution, which will be detailed in the next section.

2.5.2 Convolution and deconvolution

In optical systems, the convolution mathematically explains the degradation during the formation process of an image due to the blurring, on the premise that the random noise has been largely reduced by the average function of the microscope. The experimental point spread function is used as the convolution matrix, known as “kernel”, to convolve the real object to generate the final image. The output results can be described by

$$(2.6) \quad h = f * g.$$

where the f refers to the original object, g is the PSF, and h stands for final image. The convolution operator $*$ implies the integral of the accumulation of every interaction between f and g after the kernel is flipped and shifted to the desired time:

$$(2.7) \quad f * g(a) = \int_{-\infty}^{\infty} f(\epsilon)g(a - \epsilon)d\epsilon.$$

Since the images are discrete signals, the output volume of a point $h(x, y, z)$ with the coordinate (x, y, z) is calculated as

$$(2.8) \quad h(x, y, z)^l = \sum_{i=1}^X \sum_{j=1}^Y \sum_{k=1}^Z f^{l-1}(x-i, y-j, z-k) \times g^l(i, j, k),$$

where g^l is the 3D kernel in the l th layer with a size $X \times Y \times Z$, convolved with the input from the previous layer f^{l-1} [242].

On the contrary, deconvolution represents the restoration of a convolved image with the known result and the kernel. This indicates a simple way to achieve original object, f , by re-arranging Equ. 2.6 into $f = g/h$. In the case that the noise derived from the photon is not completely eliminated due to no or low average function applied, a correction, c , is added, as the following equation:

$$(2.9) \quad g = f * h + c,$$

in which c is hard to estimate. Therefore, we used a line average of 4 - 8 to minimise the noise. In this work we used Huygens Deconvolution Software instead of measuring our experimental PSF. This software enables us to automatically compute a theoretical PSF based on known microscopic parameters, and executes the deconvolution operation of confocal images.

2.6 Structural characterisation

2.6.1 Radial Distribution Function

The radial distribution function, $g(r)$, is an effective method to quantify the particle distribution, which describes the value of particle density as a function of distance from a central test particle. Assuming a system without any external force field, containing N particles of which the position of particle i is \mathbf{r}_i , and the potential is $U_N(\mathbf{r}_1, \dots, \mathbf{r}_N)$, the probability of an elementary conformation $P^{(n)}$ is given by [93]

$$(2.10) \quad P^{(n)}(\mathbf{r}_1, \dots, \mathbf{r}_n) = \frac{1}{Z_N} \int \dots \int e^{-\beta U_N} d\mathbf{r}_{n+1} \dots d\mathbf{r}_N,$$

where $Z_N = \int \dots \int e^{-\beta U_N} d\mathbf{r}_1 \dots d\mathbf{r}_N$ represents the normalising configurational integral. If the particles are identical, the coordinate of any i can be exchanged with any other particle without altering the $P^{(N)}$, thus the n -particle density function ρ^n is

$$(2.11) \quad \rho^{(n)}(\mathbf{r}_1, \dots, \mathbf{r}_N) = \frac{N!}{(N-n)!} P^{(n)}(\mathbf{r}_1, \dots, \mathbf{r}_N).$$

When $n = 1$, the density $\rho^{(1)}$ is explicitly calculated by $\rho = N/V$, since the other parts in $P^{(N)}$ cancels except $1/\int d\mathbf{r}_1 = 1/V$. For higher n , ρ^n is interpreted with different conditions. In the case of the ideal gas, particles are independent of the coordinate without interacting with others, giving the density $\rho^{(2)}(\mathbf{r}_1, \mathbf{r}_2) = \rho^1(\mathbf{r}_1)\rho^1(\mathbf{r}_2) = N(N-1)/V^2 \approx \rho^2$ [52]. The second-order correlation function $g^{(2)}(\mathbf{r}_1, \mathbf{r}_2)$ from $g^{(2)}(\mathbf{r}_1, \mathbf{r}_2) = \rho^{(2)}(\mathbf{r}_1, \mathbf{r}_2)/\rho^2$ is of great interest as it is uniquely determined by the inter-particle potential $u(r)$, a measurable property through various techniques, *e.g.* optical tweezers [63]. Since a fluid is isotropic, $g^{(2)}(\mathbf{r}_1, \mathbf{r}_2)$ depends only on the distance between \mathbf{r}_1 and \mathbf{r}_2 , then the super- and subscript can be removed: $g(r) = g^{(2)}(\mathbf{r}_1, \mathbf{r}_2)$. Computing the $g(r)$ requires calculating Ornstein–Zernike equation [103]. In particular, Percus–Yevick approximation provides an analytical solution under the hard sphere condition, and is used to acquire an expression of $g(r)$ [156, 322].

2.6.2 Topological cluster classification

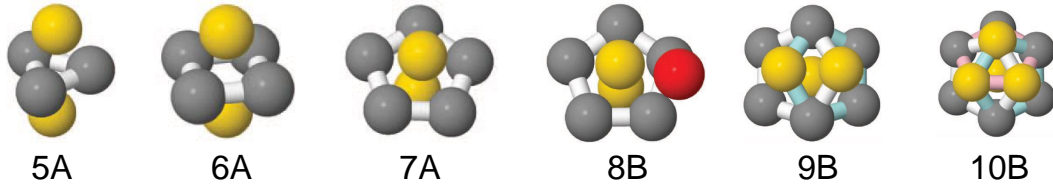


Figure 2.9: The minimum potential energy clusters captured by the topological cluster classification, reprinted from Matins *et al.* [190]. The colours represent different particle types: grey means a ring particle, yellow means a spindle particle, and red means an additional particle. The numbers in the names denote the particle number in the cluster.

The radial correlation function only represents the probability of finding a particle at a place, which is an averaged quantity with the identical value at the same distance from the central reference particle. Moreover, with the given interactions between particles, the $g(r)$ is also determined. In order to explore the spatial structures with the known position of each particle, many other measurements have been developed, for example, bond order parameters [84] and common neighbour analysis [310]. In this work we used the topological cluster classification (TCC) algorithm, established by Alex Malins and Stephen R. Williams [190], to capture the clusters whose bond topologies are similar to isolated structures of a size $n < 13$ in a minimum potential energy state. Several potentials are considered in TCC, including the variable range Morse potential, Dzugutov potential and two binary Lennard-Jones glassformers (the Wahnström and Kob-Andersen models). Instead of the standard Voronoi method, this algorithm identifies the neighbour network through a modified Voronoi method, recognising a pair of neighbouring particles only if their Voronoi cells share a face and the connecting line of their centres crosses this face. Another modification is the smaller dimensionless four-membered ring parameter f_c which specify a threshold indicating the maximum asymmetry that a 4-particle ring can reach; exceeding it leads to an identification of two rings of 3 particles. We also used the default cut-off

length $r_c = 1.4\sigma$, where σ is the diameter of the particles, as their comparison showed a weak dependence of the detection results on the r_c . [189, 190]

The process of the TCC is as follows: firstly, the neighbour network is constructed by the modified Voronoi method. Second, this work is examined for the shortest path rings consisted of 3, 4 or 5 particles, from those multiple elementary structures named as basic clusters are labelled. A basic cluster may have more members than its ring if other particles being common neighbours of all the ring members exist. Then, larger clusters are recognised through connecting basic clusters. This step involves possible addition of 1 or 2 individual bonding particles based on the preset parameters. This algorithm finally yields larger clusters of locally favoured structures. The TCC is a useful tool for structural analysis. In particular, for hard sphere systems, it has demonstrated the effect of local fivefold symmetry, including the suppression of crystallisation [296] and the dynamical deceleration of the glass transition [121]. Wood *et al.* also found that the less fivefold symmetry in the sedimentation contributes to a small fraction of the discrepancy in the experimental and the simulation nucleation rates.

MEASURING HARD SPHERE NUCLEATION RATES IN REAL SPACE

Despite being one of the simplest physical systems, hard spheres exhibit a huge discrepancy in homogeneous crystal nucleation rates between experiments and simulations. In this work, we attempted to resolve this discrepancy. A new method in real space by confocal microscopy was used, decreasing the required colloid size as well as significantly increasing the imaging volume. We used PMMA particles in two different sizes, $\sigma = 392$ nm and 1.8 μm , both modelling the softness of both through a hard-core Yukawa potential. With the help of various image processing techniques, we identified the crystal nuclei and calculated the corresponding nucleation barriers. Unfortunately, these barriers basically agreed with previous experiments, hence we concluded that this nucleation rate discrepancy remains unresolved.

3.1 Introduction

Hard sphere crystallisation is one of the most important phase transitions of first order, and has been studied over the last 50 years. Simulation techniques have measured its rate, known as the nucleation rate [12, 13, 94]. In the 1960s, convincing studies on colloidal particles, such as latex [185] and opal [148] dispersed in a solvent, shown the promising systems to approach hard sphere model in accessible experimental conditions. Since then, many investigations through light scattering techniques have been carried out on the crystallisation of hard-sphere-like colloids [107, 124–126, 267]. However, the nucleation rates of experiments strongly differed from those of the simulations, by over 10 orders of magnitude near freezing volume fraction (See Sec. 1.2.2 for a detailed comparison). This discrepancy is probably the second worst failure between theoretical calculation and experiment in physics, with the first being cosmological constant of which the astronomical measurements disagree with the theoretical prediction from

the vacuum energy by 120 orders of magnitude [131]. In this chapter, we attempted to resolve the discrepancy. Various systems have been developed to investigate the colloidal crystallisation, including polystyrene (PS) microgel particles [22, 160], poly-N-Isopropylacrylamide (PnIPAM) micro-gel particles [62, 151, 277] and silica particles [68, 69]. A colloid commonly employed, and used in our work, was poly-methylmethacrylate (PMMA) particles, grafted with poly-12-hydroxystearic acid (PHSA) [7, 230]. They were dispersed in the mixture of cis-decalin and cyclohexyl bromide (CHB) reaching both the density matching and refractive index matching.

Previous experimental investigations of nucleation rates have predominantly employed light scattering methods. While scattering allows the scanning of entire samples, highly effective in obtaining information of billions of particles, they are also constrained by the averaged results, such as the width and height of peaks, hindering the comprehensive understanding of crystallisation mechanisms. In contrast, particle resolved imaging techniques, especially confocal microscopy, can provide the positions of individual colloids and the consequent identification of crystal nuclei themselves, illuminating aspects of nucleation that are not accessible through scattering methods [107, 298]. However, no systematic studies on the nucleation rates have been developed through the confocal measurements. A key issue with the confocal technique is the resolution restricts the size of the colloids. For tracking purposes, a particle should have around 10 pixels in diameter. Considering the resolution of the confocal microscope is 50 - 100 nm, based on the premise that a degree of undersampling is allowed due to the known shape of the colloids [76, 146, 268], particles need to be at least $1\text{ }\mu\text{m}$. Since the Brownian time τ is proportional to σ^2 , larger colloids move more slowly than smaller ones, by around 1 - 2 orders of magnitude. This means they require much longer time for nucleation process, from a few hours to days or even months.

Another problem is the limited sampled volume. Traditional light scattering techniques can examine large volumes up to the entire container, while the confocal studies typically only measure a few image stacks on μm level. For example, Gasser *et al.* [107] examined a box of $58 \times 55 \times 20\text{ }\mu\text{m}$, which is much smaller compared with the container of Sinn *et al.* [285] in a size of $10 \times 5 \times 20\text{ mm}$, which was characterised by Bragg scattering and small-angle scattering and thus allowed throughout observation of the whole sample. Gasser *et al.* did not explain exactly how they obtained the nucleation rate densities, though it can be calculated by dividing the time taken to full crystallisation multiplied by the volume. Considering the total volume of their sample was $\approx 50\text{ }\mu\text{L}$, the observed volume $58 \times 55 \times 20\text{ }\mu\text{m}$ was too small to fully obtain the information of the nucleation, as it is inherently a random behaviour, and the nuclei grow throughout the sample. Especially, when entering the weakly supercooled region, the spontaneous formation of nuclei is rare, indicating that it is very difficult to capture a complete nucleation process with such a small observation volume.

Given the drawbacks listed above, we find the confocal microscopy is limited by the size of the colloids and relatively small sampled volume. However, these issues only occur when

the particle-resolved images are required. Particle-resolved information, and the consequent particle tracking results, does enable a more detailed analysis of physical mechanisms, such as the structure of clusters [107, 326] and crystallisation kinetic pathways [298]. Though, for our purpose, we might not need the particle coordinates to determine the nucleation rates. Therefore, we consider measuring the nucleation barrier instead, which is also the measured property in biased Monte Carlo methods. From the critical nucleation barrier, the nucleation rate per unit volume, I , can be calculated as

$$(3.1) \quad I = A \exp[-\beta \Delta G^*].$$

where A is a kinetic factor which can be experimentally measured. There are several advantages of this method. Firstly, we can take images of nuclei smaller than the critical size — which exist throughout the system — to get more data points for the nucleation barrier curve. These measurable data allow us to estimate the barrier even in the less deeply supercooled fluid. In the experimental conditions, this means the nuclei populations can be sampled from the period prior to final equilibrium crystallisation, though the less waiting time gives rise to possible incomplete nuclei distributions of larger sizes. Secondly, the method enables us to understand whether the nucleation barrier height decreases slowly with increasing volume fraction of particles (as in experiments) or steeply (as in simulations), without obtaining the barrier heights themselves which may require long experimental times. Finally, as noted above, the Brownian time characterising the diffusion speed of colloids is proportional to σ^2 , and thus the smaller colloidal particles, typically down to hundreds of nanometres, significantly accelerate the full crystallisation process by 1-2 orders of magnitudes when comparing with the particles of a few microns for particle-resolved imaging, and may decrease the nucleation time to an experimentally accessible timescale, especially around the freezing volume fraction, where the formation and growth of nuclei are rare events.

The probability of the formation of a crystal nucleus contains n particles is $P(n) = N_n/N$, where N_n represents the number of the nuclei of size n , and N is the total number of the particles in the system [16, 246, 299]. The corresponding Gibbs free energy $\Delta G(n)$ then can be defined as

$$(3.2) \quad \Delta G(n) = -k_B T \ln \frac{N_n}{N}.$$

Inspired by this relationship proposed by Auer and Frenkel [16], we measured nucleation barriers by counting the nuclei of different sizes in the system.

3.2 Experimental System

All the PMMA particles used in this work are sterically stabilised by grafting short poly(12-hydroxystearic acid) (PHSA) chains to their surfaces. We consider them in three batches depending on their sizes. One is the smallest particles with a quoted diameter of 303 nm measured by the

X-ray crystallography. They were obtained from Dr. A.B.Schofield at the University of Edinburgh. These particles are fluorescently labelled with NBD-TMA dye, which has an excitation maximum at 458 nm and an emission maximum at 530 nm [26]. My colleague Nicholas Wood, who was the first person starting this project in our group before, checked the polydispersity and found that the particles actually have a mean diameter of 392 ± 12 nm as determined from the SEM images, equal to a polydispersity of 3%. The second batch is intermediate size PMMA dyed by Nile Red, of which the excitation and the emission are 500 nm and 530 nm, respectively [115]. They also obtained from Dr. A.B.Schofield at the University of Edinburgh. The size of these PMMA is $\sigma = 613$ nm, with a slightly higher polydispersity of 5.7%. The final one is the largest PMMA (hereafter L-PMMA) particles, synthesised by the dispersion polymerisation [37] by the collaboration of my colleagues, Beatriz Iozzin Ríos de Anda, Levke Ortlieb and Nicholas Wood. They are fluorescently labelled with Rhodamine which is excited at 546 nm and emits at 568 nm. L-PMMA particles are highly monodispersed, with a quoted diameter of $\sigma = 1.8 \pm 0.07$ μm .

All the PMMA particles in different sizes were stored at a low volume fraction ($\sim 10\%$) in a single component solvent, cis-Decahydronaphthalene (cis-decalin, 99%, Sigma-Aldrich). Details of sample preparation can be found in Sec. 2.2. Briefly, to prepare a sample at a given volume fraction, the particles of the first ($\sigma = 392$ nm) and the third ($\sigma = 1.8$ μm) batches were first centrifuged to a sediment at random close packing $\phi = 0.64$. Cis-decalin and cyclohexyl bromide (CHB) with salt tetrabutyl ammonium bromide (TBAB) were then carefully added to obtain a solvent of simultaneous refractive index matching and density matching. The suspension was centrifuged at a higher temperature 40°C to induce a density difference between the colloids and the solvent. The sediment was further diluted with density matched solvent to obtain the desired volume fraction.

Meanwhile, the samples of the second batch, particles of $\sigma = 613$ nm, were prepared in the mixture of cis-decalin and tetralin in a good refractive index matching. This mixture is unable to attain density match, as both components have a smaller density than PMMA. Therefore, we followed the recipe of He *et al.* [126], giving a mass ratio of $m_{\text{tetralin}} : m_{\text{decalin}} = 46 : 54$ and the corresponding mixed density 0.93 g/cm³. The stock suspension was centrifuged at room temperature 20°C , then the sediment was diluted to reach the desired volume fraction, with the adding amount

$$(3.3) \quad \begin{aligned} m_{\text{tetralin}} &= \left(\frac{m_{\text{sed}}}{(0.64\rho_P + 0.36\rho_d)/V_{\text{desired}}} - 0.64 \frac{m_{\text{sed}}}{0.64\rho_P + 0.36\rho_d} \right) \times 0.93 \times 0.46, \\ m_{\text{cis-dec}} &= \frac{54}{46} m_{\text{tetralin}} - 0.36 \frac{m_{\text{sed}}}{0.64\rho_P + 0.36\rho_d} \times \rho_d, \end{aligned}$$

where ρ_P and ρ_d represent the density of PMMA and cis-decalin, respectively. This batch was an attempt at better image quality, with the reason for density mismatching and results presented in the Sec. 3.5.

3.3 Identifying crystal nuclei through image processing

In order to calculate nucleation rate densities, we have to count crystal nuclei in the system. Therefore, we need to design a procedure to detect the location of crystallites, as well as their sizes and shapes. This section details the image processing algorithms used for nuclei detection in this work, and can fall broadly into two categories. For the study of smaller PMMA ($\sigma = 392$ nm) where the identification of individual colloids is not essential, we selected the fast Fourier transform method to directly detect nuclei, with the corresponding results being re-examined by the cross-correlation (Sec. 3.3.2 - 3.3.3). Meanwhile, L-PMMA allows particle-resolved imaging techniques and the consequent particle tracking method, which is detailed in Sec. 3.3.4. The nuclei are characterised by the Topological cluster classification (TCC), as mentioned in Sec. 2.6.2 and will be discussed in Sec. 3.6.4. The corresponding python codes come from my colleagues, with private communication and permission from them: (i) the fast Fourier transform was developed by Nicholas Wood, with great help of Francesco Turci and minor modifications by myself (Sec. 3.3.2), (ii) the cross-correlation was developed by Francesco Turci, with Yushi Yang designed the simulation kernels (Sec. 3.3.3), (iii) the particle tracking method is the combination of Trackpy [3] and nplocate [336] packages, in which the latter was developed by Yushi Yang (Sec. 3.3.4).

3.3.1 Image parameters

A typical (x, y) plane image from an experimental stack of the smaller PMMA is shown in Fig. 3.1(a). The degree of zooming out was determined by eyes to ensure the individual particles could be recognised over the intrinsic noise. The size of this image is $43.4 \times 43.4 \mu\text{m}$, containing around 7000 particles in the (x, y) plane. We therefore access a much more comprehensive observation of nucleation, especially fairly rare events such as spontaneous formation of nuclei in weakly supercooled region, by confocal microscopy than studied previously. This mainly comes from two improvements: first, as mentioned before, the use of smaller colloids accelerate the crystallisation process by 1-2 orders of magnitude, since the Brownian time is proportional to σ^2 . Second, the confocal microscope allows us to take stacks up to $140 \mu\text{m}$ along z direction. We can further take multiple stacks of several samples at the same volume fraction, which enable us to achieve an imaging volume containing 2 - 3 orders of magnitude when compared with previous work of around 6×10^4 using larger particles ($1 - 2 \mu\text{m}$) [48, 76].

Theoretically, the optimal lateral and axial resolutions that a confocal microscope can achieve are around 180 nm and 500 nm, respectively [100, 268], and the pixel size should be around half these lengths. Though the known shape of the particles allows a degree of undersampling, and the pixel size can reduce to 50 nm in (x, y) planes [76, 146]. A possible approach further improving the resolution is stimulated emission depletion (STED) microscopy, depleting the fluorescence around the central focal spot by de-exciting the corresponding fluorophores via the stimulated emission, which requires the flux of stimulating photons to be high enough to suppress the spontaneous

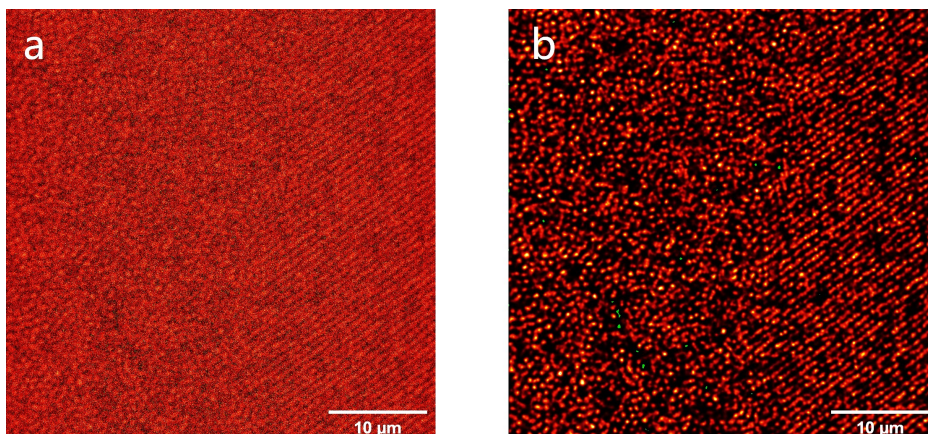


Figure 3.1: Typical (x, y) plane images of the $\sigma = 392$ nm particles used in this work. (a) An original confocal image. (b) The corresponding deconvolved image. These images show the fluid-crystal phase boundary: left: fluid; right: crystal.

fluorescence emission [318]. However, we found that the effective quenching led to dye bleaching, especially when recording z-stacks with long-term exposure to STED light. We thus performed deconvolution method instead of the STED technique to reduce the effect of diffraction. This processing was completed by the Huygens professional software [292]. The software calculates a theoretical point spread function (PSF) with the given parameters, including excitation and emission wavelength, the refractive index of glass slides, immersion oil and solvent, and the numerical aperture of the imaging lens. Then this PSF is applied to experimental images. Fig. 3.1(b) shows the deconvolved result of the original confocal image, with a more distinguishable edge of each particle. By the Nyquist rate calculator (see Sec. 2.5.1.1), a voxel size was chosen as $40 \times 40 \times 120$ nm, equal to around 10 pixels per particle in (x, y) plane, and 4 pixels in z direction. This promises the maximum gap between a nucleus and an image plane is $\leq 1/8\sigma$ as a nucleus will not be captured only if the plane intersects with its constituent particles.

3.3.2 Fourier transform

A fast Fourier Transform (FFT) is an ideal method for characterising specific states, as the ones of full fluids will look very different to those which contain crystals after processing — the fluid will have a ring pattern in which the most intense points located at a distance of the reciprocal of the particle diameter, $1/\sigma$, from the centre which is the most intense point of the image. This ring corresponds to the first peak of the pair correlation function in real space. Whereas the region containing crystals will exhibit noticeable peaks representing the lattice spacing of the crystal. We can therefore identify the state of a region according to their Fourier transform results. Here we only carry out the 2-dimensional FFT in (x, y) planes of the experimental stacks, which will be explained at the end of the next section.

However, simply performing the Fourier transform and checking peaks might still produce

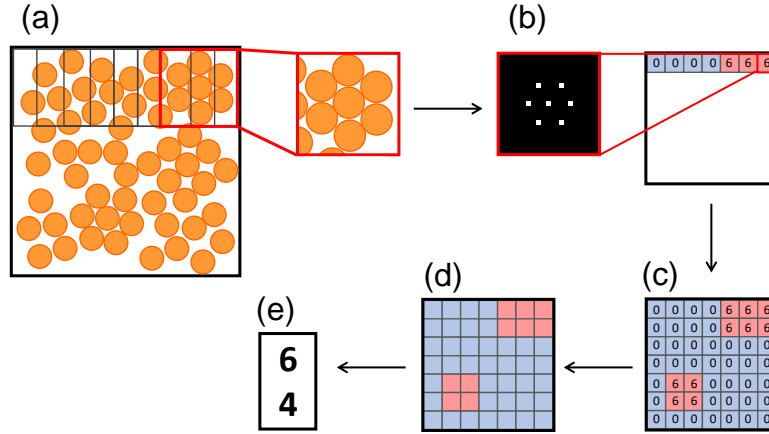


Figure 3.2: Schematic pictures of the fast Fourier transform processing on large images. The processing is performed in the (x, y) planes. (a) The initial image is divided into smaller overlapping sub-regions. This is repeated across the whole region where the sub-image advances the same pixels until the edge. These overlaps reduce the effects on the location of the grid, and improve the resolution. (b) A FFT is executed on the sub-image. The hexagonal crystal structure gives 6 peaks with the central brightest peak removed. These peaks are captured and the amount of peaks is recorded into a result array which stores the peak number of all the sub-images. (c) The full result array is generated after all the sub-images have performed Fourier transform. (d) The array is processed, including binarisation which identifies the sub-regions to crystal or non-crystal state, linking the connected crystal regions and labelling them as one nucleus. (e) A full list of all the nuclei with the size n in the initial large image is generated. Replotted from Wood [331].

large errors. The error appears when we analyse large images in order to improve the sampled volume, in which many separate nuclei may exist. These nuclei are in various sizes, and form different angles with the focal plane of the microscope due to random orientation, resulting in lower intensity crystal peaks in different places, which in turn disturbs the overall detection. Alternatively, we divide the images into smaller sections and carried out the fast Fourier transform on all the sub-images. Fig. 3.2 shows the schematic pictures of this method. It allows us to identify the location of crystal nuclei in the whole image, and obtain their size and shape, without running the time and computational costly particle tracking on much larger datasets.

3.3.2.1 Identifying peaks of Fourier transform

The peaks indicating the existence of crystals need to be identified after Fourier transform. To focus on identification, we first shift all the zero-frequency components to the centre of the spectrum, which removes the information of phase position representing the difference between the centre of most central particle and the centre of sub-image in the Fourier transform, when these two centres do not overlap due to the movement of sub-image across the whole image. There are many existing algorithms for finding peaks of image intensities, in which we selected the

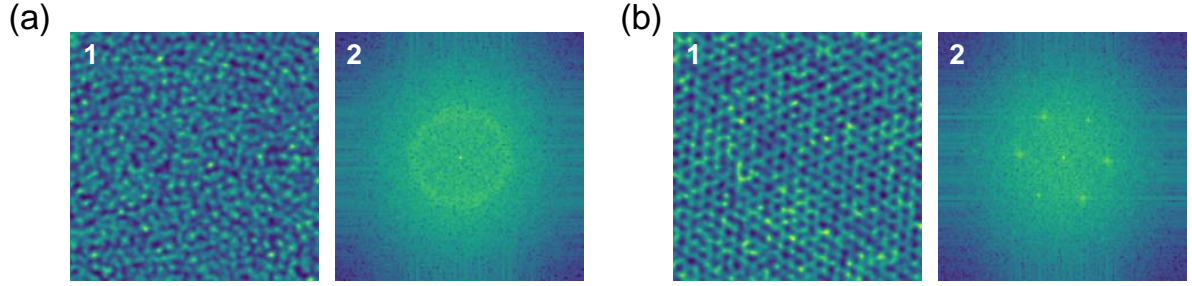


Figure 3.3: Samples of the identification of the peaks. “1” are initial sub-images, and “2” present corresponding FFT results. (a) A fluid region and the ring pattern. (b) A crystal region of hexagonal structures and the corresponding peaks. The centre point with the highest intensity will not be counted. This sub-image is therefore recorded as 6 peaks into the result array.

peak_local_max from the scikit-image library [312]. This algorithm asks for two input parameters: the minimum separation distance of detected peaks, which only keeps the brightest peak in multiple peaks closer than the given distance; the intensity threshold, which discards all the peaks less bright than the intensity threshold. We chose 2 pixels slightly shorter than σ in reciprocal space for the distance threshold, and half the average intensity of the image for the intensity threshold, which further effectively recognised peaks of clear crystal regions.

However, peaks may still appear in a clear full fluid region as a result of thermal noise in the image. In order to better capture the genuine peaks of crystal, another ring threshold is needed. The fluid ring exists at a fixed distance from the centre of the sub-image. By calculating the ratio of the average intensity at the ring distance to a peak intensity, and then comparing it with the ring threshold, we can decide whether this peak belongs to a fluid ring. Fig. 3.4 shows the relationship between the ring threshold value and the ratio of detected crystal regions in the whole image. The data are the average of 20 frames. We expected a sharp increase in the ratio of the crystal region, where the corresponding value could be taken as the ring threshold. However, in the real case, a smooth change of the ratio of crystal showed. This happened since a sub-image located at the boundary of fluid and crystal had peaks and a ring at the same time. The average intensity at the ring distance would increase continuously along with the increasing ratio of fluid area in the sub-image. Furthermore, the particles were in a non-equilibrium state when imaged, contributed to possible defects in crystal nuclei, which also promoted the generation of ring-like pattern. We therefore chose the ring threshold at 0.9, which theoretically only removed the most obvious fluid regions while kept almost everything else as the crystal. This threshold value did the best job when its results are compared with the identification results by eyes.

Given the details of peak detection, we do not perform 3D Fourier transform for several reasons. Firstly, due to the relatively weak axial resolution with such small colloids, although the minimum experimental pixel size of z direction is used (120 nm), there are only 3-4 axial pixels of one particle, which cannot provide reliable information. Secondly, the PSF of the confocal microscope has an ellipsoid or hourglass shape along its axial axis [58], indicating

that the periodical patterns of crystals are anisotropic in (x, z) or (y, z) planes. This affects the determination of the ring threshold, as well as the accuracy of the peak identification. Finally, the well-developed algorithms, such as `peak_local_max` used in our work, are mostly designed for 2D images. Therefore, we only run 2D fast Fourier transforms, then convert the 2D nuclei list to the distribution of real nuclei by merging the connected crystal planes along z axis, as detailed in the next section.

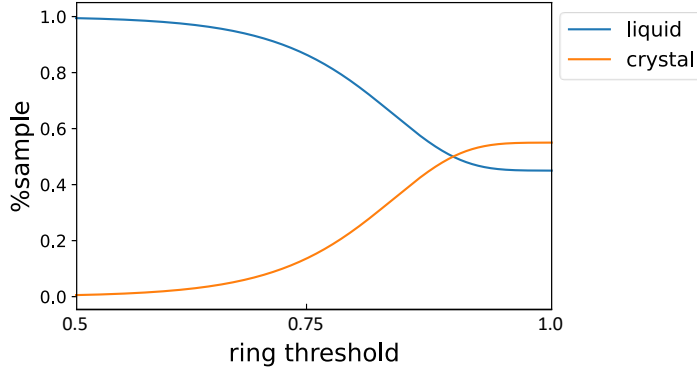


Figure 3.4: The dependence of the percentage of characterised crystal and fluid regions on the ring threshold. A lower threshold indicates a larger intensity difference between the peak and the ring pattern average, which consequently reduces the amount of crystal.

3.3.2.2 Counting nuclei

An image where all sub-images are labelled as “crystal” or “fluid” can be obtained after the Fourier analysis, which can be written as a mapping from the fluorescent image I_{ij} to a labelled image C_{ij} ,

$$C_{ij} = \begin{cases} 0 & \text{if } I_{ij} \text{ belongs to the fluid} \\ 1 & \text{if } I_{ij} \text{ belongs to the crystal} \end{cases}$$

where i and j are the row and column number of a sub-image. To get the size distribution of individual nucleus, which is directly linked to the nucleation barriers, the image C_{ij} needs to be further labelled by their corresponding nucleus indices, leading to another image L_{ij} ,

$$L_{ij} = \begin{cases} 0 & \text{if } C_{ij} = 0 \\ k & \text{if } C_{ij} \text{ belongs to the } k\text{th nucleus} \end{cases}$$

For the mapping from C_{ij} to L_{ij} , there is an efficient algorithm, `scipy.ndimage.measurements.label`, from the `scipy` library [147]. This algorithm only requires one parameter, the structuring element that defines feature connections. We used the default structuring element, treating the two regions horizontally or vertically adjacent as belonging to the same nucleus, while two regions with only diagonal adjacency are not connected. Since we work with the binarised image C_{ij} ,

we discarded the crystallographic details. For example, we can recover the crystal class of each nucleus from its corresponding Fourier transformation, where 6 peaks mean hexagonal structure (HCP or FCC), 4 peaks mean BCC (which is unlikely to occur in homogeneous crystallisation of hard spheres) or the HCP/FCC defect areas, and 2 peaks mean a possible boundary between fluid and crystal. These crystallographic details might help us better understanding the nucleation mechanism with further investigations. Nevertheless, such information loss will not affect the nuclei size distribution.

When we carried out this labelling procedure ($C_{ij} \rightarrow L_{ij}$), we sometimes found nuclei which were smaller than the size of a single particle. This might result from imaging artifacts or inaccurate peak identification. To remedy the situation, we discarded the nuclei whose size $n < 7$ when calculating the nucleation barriers, since seven is the smallest crystal structure, with a central particle plus six neighbours ordered hexagonally.

3.3.2.3 Possible errors

Fig. 3.5 shows the Fourier transform results. The top row of this figure is the original confocal image, and the bottom row is the corresponding identification result. The colours indicate the number of peaks found in the sub-image. As expected, it shows less accuracy when attempting to capture small nuclei in the image. The yellow lines circle several hexagons recognised by eye. Some of these crystallites were undetected, or assigned a smaller volume after processing. In contrast a good identification of the large crystal regions in Fig. 3.5(b) bottom was achieved using a wide range of the ring threshold (0.8-1.0). When the confocal images were analysed, we observed that the large crystal nuclei (diameter > 10 particles on the focal plane) only had hexagonal structures, in which individual particles exhibited deformation through confocal imaging, as shown in Fig. 3.5(b) bottom middle and bottom right: they extend in three directions to connect with their nearest neighbours, so that the line-like pattern forms. This is due to the linearity property of the PSF, giving a sum intensity which affects the imaging of the particle edges, while in fluid or smaller crystal regions the particles are more dilute with less effect from the PSF. Although they are more heavily deformed in the large crystal region, the universe pattern enables a better interpretation of Fourier transform results, as the Fourier transform actually reflects the periodicity of the intensity. In the crystallite region, however, the particle imaging receives a varying PSF overlapping value that depends on the distance from their neighbours. Another issue of the small crystal nuclei is that they are not always “perfect”, especially in a non-equilibrium state. Their constituent particles keep moving in the dispersion medium, leading to fluctuations and various defects. This also causes difficulties in identification methods. Improved Fourier transform results of small nuclei can be achieved by carefully adjusting the ring threshold for each image.

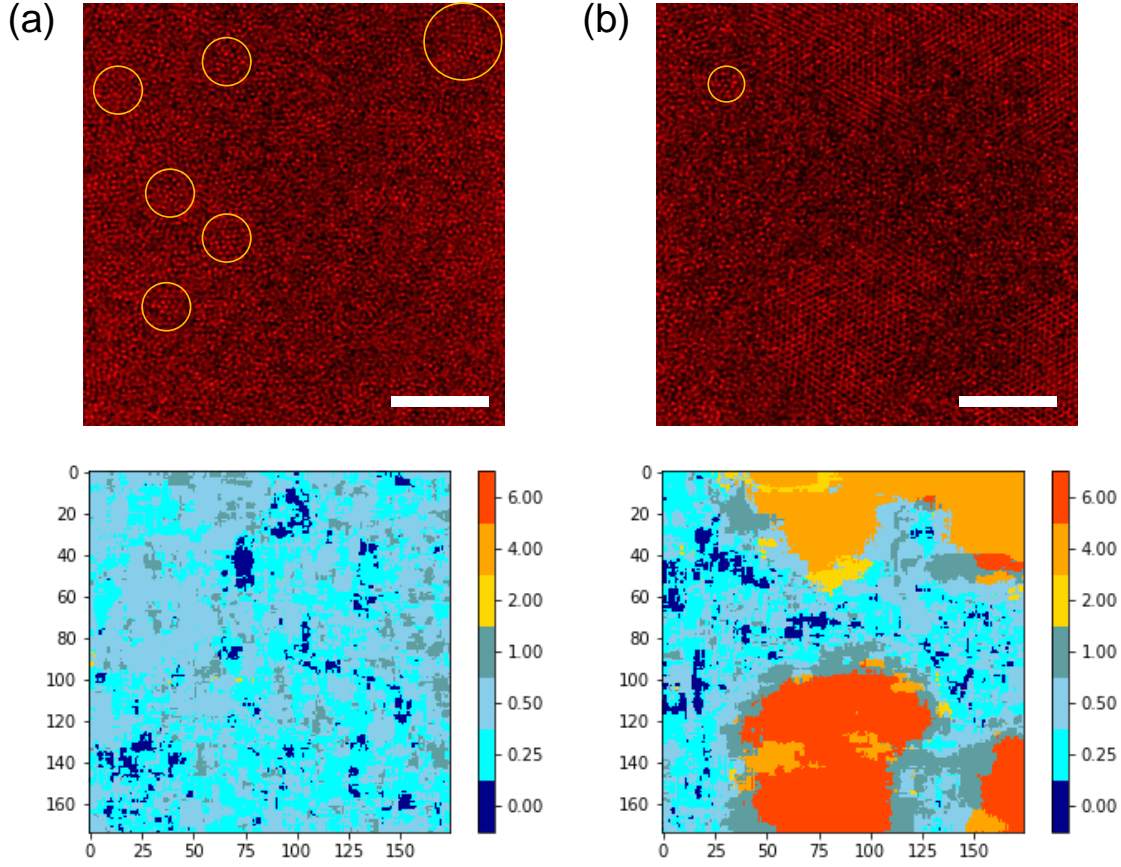


Figure 3.5: The identification results of the Fourier transform on various size of nuclei. The top row is the initial confocal image, and the bottom row is the corresponding FT result. The colours represent the number of peaks found in the sub-image, as mentioned in Sec. 3.3.2.2. (a) Small, separated nuclei, as circled by yellow solid lines. (b) Large continuous crystals.

3.3.3 Cross-correlation

Cross-correlation processing is another method we used as a comparison to review the Fourier transform results. It measures the similarity between two signals. Therefore, if a proper template, “kernel”, is selected, *i.e.* the typical crystal structure (hexagonal structure), we expect to enhance the intensity of crystal regions and weaken the intensity of fluid regions simultaneously through applying the kernel. The relevant information of the cross-correlation is shown in Fig. 3.6. A simulation kernel is generated with the same particle diameter and crystal lattice parameters of the experiments (Fig. 3.6(a1)). Meanwhile, as mentioned before, experimental crystal nuclei have defects. Therefore, 30 sub-images of the hexagon pattern are averaged to reduce the random defects for a better experimental kernel (Fig. 3.6(a1)). Since the nuclei have different orientations in an image, 90 rotations of the kernel are made, which is equal to rotating 4° each time. Then, for every rotation, a cross-correlation is applied to the image with the simulation or the experimental kernel, stacking the intensity results into a 3D array. In this step, a border as thick as half the

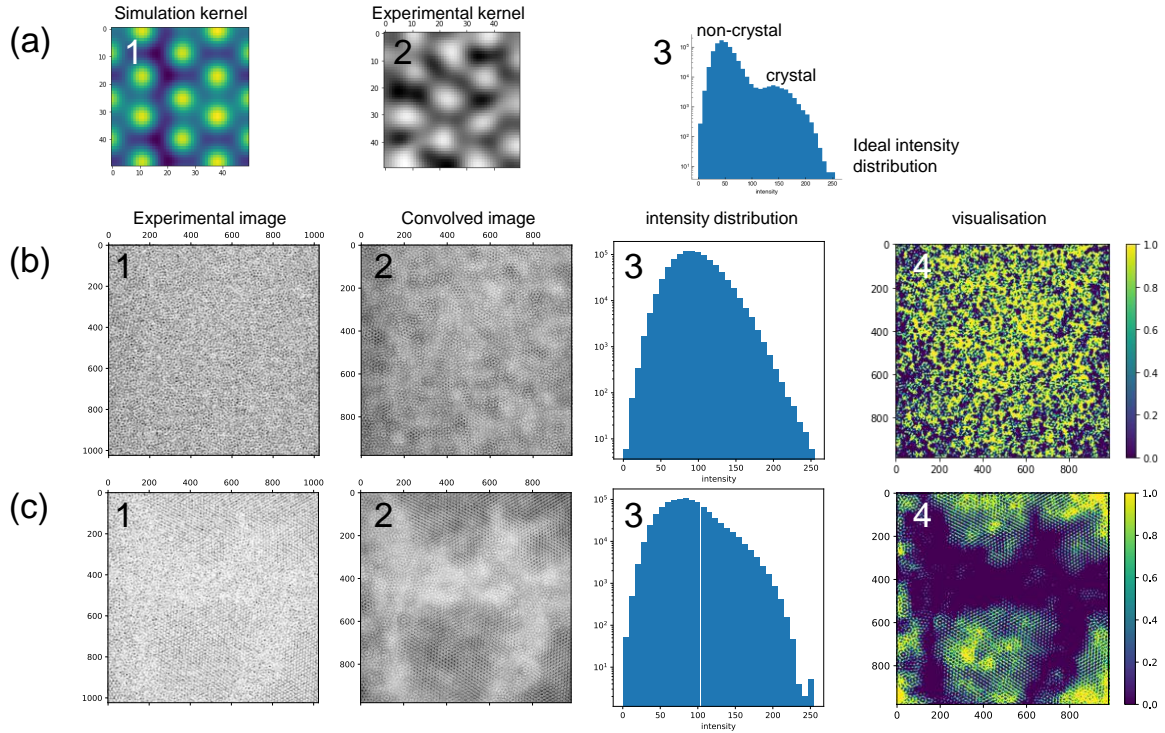


Figure 3.6: Relevant information of the cross-correlation processing method in the (x, y) plane. (a) 1,2 Two types of kernels used in this work. 3 Ideal intensity distribution for deciding a threshold for crystal identification. (b) Results of an image containing small nuclei. (c) Results of an image containing large nuclei. Column numbers 1-4 in (b) and (c) indicate the initial image, cross-correlated image, intensity distribution and visualised labelling in which 1.0 means crystal while 0.0 means fluid.

kernel is created with non-physical information, which is removed when all the kernels has been applied. Finally, the image is reconstructed by extracting the max value along the stacked dimension, which obtains enhanced intensity of crystal regions as the kernel with crystalline hexagon patterns has performed. We had expected a clear threshold of intensity to distinguish non-crystalline and crystal regions, as shown in Fig. 3.6(a3). The cross-correlated images (Fig. 3.6(b2) and (c2)) exhibited a higher contrast comparing with the original images. However, when calculated the intensity distribution (Fig. 3.6(b3) and (c3)), this proved unfeasible. A smooth change with only one peak was obtained in images containing either crystallite or large crystals, which prevented us from deciding threshold values of different states. In addition, the cross-correlation processing exhibited a weak detection ability of finding small nuclei, as indicated in visualised labelling (Fig. 3.6(b4) and (c4)). It also returned irregular, ramified structures which seems impossible in a spontaneous nucleation process of hard spheres.

We can conclude that, both image processing techniques we used (Fourier transform and cross-correlation) have a degree of inaccuracy in finding small crystal nuclei. This is due to the image quality arising from limited resolution and various defects of crystallites, which blur the

clear criterion for identifying a “crystal”. In particular, by carefully adjusting the ring threshold parameter in the Fourier transforms, better detection of nuclei can be obtained. Therefore, for the particles of $\sigma = 392$ nm, we only identified the nuclei through Fourier transform method.

3.3.4 Particle tracking

As explained in Sec. 3.3.1, the pixel size of the confocal microscope can reduce to 50 nm. Considering this resolution still restricted the imaging quality of the small PMMA particles (average diameter ≈ 400 nm), and further affected the nuclei identification, we also used another larger PMMA particles $\sigma \approx 2$ μm , which are suitable for the particle tracking algorithm that can extract the positions of all particles from the image. In this work, we used a combination of the Trackpy [3] and nplocate [336] python packages. Trackpy requires several arguments, of which two of the most important parameters are the “feature diameter”, and the “separation”. The “feature diameter” can be a number or a tuple specifying the diameters of colloids in the (z, y, x) dimensions sequentially. We chose the number of pixels as 11 as it needs to be an odd integer, and 11 gave the best tracking results among the range 9 - 13. The other key parameter is the “separation”. The algorithm has a tendency to find false overlapped colloids, *e.g.* if noise generates another local maximum besides the real centre maximum in a single particle. Hence, the separation parameter helps to remove the lower intensity particle (false particle) in a pair having centre distance closer than the given separation value. Trackpy worked well for dilute samples ($\phi < 0.3$). However, for larger particles, we increased the pixel size to about triple the Nyquist distance (See Sec. 2.5.1.1) to ensure the acceptable imaging volume. This contributed to undersampling, which biased the edges of close particles.

In order to improve the quality of tracking, we further used the python algorithm nplocate, developed by my colleague Yushi Yang and based on Trackpy. A scheme for this algorithm is shown in Fig. 3.7. Generally, it is easy to find some particles by Trackpy, even in a highly distorted image. The nplocate calculates the average shape (**S**) of the detected colloids (Fig. 3.7(a) middle column), considering the contribution of nearby neighbours. A simulation model is then created to mimic the observed shape **S** through tuning the diameter and separate Gaussian blur parameters in (x, y) and (x, z) planes, as shown in Fig. 3.7(a), where the left column shows the simulated shape **S_{sim}**, the central column shows the observed shape **S**, and the right column shows their differences. The algorithm then generates a “simulated image” **I_{sim}** by drawing the simulated shape **S_{sim}** on each location that Trackpy finds. The difference between the original image **I** and **I_{sim}** is then calculated as

$$\mathbf{D} = \mathbf{I} - \mathbf{I}_{\text{sim}}$$

and then the cross-correlation between **D** and **S_{sim}** is calculated to get a new image **P**:

$$\mathbf{P} = \mathbf{D} * \mathbf{S}_{\text{sim}}$$

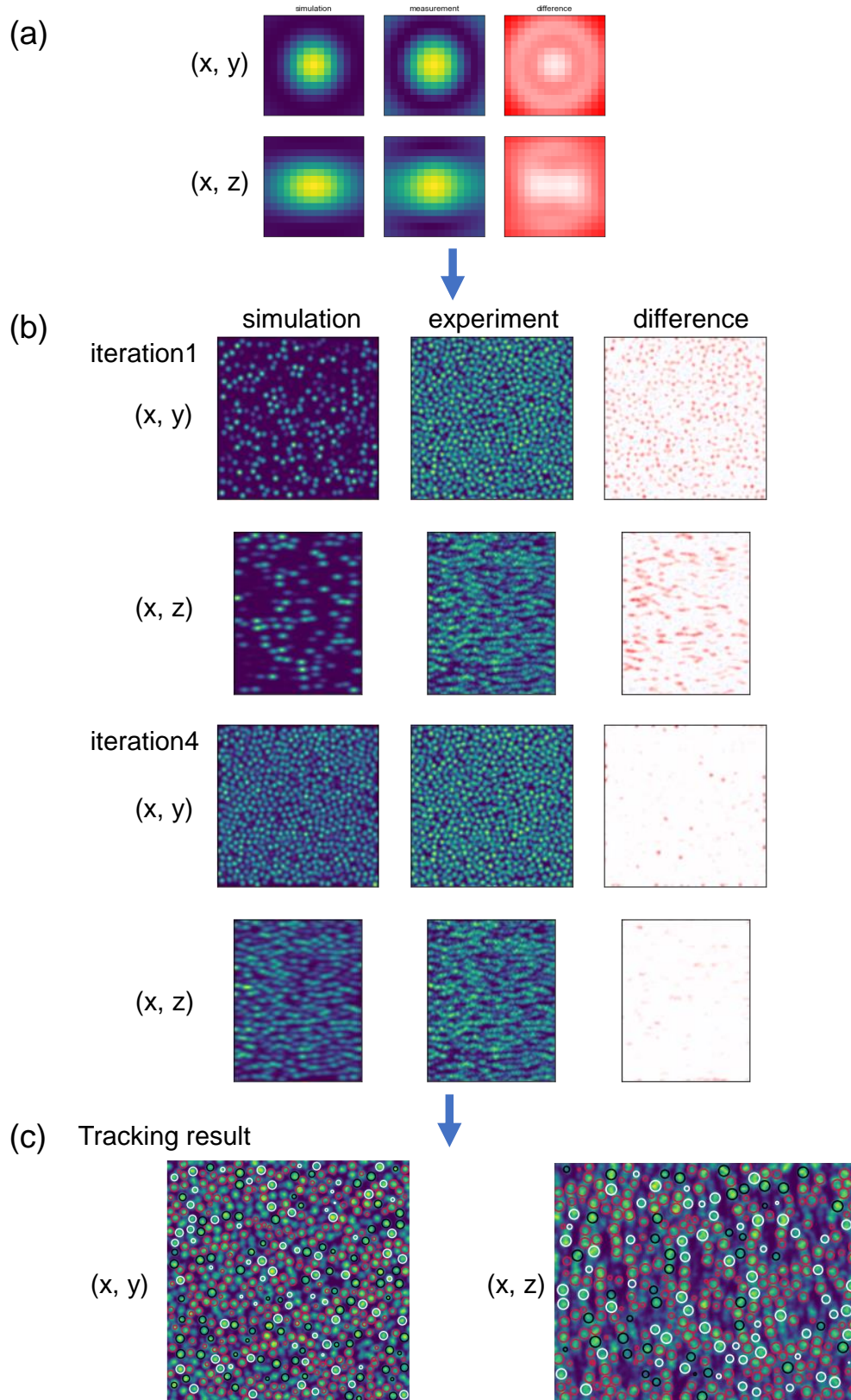


Figure 3.7: A schematic diagram of the nplocate algorithm. The black and white lines mean the particles captured by Trackpy, while the red lines are those of nplocate.

For all the pixels, \mathbf{P} encodes their probability¹ values of being a particle centre. We then execute Trackpy again for \mathbf{P} to find previously uncaptured particles. As more particles are discovered, we update our estimations of \mathbf{S}_{sim} , \mathbf{D} , and \mathbf{P} so that they are more accurate. Repeatedly, we detect more particles and update \mathbf{S}_{sim} , \mathbf{D} , and \mathbf{P} , until no new particle can be found in \mathbf{P} . Finally, a list recording the coordinates of tracked particles is obtained. Fig. 3.7(c) shows a slice of (x, y) and (x, z) plane, respectively, in which black and white lines circle the particles found by Trackpy, whilst red lines are particles found by nplocate. Additionally, black lines mean the particles whose centres are in the later slices, while white outlines indicate the particle centres being in the previous slices.

We performed the particle tracking algorithms to obtain the coordinates of L-PMMA for further analysis. However, not all the particles, with the exact total number of particles being calculated from the known stack volume, ϕ_{prep} and the volume of a single particle, can be tracked, due to the uncompleted shapes along the edges of the image and the high volume fraction which causes distorted particle boundaries when the particles have close neighbours. We will discuss the tracking quality in the Sec. 3.6.2.

3.4 Small PMMA — particles of $\sigma = 392$ nm

3.4.1 Understanding the volume fraction

The results started with the investigations of small PMMA particles. In order to compare with the literature, we need to first understand the relationship between the prepared and the core diameter of the colloids in our system. This is done by examining our preparation procedure. The PMMA particles were centrifuged to a sediment which was regarded as being a random close packing (RCP) structure with $\phi = 0.64$. The sediment was later diluted to a targeted volume fraction. However, the exact volume fraction value of this sediment is debatable. There are mainly two sources of the softness in our experiment: charge and steric stabilisation.

It is now generally thought that some degree of charge is always induced by the dispersion of the particles into a solvent, due to the dissociation of charged groups on the colloidal surfaces, or attachment of charged groups from the solvent, or both. For a charged colloid, the electrical double layer gives rise to a larger effective diameter. We can model the electrostatic interactions by a Yukawa potential $u_Y(r)$, as explained in Sec. 1.3.2. The key question is then if the centrifugal force acting in the centrifuging process can overcome this Yukawa potential to compress the particles. In our system, the composition of the solvent is fixed to obtain a final density equal to $\rho_{\text{PMMA}} = 1.196$, for which the Bjerrum length λ_B is also fixed. Leunissen [175] measured the dielectric constant of the density matching solvent as $\epsilon_r = 5.6$, giving $\lambda_B = 1.0 \times 10^{-8}$. This then changes the Debye screening length $1/\kappa$. Another parameter to consider is the colloid charge,

¹The raw values of \mathbf{P} can take any value in \mathbb{R} , therefore it is a value of likelihood (alternatively we can think of it as the “energy”). Nevertheless it is easy to normalise this image to convert the values into probabilities.

which can be described by a rule of thumb $Z\lambda_B/\sigma \approx 6$ [258, 278]. Taking the particle diameter $\sigma = 392$ nm, we calculated the relevant parameters of Yukawa potential as listed in Table 3.1.

ϵ_r	λ_B	$1/\kappa$	$\beta\epsilon_Y$
5.6	1.0×10^{-8}	5.05×10^{-8}	58.9

Table 3.1: The parameters of Yukawa potential for PMMA particles at $\sigma = 392$ nm.

Thus, the contact Yukawa force is 1.24×10^{-18} N, calculated by the negative derivative of the potential. Meanwhile, the centrifugal force can be calculated as $F = \Delta m \omega^2 r$, where Δm is the mass difference between the particles and the solvent, $\omega = 2\pi \times \text{RPM}/60$ is the rotor speed, and r is the distance from the centre of the rotor [57]. The solvent has the same density at 20 °C, though the higher temperature breaks the density matching, enabling the particles to precipitate to the bottom. Data reflecting the dependence of the CHB density on the temperature is hard to find, but that of cis-decalin reveals a density decrease of 1.5% from 20 to 30 °C [343]. This contributes to a final centrifugal force on each particle $\approx 9.32 \times 10^{-18}$ N. We therefore expected that the exerted centrifugal force overcame the Yukawa repulsion, and compressed the particles to a diameter of the steric diameter (core diameter + length of PHSA chain). Although the compression degree was difficult to measure, based on the calculations that the centrifugal force is almost 8 times stronger than the Yukawa contact force and the time used for centrifugation (120 min), we approximated the particles in the sediment packed without the presence of electric double layers.

We then considered if the PHSA layers were further compressed under such a centrifugal force. The PMMA itself is grafted with PHSA polymer chains for steric stabilisation. The manufacturer did not provide the relevant information, but it is likely to be a few nanometres [42]. In this reference, Bryant *et al.* measured the interaction induced by PHSA chains for various particle core diameters, and described the steric stabilisation by an inverse power law potential $u_{\text{steric}}(r) \approx \epsilon(\sigma_h/r)^n$, where ϵ is the strength of the repulsion, σ_h is the diameter at which the hard-core potential becomes infinite, in other words, the separation at which the PHSA chains are fully interdigitated, r is the colloidal distance, and n is the repulsive index. We took the data for the core diameter of 400 nm, which give the $\beta\epsilon = 329$. Similarly, by calculating the negative derivative of the potential, the steric force obtained was 7.04×10^{-18} N with a steric layer of 9 nm, comparable to the centrifugal force, but steeply increased to 1.00×10^{-16} N when the layer is compressed to 8 nm. Therefore, the PMMA particles in the centrifuged sediment were approximated to be separated by just the steric stabilisation layer of ≈ 8 nm, giving a steric diameter $\sigma_{\text{steric}} = 400$ nm, and the random close packing was reached by the steric diameter. In this case, for a given desired volume fraction (prepared volume fraction), ϕ_{prep} , it was equivalent to the steric volume fraction ϕ_s , and we actually obtained a sample at $\phi_{\text{core}} = 0.941\phi_s$. We took this relationship for further comparisons.

3.4.2 Phase diagram

Previous experimental work involving small particles commonly used light scattering techniques to achieve the final equilibrium crystallinity (X) at a given volume fraction [89, 126, 223, 267] (except Hallett *et al.* who measured X of $\sigma = 540$ nm PMMA particles by STED [121]). This required previous embedding of tiny paramagnetic wire into the samples. In our experiment, we used capillaries to measure the final X as well as the nucleation rate without the paramagnetic wire. Briefly, the non-sintered capillaries were used to measure the final X and sintered capillaries were used to measure the nucleation rates. For each measurement, we performed three replicas to get the mean values and indication of the experimental uncertainties. We selected the rectangular non-sintered capillaries for several reasons. Firstly, the nucleation process will not affect the final X as it is uniquely determined by the volume fraction of hard spheres. Secondly, the sample reaches X much faster than in sintered ones, as the nucleation barrier on the interfaces between the suspension and glass walls is much lower. Thirdly, the preparation of sintered capillaries is difficult, so it is better to retain them for nucleation experiments only. Finally, the confocal microscope can scan the whole depth and length of rectangular capillaries, enables a full understanding of X .

My colleague, Nicholas Wood, who developed this method, discovered a faster experimental procedure that is worth mentioning. When a capillary is not fully filled, leaving an air bubble at one side, the crystal strongly prefers to grow from the air-dispersion interface rather than wall-dispersion interface. Thus a continuous crystal forms, generating a clear phase boundary between the fluid and crystal, and the X is simplified to the length ratio of the crystal region to the whole sample. The measurement was done by the coordinate record function of the confocal microscope. We calculated the length ratio from the position of the air-dispersion interface, fluid-crystal separation boundary, and the end of the capillary. The end of the capillary was characterised by the dynamics of particles, since the particles at the end of the capillary were arrested by the glue and could not be counted. A typical fluid-crystal phase separation of an air-bubble-sealed sample is shown in Fig. 3.1, where the right part is crystal state. The updated measurement is quite accurate: if we assume an error of 100 colloidal diameters in the sum of phase boundary and the end of the capillary, since the entire capillary is several centimetres long, the final error is 0.15% on the X , which is, to our knowledge, the most accurate method to date of measuring the X in confocal experiments.

Fig. 3.8 shows the measured crystallinity of the PMMA particles with increasing prepared volume fractions ϕ_{prep} in several separate experimental runs. Here the ϕ_{prep} are quoted from the experimental preparation as stated in Sec. 2.2. As expected, a phase transition from a fluid to crystal state appeared, in which the ratio of crystal was linearly dependent on the prepared volume fraction. The freezing started at different volume fractions, though for most of the experimental runs it located around $\phi_{\text{prep}}^f = 0.24$. Additionally, the coexistence region was observed to be slight wider when examined after a longer time since sample preparation

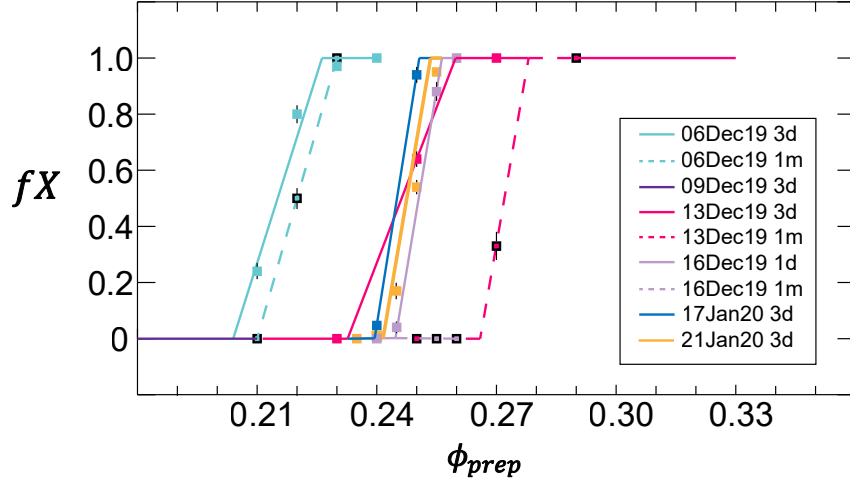


Figure 3.8: The crystallinities of PMMA of $\sigma_{\text{core}} = 392$ nm at different prepared volume fractions. Colours represent individual experimental runs with the preparation date. “d” and “m” in the legend mean day and month of waiting after preparation, respectively.

(See enclosed points in Fig. 3.8). It is obvious that the coexistence region in our system is lower than similar systems with PMMA particles dispersed in a density and refractive index matched solvent [107, 241, 285], even if the uncertainty from the measurement of X is excluded, as it only contributes a maximum error of 0.15%.

3.4.3 Discussion on the change of coexistence region

With the above relationship between the core and prepared volume fraction, our results were not in a good agreement with those of the hard sphere systems. For example, Pusey *et al.* [241] achieved the freezing and melting core volume fraction $\phi_{\text{core}}^f = 0.407$ and $\phi_{\text{core}}^m = 0.442$, respectively. Gasser *et al.* [107] reported the freezing at $\phi_{\text{core}}^f = 0.38$ and melting at $\phi_{\text{core}}^m = 0.42$. There are two possible reasons to explain our results: polydispersity and charge. Polydispersity shifts the phase transition region, but to the opposite direction. The transition region can increase by about 0.02 for a polydispersity of 0.05 [90], while higher polydispersity ($> 10\%$) suppresses the crystallisation [240]. Therefore, we believed that the main reason should be the charge.

With the same parameters of Yukawa potential shown in Table 3.1, the effective hard-sphere diameter was then calculated using the Barker-Henderson method [21]

$$(3.4) \quad \sigma_{\text{eff}} = \int_0^\infty [1 - \exp(-\beta u(r))] dr.$$

This gave a final effective diameter of 605 nm, leading to a dramatic increase of volume fraction, as the volume is proportional to σ^3 . For instance, our core freezing volume fraction of 0.226

(calculated from prepared freezing volume fraction of 0.24, the same calculation hereafter) corresponds to an effective freezing volume fraction of 0.57, even more than the hard sphere melting line. This is clearly unphysical. Therefore, we needed to consider the electrostatic properties in more details.

The electrostatic parameters listed in Table 3.1 might be inaccurate. Yethiraj *et al.*, who first constructed this model system of cis-decalin and CHB mixture with TBAB salt, demonstrated the existence of significant charging can cause a shift in phase transition from $\phi_{\text{freezing}} = 0.494$ to $\phi_{\text{freezing}} = 0.2$ [339]. Sedgwick obtained a value of around 100e [275], whereas Campbell *et al.* measured the surface charge of the particles as 140e, giving a Yukawa contact potential of $30k_B T$ [47]. Relative studies have reported the instability in the ionic strength of CHB in different batches and over time [175, 251, 257]. This affects the electrostatic interactions, and the dissociation of TBAB salt. For example, Yethiraj *et al.* found a TBAB dissociation of 0.5%, while Leunissen measured 2% [175], which causes a huge difference in the calculated effective diameter. In our case, if we assume that the particles follow hard sphere behaviours, freezing at an effective volume fraction of 0.494, then the ratio of effective to core diameter is equal to the cube root of the freezing volume fraction ratio, and the Debye screening length $1/\kappa$ is around 54 nm, which is quite similar to the value listed in Table. 3.1. A further assumption that the ions mainly comes from the dissociation of TBAB, gives a salt dissociation of 3.5%, more than 2% measured by Leunissen. Therefore, the reason for shorter effective diameter may be considered as the combination of the inconsistent ionic strength of CHB, the uncertainty of the level of surface charging given by the rule of thumb $Z\lambda_B/\sigma = 6$, and the change of the electrostatic interactions with increasing volume fraction [33, 306, 307].

Another possible explanation is that the large Bjerrum length, *e.g.* $\lambda_B \approx 10$ nm occurred due to the low dielectric constant in our case, is long enough to enable the ions on colloidal surfaces to interact with multiple counter-ions on neighbour colloids in an aggregate, and thus the ions prefer to condense around contact regions among particles, leading to an anisotropic charge distribution. This asymmetry of colloidal charge breaks the Yukawa interpretation of electrostatic repulsion [161, 254]. This suggestion is consistent with the study of the same system, PMMA particles ($\sigma = 2.16 \mu\text{m}$) dispersed in the mixture of cis-decalin and CHB, which reveals a notable decrease of colloidal charges upon increasing particle volume fraction [257]. Therefore, consequently weaker electrostatic interactions actually present in the system, although the degree of that is difficult to measure or estimate.

Given the discussions above, we present the phase diagrams by quoting the prepared (steric) volume fractions rather than the effective volume fractions, as it is difficult to determine the electrostatic conditions in our experiments. This does not affect the comparison to other systems, as we actually explore the dependence of the height of nucleation barriers on the changing volume fraction in the coexistence region. Additionally, we can still compare the height values corresponding to the distance from the freezing volume faction, which is the method Auer and

Frenkel used for nucleation of weakly charged colloidal spheres [14].

3.4.4 Nucleation barriers

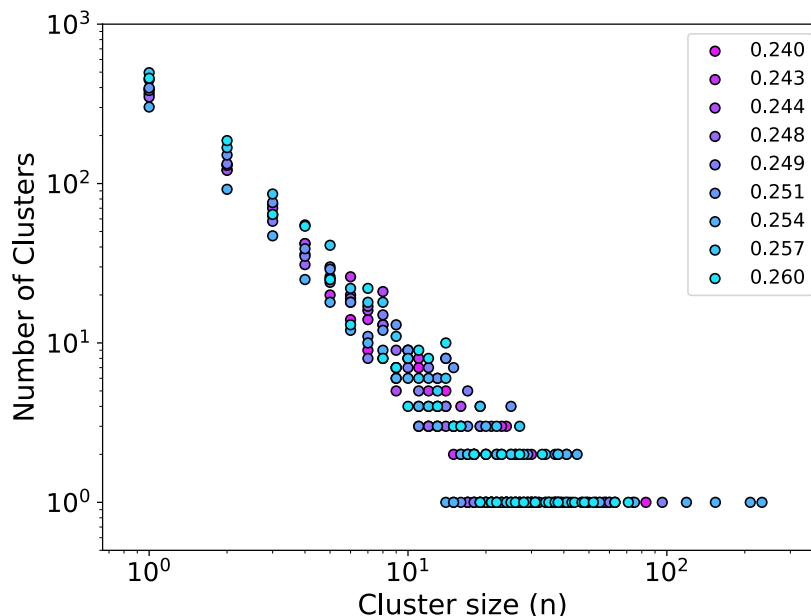


Figure 3.9: The size distribution of tested volume fractions of PMMA at $\sigma_{\text{core}} = 392$ nm. The sizes are represented by the number of particles in one nucleus.

We run the nuclei size detection methods on multiple samples which spread across the coexistence region. They are the results of $\phi_s = 0.240, 0.244, 0.249, 0.254, 0.260$ on 16th December 2019, and $\phi_s = 0.243, 0.248, 0.251, 0.257$ on 13th December 2019. Fig. 3.9 shows the size distributions of the detected nuclei using the Fourier transform method, as described in Sec. 3.3.2. It was observed that, for large sizes, *e.g.* size > 100 of $\phi_s = 0.260$, only one nucleus was found, represented as the data points in the bottom line of the figure. These were incomplete distribution information due to the limited sampled volumes, and were further discarded in the fitting procedures.

We then used classical nucleation theory (CNT) to fit the experimental nucleation size distributions, to estimate the nucleation barrier heights. The Gibbs free energy of a spherical nucleus of radius R has the following form:

$$(3.5) \quad \Delta G = \frac{4}{3}\pi R^3 \rho_s \Delta\mu + 4\pi R^2 \gamma,$$

where ρ_s is the number density of the bulk crystal, $\Delta\mu$ is the chemical potential difference between the crystal and the fluid, and γ is the fluid-crystal surface tension. The value of ρ_s is fixed as we only observed hexagonal structures (FCC and HCP) in the experiments, and both FCC and HCP

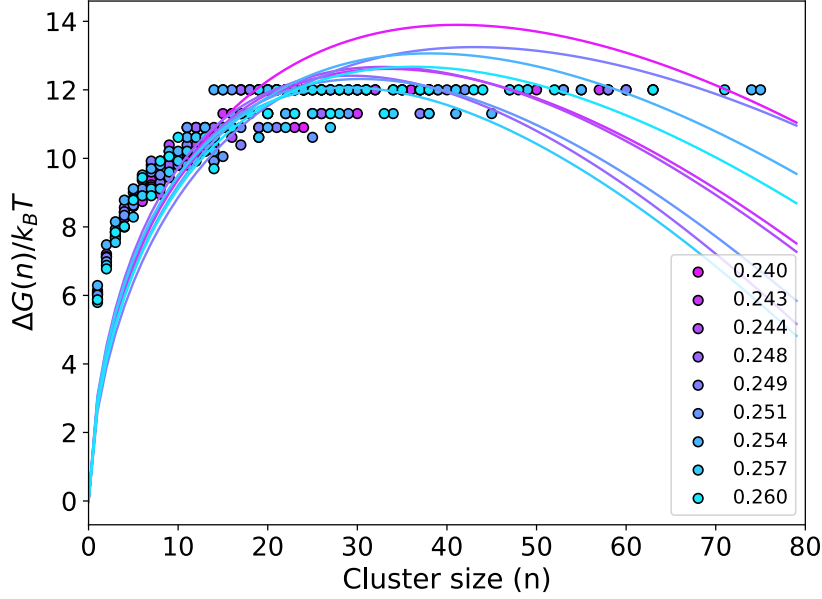


Figure 3.10: The nucleation barriers calculated from the size distribution in Fig. 3.9. The solid lines are barrier curves fitting to the CNT expression, with the colour the same as the corresponding data points.

have the same ρ_s value. The value of $\Delta\mu$ was taken from Auer *et al.* [17], with the approximation that the $\Delta\mu$ is nearly linearly dependent on $\phi - \phi_{\text{freezing}}$ reflected by the crystallinity [16, 120]. The variable γ was treated as a fitting parameter. As mentioned above, large nuclei that were only observed once were discarded. Our results for γ were around $0.5k_B T/\sigma^2$, consistent with other experimental and simulation studies of hard spheres which range between $0.11 - 0.751k_B T/\sigma^2$ [12, 64, 107, 125, 129, 166]. In particular, Palberg [217] fitted the data from Harland *et al.* [125], finding the value of $\gamma = 0.5k_B T/\sigma^2$, and the result from Heymann *et al.* [129] gave $\gamma = 0.54k_B T/\sigma^2$. Our fitted γ was in a good agreement with these experimental data, so we are confident about the accuracy of our methodology. The values of the nucleation barrier heights, encoded in the value of ΔG for the critical nucleus, were inferred from our fitting procedure, as listed in Table 3.2. It is worth mentioning that, the values of $\Delta\phi$ were calculated after all the prepared volume fractions had been scaled to hard sphere freezing volume fraction. *e.g.* a sample of $\phi_s = 0.249$ was scaled to $\phi = 0.494/0.240 * 0.251 = 0.517$.

$\Delta\phi_{\text{core}}$	0.001	0.006	0.009	0.016	0.019	0.023	0.030	0.036	0.041
$\beta\Delta G_{\text{critical}}$	13.9	12.6	12.7	12.4	13.2	12.3	13.1	12.1	12.7

Table 3.2: The nucleation barrier heights from the fitting curves of CNT form. $\Delta\phi$ means the distance from the freezing volume fraction after scaling.

A comparison is shown in Fig. 3.11. The weak dependence of the nucleation barrier height

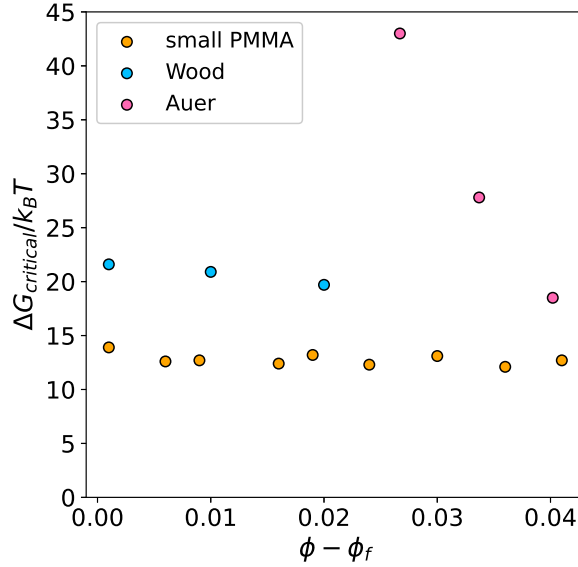


Figure 3.11: The comparison of our experimental critical nucleation free energy with those of Nicholas Wood [331], and Auer and Frenkel with similar parameters $\beta\epsilon = 20$, $\kappa = 5$ [14].

on the packing fraction is observed in both our results and those of my colleague, Nick Wood. In contrast the simulation data from Auer and Frenkel [14] exhibit strong dependence on $\Delta\phi$. Our results once again confirmed the discrepancy between the experimental observations and the simulation results. It is possible that advanced imaging techniques might lead to better agreement between the simulation and the experiment due to better identification of nuclei. However, simply adding more data obtained by the same confocal microscopy and imaging processing methods to the analysis is unlikely to resolve the discrepancy, as we achieved similar results even when the imaging volume has improved by two orders of magnitudes. We have therefore failed to explain it with the small PMMA particles of $\sigma_{core} = 392$ nm.

3.5 Intermediate PMMA particles in the mixture of cis-decalin and tetralin

Given the fact that the resolution of confocal microscopy (around 50 nm in (x, y) planes) limits the image quality for further imaging processing with such a small size ($\sigma < 400$ nm), along with the exhaustion of these particles, we considered taking another slightly larger size. Therefore, the intermediate PMMA particles with a diameter of 613 nm were used. Rather than the mixture of cis-decalin and CHB, we attempted the mixture of cis-decalin and tetralin, of which the mass fraction of two components can be carefully adjusted for a good refractive index matching. As discussed in Sec. 1.3.5, the refractive index and density match are unable to reach simultaneously in either mixture: refractive index matched cis-decalin and tetralin solvent leads to a final density of ~ 0.93 g/cm³ with a mass fraction of $m_{tetralin} : m_{decalin} = 46 : 54$ from He *et al.* [126], while the

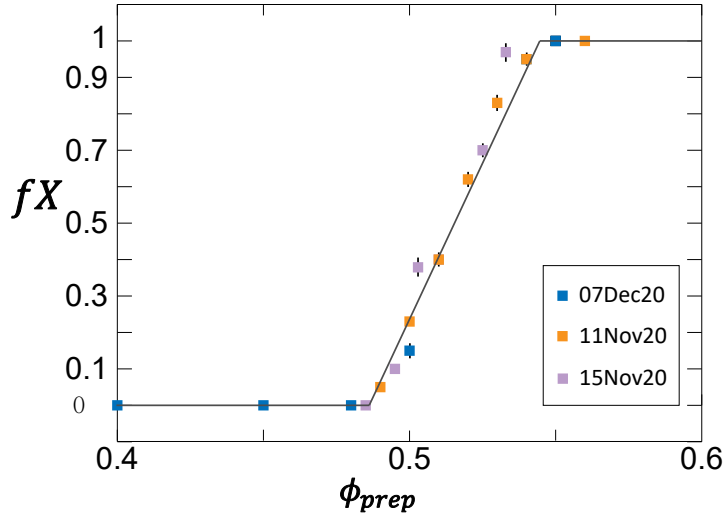


Figure 3.12: The crystallinities of PMMA of $\sigma_{\text{core}} = 613$ nm at different prepared volume fractions. Colours represent individual experimental runs with the preparation date.

density of PMMA is 1.196 [252]. For larger particles, *i.e.* $\sigma > 1 \mu\text{m}$ for tracking purposes, this density mismatch results in significant sedimentation which may influence the nucleation rates [155, 263]. On the contrary, a heavier component, CHB is selected to prepare well density matched solvent in accompany with cis-decalin, although this ignores the refractive index matching, and thus causes attenuation of intensities along z axis and degradation of PSF. Yet, in this case, the size of $\sigma = 613$ nm is rather small that a single particle sediments < 0.8 mm per 24 hours in the mixture of cis-decalin and tetralin, which is acceptable for investigating homogeneous nucleation rates.

Apart from better refractive index matching, tetralin has a much lower dielectric constant, $\epsilon = 2.77$ [4], which leads to an increased $\lambda_B \approx 22.7$ nm in the mixed solvent of cis-decalin and tetralin. We then suppose strong coupling between ions of opposite signs, and consequently weak dissociation of charged groups on colloid surfaces. With the rule of thumb $Z\lambda_B/\sigma = 6$ [258, 278], the intermediate PMMA particles gain a charge of ~ 100 . Although they are charged to some extent, the Yukawa contact potential decreases to around $5.2 k_B T$ with the Debye length of ≈ 45 nm. We therefore expect that the electrostatic interaction has much less effect on phase behaviour than the case of $\sigma = 392$ nm PMMA. Fig. 3.12 shows the crystallinity of these intermedia PMMA as a function of ϕ_{prep} . They exhibit a rather high level of hardness, with the phase transition located between $\phi_{\text{prep}} = 0.487 \sim 0.543$. It should be noted that the Yukawa parameters of this system are quite similar to those of Pusey and van Megen [241], who studied PHSA stabilised PMMA dispersed in cis-decalin and carbon disulphide with the total $\epsilon = 2.64$ and $\lambda_B \approx 22$ nm. Their model system mimicked the hard spheres by mapping an effective volume fraction. In fact, our particles are “harder” as freezing starts at $\phi_{\text{prep}} = 0.483$, which is equivalent to a $\phi_{\text{core}} \sim 0.46$ as discussed in Sec. 3.4.1, while they observed freezing occurred at $\phi_{\text{core}} = 0.407$.

Moreover, tetralin has a more stable ionic strength than CHB [88], providing a consistent size of the electrostatics, such as λ_B and κ , which facilitates the comparison with other model systems of cis-decalin and tetralin.

However, it is reported that tetralin may cause PMMA particles to swell and crack upon contact [88]. The fluorescent labelling process of these particles involved a swelling to allow free dye molecules to enter then be captured by particle shrinking through changing the solvent after the synthesis, which is different from the common procedure that the dyed monomers participate in the dispersion polymerisation process [37]. Unfortunately, the swelling induced by the tetralin released the dye molecules, and resulted in significant fading of the particles in our experiments. Although we attempted to reduce the dispersion time in the mixture by only remaining them for sample preparation and washing them as soon as the experiments ended, they became colourless to the eye and invisible by confocal microscope just after we explored the phase diagram.

3.6 Large PMMA — L-PMMA

As mentioned in Sec. 3.3.4, the resolution of the confocal microscope restricted the imaging quality of the small PMMA particles (average diameter 392 nm). This affected the nuclei identification even with careful adjustment of the relevant parameters. Furthermore, the freezing line quoted by prepared volume fraction ϕ_s^f in our system was not consistent, as shown in Fig. 3.8, which implied the unstable electrostatic properties of CHB. The electrostatics reflects the degree of “hardness” of the colloids in the case that its range is longer than that of pure steric repulsion. For example, we observed a freezing volume fraction ϕ_s^f at 0.24. If we assume the colloids start to freeze at an effective volume fraction $\phi_{\text{eff}}^f = 0.494$, the ratio of effective to steric diameter is the cube root that of volume, ≈ 1.27 , thus a thick electrical double layer around quarter the length of colloidal core radius is obtained. Simulation results [138] with similar Yukawa parameters $1/\kappa\sigma = 0.43, \beta\epsilon = 20$ show a calculated value of $\phi_{\text{core}}^f \approx 0.44$, almost 80% more than ours. In fact, it is debatable that the particles affected by such long-range and strong interactions can still be considered as “hard”. Therefore, we decided to use another larger PMMA particles, L-PMMA, as detailed in Sec. 2.2.

3.6.1 Phase diagram of L-PMMA

Fig. 3.13 shows the experimental crystallinities of samples with their prepared volume fractions. Three individual experimental runs were performed to examine the consistency of the electrostatics in our system. It was observed that they exhibited a very similar phase coexistence region, from a freezing volume fraction $\phi_{\text{prep}}^f = 0.320$ to a melting volume fraction $\phi_{\text{prep}}^m = 0.352$, over our experimental timescales.

Similarly, we examined the difference between the prepared and core volume fraction derived from the PHSA coating. Although Bryant *et al.* [42] only studied the colloids in the diameter

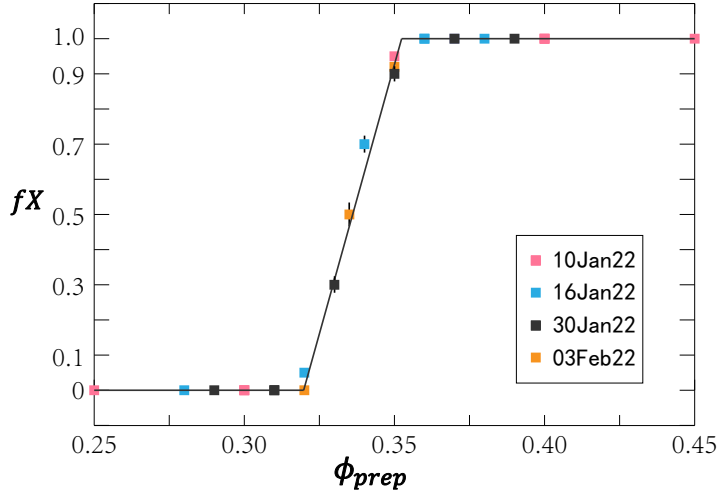


Figure 3.13: The phase diagram of L-PMMA particles at $\sigma_{\text{core}} = 1800$ nm. Colours represents separate experimental runs, labelled by the preparation date.

range 50 - 800 nm, the values of ϵ and n in the expression $u_{\text{steric}}(r) = \epsilon(\sigma_h/r)^n$ (See Sec. 1.3.3) showed a nearly linear dependence on the core diameter. Therefore, we approximated these values for L-PMMA as $\epsilon \approx 6000$ and $n \approx 1500$, leading to a steric layer of 11 nm where the centrifugal force we used was almost equal to steric repulsive force. In this case, for a given prepared volume fraction equivalent to the steric volume fraction ϕ_s , we actually obtained a sample at $\phi_{\text{core}} = 0.964\phi_s$.

In order to estimate the electrostatic properties, we used two methods which returned different Debye screening lengths $1/\kappa$. The first was to map the ϕ_s^f to hard sphere freezing line $\phi = 0.494$, which resulted in a ratio of the effective to the core radius equal to 1.16, indicating the Debye screening length $1/\kappa = 144$ nm. This is around 1.5 times longer than that in an oversaturated TBAB solution (≈ 260 nm) [175, 257]. Although this value is reasonable considering the influence from various ionic strength of CHB of different batches, and is substantially less than the radius of L-PMMA particles, it is not trivial and likely to induce a noticeable degree of softness to the particles. Continuing with the Bjerrum length $\lambda_B \approx 10$ nm and the rule of thumb $Z\lambda_B/\sigma \approx 6$, as discussed in Sec. 3.4.1, we obtain a contact potential Yukawa $\beta\epsilon_Y$ of around $38.6 k_B T$. Computer simulations of similar parameters ($\beta\epsilon_Y = 39$) [138] predicted that such a high contact potential results in a triple point when $1/\kappa\sigma \gtrsim 0.2$. In other words, two phase coexistence regions generate, namely, the fluid-BCC and BCC-FCC, as the range of the interactions and the softness are strong enough to cause the preference for forming a BCC structure than an FCC structure at lower core volume fractions. It should be noted that we did not observe any BCC crystal in confocal images.

As an alternative, we took advantage of the simulations presenting the phase diagram in the form of core volume fraction. As discussed in Sec. 3.4.3, the volume fraction in phase diagrams was actually closer to the ϕ_s , since the centrifugal force overcame the Yukawa contact force,

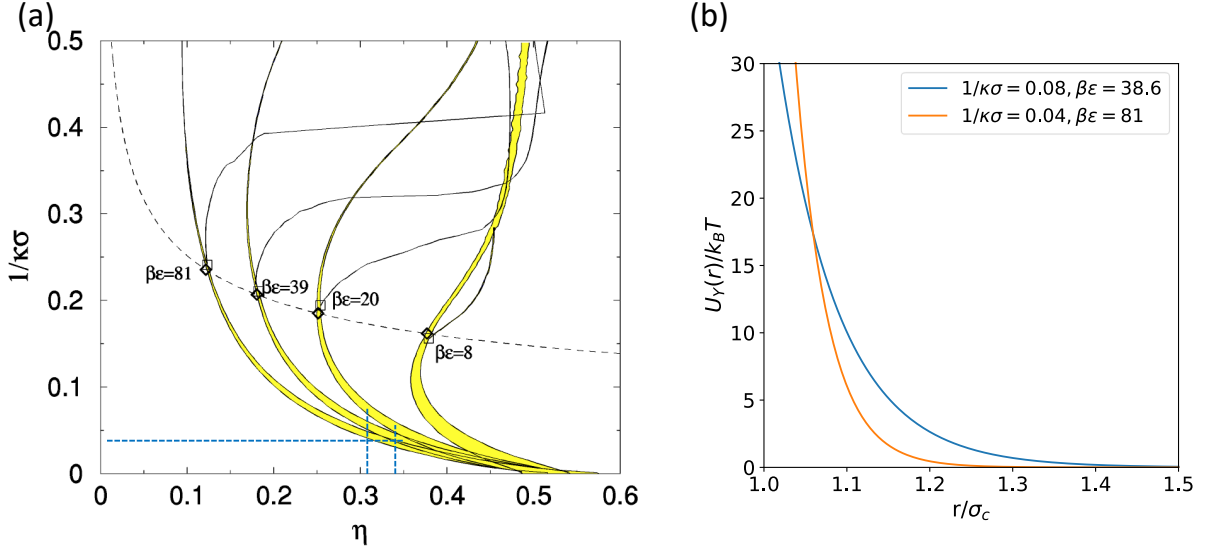


Figure 3.14: (a) Simulation phase diagram of hard-core Yukawa particles at different $\beta\epsilon_Y$. The blue dashes indicate our mapping based on the experimental coexistence region, and the corresponding value of $1/\kappa\sigma$. Reprinted from Hynninen and Dijkstra [138]. (b) The estimation of electrostatic interaction of L-PMMA. Blue line: Yukawa parameters are calculated based on $Z\lambda_B/\sigma = 6$. Orange line: κ and $\beta\epsilon_Y$ are obtained by mapping our ϕ_{core} of freezing and melting on (a).

and was likely to compress the particles to the steric length scale. Based on the experimental result that our phase transition located from $\phi_s = 0.320$ to 0.352 , we first switched the ϕ_s to ϕ_{core} by the relationship $\phi_{\text{core}} = 0.964\phi_s$. then mapped the experimental ϕ_{core} to Hynninen and Dijkstra's work [138]. As shown by the blue dashed lines in Fig. 3.14(a), with a given $1/\kappa\sigma$, the phase coexistence for different $\beta\epsilon$ is also fixed. We thus mapped our experimental freezing and melting ϕ_{core} onto coexistence regions (yellow areas) by shifting the $1/\kappa\sigma$ line up and down to find the proximate $\beta\epsilon$. We observed that our case was in a better agreement with the data at Yukawa contact value $\beta\epsilon_Y = 81$, corresponds to a Debye length $1/\kappa \approx 72$ nm. This was possible to be obtained as we dissolved the TBAB in a 40°C warm water bath, in which the supersaturation might occur. In this case the phase diagram also predicts a single phase coexistence region of fluid and FCC, consistent with our experimental observation. Given these comparisons, we expected the Yukawa parameters of the L-PMMA as listed in Table 3.3, and the effective diameter σ_{eff} equal to 1944 nm. The electrostatic interactions of these two methods are plotted in Fig. 3.14(b). It is clear that the particles with mapped Yukawa parameters are harder than these with calculated Yukawa parameters.

ϵ_r	λ_B	$1/\kappa$	Z	$\beta\epsilon_Y$
5.6	1.0×10^{-8}	7.2×10^{-8}	281	81

Table 3.3: The Yukawa parameters for the L-PMMA particles based on mapping in Fig. 3.14(a).

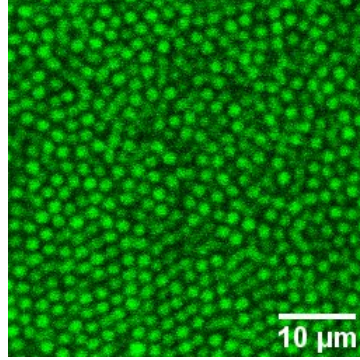


Figure 3.15: A typical (x, y) plane confocal image of L-PMMA for particle tracking methods. The bottom left region is further characterised as crystal by topological cluster classification, which will be detailed in Sec. 3.6.4.

3.6.2 Tracking quality

With good particle tracking results, we can use algorithms like the bond order parameters (BOO) [171] to classify particles into different structures, such as FCC, HCP or fluid. In this work we used the Topological Cluster Classification (TCC) algorithm [190] to identifying the structures with the tracked coordinates. A detailed description of the detection is given in Sec. 2.6.2. Briefly, the algorithm performs a modified Voronoi method to identify the neighbours of each particle, then searches the network formed by the particles and their neighbouring connections for the shortest path rings of 3, 4 and 5 members. From these rings the “basic clusters” are distinguished for further identification of larger clusters. Therefore, we can make a very crude estimation of the effect of the particle loss: if 5% particles which belong to separate shortest path rings of 5, respectively, are not tracked during tracking step, the left ones might fail to be recognised as a new ring with one less member. That is to say, up to 20% of found particles might be labelled as no connections with their neighbours, and substantial potential clusters are missed in this process. Therefore, we attempt to achieve a good particle tracking quality, *i.e.* $\geq 98\%$ particles are detected by the algorithm.

A visual picture of the tracking result is given in Fig. 3.7(c). In order to quantify this efficiency, we calculated the total volume fraction of the particles, by multiplying the tracked number N and the core volume of a single particle $V_{\text{L-PMMA}}$. The confocal stacks capture the images of a finite volume in a much larger container, so it is more than likely that the boundary cuts some particles across the stack edges. These incomplete spherical shapes cannot be tracked by the algorithm, leading to an underestimation of the efficiency. Therefore, we remove an

outer layer of a thickness equal to L-PMMA core diameter from all six faces of the cuboid (image stack), and count only the number of the particles, N_{edge} , whose centre are within the L-PMMA core radius of the new boundary. These particles only contribute half of the $V_{\text{L-PMMA}}$ in average due to the symmetry in a density matching background: the possibilities of a centre in or outside the stack in any directions are the same. While the rest of the particles are completely in the updated smaller cuboid. Accordingly, the total volume fraction of the particles can be calculated as $V_p = N_{\text{edge}} V_{\text{L-PMMA}}/2 + (N - N_{\text{edge}}) V_{\text{L-PMMA}}$, and the consequently tracking quality $\eta_{\text{track}} = V_p/V_{\text{track}}$.

We preformed the tracking process by the combination of Trackpy and nplocate (See Sec. 3.3.4) on both original and deconvolved stacks. Unfortunately, the values of η_{track} were significantly varied, from 85.5% to 99.2%, even in very close stacks, *e.g.* two image stacks of the same sample, taken successively with 3 seconds time difference and 0.5 mm movement in (x, y) plane. There are three possible reasons for this, on the premise that the conditions are very similar. Firstly, we used the “line average” function to obtain the average intensities of multiple scans of the same scanning line. Although we ensured that the Brownian time is much longer than the imaging time, the Brownian motion may still cause an imperfect spherical intensity distribution, and the consequently wrong identification. Secondly, we used a voxel size around 4 times in (x, y) and 1.2 times in z of the maximum sampling density (See Nyquist rate in Sec. 2.5.1.1), which indicates a degree of undersampling. When this happens, the original signal cannot be uniquely recovered from the sampled signal, as well as increasing aliasing artefacts. These all affect the tracking algorithm. However, we were unlikely to modify the voxel size, as the maximum image pixel size that the confocal microscope supports is 1024×1024 . If we followed the proper sampling density, say $49 \times 49 \times 146$ nm in our system, each (x, y) image would shrink to $\approx 50 \times 50 \mu\text{m}$, which meant imaging less than 800 particles, significantly decreasing the sample volume, and increasing the possibility of cutting large nuclei around the edges. Finally, even if we used the proper sampling density, in such a higher density with the electric double layer $1/\kappa \approx 68$ nm (discussed in Sec. 3.6.1), the particles were close to each other, as the double layer is only around 1/12 of the L-PMMA core radius. The particle edges could still be distorted.

To sum up, the operational parameters for the confocal imaging and the image processing for a good tracking quality were either unchangeable or difficult to optimise due to the experiment requirements. We thus only retained the stacks with $\eta_{\text{track}} > 98\%$ for further analysis. This operation, however, filtered out about 3/4 - 5/6 the stacks for different volume fractions, and significantly reduced the available imaging volume. For the good tracking results where more than 98% particles are located, we examined the structure of the system via the radial distribution function, $g(r)$, and the topological cluster classification.

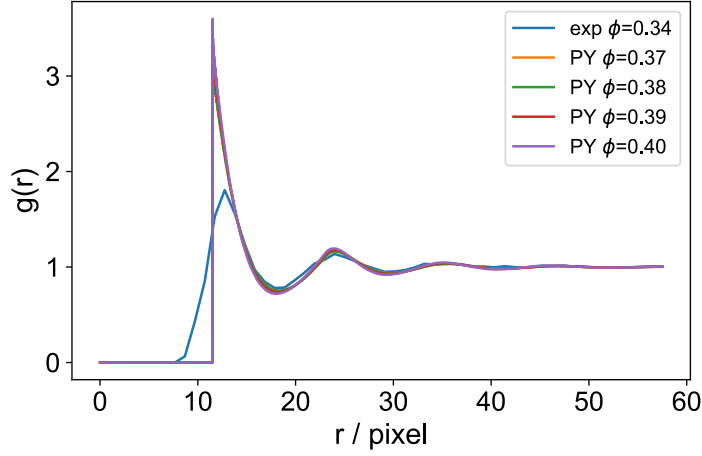


Figure 3.16: The radial distribution function of tracked particles, and Percus–Yevick approximation at different volume fractions with the same size (in pixel) as L-PMMA.

3.6.3 Radial distribution function

The radial distribution function, $g(r)$, indicates the probability of a particle occurring at a given distance, r , from a given reference particle located at the centre. In particular, the Percus-Yevick (PY) approximation of hard sphere conditions can generate hard sphere $g(r)$ curves of different volume fractions [226, 322]. In our experiments, we could determine the prepared and the core volume fraction. However, the effective volume fraction remained unknown. We lacked the direct measurements, and only estimated the electric double layer through mapping our transition region onto simulations of hard-core repulsive Yukawa particles. In order to gain a better knowledge of the effective diameter of the L-PMMA particles, we attempted to compare our experimental $g(r)$ with PY hard sphere results. We plot the $g(r)$ of a sample of $\phi_s = 0.34$, which corresponds to $\phi = 0.525$ in the hard sphere case. However, the $g(r)$ curve computed by PY hard sphere conditions exhibits the best fitting of $\phi = 0.4$. There are three possible reasons for this. The primary one is, our particles are weakly charged colloids, which fit well to the simulation data of a Yukawa contact potential $\beta\epsilon = 81$ and an average surface charge $Z = 281$, as discussed in Sec. 3.6.1. Accordingly, it might show better agreement if we simulate the $g(r)$ of charged particles of similar electrostatic properties instead of the hard spheres. Second, we observe that the computed Percus-Yevick curves are insensitive to a small change of volume fraction, *i.e.* $\Delta\phi < 0.03$. Fig. 3.16 plots several curves, among which few differences can be distinguished by eyes. Finally, the second and third peak sometimes can not simultaneously get a good fitting, which actually provides a small adjustable range of ϕ . Therefore, we expect an error of ≈ 0.05 in ϕ when we compare the experimental $g(r)$ with Percus-Yevick results.

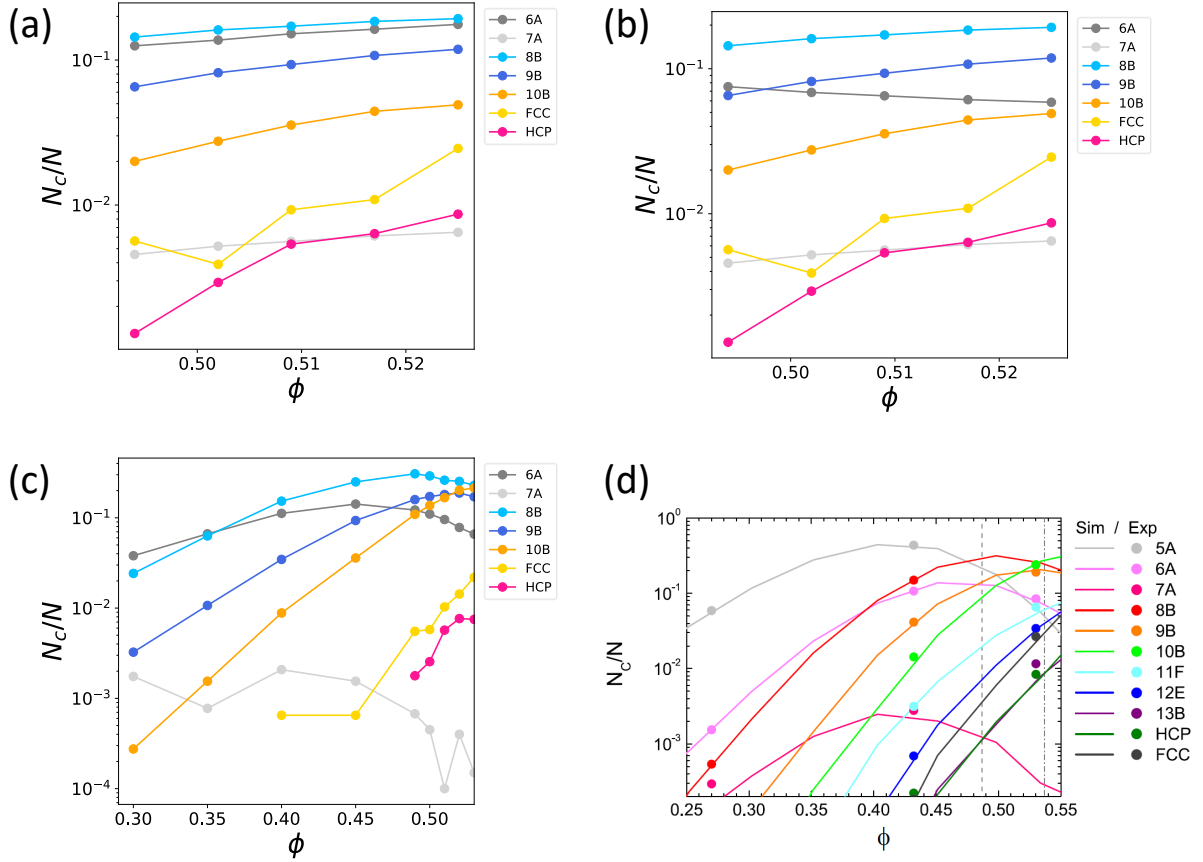


Figure 3.17: The comparison of TCC analysis. (a) TCC results of our experimental data. (b) Net TCC results of the data same as (a). The volume fractions in (a) and (b) are mapped onto the effective hard sphere volume fractions. (c) Net TCC results of Monte Carlo simulation data, with private discussion and permission from Yushi Yang. (d) TCC results of experiments (2 μm PMMA in cis-decalin and cyclohexyl bromide) and simulations (Brownian dynamics), reprinted from Taffs *et al.* [297]. Two vertical dashed lines represent their freezing and melting volume fractions of simulations.

3.6.4 Topological cluster classification

To analyse the structure of the experimental system, we constructed the bond network through a modified Voronoi method with a maximum bond length of 1.4σ [326], and then performed topological cluster classification (TCC) to find the clusters in a topological energy minima [78], which were previously studied in the hard sphere systems [297]. Before running the TCC, we mapped the volume fraction ϕ_{prep} onto the effective volume fraction, by $\phi_{\text{eff}} = 0.494/0.320 \times \phi_{\text{prep}}$, where 0.320 is the freezing ϕ_{prep} of L-PMMA. The experimental populations are shown in two ways. Fig. 3.17(a) shows the direct identification, in which repeated counting² is retained. As

²For example, if a 6A cluster is in an FCC crystal, the particles in the 6A cluster will be labelled as 6A and FCC simultaneously. In other words, one particle can be counted into multiple kinds of clusters. As a result, the sum of the possibilities, for a particle belonging to different clusters, can be larger than 1.

expected, the TCC analysis exhibits a clear tendency for the cluster population to increase with a growing volume fraction. To better compare with the literatures, we consider the “net population” of different clusters, where particles are labelled as the largest cluster they belong to³. As a result, the net population for 6A cluster decreases, since a 6A cluster is often the component of an FCC or HCP cluster, as shown in Fig. 3.17(b). For other small clusters based on icosahedral packing, *i.e.* 7A, 8B, 9B, 10B, their net populations remain the same (see Fig. 2.9 for an illustration of basic TCC clusters). My colleague, Yushi Yang, developed an algorithm using hard particle Monte Carlo simulations to generate the trajectories of $N = 40000$ particles. He shared his code with me, then I performed net TCC on different volume fractions. The results are shown in Fig. 3.17(c). Furthermore, Taffs investigated a PMMA dispersed system with a similar colloidal diameter of $\sigma = 2 \mu\text{m}$ and Debye screening length $1/\kappa = 67 \text{ nm}$, but lower Yukawa contact potential $\beta\epsilon = 1.0 \pm 0.25$. They found that 10B is the dominant cluster in the fluid for $\phi \gtrsim 0.54$, indicating that at the bulk level, crystallisation can be interpreted as the conversion of 10B into FCC environments [297]. The rise of 10B clusters in our results is consistent with both simulations of Fig. 3.17(c) and (d). Additionally, the distribution of most types of clusters is also of the same order of magnitude, for instance, 10^{-2} in ours and $\sim 0.85 \times 10^{-2}$ in experiments of Taffs *et al.* for 10B at $\phi = 0.502$. We also observed the low amount of 7A clusters. However, simulations of Taffs *et al.* reveal a slight decrease in 7A and 8B as a function of volume fraction. The decrease of 8B is supported by the results of Monte Carlo simulations, while 7A shows a downward trend but not monotonic. We consider two possible reasons that give rise to this inverse dependence. Firstly, there is a large difference in the Yukawa contact potential, from $\beta\epsilon = 81$ in our case, to $\beta\epsilon = 1.0 \pm 0.25$ in theirs, which may change the structural configurations. Secondly, they only plotted the simulation 7A and 8B distribution without showing their experimental data, for which a discrepancy may exist. In general, our results are in a good agreement with the work on weakly charged colloids. Since our experimental samples are all recorded at the same time point (3 hours after preparation) in a nonequilibrium state, further research can be carried out on the cluster population analysis of the crystallisation process.

3.6.5 Nucleation barriers of L-PMMA

Since the tracking quality filter removed some of the image stacks, not all the volume fractions have a reasonable total imaging volume to perform the nuclei distribution and consequent nucleation barrier analysis. We present the results in Fig. 3.18 of $\phi_{\text{core}} = 0.33, 0.34$ which are the only two volume fractions that still have the order of 10^5 particles after filtering. Interestingly, the samples at $\phi_{\text{core}} = 0.33$ contain more smaller nuclei of a size $n = 8 - 30$, but fewer larger nuclei. Furthermore, the nuclei with a size of $n > 40$ are only found once, which fails to indicate the true

³For example, if a 6A cluster is in an FCC crystal, the particles in the 6A cluster will be labelled as FCC only, and they *will not* be labelled as 6A, because FCC is a larger cluster ($N=13$) compared to the 6A cluster. In other words, one particle can only be counted once in the largest cluster it occurs in. As a result, the sum of the possibilities, for a particle belonging to different clusters, will be ≤ 1 (There may be some particles not belonging to any clusters).

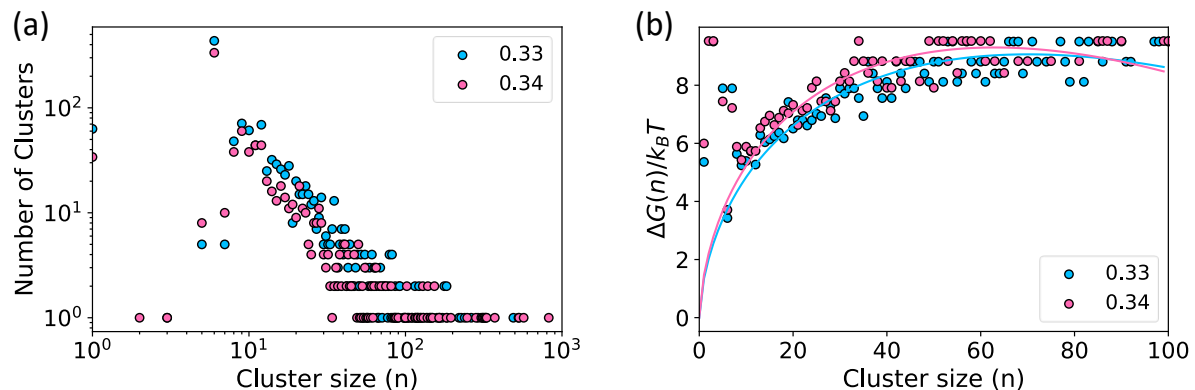


Figure 3.18: The analysis of L-PMMA particles. (a) The size distributions of the captured nuclei of $\phi_{\text{core}} = 0.33, 0.34$. (b) The measured nucleation barriers for these two volume fractions, and the corresponding CNT form fit.

distribution due to the limited imaging volume. Hence we discard these data when calculating the nucleation barriers. We also remove the nuclei of $n < 7$ as such small clusters can not be regarded as a crystal structure. The fitting method, in a CNT form, is the same as that done on small PMMA particles in Sec. 3.4.4. Figure 3.18(b) shows the measured nucleation barriers and the corresponding fitted lines. We obtain the value of γ in a range of $0.35 - 0.39 k_B T / \sigma^2$, which is slightly lower than that for small PMMA particles ($0.5 k_B T / \sigma^2$), but still lies in the range of that from literature results for hard spheres (See Sec. 3.4.4 for references).

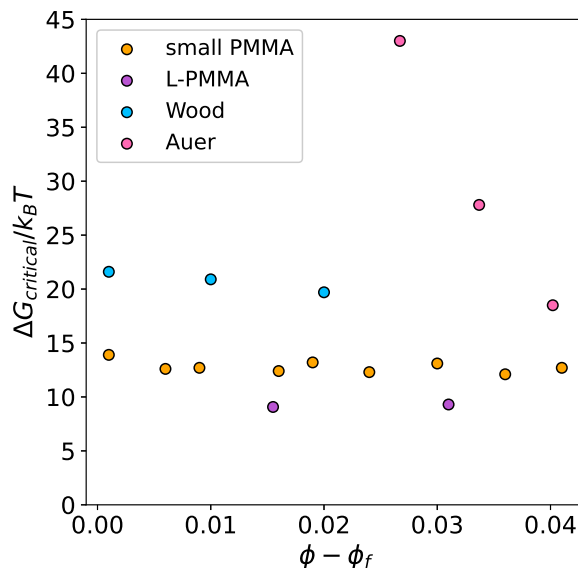


Figure 3.19: The barrier heights of experiments and simulation. Auer and Frenkel's data are extracted from [14].

To better compare the experimental results with other work, we scale the steric volume

fraction to the hard sphere case, and plot the critical nucleation barriers as a function of the distance from the freezing volume fraction, as what we previously did in Fig. 3.11. However, the result of L-PMMA is very similar to that of small PMMA, where the nucleation barrier heights are unlikely to depend on the particle packing fractions. Ketzetzi *et al.* also found the same result that there is no clear dependence of the nucleation barrier on the local volume fraction [155], which can further extend to the global volume fraction. In these experiments of both small and big PMMA particles, we have not been able to reproduce the simulation nucleation rates.

3.7 Conclusion

In this chapter, an advanced real space technique for imaging and analysing confocal results of nucleation is investigated. This method enables the image processing and analysis of smaller colloids than the typical size scale required for particle-resolved imaging, as well as much larger imaging volume [107, 155], and hence allows much rarer events during crystallisation to be observed, giving a more comprehensive knowledge of homogeneous nucleation. In addition, this method provides a more accurate measurement of the final crystallinity than previous work [218, 237], with an error down to around 0.15%.

Unfortunately, we only observed similar results to previous scattering experimental studies, with a weak dependence of the nucleation barrier height on the volume fraction. This is contradictory to simulation results of pure hard sphere systems. A possible explanation is, the particles in our system are not hard spheres. They bring noticeable charge and polydispersity, which alter both the phase behaviour and the crystal nucleation rate. By comparison to simulations, we found our particles fit better to weakly charged colloids instead of hard spheres. To test this conclusion, further work should be designed to repeat this work with less polydispersed and more weakly charged particles which are closer to the hard spheres of the simulations, through the same processing algorithm and analysis.

BINARY PROTEIN GELATION VIA DEPLETION INTERACTION

Author Contributions: Part of this chapter is based on a published work: Rui Cheng, Jingwen Li, Ioatzin Ríos de Anda, Thomas W. C. Taylor, Malcolm A. Faers, J. L. Ross Anderson, Annela M. Seddon, C. Patrick Royall, “Protein–polymer mixtures in the colloid limit: Aggregation, sedimentation, and crystallization.” *The Journal of Chemical Physics*. 155.11 (2021): 114901. Rui Cheng performed the experimental data and analysis, and drafted the manuscript. Jingwen Li developed the experimental system, carried out some data for phase diagram and assisted in the analysis. Ioatzin Ríos de Anda provided great help with biochemistry knowledge, including protein expression and characterisation, and engaged in the discussion and draft. Thomas W. C. Taylor did some data. All other authors supervised the work and participated in manuscript writing.

Proteins offer unprecedented opportunities to create new materials due to their various inherent properties. In this chapter, we present a new method of developing a protein binary gel through depletion interactions, where the initial characteristics of the proteins are preserved, and the domains of each component are distinguishable. Based on the literature and characterisation of our experimental systems, we treated our model proteins as spherical (mCherry and bovine serum albumin, BSA) and non-spherical (enhanced green fluorescent protein, eGFP) colloidal particles. We first determined the individual protein-protein interactions in the presence of the non-absorbing polymer, polyethylene glycol (PEG), then compared the theoretical and simulation predictions [174] for colloid-polymer systems with our experimental results, and found the phase behaviour of proteins were in good agreement with that of hard-sphere (mCherry and BSA) or hard-spherocylinder (eGFP) and ideal polymers. We continued with the attempt to obtain binary gels through either two-step (add another species after the gel structure of one component has formed) or simultaneous mixing strategy. The mixture of eGFP

and mCherry only formed well mixed structures, while bi-continuous gel networks with distinct domains of each component were successfully obtained by eGFP and BSA. To our knowledge, this type of binary protein gel obtained via depletion interactions has not been reported before. Although further investigations of the type and strength of the interactions between protein are needed, our research shows a promising methodology to construct functional biomaterials using functional proteins as building blocks.

4.1 Introduction

4.1.1 Binary gel networks

Colloidal gels are complex states consisting of two or more phases, typically composed of an elastic disordered arrested network dispersed in a liquid medium, where the gel components are connected with each other through physical attractions or chemical bonds [72, 276, 314]. The density of the gel is similar to that of the liquid, yet it presents solid properties, such as non-zero yield stress, which can be attributed to the formation of percolating networks and the interactions between this structure. Generally there are two routes to colloidal gelation: the non-equilibrium route involves an effective quench into the spinodal curve (the dynamical arrest occurs after crossing spinodal lines) and the spontaneous demixing into two long-lived metastable states with distinct dynamical properties and colloidal concentrations (colloid-poor and colloid-rich regions), namely, “arrested spinodal decomposition”. Whilst the equilibrium route requires the formation of gels through a continuous series of equilibrium phases which usually means a much longer waiting time than the bond life time for the structure to re-assemble, and thus may be inaccessible in experimental conditions [40, 260, 341]. In this work we only studied the non-equilibrium gelation via the depletion interaction where the attraction was induced by the addition of non-absorbing polymers, and the range of the interaction was determined by the polymer-protein size ratio $q = 2R_g/D$, where R_g is the polymer radius of gyration and D is the protein diameter.

Gel networks are of academic interest and have commercial potential due to their unique structures represented as percolated networks or space spannings [174, 281, 315]. Gel structures may be constructed by more than one species of particles and through different types of intermolecular interactions, such as depletion attractions, covalent bonds or cross-linkers. In particular, binary gels have been widely studied in various areas, such as biological, pharmaceutical and food industry [180, 271, 279, 291, 335]. Several approaches have been used to prepare binary gel structures, usually require two steps: the separated gels of each constituent particle are prepared, then mixed to obtain the binary network, sometimes with stress or heating [187, 205, 216]. For example, my colleague, Dr. Beatriz Iozzin Ríos de Anda, built bicontinuous gel networks by two fluorescent proteins, enhanced green fluorescent protein (eGFP) and mCherry, through the sequential addition of specific salts and proteins plus surface modification techniques

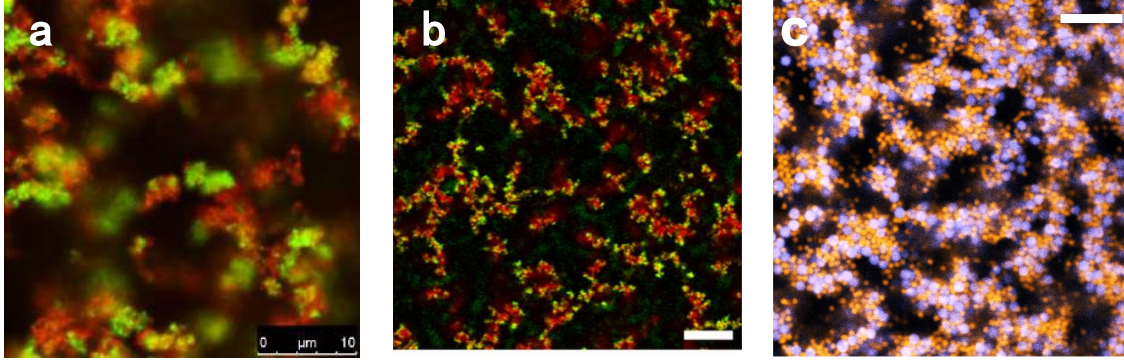


Figure 4.1: Various binary gel systems with increasing size of constituent particles. (a) Confocal microscope image of a binary gel formed via a two-step addition procedure of enhanced green fluorescent protein and cationised mCherry in the presence of salts [248]. Both protein species have the diameter of around 4 nm. (b) Confocal microscope image of a bi-continuous gel produced via instantaneous heating (which is equivalent to the fastest quench possible in rheology) of pNIPAm ($\sigma_H = 620$ nm at 20°C) and pNIPMAm polymers ($\sigma_H = 573$ nm at 20°C) [141]. (c) Confocal microscope image of a binary gel formed through depletion interaction of PMMA particles in two sizes, 1.04 and 1.84 μm , respectively [346]. All scale bars denote 10 μm .

(cationisation of mCherry), as shown in Fig. 4.1(a) [248].

Recently, a new method has been developed, where all the components are added into the medium at the same time. In this case, the bi-network with distinct domains of each component is generated when the interactions between the same particles are much stronger than that between the different ones, allowing individually undisturbed gel formation, or one species is able to firstly form a backbone to promote further association. For example, Immink *et al.* [141] investigated the reversible binary gel structures formed by the cross-linked microgel particles, poly-N-isopropylacrylamide (pNIPAm) and poly-N-isopropylmethacrylamide (pNIPMAm), of which the diameters have different sensitivities to the temperature, and thus the pair interactions are tuned by heating or cooling, as shown in Fig. 4.1(b). Zhang *et al.* [346] studied the phase behaviour induced by depletion interaction of a simple mixture of two sizes of PMMA particles plus polystyrene, in which the effective depletion attraction is determined by the polymer-particle size ratio q at a given polymer concentration. They found that the criticality and phase separation is dominated by the larger colloids, though the criticality is a joint phenomenon of the bi-system. With the known sizes of PMMA particles, they successfully obtained binary gels for the deepest quench they tested, as exemplified in Fig. 4.1(c).

Inspired by these results that proteins may serve as building blocks of gels, and the depletion interactions can be well controlled by the size ratio, we will explore the conditions to yield protein binary gels in which the domains of either protein are distinguishable to present their native properties. A brief interpretation of the desired structure is illustrated as in Fig. 4.2(b). Since the binary network possesses the biological, physical and chemical characteristics of each component,

it is promising to produce multi- or hierarchical microstructures with a higher complexity than single-component.

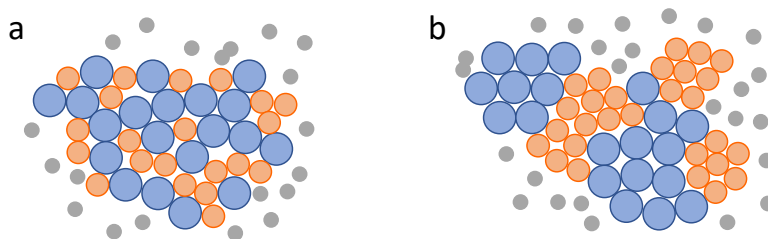


Figure 4.2: The different mixing states of binary gels through depletion interaction. Proteins with different sizes are represented as blue and orange spheres, while polymers are grey spheres. (a) Proteins are well mixed in gel networks, where interactions between different species dominate the gelation. Inherent properties of the particles may not present in the macroscopic scale due to the too small domains. (b) Proteins assemble into gels with distinct domains of each component. The latter is the structure we expect.

4.1.2 Treating proteins as colloids

As discussed in Sec. 1.4, globular proteins exhibit a metastable liquid-liquid phase separation (LLPS) with sufficiently short-ranged attractions. This phenomenon, with respect to crystallisation [99] and dynamically arrested phases within the spinodal lines [49] such as gels or glasses, is analogous to the gas-liquid coexistence of colloids, and thus can be described by treating globular proteins as spherical colloids with isotropic attractions [5]. Furthermore, colloids of anisotropy shapes, *i.e.* spherocylinder, are well-known to undergo different liquid crystalline phases as a function of the concentration. Actually, experimental works were started on biological rod-like particles (tobacco mosaic virus [56]) to explore these liquid crystals. Given the analogy between the proteins and the colloids of the same shape, we treated protein molecules as colloidal particles in our work, as well as comparing with both biochemistry and colloidal results.

The control of protein phase behaviour around this metastable LLPS is thus crucial to investigate protein crystallisation, or kinetically trapped (gel or glass) states [106, 231, 233, 330]. Different phase states can be obtained by tuning the attractions, such as depletion interactions through the addition of non-adsorbing polymers. Especially, we consider the gelation more akin to typical colloid-polymer mixture in which the protein radius is larger than polymer radius of gyration R_g , rather than common “protein limit” with a reverse size ratio ($R_g/R_{\text{protein}} \gg 1$) [35].

In our case, if we carefully select the protein species as well as preparing solutions at specific conditions, for example, an adequate electric double layer arising from proper salt concentration to render the van der Waals attraction negligible, we can minimise the contribution from some of the interactions mentioned above, then evaluate the total potential in the form of centre-to-centre

distance r :

$$(4.1) \quad U(r) = U_{HS}(r) + U_E(r) + U_{AO}(r),$$

where $U_{HS}(r)$ is the hard sphere potential, $U_E(r)$ is the electrostatic potential, and $U_{AO}(r)$ is the depletion interaction induced by the addition of non-absorbing polymers. The electrostatic repulsion can be manipulated by the addition of salt, which will be discussed in the further results section. Thus we finally model proteins to hard colloids in spite of their complex shape, surface conditions and functional groups, to further compare with typical isotropic colloid-polymer systems.

4.2 Experimental System

4.2.1 Characteristics of proteins

Two natural fluorescent proteins, enhanced green fluorescent protein (eGFP) and mCherry, were selected as the components in our model systems at the beginning, as their fluorescence can be used as an indicative of the preservation of their native structures. The green fluorescent protein (GFP) was first extracted from the jellyfish *Aequorea victoria* in the 1960s [283]. It exhibits bright green fluorescence when excited by blue to ultraviolet light [238]. Nowadays, the protein has been enhanced (enhanced green fluorescent protein, eGFP) to give stronger fluorescence. It has excitation and emission wavelengths at 488 nm and 511 nm, respectively [8]. eGFP is known to homo-dimerise with a binding affinity of 100 μ M, implying that dimers may be more favoured in the solution [202]. In order to examine this, the shape and size of the batches of eGFP used in our work were characterised by small-angle X-ray scattering (SAXS) by my colleague, Dr. Beatriz Iozzin Ríos de Anda [65]. The results revealed that two eGFP molecules form a stable head-to-head dimer in solution, with a final diameter of 4.0 ± 0.02 nm and length of 8.2 ± 0.08 nm. The illustration of the eGFP dimer is shown in Fig. 4.3(a). This measurement is consistent with previous work that eGFP forms a dimer structure. On the other hand, although the size, length, diameter, shape and molecular weight of mCherrys are similar to monomeric eGFPs, as also measured by Ríos [65], they exist as monomers after purification, and thus serve as building blocks half the size of eGFP dimers in the system. Moreover, mCherry processes the excitation and emission wavelengths at 587 nm and 610 nm, respectively, ideally to distinguish these two fluorescent proteins under the confocal microscope.

In the process of experiments, we found that eGFP and mCherry only formed well mixed domains, as shown in Fig. 4.2(a). Thus, we took another protein, bovine serum albumin (BSA), as we attempted another type of proteins with a more distinguishable shape, either a much larger/smaller size or a different shape, or both, to better manipulate the polymer-protein interactions which are essential for the distinct regions of each component. However, turning for a good size ratio ignores the intrinsic fluorescent property. In other words, BSA proteins

are not naturally fluorescent. We dyed BSA with the process explained later in Sec. 4.2.3 for observations of confocal microscopy. As a well-studied protein, BSA has an approximate shape of an elongated ellipsoid of dimensions $4.5 \times 3.2 \times 2.7$ nm in aqueous solution at pH 7.0 [228]. It remains as monomers unless they are under certain conditions, such as an acidic environment (pH < 4) [39], or when receiving an energy transfer [176]. In our experimental conditions, BSA was all treated as monomers.

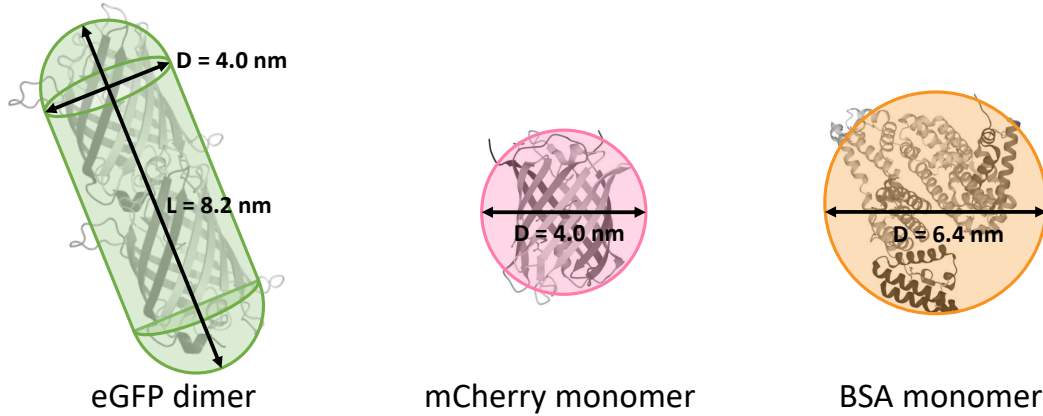


Figure 4.3: Illustration of the equivalent structures of proteins used in this chapter (not to scale). From left to right: the spherocylinder shape of eGFP dimers, the sphere shapes of mCherry and BSA, where L means the length, and D means the diameter. The 3D schematic representations (spiral strips and lines), known as Ribbon representations, of eGFP, mCherry and BSA molecules are all from protein data bank [29].

4.2.2 Protein Expression and Purification

The expression, purification and concentration of eGFP and mCherry are detailed in Sec. 2.4. Briefly, *Escherichia coli* cells transformed with the respective protein DNA plasmid were left in a nutrient solution until they cultured to a desired concentration, then activated to express proteins. A following centrifugation and lysis then extracted proteins from broken cells. Further purification was done by the affinity chromatography. Finally, the purified eGFP and mCherry were dialysed and concentrated to 1-2 mL as the stock solutions in a 25 mM HEPES buffer solution at pH = 7.0. The concentrations were 62.5 mg/mL for eGFP and 11.7 mg/mL for mCherry. The transparent green and purple colours of the protein stock solutions indicate the preservation of natural properties of eGFP and mCherry, respectively [248].

Originally, we stored the proteins in deionised water, whose pH was further found to be unstable, which might lead to aggregation. Thus, we used buffer solutions. A zwitterionic sulfonic acid, HEPES (4-(2-hydroxyethyl)-1-piperazineethanesulfonic acid), was selected to be the buffer solution, as it has a natural pH in the range of 6.8-8.2, suitable for our expected experimental conditions, and it will not attend or disturb any protein structures or phase behaviour.

BSA proteins in this work were brought from Sigma-Aldrich (lyophilised powder, essentially globulin free, low endotoxin, $\geq 98\%$). Natural BSA is non-fluorescent. Thus, in order for us to be able to characterise its behaviour and draw a phase diagram after polymer addition and its structures under the confocal microscope, we were required to label it with a fluorescent dye. The fluorescent labelling process will be explained in the next section 4.2.3. Fluorescently modified BSA was also dialysed to the 25 mM HEPES buffer at pH = 7.0 after labelling.

Finally, the different protein stock solutions were filtered by 0.22 μm syringe filters and kept at 4°C in the fridge to avoid the growth of any bacteria.

4.2.3 Cationisation and anionisation of Proteins

The detailed mechanisms for ionisation process are explained in Sec. 2.4.5. All of them require specific conditions. In our experiments, the cationisation and anionisation were performed in 0.1 M phosphate buffer at pH = 6.0 and 0.1 M Na_2CO_3 buffer solution at pH = 8.0, respectively. The phosphate buffer was prepared by dissolving sodium phosphate dibasic heptahydrate ($\text{Na}_2\text{HPO}_4 \cdot 7\text{H}_2\text{O}$) and sodium phosphate monobasic monohydrate ($\text{NaH}_2\text{PO}_4 \cdot \text{H}_2\text{O}$), then carefully adjusting to desired pH. In order to cationise natural eGFP, hexamethylenediamine ($\text{H}_2\text{N}(\text{CH}_2)_6\text{NH}_2$) was added in excess to ensure that all carboxylic acids on the surfaces reacted. 50 mg EDC was added at the beginning and again after 4 hours to improve the efficiency of the reaction. The solution was put on a tube roller with a speed 10 rpm for a total time of 8 hours. Finally, the cationised eGFPs were dialysed to 25 mM HEPES buffer at pH = 7.0, and concentrated. We did not run any tests to quantify the amount of proteins retaining the native conformation. Instead, considering the chromophore is in the centre of protein molecules, we assumed that any changes in the conformation might lead to the chromophore being exposed to the solvent and thus losing its fluorescence. Therefore, we identified the preservation of original structures by comparing the colour of cationised eGFP solution with that of natural eGFP solutions by eye at the same concentration.

On the other hand, natural BSA is non-fluorescent. In order to allow the characterisation of its phase diagram and structures formed, we added the dye, Texas Red cadaverine with an absorption and emission wavelength of 596 and 615 nm, respectively [304]. The emission wavelength enables the observation of binary structures without any overlap between two fluorescent signals from eGFP and Texas Red. This dye contains the functional group cadaverine ($\text{H}_2\text{N}(\text{CH}_2)_5\text{NH}_2$), which reacts with the carboxylic groups on the surface of BSA. For a better fluorescent labelling, BSA was first anionised. This guarantees the availability of said carboxylic groups on its surface, which can then be bonded to the dye.

10 mg of BSA were dissolved into 0.1 M Na_2CO_3 buffer solution at pH = 8.0, and put on a tube roller for 1 hour. Then 10 times the amount of succinic anhydride in molar quantity was added to the solution. The mixture was left on the roller for 2 hours. After anionisation, the crosslinking of the modified BSA and the dye followed the same rules as the cationisation. For

fluorescent labelling, Texas red cadaverine had been previously dispersed in dimethyl sulfoxide (DMSO) to obtain a stock solution at a concentration of 2 mg/mL. The modified BSA was firstly dialysed to 0.1 M phosphate buffer at pH = 6.0, then mixed with the dye stock solution at a volume ratio $V_{\text{dye}}/V_{\text{BSA}} = 0.8$. The next steps of EDC addition were followed as described above. After dialysis which removed excess dye molecules, the final purple colour indicated effective fluorescent labelling. All the protein batches subjected to ion modification were characterised by zeta potential measurements, to obtain the surface charge values, which will be detailed in the next section.

4.2.4 Protein-Protein Interactions

Polymers were employed as the depleting agents while proteins were treated as colloids with homogeneous surface charge distribution for further analysis and comparison of phase behaviour. In this case, we expect depletion interactions to be dominant. However, protein particles always carry a net charge when away from their isoelectric point (pI). Charges are needed to remain stable dispersions as proteins may form aggregates without repulsion, as well as rendering short-ranged attractions, such as van der Waals and other hydrophobic/hydrophylic interactions by a longer-range electric double layer, though screening the charges to a proper degree (usually to the scale of depletion interactions) is desirable since it simplifies the system. Furthermore, in our binary solution, different proteins have different pIs, which means the net charge of all the protein species cannot be eliminated simultaneously by adjusting pH. Therefore, we tuned the protein particles to have the charge with the same sign, rather than the similar magnitude, as opposite charges would cause them to stick to each other. In deionised water, the lack of free ions and the relatively strong charge on the proteins leads to an unscreened, long-range electrostatic repulsion, which prevents the aggregation of molecules. Salts are generally used to manipulate the ionic strength, though the concentration of salts needs to be carefully controlled: the charged regions on the surfaces of proteins are neutralised by opposite ions at low salt concentration, while the protein surfaces can become more charged with higher salt concentration, leading to a loss of neutrality and then sedimentation [81]. The classification of the ions used to stabilise or precipitate proteins is ranked by what is known as the Hofmeister Series [133], which was first proposed by Franz Hofmeister in 1888. From the up-to-date version of the Hofmeister Series, sodium chloride (NaCl) was chosen as the salt used in our experimental systems, as the corresponding dissociated ions Na^+ and Cl^- not only have a weak effect on proteins, but also maintain the initial pH.

Previous work by Dr. Beatriz Iozzin Ríos de Anda in our group shows that a concentration of 500 mM NaCl will lead to irregular, small aggregates of both eGFP and mCherry [248]. Thus, we chose the NaCl concentration to be 100 mM. As calculated by Equ. 1.11, even the Debye length can be down to a few nanometres with a mild salt concentration (The Debye length of different experimental systems will be given in the results section), that is still comparable to the size

of protein molecules. As the depletion attraction is also on this length scale, the electrostatic interaction needs to be measured to check its effect on phase behaviour. We calculated the surface charge of the proteins through the size of protein molecules and several measurable values, including the electrophoretic mobility μ_e and the zeta potential ζ , as detailed in Sec. 2.4.4.

4.2.5 Sample Preparation

Protein stock solutions were in a 25mM HEPES buffer at pH = 7.0. Two more buffer solutions at the same condition with 0 or 1.0 M NaCl were also prepared to adjust both the salt and protein concentrations of the samples. Polyethylene glycol (PEG, Polymer Laboratories) was chosen as the depletant polymer for two main advantages: firstly, the repeat unit (ethylene glycol) is small, and a wide range of molecular weights from 200 are available, which satisfies the demand of colloid limit. Secondly, it is neutral and does not change the pH of the suspension, to which the proteins are sensitive, nor will it cause protein denaturation. The R_g of PEG is calculated from an empirical expression $R_g = 0.0215M_w^{0.583}$ [111]. PEG in different sizes was used in this work to obtain the proper size ratio q . The corresponding q values are given in the following sections.

For each example, different volumes of protein stock solution were diluted with deionised water, or HEPES solution with and without salt to attain the desired protein and NaCl concentration at a fixed volume of 20 μ L. Then PEG was added by weight. All the samples were mixed for 5 s on a vortex stirrer (IKA, German) at 3,000 rpm, then immediately filled into $50 \times 1.00 \times 0.100$ mm rectangular capillaries (VitroCom Inc., 5010-050). The capillaries were glued to a glass slide by optical adhesive (Norland Optical 81) with the horizontal longest axis. The phase states were characterised by a confocal laser scanning microscope (Leica DCIM 8000) within 5 minutes.

4.3 Results

In this chapter, we investigated the phase behaviour of eGFP, mCherry and BSA plus PEG in different sizes. The results and discussions are presented following the sequence in Table 4.1. The work started from phase diagrams of individual protein species, and extended to binary mixtures to explore the potential for the formation of binary gels with expected structures, as shown in Fig. 4.2(b).

It is worth noting that, we only studied and presented samples with the protein concentration *less than 10 mg/mL* for several reasons. Firstly, biochemistry experiments have proved that the optimal protein concentration for crystallisation typically lies in the range between 8-20 mg/mL, while larger ones (kDa > 50) tend to require lower concentration [196]. Although crystallisation usually involves additional conditions, including pH, temperature and precipitating agents such as salts and polymers, we stuck at testing low concentrations to avoid unexpected aggregation analogous to possible crystallites with the known kDa of the proteins used in our work (eGFP 26.9, mCherry 28, and BSA 66.5). Secondly, Dr. Beatriz Iozzin Ríos de Anda in our group has

Protein species	Polymer species	Solution	Size ratio
eGFP	PEG620	deionised water	$q_G = 0.59^1$
eGFP	PEG620	25 mM HEPES	$q_G = 0.59$
eGFP	PEG620	25 mM HEPES + 100 mM NaCl	$q_G = 0.59$
cationised eGFP	PEG620	25 mM HEPES + 100 mM NaCl	$q_G = 0.59$
mCherry	PEG620	25 mM HEPES + 100 mM NaCl	$q_C = 0.59$
eGFP + mCherry	PEG620	25 mM HEPES + 100 mM NaCl	$q_G = q_C = 0.59$
BSA	PEG620	25 mM HEPES + 100 mM NaCl	$q_G = 0.59$
eGFP + BSA	PEG620	25 mM HEPES + 100 mM NaCl	$q_G = 0.59, q_B = 0.44$
eGFP	PEG2000	25 mM HEPES + 100 mM NaCl	$q_G = 0.82$
eGFP + BSA	PEG2000	25 mM HEPES + 100 mM NaCl	$q_G = 0.82, q_B = 0.61$

Table 4.1: The protein-polymer systems we studied in this chapter. All the solutions were at pH = 7.0. q_G , q_C and q_B mean the size ratio of polymer to eGFP, mCherry and BSA, respectively. See the footnote for the polymer radius of gyration.

successfully yielded binary gels of eGFP and cationised mCherry with a total concentration of 8 mg/mL, as shown in Fig. 4.1(a). Therefore, we believed that similar gel structures might still be accessible at $\phi_{\text{protein}} < 10$ mg/mL through depletion interactions. However, these concentrations lead to rather low protein volume fractions, *e.g.* an eGFP concentration of 10 mg/mL is equivalent to an eGFP volume fraction of ~ 0.0075 . When comparing with colloidal systems, such volume fractions are out of the range of the critical region, and thus critical fluctuations are negligible here. For example, in a depletion system consisting of hard spheres plus polymers with a size ratio of $q = 0.4$, the critical point is predicted to be at $\phi_{\text{colloid}} \sim 0.25$ [174].

4.3.1 Phase diagram of eGFP plus PEG620 in deionised water

The work began with the phase behaviour of each species of proteins plus polymers. The phase diagram of eGFP and PEG620 in deionised water at pH = 7.0 is shown in Fig. 4.4, in the plane of PEG reservoir volume fraction ϕ_P^R (for conversion from experimental to reservoir volume fractions, see Sec. 1.3.4.3 for spheres and Sec. 5.2.3 for spherocylinders) and protein volume fraction ϕ_{eGFP} .

¹For such small PEGs with the molecular weight $M_w = 620$, there are uncertainties in determining the radius of gyration, arising from the inaccuracy of the prefactor and the index in the empirical equation $R_g = 0.0215M_w^{0.583}$ [111], and a few assumptions including rigidity and ideality of polymers. Therefore, a degree of adjustment is acceptable. The mentioned equation gives $R_g = 0.80$ nm ($q = 0.40$), whereas the fitting [55], which will be discussed in the result section 4.3.2, leads to $R_g = 1.18$ nm and the consequent size ratio $q = 0.59$. In this table we take the latter throughout, consistent with the published work related to the experiments in this chapter, while the results are presented with using $q = 0.40$ at the beginning, then switching to $q = 0.59$ when further discussing the difference of theoretical and experimental phase separation.

The PEG molecular weight leads to a size ratio $q \approx 0.4$. There are only two phases appearing throughout all the explored volume fractions: a fluid phase and aggregates in coexistence with a fluid phase. The phase boundary is drawn in the middle of the fluid and aggregation state points. Although the coexistence is non-equilibrium state, it is still informative to compare them with the equilibrium phase diagram, as the aggregation and gelation are characterised with the liquid-liquid phase separation in depletion systems [184, 256]. For low ϕ_{eGFP} we did not prepare samples in the left region of phase diagram, the boundary (denoted by dashes) was plotted based on the predictions from the literature studying phase diagrams of colloid-polymer mixtures with similar size ratio [174, 234].

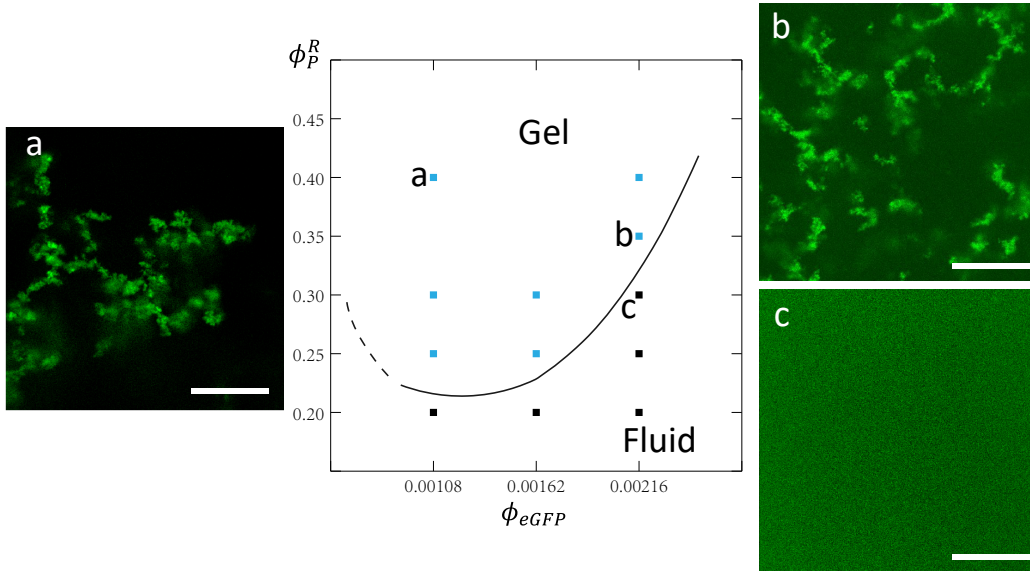


Figure 4.4: Experimental phase diagram of eGFP + PEG620 with $q = 0.40$ in deionised water. Scale bars denote $20 \mu\text{m}$. For lower ϕ_{eGFP} which we did not prepare, dashed phase boundary line was plotted based on the intuition from the literature [174].

As a function of polymer reservoir volume fraction ϕ_P^R , eGFP presents a homogeneous intensity without any observable microstructure [Fig. 4.4(c)] in the fluid phase, since the resolution of the confocal microscope (pixel size $90 \times 90 \text{ nm}$) is much larger than a single eGFP molecule. Aggregation is observed upon the increase of ϕ_P^R , in which the phase separation first occurs at $\phi_P^R = 0.22$. As shown in Fig. 4.4(b), a dim (compared with the intensity of the fluid state) but not fully black background indicates coexistence of free eGFP dimers. With more PEG, the size of aggregation extends, until all the dimers are arrested into clusters [Fig. 4.4(a)]. The aggregation in this state is found to precipitate to the bottom of the container in an accessible experimental timescale, usually 3-5 days, which reminds us of the aggregation and sedimentation phenomenon in other colloidal systems [232]. At a relative high protein concentration, the ϕ_P^R required for aggregation increases, which follows the free volume theory predictions for spherical colloids with a size ratio $q = 0.40$ [174]. The experimental phase boundary we obtained is around 0.22,

while it is theoretically predicted to occur at ϕ_P^R higher than $\gtrsim 0.4$ [174]. Therefore, to resolve this difference, we need to consider other interactions that may be present. It is worth to note that further identification of the gel network is made on (x, y) planes only, as the minimum pixel size along the z direction is 180 nm under the experimental conditions (see Sec. 2.5.1 for proper voxel size) which results in a significant loss of structural information.

4.3.2 Investigating phase behaviour in different conditions

It was observed that the pH of the deionised water without buffer or added salt is extremely unstable. This may come from incomplete purification or bacterial growth. Considering that the pH changes the net charge of proteins, we therefore transfer the solution from deionised water to 25 mM HEPES buffer solution to maintain the $pH = 7.0$. To quantify the strength of electrostatic interaction as described in Sec. 1.3.2, we first calculated the corresponding parameters with or without salt (NaCl) as listed in Table. 4.2. Here, the ions in the solvent consist of the weakly dissociated HEPES ($pK_a = 7.66$), and the completely dissociated NaCl (if added). The Debye screening length decreases significantly from 963 nm (H_2O) to 124 nm (25 mM HEPES without NaCl), and continues diminishing to the protein size scale, 0.961 nm, with the addition of NaCl (100 mM), as well as reducing the contact potential $\epsilon_Y/k_B T$ by about one fourth. Further increase of the NaCl concentration, from 100 mM to 500 mM, only leads to a small drop in Debye screening length when compared with the change of 2 orders of magnitude before. However, $\epsilon_Y/k_B T$ rises again, which is consisting with the prediction of previous work that protein surfaces gain stronger electrostatic interactions with higher salt concentration, leading to uncontrollable sedimentation [81]. Therefore, we fixed the NaCl concentration at $c_{NaCl} = 100$ mM.

NaCl concentration (mM)	$\kappa^{-1}(\text{nm})$	Z	$\epsilon_Y/k_B T$
0 (in deionised water)	963	0.42	0.0415
0 (in 25 mM HEPES)	124	0.42	0.0403
100 (in 25 mM HEPES)	0.961	1.5	0.0304
500 (in 25 mM HEPES)	0.0431	3.07	0.0351

Table 4.2: Calculations of Yukawa potential for eGFP at different ionic strength, where Z is the protein net charge, and $\epsilon_Y/k_B T$ is the scaled contact potential.

The phase diagram of eGFP plus PEG620 in 25mM HEPES, $pH = 7.0$ is shown in Fig. 4.5(a). The polymer reservoir volume fraction needed for phase separation decreased a little to around 0.2, but is almost indistinguishable from the system in deionised water at the same pH. Further addition of NaCl, though, results in a lower polymer reservoir volume fraction required for phase separation, as shown in Fig. 4.5(b). We can calculate the AO potential $\epsilon_{AO}/k_B T$ following the Equ. 1.22, where the well depth is proportional to polymer concentration. We therefore choose

$\phi_P^R = 0.25$, a volume fraction that is a little bit higher than the phase boundary ϕ_P^R observed in each system, giving the value $u(AO)/k_B T = -2.84$. Meanwhile, as listed in Table. 4.2, the electrostatic contact potential $\epsilon_Y/k_B T$ is around 0.04. Hence we conclude that the electrostatic interaction is effectively screened and can be neglected in the solutions with 100 mM NaCl, and our system can be regarded as a simple depletion system composed of colloids plus non-adsorbing polymers, where the only additional complexity is an approximate estimation of the shape anisotropy of the eGFP dimers.

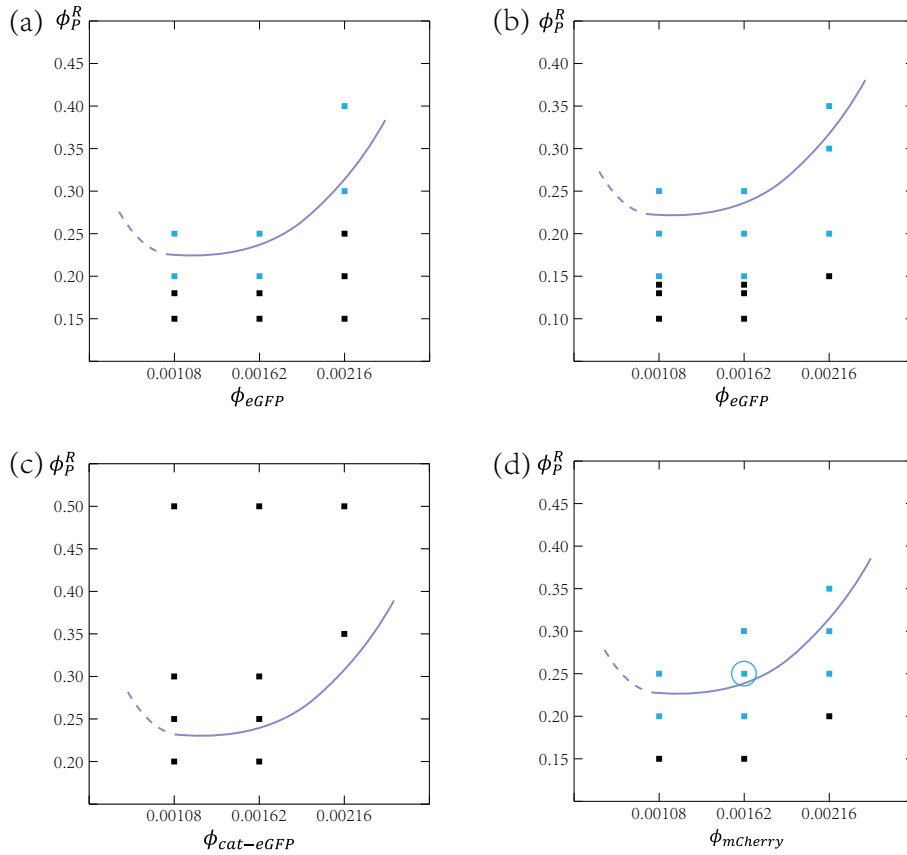


Figure 4.5: Experimental phase diagrams of fluorescent proteins (updated $q = 0.59$) dispersed in 25 mM HEPES at pH = 7.0 under various conditions. (a) Natural eGFP + PEG620 without salt. (b) Natural eGFP + PEG620 with 100 mM NaCl. (c) Cationised eGFP + PEG620 with 100 mM NaCl. (d) Natural mCherry + PEG620 with 100 mM NaCl. Blue points indicate that the corresponding sample forms aggregates, while black points indicate fluids. The purple lines in each figure (dashed and solid) are the phase boundary of eGFP + PEG620 in deionised water, the same as that in Fig. 4.4, as a comparison. The total volume fraction used for eGFP-mCherry binary gel is equal to that of the point circled by the blue line in (d).

We thus assumed that the difference between theoretical and experimental phase separation

boundary, may come from the inaccuracy of determining the polymer radius of gyration, R_g , which sequentially affects the size ratio q , since the calculation of R_g from the empirical expression $R_g = 0.0215M_w^{0.583}$ may not be accurate for such small PEGs. In the published work collaborating with Rui Cheng in our group investigating eGFP phase behaviour in the same buffer solution but a lower salt concentration ($c_{\text{NaCl}} = 10$ mM), a power law $Z_{\text{pol}} = a - b\phi_{\text{eGFP}}^c$ at low protein volume fractions $\phi_{\text{eGFP}} \approx 10^{-2}$ in terms of q was used, where Z_{pol} is equal to the polymer number density ρ_p^{res} in a reservoir in thermodynamic equilibrium with the system, a , b and c are constants, to fit the theoretical and simulation predictions for spheres [316] and spherocylinders [266] of a larger aspect ratio than eGFP dimers here ($L/D = 6$). An adjustment of R_g of PEG620 was made after fitting, increasing the value from 0.80 nm to 1.18 nm as well as the size ratio from 0.40 to 0.59 [55]. Further discussion on the comparison between experimental results and theoretical colloid-polymer mixture phase diagrams will be detailed in the following section, when BSA-polymer phase behaviour is also discussed.

Unmodified eGFP has an isoelectric point of 5.58 [109], which means it has a negative net charge at pH 7.0. Fig. 4.5(c) shows another attempt to eliminate the effect of charge. We tried to achieve neutral eGFP dimers at pH 7.0, by cationising eGFP by hexamethyldiamine as mentioned in Sec. 4.2.3, and then checking with the zeta potential measurements. It is expected that through cationisation, extra positive charged groups are linked to the surface, enabling the protein molecules to neutralise more OH^- with increasing pH. Unfortunately, this failed due to the complex distribution of the carboxylic groups on the protein surface, and the randomness in which hexamethyldiamine can react with any carboxylic group. A charge reversion to +1.9 of cationised eGFP was obtained in comparison with their native negative charge of -0.66 (both in 25 mM HEPES with 100 mM NaCl). Actually, the charge value of +1.9 was the lowest net charge we obtained among all the cationised batches at pH 7.0. Furthermore, the zeta potential measurements detected a mixture of different charged particles rather than a uniform charge distribution observed with unmodified eGFP dimers. The phase behaviour of the cationised batch with the lowest net charge was determined as plotted in Fig. 4.5(c). No aggregation appeared at any experimentally tested ϕ_p^R . We infer that the main reason for this is the cationised molecules, hexamethyldiamine, have long carbon chains, which may be regarded as polymer chains to produce steric stabilisation and thus increase the steric repulsion (see Sec. 1.3.3). The effect from electrostatic interactions, although increases with the absolute net charge value from -0.66 to +1.9, is still negligible, as can be deduced from Table. 4.2. Since the aim of neutralising eGFP dimers at pH 7.0 could not be achieved, the unmodified dimers were used in further experiments.

When investigating the phase behaviour, we found that PEG is labelled as a ligand to eGFP in the Protein Data Bank website. Previous work reveals that for the formation of a covalent bond between eGFP and PEG, the hydroxyl groups of the polymer need to be activated first, to link to an appropriate surface group which can be replaced by the epsilon-amino terminal of nucleophilic groups (for example, lysine residues) through nucleophilic attack on protein

surfaces [71]. In most cases, one eGFP molecule can be linked with several PEG molecules, and the activating chemicals (agent) are bonds between proteins and PEG [197]. Other eGFP-PEG coupling approaches include coating on nanoparticles (PEGylated NPs) to optimise its binding properties [215], or using derivatives of PEG [6]. To our knowledge, no literature has reported the experimental observation of a direct covalent bond between eGFP and PEG without activating methods. We were unable to detect the formation of this type of covalent bond, neither. Therefore, we are confident that PEG performs the same way as non-absorbing polymers in a typical depletion system. A further investigation was carried out on mCherry, a protein which has a very similar size, shape and surface charge to a eGFP monomer, but does not take PEG as ligands. The phase diagram of mCherry plus PEG620 in 25 mM HEPES with 100 mM NaCl at pH 7.0 is shown in Fig. 4.5(d). Unlike eGFP, mCherry remains in its monomer state in solution, whereas the systems of eGFP dimers or mCherry monomer possess the same size ratio, $q \approx 0.4$, as the calculations both use the diameter of the spherocylinders or the spheres. It is less informative to contrast the phase behaviour of distinct particle shape, even with the same q , though the results of mCherry are comparable to those of spheres from literatures. It is worth noticing that, at $q = 0.4$, both a critical point (CP) and a triple point (TP) are theoretically predicted to appear in the phase diagram (polymer reservoir concentration versus particle concentration) of hard spheres [108]. Between the CP and TP, a concentrated fluid (“colloidal liquid”) coexists with a dilute fluid (“colloidal gas”). However, this phase state was not observed in our mCherry-PEG mixture. A possible explanation is, as mentioned before, the confocal resolution (pixel size 90×90 nm) is much larger than a single protein molecule (diameter ≈ 4 nm), thus the details of the microstructures will be lost during imaging.

4.3.3 Binary Gel of eGFP and mCherry

After we had characterised the phase behaviour of two individual proteins, eGFP and mCherry, we attempted to construct binary gel networks. The start point was chosen to be the point when both proteins form aggregates, as indicated by the blue circle in Fig. 4.5(d). This gives the corresponding total protein volume fraction, $\phi_{\text{protein}} = \phi_{\text{eGFP}} + \phi_{\text{mCherry}} = 0.00162$. Each protein species contributes half of the total volume fraction. The first sample was prepared by adding eGFP and mCherry at the same time. The ideal binary structure as illustrated in Fig. 4.2(b) did not form however; the two proteins were well mixed, with no clear separate large domains of either of them. The networks almost fully overlapped. This may be due to the high similarity between eGFP and mCherry molecules that leads to a non-specific interaction. In other words, PEG treats them as similar colloids, even if eGFPs have formed dimers so that they have a non-spherical shape, and are twice the size of mCherry monomers.

In particular, only small aggregates of individual mCherry were observed, as circled by the white line in Fig. 4.6(c), which indicates a potential process that mCherry may first form a “backbone structure”, that allows eGFP to further precipitate on top of it when more polymers are

added. This sequential formation is similar to the results of Ioatzin Ríos de Anda's, who developed a two-step procedure producing binary gels through first assemble eGFP network by the addition of YCl_3 , and then bond cationised mCherry by the addition of $(\text{NH}_4)_2\text{SO}_4$ [65]. We therefore tried to add the mCherry and eGFP sequentially, to hopefully achieve a more distinguishable mCherry bone network before mixing with eGFP. However, the results are very similar. We concluded that, the mixing step — 3000 rpm on a vortex for 1 minute — fully breaks the aggregation, and the network re-construction process is the same as the case when two proteins are added simultaneously, even if there may be a coexistence of a mCherry backbone and eGFP fluids in the intermediate step.

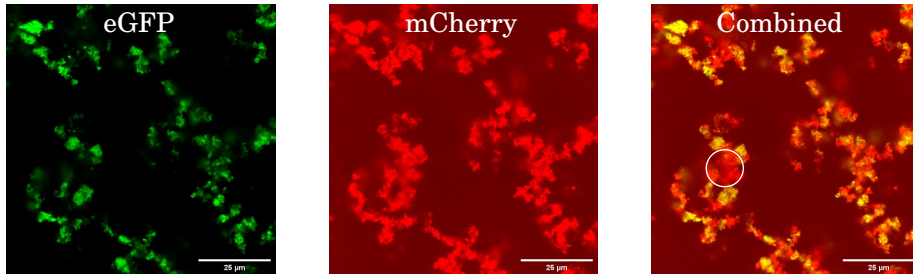


Figure 4.6: Confocal images of the binary structure of eGFP and mCherry in separate and combined channels. This state point is circled in Fig. 4.5(d), with the protein volume fraction $\phi_{\text{eGFP}} = \phi_{\text{mCherry}} = 0.00081$ and $\phi_p^R = 0.25$. The white circle in (c) shows an individual mCherry domain. Scale bars denote $25 \mu\text{m}$.

4.3.4 Phase Behaviour of BSA in the presence of non-adsorbing PEG

As mentioned above, eGFP and mCherry could not be distinguished by the polymer to form the desired gel networks. Thus, we considered optimising the system to generate distinct interactions between the two types of proteins by choosing a protein with a different size and shape to eGFP. The depletion interaction, as introduced in Sec. 1.3.4.3, is determined by the total overlap volume of the depletion layers, which is regulated by the size and shape of the colloids at a given concentration of polymers. Based on both Zhang's work that the different characteristics and responses of two colloidal particles are determined by their large difference in size plus non-absorbing polymers [346], and the observation that eGFPs behave like spherocylinders in our systems, a well-studied protein, BSA, with a higher size and shape difference to eGFP, was chosen to be the second component along with eGFP. The BSA has an oblate shape with ellipsoid radii of $4.0 \times 3.2 \times 2.7 \text{ nm}$ at pH 7.0 [333]. This is larger than eGFP dimers by volume, also leads to a polymer-protein size ratio $q \approx 0.44$ (calculated with the updated $R_g = 1.2 \text{ nm}$ in Sec. 4.3.2).

Zhang *et al.* studied the effect of ionic strengths (I) on natural BSA through light scattering techniques. They demonstrated that, at a low ionic strength, $I < 0.3 \text{ M}$, the total interaction is dominated by electrostatic repulsion, which is less than that in salt-free solution, since the

surface charge is screened. In this case the data fits well to a screened Coulomb potential model. Yet, upon the increase of salt (0.3 - 0.5 M), the surface charges become fully screened, leading to a hard sphere-like model. Finally, when $I > 1.0$ M, the total interaction exhibits an additional attraction, and can be described as a square-well potential model [344]. We were especially interested in the intermediate ionic strength environment of 0.3 - 0.5M, at which point natural BSA behaves like hard spheres. In our experiments, we first anionised BSA to achieve better fluorescent labelling, as detailed in Sec. 4.2.3. However, they were extremely unstable when mixed with succinic anhydride, even with slight mixing (10 rpm on the tube roller). The aggregates were inferred by the observation of a turbid solution from a transparent state. Thus, we directly linked the dye to natural BSA molecules. From here on, “BSA” refers to fluorescently labelled BSA with Texas Red cadaverine. Through zeta potential measurements, we found that the average amount of elementary charge Z associated with BSA exhibited a negligible change during dye labelling process, from 0.73 (natural) to 0.68 (dyed), which is quite similar to $Z_{\text{eGFP}} = 0.66$ (See Table. 4.2). We therefore assumed that, firstly, dyed BSA has a very similar shape and net charge to natural BSA, and can be modelled as hard spheres at moderate salt concentrations. Moreover, the conditions we used in our experiments (25 mM HEPES plus 100 mM NaCl at pH 7.0) effectively screen the surface charge of both protein species due to the similar Z values, and our binary protein mixture can be simplified to a binary system, in which the asymmetry uniquely arises from the size, and protein attractions depend only on the polymer volume fraction.

The phase diagram of BSA in 25 mM HEPES with 100 mM NaCl at pH 7.0 is plotted in Fig. 4.7. As a function of polymer reservoir volume fraction, BSA first exhibits homogeneous intensities under confocal microscope, representing a stable fluid state. Upon increasing ϕ_P^R , small and individual clusters appear, while the brightness in the background indicates the presence of a coexisting fluid phase. Further increase of ϕ_P^R leads to a clear gel structure. Here we observed two main differences between BSA and eGFP: first, BSA clusters generated at intermediate ϕ_P^R are mostly separated even with higher protein concentration, as shown in Fig. 4.7(b) and (c). eGFP aggregation, meanwhile, has more extended, ramified shapes, and the preference for connecting neighbours (see Fig. 4.3.1(b)). Second, BSA shows three phase states: at low depletant concentrations, only a fluid phase is present. An intermediate ϕ_P^R (see the region in the middle of two black lines in Fig. 4.7) leads to a phase separation between the protein-rich regions coexist with a dilute protein fluid. At higher ϕ_P^R , a metastable gel coexists with a very dilute protein fluid. These phase transitions, are highly consistent with the simulations [108] and the predictions of free volume theory [173] for colloid-polymer mixtures at a size ratio $q = 0.4$. It is worth noticing that, although confocal images captured dense regions, we actually can not investigate the density or microstructure of those aggregates due to our resolution, nor do we have a clear intensity threshold for distinguishing between fluid and aggregation. The phase separation could only characterised by the emergence of distinct intensity difference.

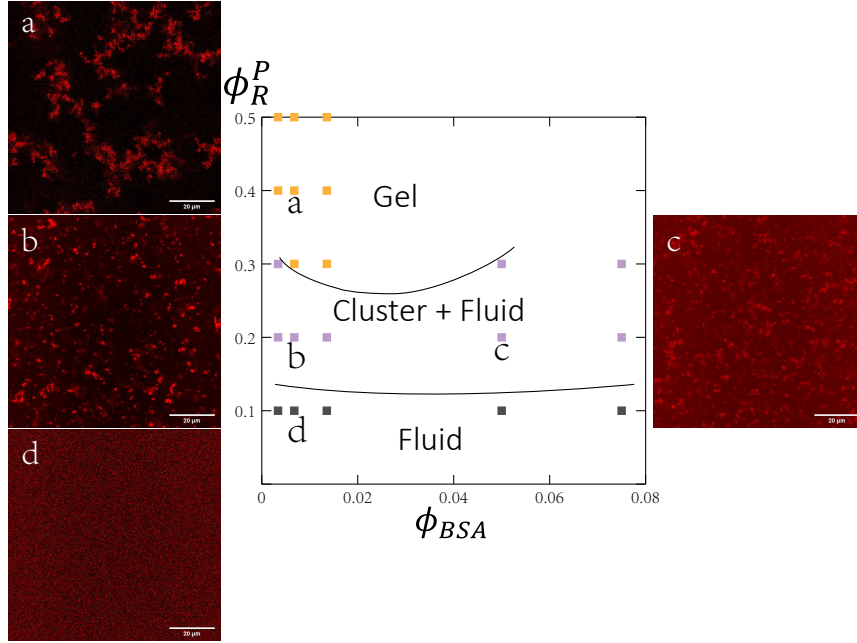


Figure 4.7: Phase diagram of fluorescent labelled BSA with $q = 0.44$ in 25 mM HEPES plus 100 mM NaCl at pH 7.0. (b) and (d) indicate that BSA clusters prefer un-ramified shape before final connection and formation of gel networks. Scale bars denote 20 μm .

4.3.5 Comparison with colloid-polymer mixtures

So far, we have only compared the ϕ_P^R required for experimental phase separation with the *equilibrium* theoretical and computer simulation predictions. The phase separation of BSA fits well to the predictions of colloid-polymer mixture that the colloids undergo three phase states upon increasing polymer volume fraction at $q = 0.4$, as mentioned at the end of previous section. However, the equilibrium phase states are not always achieved experimentally. Due to the ability to adjust the size and concentration of the polymer, the systems are seen to exhibit complex phase states such as metastable liquid-liquid phase separation. The mixtures of colloidal particles and polymers often undergo dynamical arrest into metastable non-equilibrium gel or glass phases. For instance, in our experiments, eGFP only has one fluid — aggregation transition, which is closer to the case of size ratio $q < 0.2$ in equilibrium. This condition might be satisfied by decreasing R_g to obtain a smaller $q = 2R_g/D_{\text{eGFP}}$, as we have discussed that the uncertainty of determining R_g of such small PEG molecules (see Sec. 4.3.2) allows a degree of adjustment of R_g . However, this simultaneously affects the comparison of mCherry and BSA results between simulations and our experiments. Alternatively, if we consider non-equilibrium states, especially gels, more consistent results can be found in the literature. As plotted in Fig. 4.8(a), the dynamically trapped state, gel is observed at a rather high polymer volume fraction. To make a comparison under different size ratios q , we calculated the well depth of depletion interaction ($\sigma = r$) as Equ. 1.22. In Fig. 4.8(a),

a potential of $\approx -3k_B T$ is required for the appearance of the gel, which is in good agreement with our result $u_{AO} = -2.84k_B T$ calculated in Sec. 4.3.2. Further comparison was drawn by inspecting the phase behaviour with Lennard-Jones (LJ) interaction, which is chosen because both LJ and AO potential can be approximated by a Morse potential [2]. The attraction of $\approx -3k_B T$ leads to an unstable region via a rather deep quench in the LJ simulation phase diagram [123]. In fact, such a strong interaction corresponds to the deep undercooling in molecular systems, and the system is expected to be arrested into long-lived metastable gel structure [174]. The emergence of gels has been investigated extensively at $q < 0.3$ [50, 67, 236, 250, 352], while few studies have been done when $q > 0.3$.

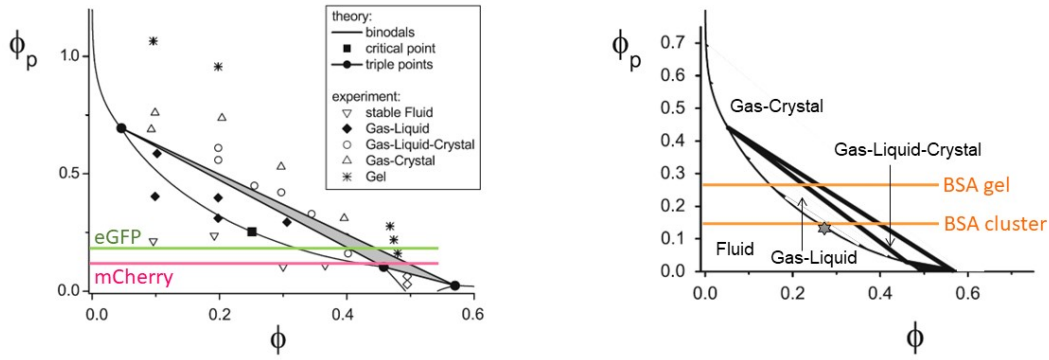


Figure 4.8: Comparison of theoretical and experimental phase states at two size ratios. (a) Theoretical phase diagram predicted by generalised free volume theory at $q = 0.57$, comparing with eGFP and mCherry of $q = 0.59$. The experimental ϕ_{polymer} for phase separation in our work are indicated by green (eGFP) and pink (mCherry) lines. Reprinted from Lekerkerker and Tuinier [174] coming with the experiment data (denoted by symbols) of PMMA plus polystyrene dispersed in cis-decalin [140, 309]. (b) Theoretical phase diagram calculated by free volume theory at $q = 0.4$, comparing with BSA of $q = 0.44$. Thick lines indicate triple lines. The critical point is denoted by the grey star. The experimental ϕ_{polymer} for different phase states of BSA are presented following the results in Fig. 4.7. Reprinted from Lekerkerker and Tuinier [174].

Previous work, as referred to above, also reveals that there are intermediate states between the fluid and metastable gel phases, such as gas-liquid coexistence and gas-liquid-crystal triple-existence, as a function of the attraction range. Though our experimental measurement, confocal microscope, has the highest resolution of around $50 \times 50 \times 180$ nm [146, 268], it can not capture the inner structures of different phases, nor do give the threshold for a specific state, resulting in an uncertainty between the gas and the liquid in our observations: only the phase coexistence can be identified through distinct intensity distribution of the confocal images. Rather than gels, the crystal nucleation process was more widely investigated in protein-related systems. It has been proposed that a two-step crystallisation will occur in the metastable liquid-liquid phase separation (LLPS) region: first, small droplets of a high protein concentration, either associated with the LLPS [117], or attributed to critical fluctuations of concentration [330], forms. Second, the crystallite forms inside the liquid-like droplets. In order to compare our results with the

literature, we make the bold assumption that the mentioned crystallisation and the gelation occur inside the spinodal curve through the LLPS: a slow increase of polymer (equivalent to a slow decrease of temperature) allows the sufficient diffusion of the proteins for the growth of crystallites, while a quench results to the spinodal decomposition where the protein-rich regions form gels as a consequence of dynamical arrest. This assumption is supported by previous work [98, 174, 184, 314] and our observations — once a phase separation occurs, a gel state would always be achieved upon further increase of the polymer concentration. Thus, we investigated the ϕ_P^R required for the phase separation, in terms of the reduced second virial coefficient, $B_2^*(T)$, which was further simplified to B_2^* since all our experiments were carried out at 20°C. As explained in Sec. 1.6, B_2^* is a convenient scale of the strength of the interaction. Besides common colloidal systems, it has been used as a predictor for the protein solubility in aqueous solution [116, 117] and protein crystallisation [110, 111]. Vliegenthart and Lekkerkerker observed that the value of B_2^* at the critical point lies around -1.5 for different attractions [319]. We plotted the phase boundaries for all our experimental systems, as shown in Fig. 4.9(a). The B_2^* values are located in $-0.5 \sim -1.5$. As noted in Sec. 4.3, our tested ϕ_{protein} are all out of the critical region, though the spinodal lines can be flat in a large range of ϕ_{colloid} for short-ranged attractions (see [260] for a flat phase boundary obtained by molecular dynamics simulations with a square well potential of width $0.03D$ in the case of spheres, and see [256] for a review of colloidal gels with phase diagrams for spinodal decomposition), indicating that B_2^* can also remain the value of ~ -1.5 at the protein volume fractions we measured. Therefore, we conclude that our results are in a quite good agreement with the literature. We also compared the values to Haas *et al.* [116] who measured B_2^* for a number of proteins including natural BSA which has a value of $B_2^* = -3.1$. We inferred that the difference may come from the fluorescent label and the consequent slightly smaller q . This possibility is left for further investigation.

Another positive aspect of examining the B_2^* is that, as also mentioned in Sec. 1.6, it enables the measurement of the effective range of the attractive potentials, which allows the further prediction whether a system exhibit a stable LLPS, analogous to those of a simple mono-atomic system, or only a fluid-solid coexistence indicating this transition is substituted by freezing [108, 173, 207]. In particular, the former type, namely, phase states of fluid - LLPS - [gas-crystal coexistence (G-C)] upon increasing the polymer concentration, is consistent with the observations of BSA where the denser regions in both G-L and G-C states are dynamically arrested to form a gel, while the latter with single phase separation fits the case of eGFP well. It is well accepted that sufficiently short-ranged attraction prevents the LLPS [118, 140, 198]. Noro and Frenkel [207] presented the critical points of various attractions in the $(T^* - R)$ plane, where $T^* = k_B T / \epsilon$ means the reduced temperature scaled by the energy parameter ϵ (The value of ϵ depends on the specific potential, *e.g.* the depth in the square well / the Lennard-Jones potential, and the contact potential in the Yukawa form), and R is the range of the attraction calculated by subtracting 1 from the ratio of particle distance to particle diameter, $R = r/\sigma - 1$, as shown in Fig. 4.9(b). They

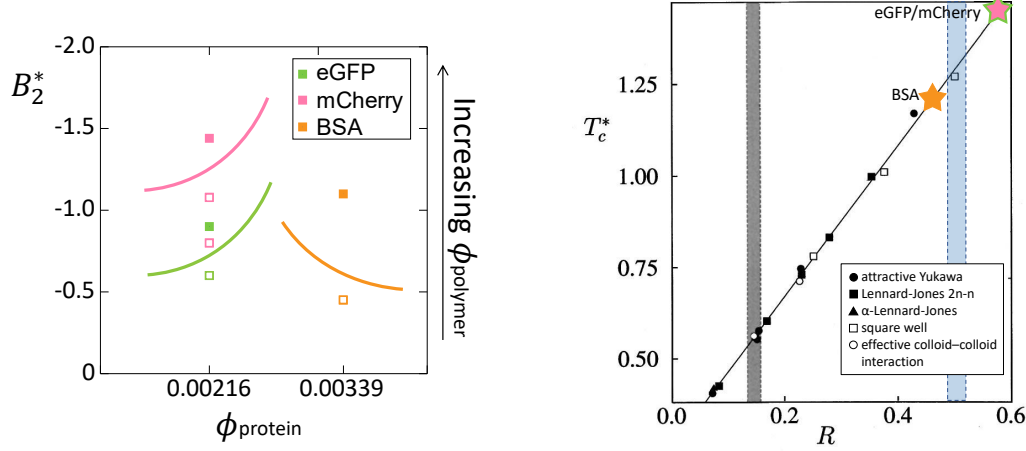


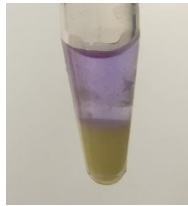
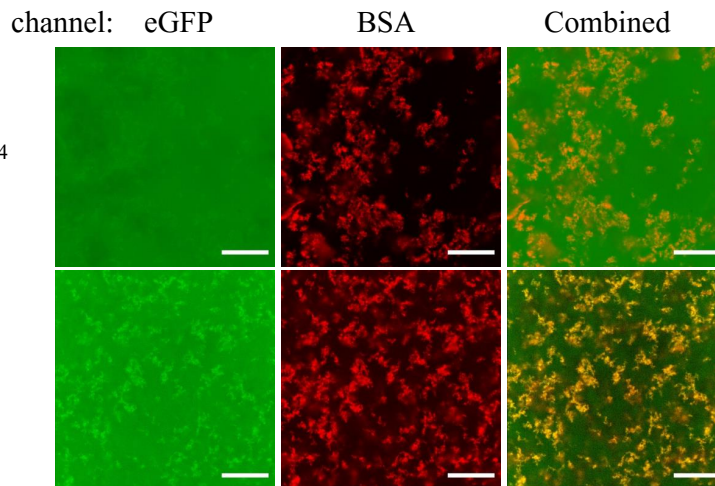
Figure 4.9: (a) Phase diagram of measured proteins in the $(B_2^* - \phi_{\text{protein}})$ plane. The solid lines denote the phase boundary obtained from Fig. 4.5 and 4.7. The open symbols indicate fluids while the closed symbols indicate the appearance of phase separation, as identified by confocal microscope images. (b) Critical points of different attractions in the $(T^* - R)$ plane. Reprinted from Noro and Frenkel [207]. The grey region indicates the boundary between stable and metastable LLPS. Our experimental results are represented by closed stars with the same colours used in (a), in which the ones denoting eGFP and mCherry overlap as they have the same R , and on the extended line of the fitting result. The blue region is the estimated boundary from our results.

observed a linear relationship between R and T^* , and the boundary for stable LLPS locating around 0.13 - 0.15 for various attractive potentials. They emphasised that their conclusion should be extended to out-of-critical regions despite restricting their simulation around the critical point. Therefore, we plotted the results of three proteins onto the $T^* - R$ fitting line in Fig. 4.9(b) by taking $R = q$. Clearly, the data are sorted in two groups. One consists of eGFP and mCherry with $q = 0.59$, and the other is that of BSA with $q = 0.44$. The boundary between stable and metastable gas-liquid transition thus locates within 0.44 - 0.59, acceptable when compared with mentioned work. Therefore, given that the phase behaviour we observed is similar to that of experimental, theoretical and simulation results from previous work, we conclude that our system is more likely to behave in a way akin to a depletion system with hard colloids plus non-absorbing polymers.

4.3.6 Phase behaviour of eGFP + BSA

So far, we have studied the phase behaviour of individual eGFP and BSA, and now we switch to binary mixtures of the two. As attempted at eGFP and mCherry binary gels, we designed a two-step formation protocol: from the phase diagrams, eGFP forms a gel structure at a lower polymer concentration than that of BSA. So, we first form a eGFP gel at $\phi_p^R = 0.2$, then added BSA with the same volume as eGFP, which leads to a concentration ratio $c_{\text{BSA}}/c_{\text{eGFP}} = 0.91$ inversely proportional to the ratio of their individual volume $V_{\text{BSA}}/V_{\text{eGFPdimer}} = 1.1$. Subsequently, PEG was added to precipitate BSA onto the existing gel. However, this protocol did not work. The

(a) Two-step addition.


 (b) Co-precipitation
of eGFP+BSA+PEG620.
The top row: $\phi_P^R = 0.2$
The bottom row: $\phi_P^R = 0.4$

 (c) Independent gel formation
of eGFP+BSA+PEG2000
with increasing ϕ_P^R .

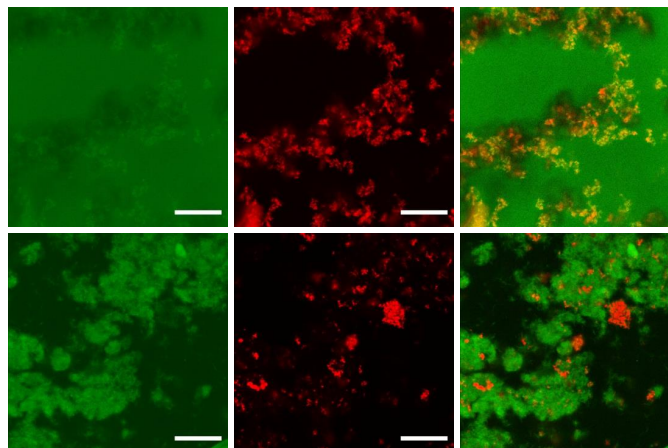
 The top row: $\phi_P^R = 0.2$
The bottom row: $\phi_P^R = 0.4$


Figure 4.10: Attempts at eGFP-BSA binary gels. (a) A photo of separate layers of top BSA fluid (transparent purple solution) and bottom eGFP gel (opaque green), taken three days after addition of BSA solution. (b) eGFP+BSA+PEG620: only full fluid or co-precipitation occurs. (c) eGFP+BSA+PEG2000: binary gel networks form. Scale bars denote 20 μm .

BSA solution failed to mix with the eGFP solution, and the clear layer boundary between them persisted for several days, as shown in Fig. 4.10(a). It is worth highlighting that the aggregated states of proteins in aqueous solution, including separated clusters and gels, can be characterised by the solution turbidity, as the protein aggregates scatter light in the visible wavelength region, and the turbidity reflects the relative loss of scattered light [119, 188]. Thus, Fig. 4.10(a) also reveals that the BSA was in the fluid state, implied by the transparency. This was later verified

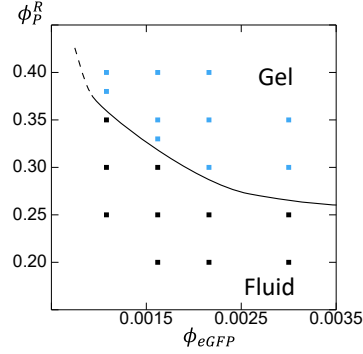


Figure 4.11: Experimental phase diagram of eGFP + PEG2000 with $q = 0.82$ in 25 mM HEPES plus 100 mM NaCl at pH 7.0.

through confocal microscope images. We infer that, for the subsequent formation of BSA gel structures around eGFP, the BSA molecules need to diffuse effectively from the top layer to the bottom, whereas the existing eGFP gel implies a strong attraction, which can suppress the diffusion of BSA over experimental timescales. Local small gelation of BSA may occur around the layer boundary, but we did not attempt to investigate this. Furthermore, we could not control the mixing force to get a proper/threshold potential which is unable to break eGFP gels while promote the diffusion of BSA in our experimental conditions, as there are only two types of mixer: the tube roller with maximum speed at 100 rpm, and the vortex with a minimum speed at 2500 rpm. Thus, we decided to mix all the components at the same time and then stir the sample on the vortex mixer. At this point, the sample was considered as fully re-mixed, and all the initial configuration before mixing was broken in this process.

Although eGFP and BSA did exhibit a difference in phase behaviour, their mixture co-precipitated: As shown in Fig. 4.10(b), at a low polymer volume fraction of $\phi_P^R = 0.2$, BSA first forms gel structures, while eGFP remains fluid. There are eGFP regions of heterogeneous intensity which may imply possible aggregation states, but when examining with the combined channel, this proves illusory, as these regions always overlap with BSA gels, and are more likely to be eGFP heterogeneous distribution around the occupied space by BSA. With higher polymer volume fraction, *i.e.* $\phi_P^R = 0.4$ as the second row in Fig. 4.10(b), eGFP exhibits gel networks, yet they completely overlay BSA gels. We thus conclude that in this mixture, eGFP cannot individually form gels, though the existing BSA backbone structure and higher ϕ_P^R facilitate its settling, and then the simultaneous precipitation, namely co-precipitation, occurs. In this case, no obvious domain of either component emerged. The distinct phase behaviour between separate and mixed protein species may come from the net charge and many-body interactions, which we left for further investigation.

We then switched to a larger polymer, PEG2000. According to the relationship $R_g = 0.0215M_w^{0.583}$ [111], PEG2000 has a $R_g = 1.64$ nm, roughly twice that of PEG620. This size leads to a size ratio of $q_G = 0.82$ for eGFP, and $q_B = 0.61$ for BSA, respectively. The phase diagram of eGFP +

PEG2000 in 25 mM HEPES plus 100 mM NaCl at pH 7.0 is shown in Fig. 4.11. As expected, larger size ratio leads to a higher polymer volume fraction required for phase separation. It should be noted that we did not examine separate phase behaviour of BSA plus PEG2000. The main reason is, it was extremely difficult to produce dyed BSA with mono-dispersed net charges. Firstly, the whole preparation usually took a week as it involved dialysis. Secondly, the fluorescent labelling process is equivalent to the cationisation, where a single BSA molecule has more than 40 active sites (carboxylic group) throughout the surface to be linked, indicating the uncertainty of the amount of dye molecules attached to a BSA monomer. Moreover, natural BSA is readily to form aggregation even with slight shake or larger container at a low concentration, compelling us to prepare independent batches. When characterising the net charge via zeta potential measurements, we usually found polydispersed net charges in one batch, and among different batches. Considering the modelling which treats BSA as spherical colloids, these dyed BSA monomers of heterogeneous charge distribution may fail to reflect the phase behaviour of isotropic colloids. Given the information above, we only obtained a small amount of dyed BSA with monodispersed net charge. Therefore, we decided not to perform the phase diagram of BSA + PEG2000.

We attempted the mixture of eGFP and BSA plus PEG2000, and successfully achieved binary gels with desired structure in this system. At low polymer concentrations, BSA first forms gel structures, while eGFP remains fluid, as shown by the split channels in the first row of Fig. 4.10(c). The darker regions in the eGFP channel indicate the space occupied the BSA gels rather than possible eGFP aggregation, as discussed above. Upon increase of the polymer volume fraction, independent gels of both proteins formed. This independence was so good that they looked like two fully separate systems. In particular, eGFP presented a cotton-like, rather than common ramified, network structure under bi-gelation conditions. This has been little studied before and deserve further investigations.

4.4 Conclusion

In this chapter, several experimental methods were used to study binary protein gels with distinct domains of each component via the depletion interaction. Here, we exploited the fact that said interactions are dominated by the size ratio between the proteins and the polymers as studied for other colloidal systems before. Therefore, we chose proteins with different sizes, investigated their behaviour at different polymer concentrations and identified the conditions that yielded a different behaviour in order to gain control over the gelation and the formation of binary structures. Instead of the commonly used “protein limit” [35], we considered the case more akin to colloid–polymer mixtures, where the polymer radius of gyration R_g is smaller than or comparable to the protein radius. It also meant to coarse grain the surface charge and shape complexity of proteins and treat them as isotropic systems to facilitate the calculation of their interactions.

We studied the proteins eGFP, mCherry and fluorescently labelled BSA as our model systems. PEG in different sizes was used as the depletant. The size ratios obtained were 0.59 for eGFP and mCherry and 0.44 for BSA using PEG620, while 0.82 for eGFP and 0.61 for BSA using PEG2000. Unstable pH, anisotropic protein surface charges and uncontrollable electrostatic interactions were found when the proteins were kept in deionised water. Thus, we changed the proteins to a buffer solution of 25 mM HEPES plus 100 mM NaCl. The electrostatic repulsion was then calculated and we found it to be negligible under these conditions. Therefore, the depletion interaction dominates the phase behaviour in our experimental systems.

The phase diagram of eGFP, its cationised version, and mCherry were obtained. This helped us to identify polymer concentration regions where the phase separation happened so we could produce a binary gel with distinctive domains. However, unexpected well-mixed domains occurred as a result of the high similarity between eGFP and mCherry molecules, and we were unable to achieve the desired structures. Fluorescently labelled BSA was then tested. This protein has an approximately spherical shape different to eGFP, and gives a slightly larger size ratio. As such, we were expecting the behaviour to be sufficiently different in the presence of polymers. Compared with existing colloid-polymer work, we found that BSA phase states were in good agreement with theoretical and simulation predictions for equilibrium at size ratio $q = 0.4$ [75, 173, 174], while eGFP is more complex as it forms dimers in aqueous solution, resulting in a spherocylinder shape rather than spheres. Moreover, our experimental data showed the emergence of gels, which corresponds to metastable nonequilibrium states, in the case of eGFP, which is consistent with the observations from the studies with similar q [140, 308]. Further studies were carried on by the analysis of the reduced second virial coefficient B_2^* , which exhibited a quite good agreement with previous literature

The phase behaviour of individual proteins fits the previous work on isotropic colloid-polymer mixtures well. However, our experiments are rather more complex in reality. Due to the limitation of our imaging resolution, the detailed information behind microstructure was lost, leading to a poor characterisation of phase states, especially the protein-rich regions. Indeed, the possibility of other interactions, due to functional groups, hydrophobic and hydrophilic effects, cannot be excluded. Nevertheless, the achievement of distinct binary gel networks gives us some optimism that the depletion interaction does dominate the behaviour of proteins in a controlled environment, and may further predict the phase behaviour of other protein species under similar conditions, which sets a precedent to develop a novel class of functional biomaterials. To our knowledge, our binary gels are the first binary structure consisting of functional proteins formed via depletion interaction.

GELATION OF COLLOIDAL ROD-POLYMER MIXTURES: MEAN-FIELD-LIKE ARREST IN 3D

Rod-like colloids are of great interest due to their anisotropic properties. We examine the influence of depletion interactions on a model system consisting of rigid rod-like particles, sepiolite clay B20, with a rather high aspect ratio ($L/D \approx 30$) plus polystyrene as depletants. Since the sedimentation arising from density mismatching between the solvent and the particles occurs during the timescale of experiments, we sort our results into phase behaviour in the presence/absence of gravity. The former type, with phase states identified by the percolating analysis of the 3D renderings of confocal images, successfully achieved gels at an extremely low volume fraction of rods $\phi_R = 0.00122$, of which the network can remain for more than three months. Meanwhile, by comparing structural and dynamical properties of the latter when crossing the phase boundary with those of high-dimensional hard sphere glass transitions [54], we prove that if the phase behaviour is dominated by the number of interactions, our system is analogous to the case of hard sphere vitrification in high dimensions, and thus is able to reconstruct it in simple experimental conditions.

5.1 Introduction

Although amorphous materials, such as glasses and grains, are common, the theoretical understanding of their behaviour remains poor. The dynamic arrest during the glass transition, the emergence of rigidity without freezing, is still an extremely challenging problem despite decades of work [31, 54]. However, a potential approach developed in recent years is to solve the problem in a high — especially infinite-dimensional — mean-field limit, $d \rightarrow \infty$, setting $1/d$ as a small parameter, in which the phase behaviour is in accordance with the case of $d = 3$ [157–159, 221].

The physical properties of particles in higher dimensions are different to those in $d = 3$. Especially, each sphere interacts with many other spheres, compared with the maximum of 12 neighbours in $d = 3$, giving rise to a noticeable decline of the short-range ordering, such as the structure factor $S(q)$ and the pair correlation function $g(r)$. Furthermore, the unconstrained correlations completely vanish in infinite-dimensional case, $d \rightarrow \infty$, as predicted by the recently claimed “decorrelation principle” [54, 286, 305].

In this work, we explore the possibility of recovering some features of such higher-dimensional hard sphere dynamical arrest via experimental rod-polymer mixture. Rather than vitrification, we investigate the gelation process, in which the phase transition behaviour of rods is actually better explained than in the case of vitrification [36, 174]. We choose a model system of colloidal hard rod particles in a high aspect ratio (length(L) / diameter(D) ≈ 30) plus polymers. The arrest, gelation, is controlled by depletion interaction induced by the addition of non-absorbing polymer [9, 181, 321] in our system. Due to the high aspect ratio, every rod particle is allowed to interact with many others, like spheres in higher dimensions. Therefore, we hypothesise that if the phase behaviour of the system is dominated by the number of interactions, the colloidal rods can recover high-dimensional hard sphere dynamical arrest process in reality. For example, the pair correlation function $g(r)$ is expected to exhibit very few changes during the process of the phase separation [259, 286].

Although hard rod particles undergo an isotropic-nematic phase transition in the absence of polymers which is distinct from hard spheres, the rod-polymer system follows the same general rules as sphere-polymer systems. For example, at similar size parameters (polymer-rod size ratio $q = 2R_g/D \approx 0.3$ and rod aspect ratio $L/D \approx 20$), a nematic-nematic phase coexistence is predicted to occur by the free volume theory [174]. Such demixing is the equivalent of the colloidal liquid-liquid phase separation in the case of sphere-polymer systems, where colloid-poor and colloid-rich regions coexist [173]. However, only a few works have been done with such a high aspect ratio as ours. Lekkerkerker and Tuinier [174] plotted computed phase diagrams for hard rods plus polymers using Gaussian approximation for the orientational distribution function. They revealed that for a given aspect ratio ranging from 5 to 200, the appearance of the triple point is a function of the size ratio, q . Small polymers, implying short-range attractions, lead to an equilibrium isotropic-nematic(dilute)-nematic(dense) (I-N₁-N₂) triple-existence. Intermediate q ceases both the mentioned N₁-N₂ and isotropic(dilute)-isotropic(dense) (I₁-I₂) critical points. Yet further increase of q recovers the (I₁-I₂) critical point. These relatively long-ranged attractions result in the triple-existence of I₁ + I₂ + N. Experimental systems of rod-like particles and polymers, such as rigid tobacco mosaic virus (TMV, $L/D \approx 20$) [101] and semi-rigid feline distemper ($L/D \approx 130$) [77], show similar isotropic and nematic phases. Although a degree of discrepancy on the values of ϕ_P and ϕ_R for the phase boundaries exhibits, the overall agreement between the experiments and the simulations is acceptable, considering the softness of the particles and the uncalculated electrostatic repulsion.

Furthermore, rod gels and glasses analogous to the dynamically arrested states of hard spheres can occur in real cases [290]. Many experimental works have reported the gelation of a diverse range of rod-like particles. Mohraz and Solomon [200] achieved gels of boehmites, a natural mineral with rod-like shape, at several aspect ratios $L/D = 3.9, 8.6$, and 30.1 . Adams *et al.* [1] observed the gelation of TMV and polyethylene oxide (PEG). PEGs of different molecular weights, giving corresponding size ratios $q = 0.29, 0.39, 0.67$, and 3.1 , were all able to induce a gel phase from the dilute isotropic phase. A positive aspect of gelation with rods is that, it can occur at low ϕ_R . This type of gel network formed by colloidal rod aggregates are commonly highly thin with fractal structures. For examples, Wilkins *et al.* [324] studied the mixture of rod-like polyamides plus depletants with the aspect ratio $L/D = 54$ and the size ratio $q = 0.11$ at $\phi_{\text{rods}} = 0.0005 - 0.01$. The rods prefer to form bundles in which multiple rod molecules align. These bundle structure change a little with further increase of polymers. Krall *et al.* [163] examined extremely weak networks at $\phi_R = 1.0 \times 10^{-4} - 5.0 \times 10^{-3}$, in which the gel structure can be broken by gentle shaking of the container.

Inspired by these works, we investigate the phase behaviour of rod-polymer mixture, especially gelation at low rod volume fractions as less computational resources are required for further simulations with fewer particles and interaction numbers. The length-polydispersed hard rods are fluorescently labelled [332], enabling confocal imaging. We demonstrate that the gelation can be obtained at a much lower polymer volume fraction than in the case of sphere-polymer systems with similar experimental conditions [255]. We further analyse the structural and dynamical behaviour in the absence of gravity by the radial distribution function, $g(r)$, and the time correlation function, $c(t)$, respectively, to examine the analogy between our system and hard sphere vitrification in high dimensions.

5.2 Experimental System

5.2.1 Preparation of stock suspensions

Colloidal rod suspensions were prepared from sepiolite clay particles B20 purchased from Tolsa (Spain). Sepiolite clay B20 is a naturally occurring mineral which has a rod-like shape. Their internal channels include two types of water molecules: coordinated and zeolitic water, as detailed in Sec. 2.3.1, in which the zeolitic water can be replaced by encapsulating external molecules. This characteristic was used to label the rod particles fluorescently in this work.

The preparation process generally follows the work by Zhang and van Duijneveldt [349]. To avoid large clusters, which tends to occur when the clays are dispersed into the solvent without stabilisers, 5 g of sepiolite clay B20 was gradually added into 100 mL toluene with the vigorous stirring by a high speed mixer (Ultra Turrax) at 10,000 rpm for 10 minutes to break the aggregates. Following that, the mixer is cleaned to avoid the stirrer becoming blocked. The mixing-clean step was repeated 3 times. The suspension was then ultra-sonicated (IND 500D,

Ultrawave) at 30°C for 30 min whilst being shaken by hand every 5 minutes to obtain a clear change in viscosity. Moreover, to increase the stabilisation of particles, SAP230 was used. Buining *et al.* found that the SAP230 was likely to be anchored to rod-shaped boehmite particles through chemical bonds [44]. Zhang then demonstrated that this grafting technology could also be carried out on sepiolite clays, and effectively increase the steric stabilisation of particles. 5 g SAP230 (Infineum, UK) was dissolved in 10 mL toluene and then added to the previous suspension with a magnetic stirrer. The addition of SAP230 caused a dramatic decrease in the viscosity of the dispersion. Then the whole sample was left overnight on the magnetic stirrer at 500 rpm.

5 mg of acridine orange (AO, content 75%, Aldrich) was added to the sample on the second day as the fluorescently labelling chemical, with the magnetic stirring at 500 rpm for 30 minutes, followed by a sonication for 10 minutes. Finally, to obtain a lower polydispersity, the suspension was firstly centrifuged at $4000\times g$ for 15 minutes to remove the sediment composed of large rod particles and unbroken clusters. The preserved supernatant was sequentially centrifuged at $8000\times g$ for 15 minutes to remove the new generated supernatant containing small rods, clusters, excess SAP230 and AO molecules, while the sediment consisting of particles with desired (intermediate and lower level of polydispersity) sizes was kept, which was then re-dispersed in pure toluene. The process of centrifugation at $8000\times g$ and re-dispersion was repeated several times as the clean step, until the supernatant became colourless by eye. Finally, a stock suspension of 20.74 wt.% was obtained. The exact bare mass fraction was measured by drying a small amount of the suspension.

Polystyrene (PS) in two different sizes ($M_w = 500000$, $R_g = 31.0$ nm; $M_w = 35000$, $R_g = 6.28$ nm [92, 300], Aldrich) were used as the depletants to control the range of depletion interactions. Polystyrene was also dispersed in toluene to prepare a polymer stock solution of 20 wt.%.

5.2.2 Particle characterisation

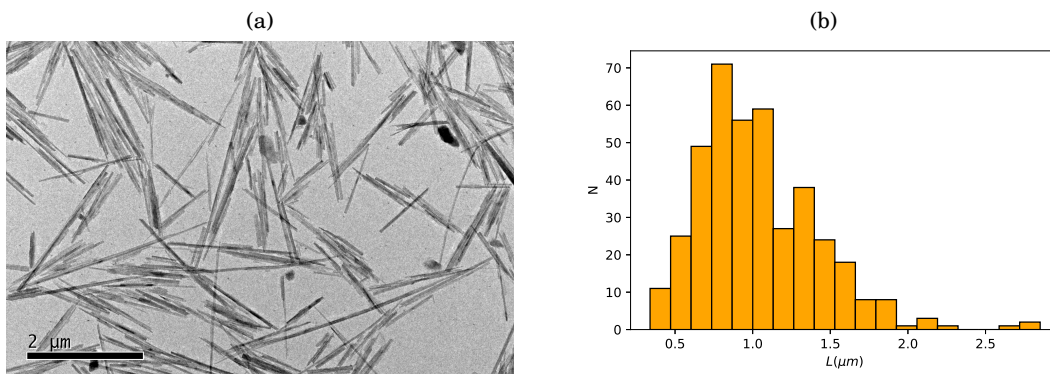


Figure 5.1: (a) A TEM image used for calculating the size of sepiolite clay B20 particles. (b) The length distribution of 400 rod particles.

Transmission electron microscope (TEM, JEOL JEM 1200-EX) was used to measure the

particle sizes. The sample was prepared by dehydrating a small drop of the suspension at 0.05 wt% onto a copper coated grid. The bare average length is $\langle L \rangle = 1035$ nm with a polydispersity of 37%, and the bare average diameter is $\langle D \rangle = 32$ nm with a polydispersity of 21%. These values were obtained by measuring 400 rod particles for each quantity. Fig. 5.1(a) shows one of the TEM images used for the measurement. Only rod particles with a clear edge were measured for dimensions. The bare dimensions do not count the thickness of the SAP230 layer, which is assumed to be $\delta = 2$ nm [289]; therefore, the effective diameter $\langle D_{\text{eff}} \rangle$ and $\langle L_{\text{eff}} \rangle$ were $\langle D_{\text{eff}} \rangle = \langle D \rangle + 2\delta$ and $\langle L_{\text{eff}} \rangle = \langle L \rangle + 2\delta$.

The effect of high polydispersity needs to be considered in any calculation that involves the particle sizes. Therefore, the effective aspect ratio $\langle L_{\text{eff}}/D_{\text{eff}} \rangle$ and its corrected standard deviation σ were calculated as 30.1 ± 12.3 by a second-order Taylor expansion, following [59]:

$$(5.1) \quad \begin{aligned} \left\langle \frac{L_{\text{eff}}}{D_{\text{eff}}} \right\rangle &= \frac{\langle L_{\text{eff}} \rangle}{\langle D_{\text{eff}} \rangle} \left(1 + \left(\frac{\sigma_D}{\langle D_{\text{eff}} \rangle} \right)^2 \right), \\ \sigma &= \frac{\langle L_{\text{eff}} \rangle}{\langle D_{\text{eff}} \rangle} \sqrt{\left(\frac{\sigma_L}{\langle L_{\text{eff}} \rangle} \right)^2 + \left(\frac{\sigma_D}{\langle D_{\text{eff}} \rangle} \right)^2}, \end{aligned}$$

where σ_L and σ_D are the standard deviation of $\langle L \rangle$ and $\langle D \rangle$, respectively.

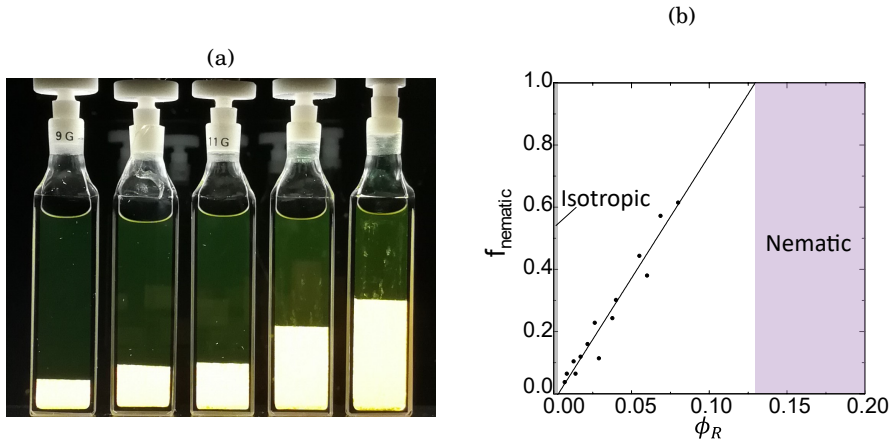


Figure 5.2: (a) A crossed polariser photo used for measuring the fraction of nematic phase. The total height is the length of a vertical line from the bottom to the lowest point of the meniscus. (b) Isotropic-nematic phase transition of the polydispersed rod particles in our system.

The phase diagram of isotropic-nematic phase transition without polymer was obtained by filling $40 \times 10 \times 1.5$ mm rectangular glass cuvettes (Vitrocom Inc.), sealed by Teflon stoppers and tape at different mass fractions m , and keeping still them vertically for 48 h to allow phase separation. Birefringence images of cuvettes between crossed polarisers were taken to calculate the nematic fraction by measuring the height ratio of bright regions. Fig. 5.2(a) shows a photo of cuvettes used for the nematic fraction. The bare volume fraction $\phi_{R_{\text{bare}}}$ was calculated using the

following equation:

$$(5.2) \quad \phi_{R_{\text{bare}}} = \frac{m_R/\rho_R}{m_R/\rho_R + m_T/\rho_T},$$

where the rod particle density, $\rho_R = 2.10 \text{ g/mL}$, is assumed to be equal to dried pure sepiolite clays [19], and $\rho_T = 0.867 \text{ g/mL}$ is the toluene density. The effective volume fraction was then obtained, with the assumption that the bare rod particles are cuboid while the attached SAP230 form a cylinder shape enclosing the cuboid, as the following equation:

$$(5.3) \quad \phi_{R_{\text{eff}}} = \frac{\pi}{4} \phi_{R_{\text{bare}}} \left[1 + \frac{2\delta}{\langle D \rangle} \left(1 + \left(\frac{\sigma_D}{\langle D \rangle} \right)^2 \right) \right]^2,$$

where the polydispersity has been considered, as described when calculating the effective aspect ratio. Table 5.1 shows parts of the mass concentration and corresponding volume fraction values used for the phase diagram, as the black points in Fig. 5.2(b). Hereafter $\phi_R = \phi_{R_{\text{eff}}}$. The concentrations of the isotropic and the nematic phases were obtained by linear fitting of the points. The values calculated were $\phi_{\text{iso}} = 0.0084$ and $\phi_{\text{nem}} = 0.129$.

m_R	0.0135	0.027	0.035	0.06	0.085	0.105
$\phi_{R_{\text{bare}}}$	0.00562	0.0115	0.0145	0.0251	0.0367	0.0458
$\phi_{R_{\text{eff}}}$	0.00843	0.0172	0.0217	0.0377	0.0551	0.0687
f_{nem}	0.0647	0.120	0.159	0.243	0.444	0.572

Table 5.1: Rod mass fractions m and the calculated $\phi_{R_{\text{bare}}}$, $\phi_{R_{\text{eff}}}$, f_{nem} values.

Woolston and van Duijneveldt compared the experimental phase diagram of colloidal suspensions of sepiolite clays with the theoretical predictions of length-polydispersed particles [172, 332]. They investigated the relationship between the volume fraction ratio $\phi_{\text{iso}}/\phi_{\text{nem}}$ — which affects the width of the transition — and the relative polydispersity of the aspect ratio $\sigma/\langle L_{\text{eff}}/D_{\text{eff}} \rangle$. The values of $\phi_{\text{iso}}/\phi_{\text{nem}} = 0.065$ and $\sigma/\langle L_{\text{eff}}/D_{\text{eff}} \rangle = 0.425$ were calculated from experimental data in this chapter, close to the conclusions in their work.

5.2.3 Phase diagram characterisation

We investigated the phase behaviour of rod-polymer gelation, with a particular interest in obtaining percolating networks at low volume fractions. However, the density matched system is hard to construct, due to the limitation of selecting the shape of colloids and the requirement of a good solvent for the given polymers. Therefore, gravity needs to be taken into consideration. Two types of phase diagram are presented: the long-term phase diagram, in which all the samples were left to rest for 48 hours before being checked, and were confirmed to keep the corresponding state for at least 3 months, and the instantaneous phase diagram, in which the measurements were taken within 120 s from the time point that the samples were removed from the vortex.

More details of the instantaneous phase diagram will be given in Sec .5.3.2 to prove that in such a short timescale, the effect of gravity is trivial and can be neglected.

In both types of phase diagrams, the same methods were used to calculate the volume fractions. For the bare rod volume fraction, Equ. 5.2 is updated to include the polymer volume, so that,

$$(5.4) \quad \phi_{R_{\text{bare}}} = \frac{m_R/\rho_R}{m_R/\rho_R + m_T/\rho_T + m_P/\rho_P},$$

where $\rho_P = 1.05 \text{ g/mL}$ is the pure polystyrene density. Then the effective rod volume fraction is calculated by Equ. 5.3. The conversion of polystyrene volume fraction from the mass fraction in colloidal rod-polymer mixtures is more complicated. As mentioned in Sec. 1.3.4, the polymer molecules exhibit a large volume expansion during dispersion into the medium. They will not overlap when the concentration is less than the overlap concentration in a good solvent. The overlap concentration is calculated by $c^* = 3M_w/(4\pi R_g^3 N_A)$, where M_w is the weight average molecular weight of polymers, R_g is radius of gyration, and N_A is Avogadro's number. Since the highest experimental PS concentration used in this work is less than the overlap concentration, the polymer molecules are regarded as spheres with the radius of gyration $R_g = 0.0118M_w^{0.6} \text{ nm}$ at 25°C [300], so that the experimental PS volume fraction is obtained by:

$$(5.5) \quad \phi_P = \frac{m_P/M_w \times \frac{4}{3}\pi R_g^3 N_A}{m_R/\rho_R + m_P/\rho_P + m_T/\rho_T},$$

where $\rho_P = 1.05 \text{ g/cm}^3$ is the pure polystyrene density.

Furthermore, to compare with the predictions from depletion theory and simulation, the fraction of available volume for depletants, α , is used to estimate the reservoir polymer volume fraction from that in the experimental system, $\phi_P^R = \alpha\phi_P$ (see Sec. 1.3.4.3 and Fig. 1.9). α is calculated by the aspect ratio $\gamma = L/D$, the size ratio $q = 2R_g/D$ and the rod volume fraction ϕ_R , as expressed by Equ. 1.23.

5.2.4 Sample setup for confocal microscope

Confocal images were taken with a Leica DCIM 8000 confocal laser scanning microscope with a white light laser emitting at centred 520 nm. The suspensions of fluorescently labelled rod particles were fully mixed by a vortex stirrer (IKA, Germany) at 3000 rpm for 2 min, and were then filled into $50 \times 1.00 \times 0.10 \text{ mm}$ rectangular capillaries (Vitrocom Inc., 5010-050) at different volume fractions of both rods and PS. Our experimental system is affected by gravity due to the density difference between sepiolite clay and toluene. Therefore, to record the time gap, the start time point $t = 0$ is defined as the moment when the stirring stops. The capillaries with suspensions were glued to a glass slide along the horizontal longest axis. The image stacks were taken along the z direction. Fig. 5.3 shows a schematic image which indicates a scanned stack.

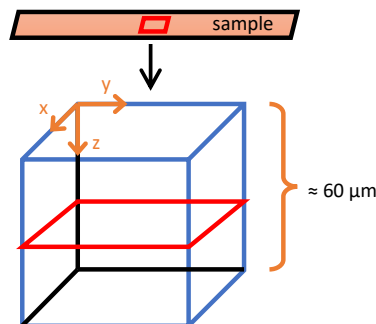


Figure 5.3: Illustration of the scanned region in capillaries under the confocal microscope. Replotted from Cordova [59].

5.3 Results

As previously stated, our system was not density matched, leading to sedimentation in accessible experimental timescale. Generally, in tested concentrations of both rods and polymers, a sample required about 24 hours to reach a stable density profile which could insist for several months. The photos through the crossed polariser of those stable density distribution under gravity are shown in Fig. 5.4. Meanwhile, we also investigated the phase behaviour in the condition of minimising the effect of gravity, by shortening the time gap between the preparation and the observation of the samples. The results involving or excluding the gravity are presented in the following Sec. 5.3.1 and 5.3.2, respectively, in which the latter is expected to recover the hard higher-dimensional sphere phase behaviour.

5.3.1 Long-term phase behaviour

5.3.1.1 Polariser images

Polystyrene with $M_w = 500000$ and $R_g = 31.0$ nm was used in this part to obtain a polymer-rod diameter size ratio $q \approx 1$. A complete set of all the crossed polariser photos of cuvettes is shown in Fig. 5.4. Permanent birefringence results were obtained, which provide a rough estimation of the phase state at different rod and polymer volume fractions. Three states are observed in this figure: isotropic, isotropic-nematic coexistence, and gel phases. The isotropic phase is dark and transparent when seen between a polariser, as in the left column, while the nematic phase exhibits distinct Schlieren textures (see Sec. 1.5.1). The nematic domain diffuses along with the increase in polymer volume fraction at a fixed ϕ_R . A sample with full bright pattern will be initially regarded as a gel phase, with further accurate identification by the percolation analysis in the following section.

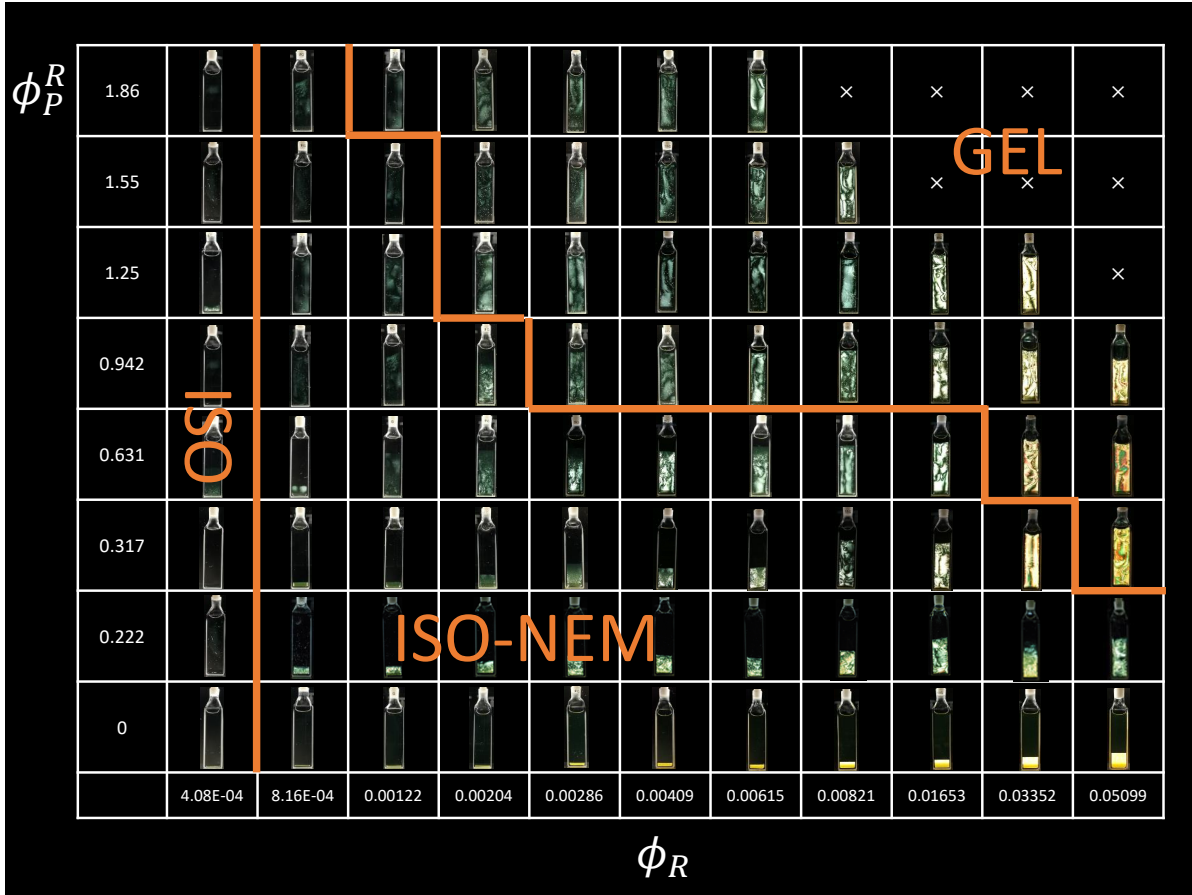


Figure 5.4: Polariser photos of all the samples. For a clear phase transition, *i.e.*, the increasing nematic phase to the percolated gel as a function of ϕ_R , see the row of $\phi_P^R = 0.317$. From left to right: isotropic, isotropic-nematic coexistence and gel phases. Note that this is not linear scale.

5.3.1.2 Confocal images and percolating analysis

Confocal microscope image stacks provide the three-dimensional structures of the systems. According to the Nyquist theorem and the limitation of the point spread function (see Sec. 2.5.1.1 and 2.5.1.2), the maximum voxel size is $50 \times 50 \times 176$ nm in the (x, y, z) direction. A size of $240 \times 240 \times 240$ nm was actually used to include more rod particles for further analysis, as well as comparing with previous work investigating the phase behaviour of highly similar rods [91]. Noticed that the width of the rods was much smaller than the pixel resolution, around 1/6 of pixel size, our analysis gave a coarse-grained result rather than identifying individual rods. Fig. 5.5 shows (x, y) plane images of samples near the phase boundary estimated by the polariser photos. The rod clusters remain a similar width with increasing ϕ_R , indicating less preference of should-to-should aggregation. Moreover, the directional disorder rises with higher ϕ_P^R , especially at higher ϕ_R . This phenomenon was further checked by 3D reconstruction, since (x, y) plane lacks the information along z direction. The 3D reconstructions were used to characterise the percolating state of the networks. In Fig. 5.6, the images present the three biggest connected

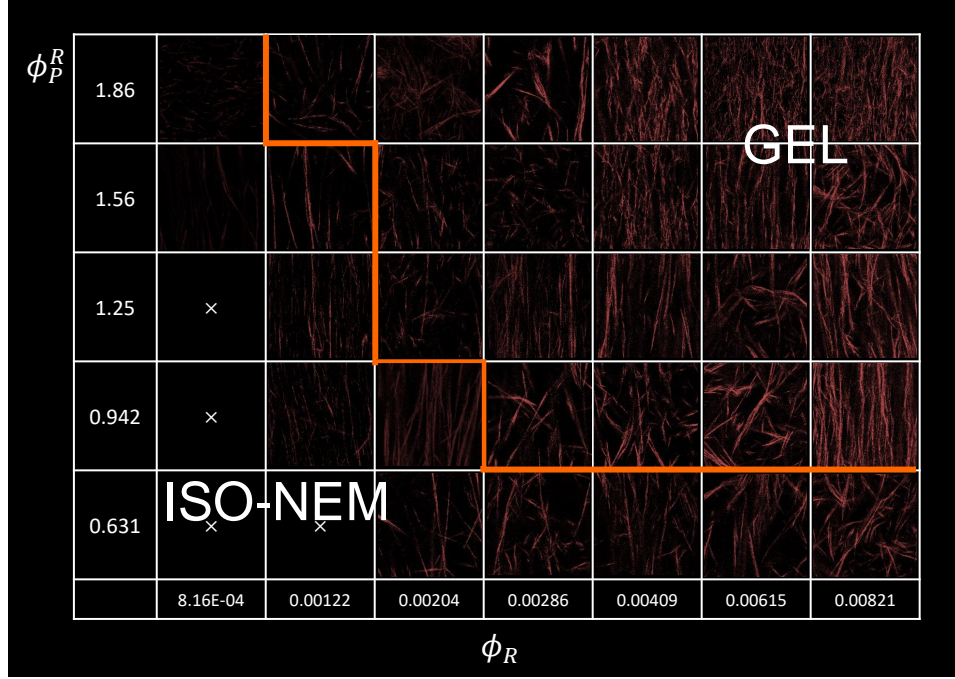


Figure 5.5: Confocal microscope images of the samples near the estimated phase boundary at rod volume fraction 0.000408 - 0.00615. The bright orange pixels represent the rods. All the images are in size of 93.14 nm square.

clusters in the stack by red, green and blue.

A universal definition of the colloidal gel is still not clear (see [51, 341] for reviews). Therefore, we identified a “percolated gel” if the state point simultaneously satisfies two conditions: (i) the Schlieren texture fills the whole volume through the polariser; and (ii) a cluster is found to percolate along any direction in the volume. The accurate phase boundary between isotropic-nematic coexistence and such percolated gel phases was drawn by the percolation analysis. Although clusters exhibit a higher disorder in (x, y) plane, 3D reconstructions reveal clusters in both I-N coexistence and gel phases have a peculiar elongated shape, which has not been observed previously. Such a shape is quite different to the spindle-like droplets that have been reported previously [143, 239].

5.3.1.3 Phase diagrams

Fig. 5.7 presents the phase diagrams of experimental data and simulation results. The experimental phase diagrams are plotted after the mass fraction has been converted into volume fraction. In particular, the polymer volume fraction is in the reservoir format, as explained in Sec. 5.2.3, to compare with simulation results. Fig. 5.7(b) presents the maximum potential ϵ_{\max} in $k_B T$ scale versus ϕ_R , with ϵ_{\max} calculated by the product of the maximum overlap volume of the depletion layers (obtained through shoulder-to-shoulder approaching of two particles) times the polymer number density, while a logarithmic scale was used in Fig. 5.7(c) to give a clear view of low

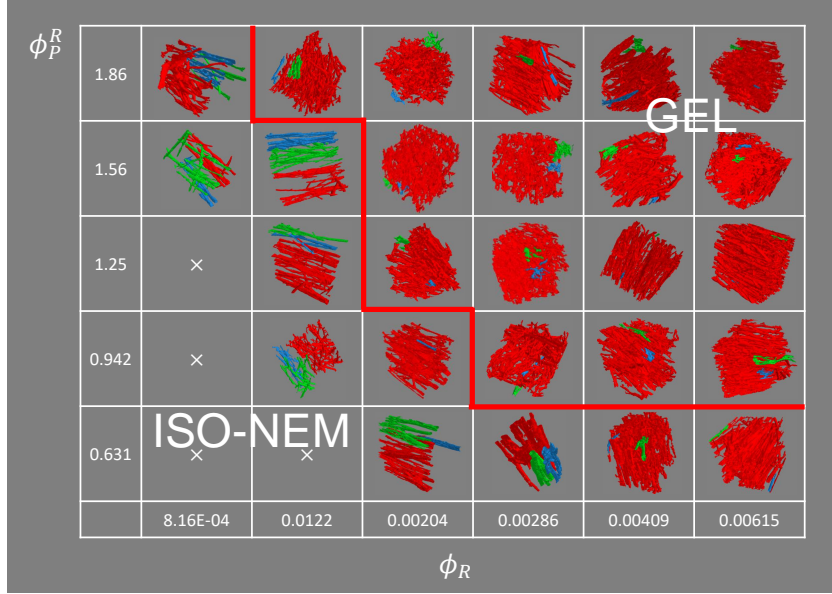


Figure 5.6: 3D reconstruction of confocal image stacks for percolation analysis. Red, green and blue colours represent the three biggest connected clusters.

ϕ_R region. Fig. 5.7(d) shows the simulation phase diagram of spherocylinders predicted by free volume theory with a comparable aspect ratio $L/D = 20$ and a size ratio $q = 1$. [174]. The curves are calculated by the Gaussian orientational distribution function. Comparing Fig. 5.7(a) and (d), we observe that a larger ϕ_P^R is required to form a gel network in experiment. The simulation predicts that the phase separation occurs at $\phi_P^R \approx 0.23$, while our data is above 0.78. Furthermore, the range of experimental I-N phase coexistence increases due to rod length polydispersity. The existence of the pure isotropic phase is barely observable, as a low polymer volume fraction and the consequently weak depletion attraction is unable to resist the gravity, leading to sediment of large particles which further facilitates the formation of the nematic phases at denser regions (the bottom of the container). Although our rod-polymer system requires higher polymer concentration for a phase transition in contrast with the simulation, the minimum rod volume fraction needed to realise a percolating gel is 0.00122, showing that even at low concentration the gel structure can be achieved.

5.3.2 Phase behaviour neglecting gravity

With the aim to achieve percolating gel networks at low volume fraction of rod particles, in this section we only prepared and checked the phase states at low ϕ_R . Furthermore, we converted to smaller PS, with $M_w = 35000$ and $R_g = 6.3$ nm, to tune to a shorter ranged interaction, since simulations reveals that lower polymer volume fraction is needed for an arrested state in this case [174], and more works studied the phase behaviour of spheres with short-ranged attractions [51, 74, 229, 234, 342]. The choice of polymer updated the size ratio q to 0.2. A key issue in our

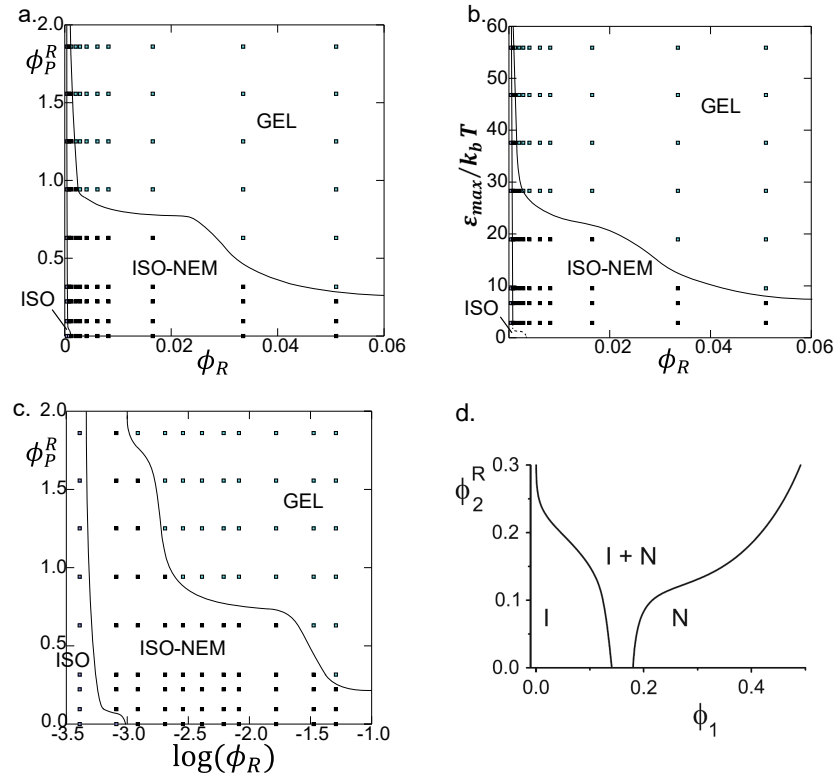


Figure 5.7: Phase diagrams of experimental ((a)-(c), $L/D = 30$ and $q \approx 1$) and simulation ((d), $L/D = 20$ and $q = 1$ [174]) results. (a)-(c) are the same data in different representations. The polymer concentrations are switched to reservoir volume fractions ϕ_P^R to compare with the simulation prediction.

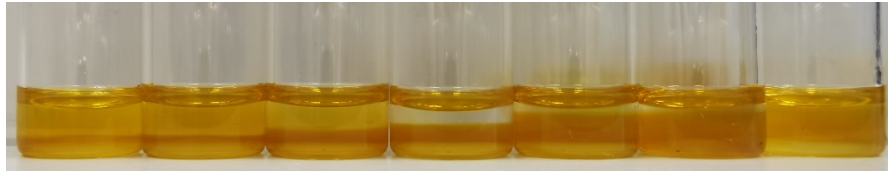


Figure 5.8: A photo of the samples at $\phi_R = 0.0169$ and $q = 0.2$ with the increasing ϕ_P from left to right. This photo was taken three days after preparation. Although all the samples exhibit full gel state along z-axis, identified via the observation of confocal microscopy as well as the dynamic measurement, the formed gel network may collapse due to the gravity, as shown by the fourth sample.

system is that it is affected by gravity due to the density difference between rod-like colloids and the solvent. Some work has investigated the sedimentation induced by gravity of rod-like particles [122, 132]. However, the sedimentation speed in our system is hard to measure. Firstly, the viscosity dramatically increases when the sepiolite rod particles are dispersed in toluene, indicating the change of motions. Secondly, the depletion interactions induced by polymers have different directions depending on the spatial orientation of the rods, while gravity always points

down. A general sedimentation photo of the samples at $\phi_R = 0.0169$ with increasing polymer concentration, taken three days after preparation, is shown in Fig. 5.8. We can see that, although all the samples in this photo are further characterised as gel states full in z direction at $t = 60$ s by the dynamical analysis in the next section, the gel structures at different polymer volume fractions do have distinct resistance to gravity. At low polymer concentrations, gels are rather stable, while little sediment forms (indicated as a darker brown layer at the bottom of the container). Yet, as the amount of polymers increase, the gel branches become large enough that significant quantities collapse, resulting in a denser sediment at the bottom, which reminds us of the aggregation and sedimentation in colloidal systems [232]. The size of the gel branch can be observed through confocal images in Fig. 5.9. Finally, at high polymer concentrations, which is equivalent to a quickly deep quench, the particles are effectively arrested into the network, and the gel can remain for a long time. We therefore roughly measured the sedimentation speed of the most unstable sample, which usually corresponds to an intermediate polymer concentration, at each rod volume fraction. For example, when $\phi_R = 0.0169$ and $\phi_P^R = 0.115$, the capillary is full along z direction until $t = 65$ s; $t = 145, 220$ s, the top interface between the supernatant and the denser sediment drops to 90%, 80% of z height. Although higher volume fraction results in lower dynamics, and requires taking longer time sequence stacks by confocal microscope, we ensured that all the data were obtained within the time that the sedimentation maybe reasonably neglected as the top interface is still higher than 95% of z height.

Fig. 5.9 shows the phase diagram of rod particles and PS35000 of a size ratio $q = 0.2$, along with (x, y) plane confocal images of some state points which represent the changes of clusters as a function of ϕ_P^R : At low polymer volume fractions (Fig. 5.9(a1)) where the system shows an isotropic phase, the rod particles are either separate (inferred from the intensity of the background) or form small clusters which lengths are mainly less than 10 times that of individual colloids. With very shallow quench (Fig. 5.9(a2) and (b1)) the clusters extend in both length and width. At this point, not all the colloids are arrested to an aggregate, though the gel state characterised by the dynamical analysis in the next section has formed. The amount of free individual rod molecules is proportional to the rod volume fraction, as still indicated by the intensity of the background. However, further increase of ϕ_P^R force these free molecules attaching to the network. In addition, the rod bundles exhibit strong preference of alignment, parallel to the longest axis of the rectangular capillaries (corresponding to y direction in Fig. 5.3), with the length exceeding $100 \mu\text{m}$, longer than the width of the capillaries (Fig. 5.9(a3) and (b2)). The samples were introduced via capillarity, so the flux along the capillaries in combination with the length and rigidity of bundles lead to the alignment, whereas we cannot exclude the possibility that the bundles have distinct directions in a much larger container. Unfortunately the alignment could not be successfully suppressed in the sample preparation with capillaries, and we left this for further experimental improvements. Finally, with sufficiently high ϕ_P^R (Fig. 5.9(a4) and (b3)), the long bundles break to shorter ones, and the crossed structures *re-form*. The changes of clusters are

consistent with Fig. 5.8: the crossed gel networks at low or high polymer volume fractions have a degree of resistance to the gravity, while the aligned structures induced by the intermediate ϕ_P^R are easy to sediment due to the lack of supports along z direction.

Compared with the long-term phase diagram, the gel phase appears at a much lower ϕ_P , as well as showing a sharp decline of ϕ_P required for gelation, which is in good agreement with the simulations [174]. As mentioned in Sec. 5.3.1.2, the width of the rod particles (≈ 30 nm) was under the confocal resolution. In the gel networks, several particles may align and contribute to one pixel, as indicated in Fig. 5.9(c). Therefore, the following analysis of the dynamics and the structure (see the next two sections) shows coarse-grained results rather than identifying separate rods.

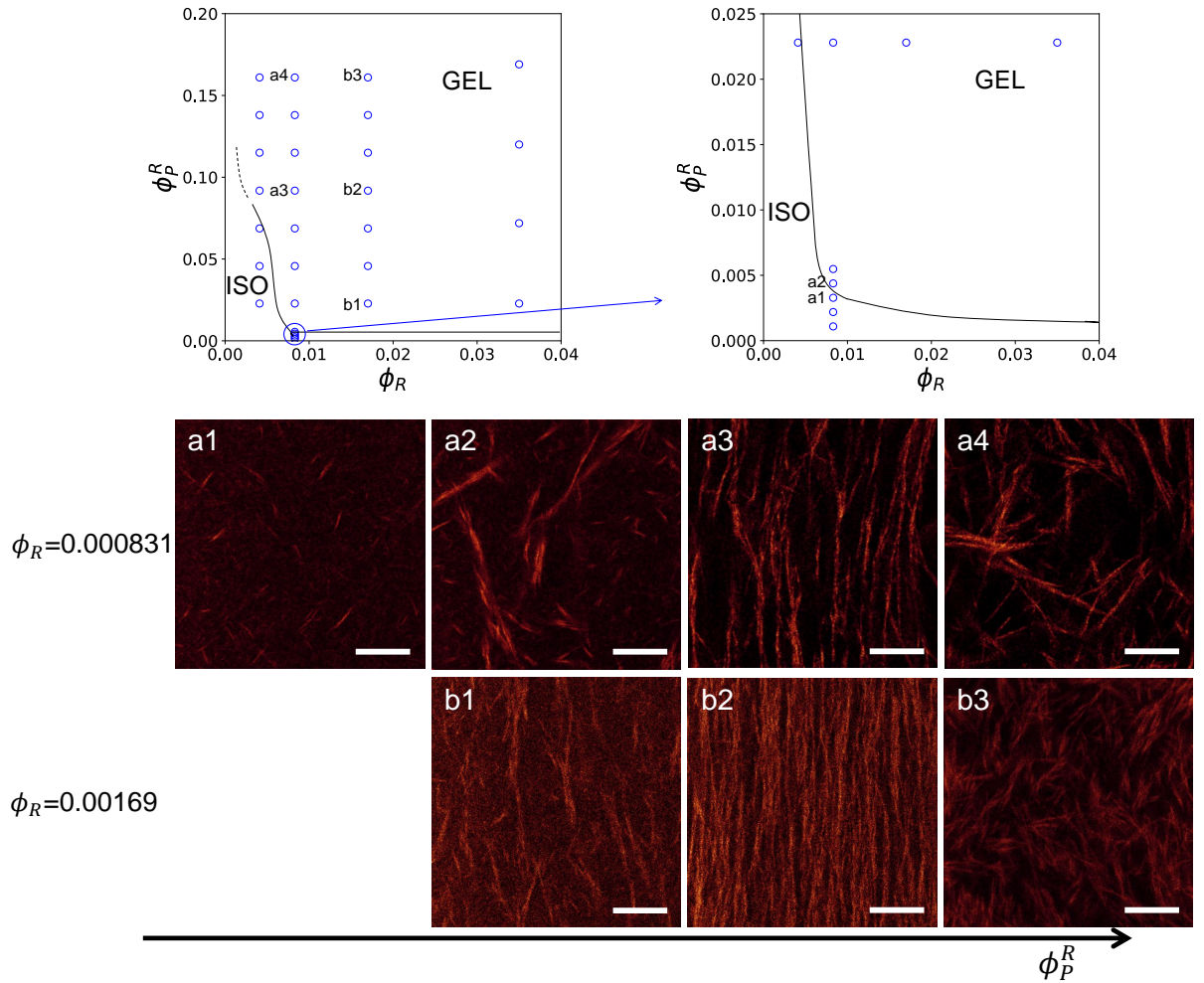


Figure 5.9: Phase diagram of rods and PS 35000 mixture of $L/D = 30$ and $q = 0.2$, with part of the corresponding confocal images. The right magnifies the region at the bottom of the second column in the left phase diagram. “a” and “b” denote a series of samples of $\phi_R = 0.0083$ and $\phi_R = 0.0169$, respectively. The re-formation of crossed networks is clearly exhibited with increasing ϕ_P^R . Scale bars denote $20 \mu\text{m}$ in confocal images.

5.3.2.1 Dynamics

The dynamic properties of different phases were measured by a time correlation function $c(t)$. Considering the image intensity measured at two time points, t_0 and $t_0 + t'$, if t' is long enough compared to the characteristic timescale for diffusion, the corresponding intensity values will be little correlated. On the contrary, if t' is short, the intensity values will have a correlation that depends on the particle diffusion rates. Quantitatively, a time correlation function indicates the time that a measured variable of a system remains until it is averaged out by motions of the system, revealing how and when a statistical relationship has vanished. Such a function $c(t)$ was calculated by intensity of pixels $I(\mathbf{r}, t)$ of the time sequences of (x, y) plane images, and can be expressed as [91]

$$(5.6) \quad C^i(t', t) = \frac{\langle I(\mathbf{r}, t) I(\mathbf{r}, t + t') \rangle}{\langle I(\mathbf{r}, t) \rangle \langle I(\mathbf{r}, t + t') \rangle} - 1,$$

where $\langle \rangle$ means average of all the pixels in the image. As mentioned in Sec. 5.3.1, a coarse-grained measure was taken instead of distinguishing separate rods for all the confocal images, since the rod width is much smaller than the pixel size. $C^i(t', t)$ can be further normalised by the initial value at $t = 0$ to $c^i(t', t) = C^i(t', t)/C^i(0, t)$.

The time sequences of the (x, y) plane images were all taken at $t = 40$ s, and the time duration depends on both rod and polymer volume fractions. Each sample was imaged at the central z position, 50 μm high above the bottom, and far from the two sides where glue may be present. In $c(t)$ calculation, t was counted from the moment the imaging started, as we assumed that $c^i(\tau, t)$ keeps relatively constant if the dynamics change in a much larger timescale compared with t for a fixed value of τ . The correlations were fitted to a stretched exponential function $c(t) = c(0)[\exp(-t/\tau)^b]$, where $c(0)$ is the first point, and was used to normalise all the values on the correlation curve [91]. τ can be interpreted as a structural relaxation time of each phase. Fig. 5.10(b) shows the time correlation fitting curves. The phase boundary was determined by noting the dramatic increase of τ from the isotropic to gel phase, as the latter is a dynamically arrested state. For example, $\tau_{\text{iso}} = 3.2$ s and $\tau_{\text{gel}} = 64$ s at $\phi_R = 0.00415$. Some gel state points did not obtain a convincing τ from the fitting, *e.g.* $\phi_P^R = 0.115$ in Fig. 5.10(b1) since it was deeply quench and was unable to completely relax in the tested experimental timescale (no apparent signs of gel collapse due to gravity). Though this lack of τ values had no effect on the identification of gelation. The steep increase of the structural relaxation time is comparable to the case of hard spheres, where τ exhibits a highly similar tendency when continuously approaching the glass state, as shown in Fig. 5.10(d) [260]. Moreover, It is worth noting that in the shallow quench region, the state point at which the time correlation decays slower in the initial image frames can be fitted to a shorter relaxation time, as shown by $\phi_P^R = 0.00438$ (closed circles, $\tau = 83$ s) and $\phi_P^R = 0.00548$ (closed squares, $\tau = 117$ s) in Fig. 5.10(b2), which might be due to different gel networks formed by varying degrees of bundling, and we left this phenomenon for further investigation.

5.3.2.2 Structures

To obtain a full description of structure in our system, the radial distribution function $g(r)$ of pixels was calculated on (x, y) plane images. The value obtained from $g(r)$ was then fitted to an exponential decay $h(r) = A \exp(-r/\xi)$, where $h(r) = g(r) - 1$, to calculate characteristic lengths ξ [91]. The distance was plotted based on the pixel number and size (240 nm). Although $h(r)$ curves present specious peaks, they are undersampled acquisition of a record frequency about 8 times larger than that of the typical $h(r)$ usually represented in units of the particle diameter (in our case is the width of the rods of around 30 nm), and thus they fail to recover the complete information of the density distribution as a function of the particle distance in our experiments. However, we can still make comparison between the correlation functions $h(r)$ at different ϕ_R and ϕ_P^R . Apparently, the $h(r)$ curves of isotropic phase are similar to those of shallow quenches, as shown in Fig. 5.10(c). Moreover, it is expected by the “decorrelation principle” that unconstrained spatial correlations of hard spheres diminish with the increasing dimension, and eventually vanish in the limit of $d \rightarrow \infty$. This limit predicts that the pair correlation function $g_2(r)$ only remains the delta-function contribution from the nearest neighbouring particles and loses all the peaks of larger distance, as well as enabling the entire calculation of n-particle correlation function $g_n(r)$ through the known $g_2(r)$ and the bulk number density of hard spheres [286, 305]. Fig. 5.10(e) presents corresponding simulation work of Stoke *et al.* [286], with $g(r)$ curves continuously diminishing as a function of increasing dimensions. Similarly, our results exhibit an evident peak at contact, then extend with fluctuated values and trivial peaks, which is consistent with the mentioned decorrelation principle that dense packings may be disordered.

In order to quantitatively measure the length scale of the regime size, the characteristic length ξ was further calculated. Fig. 5.10(c) shows the $h(r)$ results, and corresponding fitting curves. Notice that not all the $h(r)$ have been fitted, because fluctuating $h(r)$ values with increasing distance (See Fig. 5.10(c2)) sometimes led to a bad fitting result, for example, negative characteristic lengths, which are unphysical. Table 5.2 lists ξ of different polymer volume fractions at $\phi_R = 0.00415$. Similar ξ values were obtained from isotropic phases to gel phases. Although $h(r)$ fittings at $\phi_R = 0.00836$ were inaccessible, we can roughly get the same conclusion that $h(r)$ curves remains similar shape and tendency during phase transition.

ϕ_P^R	0.0228	0.0457	0.0687	0.0919	0.115
ξ	1.49	1.23	1.57	1.52	1.41

Table 5.2: Characteristic lengths ξ obtained by fitting $h(r)$ at $\phi_R = 0.00415$.

The analysis explained above suggests that our colloidal rod-polymer mixture may serve as a model system to study the hard sphere vitrification in higher dimensions. Generally, two properties connect these two cases. Firstly, rods with short-ranged attractions exhibit a continuous but steep increase of the structural relaxation time from isotropic phase to shallow quenches in

dynamical analysis, consistent with the dynamic properties in glass transition of hard sphere experiments and simulations [54, 260]. Secondly, structural analysis reveals that very few changes of the colloidal structure, characterised by the pair correlation function $g(r)$ and the fitted characteristic length ξ , can be found during the phase transition, which follows the prediction of hard spheres that the higher-order correlations beyond the sphere diameter vanish in high d , leaving a uniform value for larger distances [286, 305]. Therefore, we can mimic the hard sphere structureless dynamical arrest in higher dimensions through simple rod-polymer experimental system in reality.

5.4 Conclusion

In this section, a stable and reproducible preparation of the dispersion of sepiolite clay particles and non-absorbing polymers was developed. Based on this, a model system was established with rather high polydispersity, which was used to explore the possibility to recover the hard sphere vitrification in higher dimensions. In particular, the phase behaviour at low rod volume fractions was investigated, while the high aspect ratio (≈ 30) gives large interaction numbers with other particles. The system was firstly characterised by the isotropic-nematic phase transition without polymer, which shows a wider gap between the two phases due to the polydispersity. The addition of polystyrene induced depletion interaction among colloidal rods, leading to the gelation. Experimental phase diagrams of PS500000 ($q=1$), as well as the comparison to simulation ones, were then obtained. We successfully obtained gel structure at an extremely low volume fraction $\phi_R = 0.00122$.

A smaller polymer, PS35000 ($q=0.2$), was selected for a study of the shorter-ranged attraction. Lower ϕ_P was required for phase separation, as predicted by theory. A localised phase diagram in the isotropic region was presented. Two properties were characterised to compare the similarity to hard sphere dynamic arrest in higher dimensions, namely, the time correlation function $c(t)$ and the radial distribution function $g(r)$. During gelation, the structural relaxation time τ calculated by $c(t)$ exhibits a continuous but significant increase, while the system structure, indicated by $g(r)$, remains similar to its initial state. We conclude that, this loss of ergodicity in our rod-polymer model system is akin to the dynamical arrest in the hard sphere high-dimensional case, and thus provide a potential approach to interpret this phenomenon by such simple depletion interactions induced by polymers between hard rods in experiments.

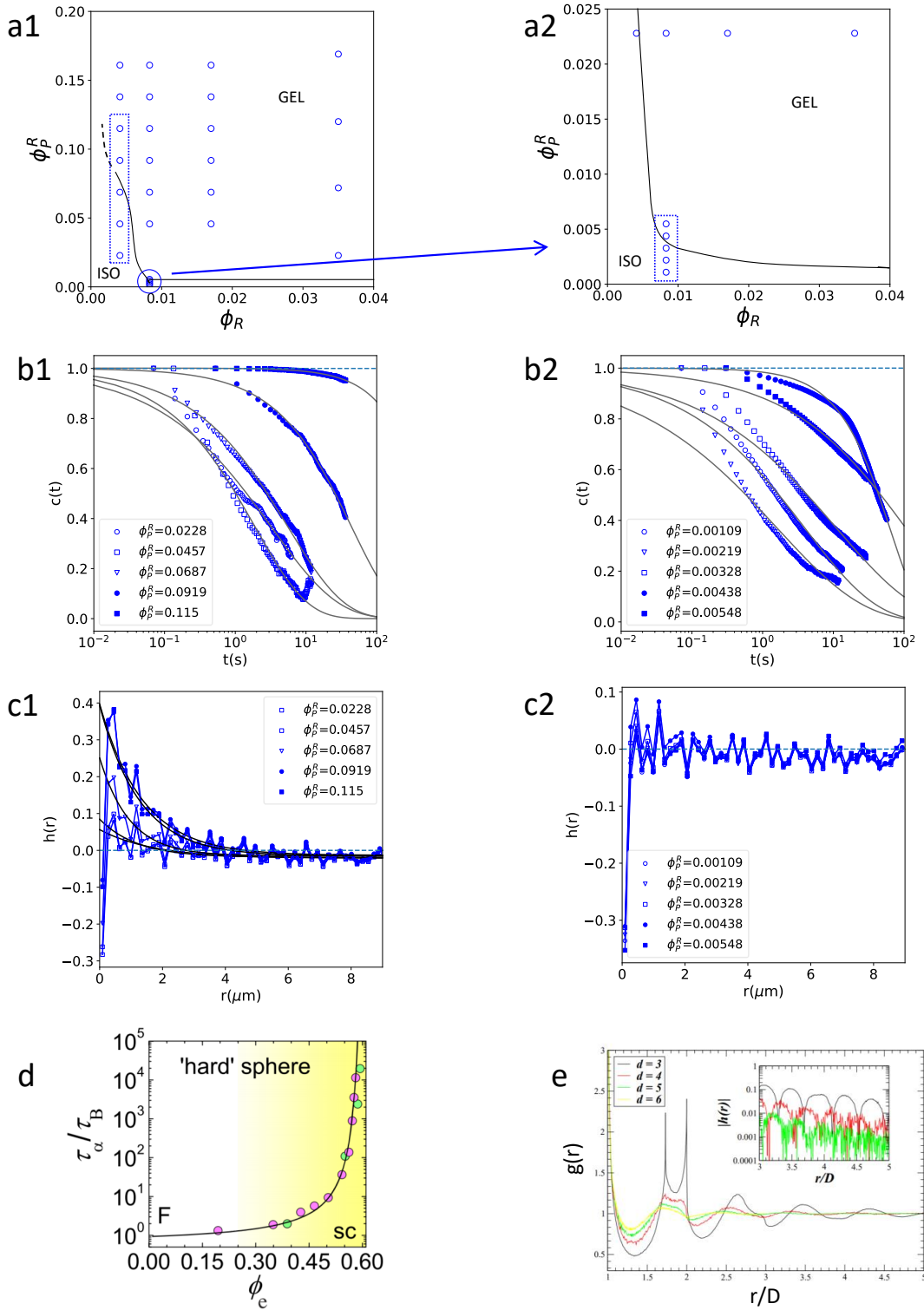


Figure 5.10: The full comparison of the similarity between our rod-polymer mixtures and hard sphere high-dimensional vitrification. Column number “1” and “2” denote samples at $\phi_R = 0.00415$ and 0.00836 , respectively. (a) Phase diagrams of rods plus PS 35000 with $L/D = 30$ and $q = 0.2$. For ϕ_R below those tested, dashes are plotted based on the intuition from the literature [174, 266]. Points enclosed by dotted lines are taken for following dynamical and structural analysis. (b) The time correlation functions $c(t)$ of the isotropic (open symbols) and the gel (closed symbols) phase during phase transition. The same symbols are used in (c). (c) The pair correlation functions $h(r)$ results. (d) Structural relaxation time τ_α of experimental hard sphere glass transition. Reprinted from Royall *et al.* [260]. (e) $g(r)$ for maximally random jammed packings of hard spheres at $d = 3, 4, 5, 6$. Replotted from Skoge *et al.* [286].

CONCLUSION AND FUTURE WORK

This thesis investigates self-assembly behaviour of multiple model systems consisting of colloids and proteins, as well as the consequently formed structures. The conclusions fall broadly into three sections, with increasing complexity of particle shape and interactions: hard sphere homogeneous nucleation rates, and gelation of proteins and hard rod-like colloids via depletion attractions. The main results for each topic will be discussed in the following sections. Moreover, recommendations for further work will be made at the end of each section.

6.1 Hard sphere nucleation rates

The chapter states a real-space technique for processing and analysing confocal microscopy results of nucleation, to attempt to resolve the significant discrepancy between the experimental and simulation hard sphere nucleation rate densities. This method enables the crystal identification of smaller colloids than the typical size required for particle-resolved imaging, as well as much larger imaging volume, allowing much rarer events during crystallisation to be observed. In other words, it can detect the weakly supercooled region, where the largest gap exists, than previous particle tracking research. Therefore, this method provides more comprehensive knowledge of the homogeneous nucleation. Furthermore, a more accurate measurement of the final crystallinity was presented.

Sterically stabilised PMMA particles of different sizes, $\sigma_{\text{core}} = 392, 613$ and 1800 nm, were examined independently. However, the results from our experiments did not match the simulation results of pure hard sphere systems. We only observed a weak particle volume fraction dependence of the nucleation rate density throughout the phase transition regime, as obtained by previous experimental studies. We then compared our systems to the simulations of weakly charged colloids, and concluded that the particles used in the experiments were not hard spheres with

a degree of polydispersity and noticeable net charge, which altered the phase behaviour and crystal nucleation rates. Our particles indeed fit better to weakly charged colloids than hard spheres. We thus propose further work repeating the experiments with less polydispersed and more weakly charged particles which are closer to the hard spheres of the simulations, with the same processing algorithms and analysis.

6.2 Binary protein gels via depletion interaction

In this study, we produced binary protein gel structures with distinct domains of each component through the depletion interaction. By exploiting the size ratio of polymers to proteins, we identified the individual phase behaviour of used protein species under different conditions to gain control over the formation of binary structures. Instead of the common “protein limit” [35], we considered the typical colloidal cases where $R_g \leq R_{\text{protein}}$. We averaged the surface charge of proteins, and treated them as spheres or spherocylinders based on the molecular aspect ratio to facilitate the calculation of their interactions. During experiments, unstable pH and the consequent uncontrollable electrostatic interactions were found when the proteins were kept in deionised water. Thus, we changed the proteins to a buffer solution of 25 mM HEPES plus 100 mM NaCl, where the charges were effectively screened, and the depletion interaction dominated the phase behaviour.

The model systems consisting of natural fluorescent proteins (eGFP or mCherry) or fluorescently labelled BSA plus PEGs in different sizes as the depletants were examined. At the beginning, The phase diagram of eGFP, its cationised version, or mCherry with PEG620 were separately plotted, identifying the corresponding polymer concentration required for phase separation. The radius of gyration for PEG620 was then adjusted, to fit the phase boundary from literatures of spheres [316] and spherocylinders [266], giving an updated size ratio $q_G = q_C = 0.59$. Further experiments were performed for possible binary gels. However, when blended these two proteins, unexpected well-mixed domains occurred due to the high similarity between eGFP and mCherry molecules, and we were unable to achieve the desired structures. Fluorescently labelled BSA plus PEG620 with a size ratio $q_B = 0.44$ was then tested, showing three phase states in the presence of polymers, with the states consistent with those from theoretical and simulation predictions for equilibrium colloid-polymer mixture at size ratio $q = 0.4$. Comprehensive studies of all the protein types were carried out by analysing the reduced second virial coefficient, which exhibited good agreement with previous works.

The mixture of eGFP and BSA plus PEG620 only presented co-precipitation, while the mixture of eGFP and BSA plus PEG2000, with the size ratio $q_G = 0.82$ and $q_B = 0.61$, successfully obtained binary gel networks. Although the protein molecules are complex, and the detailed information behind microstructure is lost due to the limitation of our imaging resolution, the achievement of distinct binary gel networks provides optimism that the depletion interaction

dominates the behaviour of proteins in a controlled environment. The development of a novel class of functional biomaterials is possible based on our precedent to predict the phase behaviour of other protein species under similar conditions. To our knowledge, our binary gels are the first binary structure composed of functional proteins via the depletion interaction.

Further experiments could test the phase behaviour of the binary mixture as a function of R_g . As observed, if focusing on the size ratio of polymer to eGFP, a small increasing of q_G , from 0.59 to 0.82, leads to different aggregation states. Moreover, other protein species, such as lysozyme which is smaller than an eGFP monomer and can be regarded as globular, can be used with BSA to examine if the formation of binary gels with distinguishable domains of each component is always accessible with sufficiently size and/or shape differences through the depletion interaction.

6.3 Gelation of Colloidal Rod-Polymer Mixtures: Mean-field-like Arrest in 3D

In this section, we reported the development of a stable and reproducible method for preparing a dispersion of sepiolite clay particles and non-absorbing polymers. Utilising this method, we established a model system of hard rod-like colloids with a high degree of polydispersity plus polymers to explore the possibility of recovering higher-dimensional hard sphere vitrification due to the large interaction numbers associated with the high aspect ratio of rods. Specifically, we investigated the phase behaviour at low rod volume fractions. Our system was first characterised by the isotropic-nematic phase transition without polymer, which exhibited a wider gap between the two phases due to the polydispersity. The addition of polystyrene induced depletion interaction among colloidal rods and led to gelation. We obtained experimental phase diagrams for PS500000 ($q = 1$) and compared them to simulation results. This system successfully formed gel structures at extremely low rod volume fractions down to $\phi_R = 0.00122$, which are stable for more than three months under gravity.

Furthermore, we switched to a smaller polymer, PS35000, to study shorter-ranged attraction. As predicted by theory, a lower polymer volume fraction was required for phase separation with a smaller size ratio [174]. We presented a localised phase diagram in the isotropic region and examined two properties, the time correlation function $c(t)$ and the radial distribution function $g(r)$, to compare the similarity to hard sphere dynamic arrest in higher dimensions. During gelation, the structural relaxation time calculated by $c(t)$ exhibited a continuous but significant increase, while the system structure, indicated by $g(r)$, remained similar to its initial state over experimental timescales. We conclude that the loss of ergodicity in our rod-polymer model system is similar to the dynamical arrest observed in the higher-dimensional case of hard sphere glass transition. Therefore, this depletion interaction induced by polymers between hard rods provides a potential approach to interpreting this phenomenon in reality. Since the width of rod particles (~ 30 nm) in this work was smaller than the confocal resolution (lateral 180 nm and axial 500

nm), one pixel may contain multiple rods, and our dynamical and structural analysis presented coarse-grained results rather than identifying separate colloids. Further improvement can be performed by using wider particles which are over resolution to give true time correlation function and radial distribution function.

BIBLIOGRAPHY

- [1] M. ADAMS AND S. FRADEN, *Phase behavior of mixtures of rods (tobacco mosaic virus) and spheres (polyethylene oxide, bovine serum albumin)*, Biophysical journal, 74 (1998), pp. 669–677.
- [2] M. AL-RAEEI, *Morse potential specific bond volume: a simple formula with applications to dimers and soft-hard slab slider*, Journal of Physics: Condensed Matter, 34 (2022), p. 284001.
- [3] D. B. ALLAN, T. CASWELL, N. C. KEIM, C. M. VAN DER WEL, AND R. W. VERWEIJ, *soft-matter / trackpy: Trackpy v0.5.0*, Apr. 2021.
- [4] A. P. ALTSHULLER, *The dielectric constants, polarizations and dipole moments of some alkylbenzenes*, The Journal of Physical Chemistry, 58 (1954), pp. 392–395.
- [5] V. J. ANDERSON AND H. N. LEKKERKERKER, *Insights into phase transition kinetics from colloid science*, Nature, 416 (2002), pp. 811–815.
- [6] B. ANDREWS, D. HEAD, P. DUNTHORNE, AND J. ASENJO, *Peg activation and ligand binding for the affinity partitioning of proteins in aqueous two-phase systems*, Biotechnology techniques, 4 (1990), pp. 49–54.
- [7] L. ANTL, J. GOODWIN, R. HILL, R. H. OTTEWILL, S. OWENS, S. PAPWORTH, AND J. WATERS, *The preparation of poly (methyl methacrylate) latices in non-aqueous media*, Colloids and Surfaces, 17 (1986), pp. 67–78.
- [8] J. A. ARPINO, P. J. RIZKALLAH, AND D. D. JONES, *Crystal structure of enhanced green fluorescent protein to 1.35 Å resolution reveals alternative conformations for glu222*, (2012).
- [9] S. ASAKURA AND F. OOSAWA, *On interaction between two bodies immersed in a solution of macromolecules*, The Journal of chemical physics, 22 (1954), pp. 1255–1256.
- [10] ———, *Interaction between particles suspended in solutions of macromolecules*, Journal of polymer science, 33 (1958), pp. 183–192.

BIBLIOGRAPHY

- [11] N. ASHERIE, A. LOMAKIN, AND G. B. BENEDEK, *Phase diagram of colloidal solutions*, Physical review letters, 77 (1996), p. 4832.
- [12] S. AUER AND D. FRENKEL, *Prediction of absolute crystal-nucleation rate in hard-sphere colloids*, Nature, 409 (2001), pp. 1020–1023.
- [13] ———, *Suppression of crystal nucleation in polydisperse colloids due to increase of the surface free energy*, Nature, 413 (2001), pp. 711–713.
- [14] ———, *Crystallization of weakly charged colloidal spheres: a numerical study*, Journal of Physics: Condensed Matter, 14 (2002), p. 7667.
- [15] ———, *Line tension controls wall-induced crystal nucleation in hard-sphere colloids*, Physical review letters, 91 (2003), p. 015703.
- [16] ———, *Numerical prediction of absolute crystallization rates in hard-sphere colloids*, The Journal of chemical physics, 120 (2004), pp. 3015–3029.
- [17] ———, *Quantitative prediction of crystal-nucleation rates for spherical colloids: A computational approach*, Annual review of physical chemistry, 55 (2004), pp. 333–361.
- [18] S. AUER, W. POON, AND D. FRENKEL, *Phase behavior and crystallization kinetics of poly-12-hydroxystearic-coated polymethylmethacrylate colloids*, Physical Review E, 67 (2003), p. 020401.
- [19] S. BALCI, *Effect of heating and acid pre-treatment on pore size distribution of sepiolite*, Clay Minerals, 34 (1999), pp. 647–655.
- [20] V. BARANAU AND U. TALLAREK, *Random-close packing limits for monodisperse and polydisperse hard spheres*, Soft Matter, 10 (2014), pp. 3826–3841.
- [21] J. A. BARKER AND D. HENDERSON, *What is "liquid"? understanding the states of matter*, Reviews of Modern Physics, 48 (1976), p. 587.
- [22] E. BARTSCH, S. KIRSCH, P. LINDNER, T. SCHERER, AND S. STÖLKEN, *Spherical microgel colloids—hard spheres from soft matter*, Berichte der Bunsengesellschaft für physikalische Chemie, 102 (1998), pp. 1597–1602.
- [23] F. BAWDEN, N. PIRIE, J. BERNAL, AND I. FANKUCHEN, *Liquid crystalline substances from virus-infected plants*, Nature, 138 (1936), pp. 1051–1052.
- [24] A. H. BECKETT AND J. B. STENLAKE, *Practical Pharmaceutical Chemistry: Part II Fourth Edition*, vol. 2, A&C Black, 1988.

-
- [25] J. R. BECKWITH, *Regulation of the lac operon: Recent studies on the regulation of lactose metabolism in escherichia coli support the operon model.*, Science, 156 (1967), pp. 597–604.
- [26] D. BEDNARCZYK, E. A. MASH, B. R. AAVULA, AND S. H. WRIGHT, *Nbd-tma: a novel fluorescent substrate of the peritubular organic cation transporter of renal proximal tubules*, Pflügers Archiv, 440 (2000), pp. 184–192.
- [27] J. M. BERG, J. L. TYMOCZKO, AND L. STRYER, *Protein structure and function*, Biochemistry, 262 (2002), pp. 159–173.
- [28] F. BERGAYA AND G. LAGALY, *General introduction: clays, clay minerals, and clay science*, in Developments in clay science, vol. 5, Elsevier, 2013, pp. 1–19.
- [29] H. M. BERMAN, J. WESTBROOK, Z. FENG, G. GILLILAND, T. N. BHAT, H. WEISSIG, I. N. SHINDYALOV, AND P. E. BOURNE, *The protein data bank*, Nucleic acids research, 28 (2000), pp. 235–242.
- [30] J. G. BERRYMAN, *Random close packing of hard spheres and disks*, Physical Review A, 27 (1983), p. 1053.
- [31] L. BERTHIER AND G. BIROLI, *Theoretical perspective on the glass transition and amorphous materials*, Reviews of modern physics, 83 (2011), p. 587.
- [32] H. BLOCK, B. MAERTENS, A. SPRIESTERSBACH, N. BRINKER, J. KUBICEK, R. FABIS, J. LABAHN, AND F. SCHÄFER, *Immobilized-metal affinity chromatography (imac): a review*, Methods in enzymology, 463 (2009), pp. 439–473.
- [33] L. BOCQUET, E. TRIZAC, AND M. AUBOUY, *Effective charge saturation in colloidal suspensions*, The Journal of Chemical Physics, 117 (2002), pp. 8138–8152.
- [34] P. BOLHUIS, A. LOUIS, AND J. HANSEN, *Influence of polymer-excluded volume on the phase-behavior of colloid-polymer mixtures*, Physical review letters, 89 (2002), p. 128302.
- [35] P. G. BOLHUIS, E. J. MEIJER, AND A. A. LOUIS, *Colloid-polymer mixtures in the protein limit*, Physical review letters, 90 (2003), p. 068304.
- [36] P. G. BOLHUIS, A. STROOBANTS, D. FRENKEL, AND H. N. LEKKERKERKER, *Numerical study of the phase behavior of rodlike colloids with attractive interactions*, The Journal of chemical physics, 107 (1997), pp. 1551–1564.
- [37] G. BOSMA, C. PATHMAMANOHRAN, E. H. DE HOOG, W. K. KEGEL, A. VAN BLAADEREN, AND H. N. LEKKERKERKER, *Preparation of monodisperse, fluorescent pmma-latex colloids by dispersion polymerization*, Journal of Colloid and Interface Science, 245 (2002), pp. 292–300.

- [38] C. D. BOSTICK, S. MUKHOPADHYAY, I. PECHT, M. SHEVES, D. CAHEN, AND D. LEDERMAN, *Protein bioelectronics: A review of what we do and do not know*, Reports on Progress in Physics, 81 (2018), p. 026601.
- [39] A. BRAHMA, C. MANDAL, AND D. BHATTACHARYYA, *Characterization of a dimeric unfolding intermediate of bovine serum albumin under mildly acidic condition*, Biochimica et Biophysica Acta (BBA)-Proteins and Proteomics, 1751 (2005), pp. 159–169.
- [40] S. BROCCA, R. GRANDORI, S. LONGHI, AND V. UVERSKY, *Liquid–liquid phase separation by intrinsically disordered protein regions of viruses: Roles in viral life cycle and control of virus–host interactions*, International Journal of Molecular Sciences, 21 (2020), p. 9045.
- [41] M. L. BROIDE, C. R. BERLAND, J. PANDE, O. O. OGUN, AND G. B. BENEDEK, *Binary-liquid phase separation of lens protein solutions.*, Proceedings of the National Academy of Sciences, 88 (1991), pp. 5660–5664.
- [42] G. BRYANT, S. R. WILLIAMS, L. QIAN, I. SNOOK, E. PEREZ, AND F. PINCET, *How hard is a colloidal “hard-sphere” interaction?*, Physical Review E, 66 (2002), p. 060501.
- [43] C. BÜCHEL, *Evolution and function of light harvesting proteins*, Journal of Plant Physiology, 172 (2015), pp. 62–75.
- [44] P. BUINING, Y. VELDHUIZEN, C. PATHMAMANOCHARAN, AND H. LEKKERKERKER, *Preparation of a non-aqueous dispersion of sterically stabilized boehmite rods*, Colloids and surfaces, 64 (1992), pp. 47–55.
- [45] J. BUITENHUIS, L. N. DONSELAAR, P. A. BUINING, A. STROOBANTS, AND H. N. LEKKERKERKER, *Phase separation of mixtures of colloidal boehmite rods and flexible polymer*, Journal of colloid and interface science, 175 (1995), pp. 46–56.
- [46] J. N. BUTLER, *Ionic equilibrium: solubility and pH calculations*, John Wiley & Sons, 1998.
- [47] A. I. CAMPBELL, V. J. ANDERSON, J. S. VAN DUIJNEVELDT, AND P. BARTLETT, *Dynamical arrest in attractive colloids: The effect of long-range repulsion*, Physical review letters, 94 (2005), p. 208301.
- [48] A. I. CAMPBELL AND P. BARTLETT, *Fluorescent hard-sphere polymer colloids for confocal microscopy*, Journal of Colloid and Interface Science, 256 (2002), pp. 325–330.
- [49] F. CARDINAUX, T. GIBAUD, A. STRADNER, AND P. SCHURTENBERGER, *Interplay between spinodal decomposition and glass formation in proteins exhibiting short-range attractions*, Physical Review Letters, 99 (2007), p. 118301.

- [50] M. CARPINETI AND M. GIGLIO, *Spinodal-type dynamics in fractal aggregation of colloidal clusters*, Physical review letters, 68 (1992), p. 3327.
- [51] M. E. CATES, M. FUCHS, K. KROY, W. C. POON, AND A. M. PUERTAS, *Theory and simulation of gelation, arrest and yielding in attracting colloids*, Journal of Physics: Condensed Matter, 16 (2004), p. S4861.
- [52] D. CHANDLER, *Introduction to modern statistical*, Mechanics. Oxford University Press, Oxford, UK, 5 (1987), p. 449.
- [53] D. E. CHANDLER AND R. W. ROBERSON, *Bioimaging: current concepts in light and electron microscopy*, (2009).
- [54] P. CHARBONNEAU, J. KURCHAN, G. PARISI, P. URBANI, AND F. ZAMPONI, *Glass and jamming transitions: From exact results to finite-dimensional descriptions*, Annual Review of Condensed Matter Physics, 8 (2017), pp. 265–288.
- [55] R. CHENG, J. LI, I. RÍOS DE ANDA, T. W. TAYLOR, M. A. FAERS, J. R. ANDERSON, A. M. SEDDON, AND C. P. ROYALL, *Protein–polymer mixtures in the colloid limit: Aggregation, sedimentation, and crystallization*, The Journal of Chemical Physics, 155 (2021), p. 114901.
- [56] S. S. COHEN, *The isolation and crystallization of plant viruses and other protein macro molecules by means of hydrophilic colloids*, Journal of Biological Chemistry, 144 (1942), pp. 353–362.
- [57] J. L. COLE, J. W. LARY, T. P. MOODY, AND T. M. LAUE, *Analytical ultracentrifugation: sedimentation velocity and sedimentation equilibrium*, Methods in cell biology, 84 (2008), pp. 143–179.
- [58] R. W. COLE, T. JINADASA, AND C. M. BROWN, *Measuring and interpreting point spread functions to determine confocal microscope resolution and ensure quality control*, Nature protocols, 6 (2011), pp. 1929–1941.
- [59] C. E. F. CORDOVA, *Structure formation in colloidal rod suspensions: experiments and computer simulations*, PhD thesis, University of Bristol, 2016.
- [60] T. COSGROVE, *Colloid science: principles, methods and applications*, John Wiley & Sons, 2010.
- [61] G. COUTURE, L. GRANADO, F. FANGET, B. BOUTEVIN, AND S. CAILLOL, *Limonene-based epoxy: Anhydride thermoset reaction study*, Molecules, 23 (2018), p. 2739.

- [62] J. J. CRASSOUS, M. SIEBENBÜRGER, M. BALLAUFF, M. DRECHSLER, O. HENRICH, AND M. FUCHS, *Thermosensitive core-shell particles as model systems for studying the flow behavior of concentrated colloidal dispersions*, The Journal of chemical physics, 125 (2006), p. 204906.
- [63] J. C. CROCKER AND D. G. GRIER, *Microscopic measurement of the pair interaction potential of charge-stabilized colloid*, Physical review letters, 73 (1994), p. 352.
- [64] R. L. DAVIDCHACK AND B. B. LAIRD, *Crystal structure and interaction dependence of the crystal-melt interfacial free energy*, Physical review letters, 94 (2005), p. 086102.
- [65] I. R. DE ANDA, A. COUTABLE-PENNARUN, C. BRASNETT, S. WHITELAM, A. SEDDON, J. RUSSO, J. R. ANDERSON, AND C. P. ROYALL, *Decorated networks of native proteins: nanomaterials with tunable mesoscopic domain size*, Soft Matter, 17 (2021), pp. 6873–6883.
- [66] K. DE HAAN, Z. S. BALLARD, Y. RIVENSON, Y. WU, AND A. OZCAN, *Resolution enhancement in scanning electron microscopy using deep learning*, Scientific reports, 9 (2019), pp. 1–7.
- [67] E. H. DE HOOG, W. K. KEGEL, A. VAN BLAADEREN, AND H. N. LEKKERKERKER, *Direct observation of crystallization and aggregation in a phase-separating colloid-polymer suspension*, Physical Review E, 64 (2001), p. 021407.
- [68] C. DE KRUIF, W. BRIELS, R. MAY, AND A. VRIJ, *Hard-sphere colloidal silica dispersions. the structure factor determined with sans*, Langmuir, 4 (1988), pp. 668–676.
- [69] C. DE KRUIF, P. ROUW, J. JANSSEN, AND A. VRIJ, *Hard sphere properties and crystalline packing of lyophilic silica colloids*, Le Journal de Physique Colloques, 46 (1985), pp. C3–295.
- [70] Á. V. DELGADO, F. GONZÁLEZ-CABALLERO, R. HUNTER, L. KOOPAL, AND J. LYKLEMA, *Measurement and interpretation of electrokinetic phenomena*, Journal of colloid and interface science, 309 (2007), pp. 194–224.
- [71] C. DELGADO, G. FRANCIS, AND D. FISHER, *The uses and properties of peg-linked proteins*, Critical reviews in therapeutic drug carrier systems, 9 (1992), p. 249–304.
- [72] U. DEMIRCI AND A. KHADEMHOSEINI, *Gels Handbook: Fundamentals, Properties, Applications (In 3 Volumes)*, World scientific, 2016.
- [73] B. DERJAGUIN AND L. LANDAU, *Stability theory of strongly charged lyophobic sols and of the adhesion of strongly charged particles in electrolyte solutions*, Acta Physicochim. URSS, 14 (1941), pp. 633–662.

-
- [74] C. J. DIBBLE, M. KOGAN, AND M. J. SOLOMON, *Structure and dynamics of colloidal depletion gels: Coincidence of transitions and heterogeneity*, Physical Review E, 74 (2006), p. 041403.
- [75] M. DIJKSTRA, R. VAN ROIJ, R. ROTH, AND A. FORTINI, *Effect of many-body interactions on the bulk and interfacial phase behavior of a model colloid-polymer mixture*, Physical Review E, 73 (2006), p. 041404.
- [76] A. D. DINSMORE, E. R. WEEKS, V. PRASAD, A. C. LEVITT, AND D. A. WEITZ, *Three-dimensional confocal microscopy of colloids*, Applied optics, 40 (2001), pp. 4152–4159.
- [77] Z. DOGIC AND S. FRADEN, *Smectic phase in a colloidal suspension of semiflexible virus particles*, Physical review letters, 78 (1997), p. 2417.
- [78] J. P. DOYE, D. J. WALES, AND R. S. BERRY, *The effect of the range of the potential on the structures of clusters*, The Journal of chemical physics, 103 (1995), pp. 4234–4249.
- [79] J. DRENTH, *Proceeds of the 2nd international-conference on protein crystal-growth, bischenberg, strasbourg, france, 19-25 july, 1987-concluding remarks*, 1988.
- [80] A. C. DUMETZ, A. M. CHOCKLA, E. W. KALER, AND A. M. LENHOFF, *Protein phase behavior in aqueous solutions: crystallization, liquid-liquid phase separation, gels, and aggregates*, Biophysical journal, 94 (2008), pp. 570–583.
- [81] K. C. DUONG-LY AND S. B. GABELLI, *Salting out of proteins using ammonium sulfate precipitation*, in Methods in enzymology, vol. 541, Elsevier, 2014, pp. 85–94.
- [82] J. C. DYRE, *Simple liquids’ quasiuniversality and the hard-sphere paradigm*, Journal of Physics: Condensed Matter, 28 (2016), p. 323001.
- [83] A. EINSTEIN, *Annalen der physik*, 17 (1905), pp. 549–560.
- [84] H. ESLAMI, P. SEDAGHAT, AND F. MÜLLER-PLATHE, *Local bond order parameters for accurate determination of crystal structures in two and three dimensions*, Physical Chemistry Chemical Physics, 20 (2018), pp. 27059–27068.
- [85] D. H. EVERETT, *Manual of symbols and terminology for physicochemical quantities and units, appendix ii: Definitions, terminology and symbols in colloid and surface chemistry*, Pure and Applied Chemistry, 31 (1972), pp. 577–638.
- [86] D. H. EVERETT, *Basic principles of colloid science*, Royal society of chemistry, 2007.
- [87] T. E. EVERHART AND R. THORNLEY, *Wide-band detector for micro-microampere low-energy electron currents*, Journal of scientific instruments, 37 (1960), p. 246.

- [88] D. FAN, R. LI, M. HE, X. LI, J. LI, J. WEN, Y. HU, Y. LI, Y. LI, L. GU, ET AL., *Review of refractive index-matching techniques of polymethyl methacrylate in flow field visualization experiments*, International Journal of Energy Research, 2023 (2023).
- [89] M. FASOLO AND P. SOLLICH, *Equilibrium phase behavior of polydisperse hard spheres*, Physical review letters, 91 (2003), p. 068301.
- [90] ———, *Fractionation effects in phase equilibria of polydisperse hard-sphere colloids*, Physical Review E, 70 (2004), p. 041410.
- [91] C. FERREIRO-CÓRDOVA, C. P. ROYALL, AND J. S. VAN DUIJNEVELDT, *Anisotropic viscoelastic phase separation in polydisperse hard rods leads to nonsticky gelation*, Proceedings of the National Academy of Sciences, 117 (2020), pp. 3415–3420.
- [92] L. FETTERS, N. HADJICHRISTIDIS, J. LINDNER, AND J. MAYS, *Molecular weight dependence of hydrodynamic and thermodynamic properties for well-defined linear polymers in solution*, Journal of physical and chemical reference data, 23 (1994), pp. 619–640.
- [93] R. P. FEYNMAN, *Statistical mechanics: a set of lectures*, CRC press, 2018.
- [94] L. FILION, M. HERMES, R. NI, AND M. DIJKSTRA, *Crystal nucleation of hard spheres using molecular dynamics, umbrella sampling, and forward flux sampling: A comparison of simulation techniques*, The Journal of chemical physics, 133 (2010), p. 244115.
- [95] L. FILION, R. NI, D. FRENKEL, AND M. DIJKSTRA, *Simulation of nucleation in almost hard-sphere colloids: The discrepancy between experiment and simulation persists*, The Journal of chemical physics, 134 (2011), p. 134901.
- [96] G. FLEER, M. C. STUART, J. M. SCHEUTJENS, T. COSGROVE, AND B. VINCENT, *Polymers at interfaces*, Springer Science & Business Media, 1993.
- [97] P. J. FLORY, *Principles of polymer chemistry*, Cornell university press, 1953.
- [98] G. FOFFI, C. DE MICHELE, F. SCIORTINO, AND P. TARTAGLIA, *Arrested phase separation in a short-ranged attractive colloidal system: A numerical study*, The Journal of chemical physics, 122 (2005), p. 224903.
- [99] G. FOFFI, G. D. MCCULLAGH, A. LAWLOR, E. ZACCARELLI, K. A. DAWSON, F. SCIORTINO, P. TARTAGLIA, D. PINI, AND G. STELL, *Phase equilibria and glass transition in colloidal systems with short-ranged attractive interactions: application to protein crystallization*, Physical Review E, 65 (2002), p. 031407.
- [100] C. FOUQUET, J.-F. GILLES, N. HECK, M. DOS SANTOS, R. SCHWARTZMANN, V. CANNAYA, M.-P. MOREL, R. S. DAVIDSON, A. TREMBLEAU, AND S. BOLTE, *Improving axial*

- resolution in confocal microscopy with new high refractive index mounting media*, PloS one, 10 (2015), p. e0121096.
- [101] S. FRADEN, G. MARET, D. CASPAR, AND R. B. MEYER, *Isotropic-nematic phase transition and angular correlations in isotropic suspensions of tobacco mosaic virus*, Physical review letters, 63 (1989), p. 2068.
- [102] M. H. FRANKE, *Experimentelle Untersuchung von Phasenübergängen im kolloidalen Modellsystem harter Kugeln*, PhD thesis, Mainz, Univ., Diss., 2014, 2014.
- [103] H. L. FRISCH AND J. L. LEBOWITZ, *The equilibrium theory of classical fluids: a lecture note and reprint volume*, WA Benjamin, 1964.
- [104] R. L. FROST, O. B. LOCOS, H. RUAN, AND J. T. KLOPROGGE, *Near-infrared and mid-infrared spectroscopic study of sepiolites and palygorskites*, Vibrational Spectroscopy, 27 (2001), pp. 1–13.
- [105] J. FUTAMI, M. KITAZOE, T. MAEDA, E. NUKUI, M. SAKAGUCHI, J. KOSAKA, M. MIYAZAKI, M. KOSAKA, H. TADA, M. SENO, ET AL., *Intracellular delivery of proteins into mammalian living cells by polyethylenimine-cationization*, Journal of bioscience and bioengineering, 99 (2005), pp. 95–103.
- [106] O. GALKIN AND P. G. VEKILOV, *Control of protein crystal nucleation around the metastable liquid–liquid phase boundary*, Proceedings of the National Academy of Sciences, 97 (2000), pp. 6277–6281.
- [107] U. GASSER, E. R. WEEKS, A. SCHOFIELD, P. PUSEY, AND D. WEITZ, *Real-space imaging of nucleation and growth in colloidal crystallization*, Science, 292 (2001), pp. 258–262.
- [108] A. GAST, C. HALL, AND W. RUSSEL, *Polymer-induced phase separations in nonaqueous colloidal suspensions*, Journal of Colloid and Interface Science, 96 (1983), pp. 251–267.
- [109] E. GASTEIGER, C. HOOGLAND, A. GATTIKER, M. R. WILKINS, R. D. APPEL, A. BAIROCH, ET AL., *Protein identification and analysis tools on the expasy server*, The proteomics protocols handbook, (2005), pp. 571–607.
- [110] A. GEORGE, Y. CHIANG, B. GUO, A. ARABSHAHI, Z. CAI, AND W. W. WILSON, *[6] second virial coefficient as predictor in protein crystal growth*, in Methods in enzymology, vol. 276, Elsevier, 1997, pp. 100–110.
- [111] A. GEORGE AND W. W. WILSON, *Predicting protein crystallization from a dilute solution property*, Acta Crystallographica Section D: Biological Crystallography, 50 (1994), pp. 361–365.

- [112] S. C. GILL AND P. H. VON HIPPEL, *Calculation of protein extinction coefficients from amino acid sequence data*, Analytical biochemistry, 182 (1989), pp. 319–326.
- [113] R. GIUSTETTO, F. X. LLABRÉS I XAMENA, G. RICCHIARDI, S. BORDIGA, A. DAMIN, R. GOBETTO, AND M. R. CHIEROTTI, *Maya blue: a computational and spectroscopic study*, The Journal of Physical Chemistry B, 109 (2005), pp. 19360–19368.
- [114] H. GLEITER, *Nanostructured materials: basic concepts and microstructure*, Acta materialia, 48 (2000), pp. 1–29.
- [115] P. GREENSPAN AND S. D. FOWLER, *Spectrofluorometric studies of the lipid probe, nile red.*, Journal of lipid research, 26 (1985), pp. 781–789.
- [116] C. HAAS AND J. DRENTH, *The protein- water phase diagram and the growth of protein crystals from aqueous solution*, The Journal of Physical Chemistry B, 102 (1998), pp. 4226–4232.
- [117] ———, *Understanding protein crystallization on the basis of the phase diagram*, Journal of crystal growth, 196 (1999), pp. 388–394.
- [118] M. HAGEN AND D. FRENKEL, *Determination of phase diagrams for the hard-core attractive yukawa system*, The Journal of chemical physics, 101 (1994), pp. 4093–4097.
- [119] D. HALL, R. ZHAO, I. DEHLSSEN, N. BLOOMFIELD, S. R. WILLIAMS, F. ARISAKA, Y. GOTO, AND J. A. CARVER, *Protein aggregate turbidity: Simulation of turbidity profiles for mixed-aggregation reactions*, Analytical biochemistry, 498 (2016), pp. 78–94.
- [120] K. R. HALL, *Another hard-sphere equation of state*, The Journal of Chemical Physics, 57 (1972), pp. 2252–2254.
- [121] J. E. HALLETT, F. TURCI, AND C. P. ROYALL, *Local structure in deeply supercooled liquids exhibits growing lengthscales and dynamical correlations*, Nature communications, 9 (2018), pp. 1–10.
- [122] A. HAMID, A. ARSHAD, S. MEHDI, M. QASIM, A. ULLAH, J. MOLINA, AND R. YAMAMOTO, *A numerical study of sedimentation of rod like particles using smooth profile method*, International Journal of Multiphase Flow, 127 (2020), p. 103263.
- [123] J.-P. HANSEN AND L. VERLET, *Phase transitions of the lennard-jones system*, physical Review, 184 (1969), p. 151.
- [124] J. HARLAND, S. HENDERSON, S. M. UNDERWOOD, AND W. VAN MEGEN, *Observation of accelerated nucleation in dense colloidal fluids of hard sphere particles*, Physical review letters, 75 (1995), p. 3572.

- [125] J. HARLAND AND W. VAN MEGEN, *Crystallization kinetics of suspensions of hard colloidal spheres*, Physical Review E, 55 (1997), p. 3054.
- [126] Y. HE, B. J. ACKERSON, W. VAN MEGEN, S. M. UNDERWOOD, AND K. SCHÄTZEL, *Dynamics of crystallization in hard-sphere suspensions*, Physical Review E, 54 (1996), p. 5286.
- [127] G. T. HERMANSON, *Chapter 3 - the reactions of bioconjugation*, in Bioconjugate Techniques (Third Edition), G. T. Hermanson, ed., Academic Press, third edition ed., 2013, pp. 229–258.
- [128] W. M. HESTON JR, E. J. HENNELLY, AND C. P. SMYTH, *Dielectric constants, viscosities, densities, refractive indices and dipole moment calculations for some organic halides*¹, Journal of the American Chemical Society, 72 (1950), pp. 2071–2075.
- [129] A. HEYMANN, A. STIPP, C. SINN, AND T. PALBERG, *Observation of oriented close-packed lattice planes in polycrystalline hard-sphere solids*, Journal of colloid and interface science, 207 (1998), pp. 119–127.
- [130] P. C. HIEMENZ AND R. RAJAGOPALAN, *Principles of Colloid and Surface Chemistry, revised and expanded*, CRC press, 2016.
- [131] M. P. HOBSON, G. P. EFSTATHIOU, AND A. N. LASENBY, *General relativity: an introduction for physicists*, Cambridge University Press, 2006.
- [132] R. M. HÖFER, *Sedimentation of particle suspensions in Stokes flows*, PhD thesis, Universitäts-und Landesbibliothek Bonn, 2020.
- [133] F. HOFMEISTER, *Zur lehre von der wirkung der salze: zweite mittheilung*, (1888).
- [134] W. G. HOOVER AND F. H. REE, *Melting transition and communal entropy for hard spheres*, The Journal of Chemical Physics, 49 (1968), pp. 3609–3617.
- [135] L. HU, R. ZHANG, AND Q. CHEN, *Synthesis and assembly of nanomaterials under magnetic fields*, Nanoscale, 6 (2014), pp. 14064–14105.
- [136] X. HU, P. CEBE, A. S. WEISS, F. OMENETTO, AND D. L. KAPLAN, *Protein-based composite materials*, Materials today, 15 (2012), pp. 208–215.
- [137] R. J. HUNTER, *Foundations of colloid science*, Oxford university press, 2001.
- [138] A.-P. HYNINEN AND M. DIJKSTRA, *Phase diagrams of hard-core repulsive yukawa particles*, Physical Review E, 68 (2003), p. 021407.
- [139] S. IACOPINI, T. PALBERG, AND H. J. SCHÖPE, *Ripening-dominated crystallization in polydisperse hard-sphere-like colloids*, Physical Review E, 79 (2009), p. 010601.

- [140] S. M. ILETT, A. ORROCK, W. POON, AND P. PUSEY, *Phase behavior of a model colloid-polymer mixture*, Physical Review E, 51 (1995), p. 1344.
- [141] J. N. IMMINK, J. E. MARIS, J. J. CRASSOUS, J. STENHAMMAR, AND P. SCHURTENBERGER, *Reversible formation of thermoresponsive binary particle gels with tunable structural and mechanical properties*, ACS nano, 13 (2019), pp. 3292–3300.
- [142] J. N. ISRAELACHVILI, *Intermolecular and surface forces*, Academic press, 2011.
- [143] V. JAMALI, N. BEHABTU, B. SENYUK, J. A. LEE, I. I. SMALYUKH, P. VAN DER SCHOOT, AND M. PASQUALI, *Experimental realization of crossover in shape and director field of nematic tactoids*, Physical Review E, 91 (2015), p. 042507.
- [144] J. JANIN, R. P. BAHADUR, AND P. CHAKRABARTI, *Protein–protein interaction and quaternary structure*, Quarterly reviews of biophysics, 41 (2008), pp. 133–180.
- [145] M. JENKINS, *Quantitative confocal microscopy of dense colloidal systems*, (2006).
- [146] M. C. JENKINS AND S. U. EGELHAAF, *Confocal microscopy of colloidal particles: towards reliable, optimum coordinates*, Advances in colloid and interface science, 136 (2008), pp. 65–92.
- [147] E. JONES, T. OLIPHANT, P. PETERSON, ET AL., *Scipy: Open source scientific tools for python*, (2001).
- [148] J. JONES, J. SANDERS, AND E. SEGNIT, *Structure of opal*, Nature, 204 (1964), pp. 990–991.
- [149] R. A. L. JONES, R. A. JONES, R. JONES, ET AL., *Soft condensed matter*, vol. 6, Oxford University Press, 2002.
- [150] M. KAISHIMA, J. ISHII, T. MATSUNO, N. FUKUDA, AND A. KONDO, *Expression of varied gfps in saccharomyces cerevisiae: codon optimization yields stronger than expected expression and fluorescence intensity*, Scientific reports, 6 (2016), pp. 1–15.
- [151] M. KARG, T. HELLWEG, AND P. MULVANEY, *Self-assembly of tunable nanocrystal superlattices using poly-(nipam) spacers*, Advanced Functional Materials, 21 (2011), pp. 4668–4676.
- [152] D. KASHCHIEV, *Chapter 6 - properties of clusters*, in Nucleation, D. Kashchiev, ed., Butterworth-Heinemann, Oxford, 2000, pp. 70–82.
- [153] S. KATHIRVEL, S. MURUGESAN, AND A. MARATHAKAM, *Recent updates on methods, applications, and practical uses of scanning electron microscopy in various life sciences*, in Microscopic Techniques for the Non-Expert, Springer, 2022, pp. 187–199.

-
- [154] K. F. KELTON, *Crystal nucleation in liquids and glasses*, in Solid state physics, vol. 45, Elsevier, 1991, pp. 75–177.
- [155] S. KETZETZI, J. RUSSO, AND D. BONN, *Crystal nucleation in sedimenting colloidal suspensions*, The Journal of chemical physics, 148 (2018), p. 064901.
- [156] D. J. KINNING AND E. L. THOMAS, *Hard-sphere interactions between spherical domains in diblock copolymers*, Macromolecules, 17 (1984), pp. 1712–1718.
- [157] T. KIRKPATRICK AND D. THIRUMALAI, *Random solutions from a regular density functional hamiltonian: a static and dynamical theory for the structural glass transition*, Journal of Physics A: Mathematical and General, 22 (1989), p. L149.
- [158] T. KIRKPATRICK AND P. WOLYNES, *Stable and metastable states in mean-field potts and structural glasses*, Physical Review B, 36 (1987), p. 8552.
- [159] T. R. KIRKPATRICK, D. THIRUMALAI, AND P. G. WOLYNES, *Scaling concepts for the dynamics of viscous liquids near an ideal glassy state*, Physical Review A, 40 (1989), p. 1045.
- [160] S. KIRSCH, A. DOERK, E. BARTSCH, H. SILLESCU, K. LANDFESTER, H. W. SPIESS, AND W. MAECHTLE, *Synthesis and characterization of highly cross-linked, monodisperse core-shell and inverted core-shell colloidal particles. polystyrene / poly (tert-butyl acrylate) core-shell and inverse core-shell particles*, Macromolecules, 32 (1999), pp. 4508–4518.
- [161] C. L. KLIX, K.-I. MURATA, H. TANAKA, S. R. WILLIAMS, A. MALINS, AND C. P. ROYALL, *Novel kinetic trapping in charged colloidal clusters due to self-induced surface charge organization*, Scientific reports, 3 (2013), pp. 1–6.
- [162] T. E. KODGER, R. E. GUERRA, AND J. SPRAKEL, *Precise colloids with tunable interactions for confocal microscopy*, Scientific reports, 5 (2015), pp. 1–10.
- [163] A. KRALL AND D. WEITZ, *Internal dynamics and elasticity of fractal colloidal gels*, Physical review letters, 80 (1998), p. 778.
- [164] W. KUANG, G. A. FACEY, C. DETELLIER, B. CASAL, J. M. SERRATOSA, AND E. RUIZ-HITZKY, *Nanostructured hybrid materials formed by sequestration of pyridine molecules in the tunnels of sepiolite*, Chemistry of Materials, 15 (2003), pp. 4956–4967.
- [165] R. KURITA AND E. R. WEEKS, *Experimental study of random-close-packed colloidal particles*, Physical review E, 82 (2010), p. 011403.
- [166] B. B. LAIRD AND R. L. DAVIDCHACK, *Direct calculation of the crystal- melt interfacial free energy via molecular dynamics computer simulation*, 2005.

- [167] A. LE GRAND AND G. PETEKIDIS, *Effects of particle softness on the rheology and yielding of colloidal glasses*, Rheologica Acta, 47 (2008), pp. 579–590.
- [168] E. S. LEACH, A. HOPKINSON, K. FRANKLIN, AND J. S. VAN DUIJNEVELDT, *Nonaqueous suspensions of laponite and montmorillonite*, Langmuir, 21 (2005), pp. 3821–3830.
- [169] R. LEBERMAN, *The isolation of plant viruses by means of “simple” coacervates*, Virology, 30 (1966), pp. 341–347.
- [170] N. I. LEOVKA, *Aggregation of charged colloidal particles*, Polyelectrolyte Complexes in the Dispersed and Solid State I, (2012), pp. 57–96.
- [171] W. LECHNER AND C. DELLAGO, *Accurate determination of crystal structures based on averaged local bond order parameters*, The Journal of chemical physics, 129 (2008), p. 114707.
- [172] H. LEKKERKERKER AND G. VROEGE, *Lyotropic colloidal and macromolecular liquid crystals*, Philosophical Transactions of the Royal Society of London. Series A: Physical and Engineering Sciences, 344 (1993), pp. 419–440.
- [173] H. N. LEKKERKERKER, W.-K. POON, P. N. PUSEY, A. STROOBANTS, AND P. . WARREN, *Phase behaviour of colloid+ polymer mixtures*, EPL (Europhysics Letters), 20 (1992), p. 559.
- [174] H. N. LEKKERKERKER AND R. TUINIER, *Colloids and the Depletion Interaction*, vol. 833, Springer, 2011.
- [175] M. LEUNISSEN, *Manipulating colloids with charges and electric fields*, PhD thesis, Utrecht University, 2007.
- [176] V. LEVI AND F. L. G. FLECHA, *Reversible fast-dimerization of bovine serum albumin detected by fluorescence resonance energy transfer*, Biochimica et Biophysica Acta (BBA)-Proteins and Proteomics, 1599 (2002), pp. 141–148.
- [177] Y. LI, A. M. SIERRA, H.-W. AI, AND R. E. CAMPBELL, *Identification of sites within a monomeric red fluorescent protein that tolerate peptide insertion and testing of corresponding circular permutations*, Photochemistry and photobiology, 84 (2008), pp. 111–119.
- [178] F. LI-IN-ON, B. VINCENT, AND F. WAITE, *Stability of sterically stabilized dispersions at high polymer concentrations*, ACS Publications, 1975.
- [179] H. LIU, S. K. KUMAR, AND F. SCIORTINO, *Vapor-liquid coexistence of patchy models: Relevance to protein phase behavior*, The Journal of chemical physics, 127 (2007), p. 084902.

- [180] J. LIU AND B. XU, *A comparative study on texture, gelatinisation, retrogradation and potential food application of binary gels made from selected starches and edible gums*, Food chemistry, 296 (2019), pp. 100–108.
- [181] J. LONG, D. OSMOND, AND B. VINCENT, *The equilibrium aspects of weak flocculation*, Journal of Colloid and Interface Science, 42 (1973), pp. 545–553.
- [182] L. LÓPEZ-FLORES, H. RUÍZ-ESTRADA, M. CHÁVEZ-PÁEZ, AND M. MEDINA-NOYOLA, *Dynamic equivalences in the hard-sphere dynamic universality class*, Physical Review E, 88 (2013), p. 042301.
- [183] H. LÖWEN, T. PALBERG, AND R. SIMON, *Dynamical criterion for freezing of colloidal liquids*, Physical review letters, 70 (1993), p. 1557.
- [184] P. J. LU, E. ZACCARELLI, F. CIULLA, A. B. SCHOFIELD, F. SCIORTINO, AND D. A. WEITZ, *Gelation of particles with short-range attraction*, Nature, 453 (2008), pp. 499–503.
- [185] W. LUCK, M. Klier, AND H. WESSLAU, *Kristallisation übermolekularer bausteine*, Naturwissenschaften, 50 (1963), pp. 485–494.
- [186] Q. LUO, C. HOU, Y. BAI, R. WANG, AND J. LIU, *Protein assembly: versatile approaches to construct highly ordered nanostructures*, Chemical Reviews, 116 (2016), pp. 13571–13632.
- [187] F. LUPI, L. GENTILE, D. GABRIELE, S. MAZZULLA, N. BALDINO, AND B. DE CINDIO, *Olive oil and hyperthermal water bigels for cosmetic uses*, Journal of colloid and interface science, 459 (2015), pp. 70–78.
- [188] H.-C. MAHLER, W. FRIESS, U. GRAUSCHOPF, AND S. KIESE, *Protein aggregation: pathways, induction factors and analysis*, Journal of pharmaceutical sciences, 98 (2009), pp. 2909–2934.
- [189] A. MALINS, *A Structural Approach to Glassy Systems*, PhD thesis, University of Bristol, 2013.
- [190] A. MALINS, S. R. WILLIAMS, J. EGGERS, AND C. P. ROYALL, *Identification of structure in condensed matter with the topological cluster classification*, The Journal of chemical physics, 139 (2013), p. 234506.
- [191] J. D. MARTIN, C. L. KEARY, T. A. THORNTON, M. P. NOVOTNAK, J. W. KNUTSON, AND J. C. FOLMER, *Metallotropic liquid crystals formed by surfactant templating of molten metal halides*, Nature materials, 5 (2006), pp. 271–275.
- [192] S.-C. MAU AND D. A. HUSE, *Stacking entropy of hard-sphere crystals*, Physical Review E, 59 (1999), p. 4396.

- [193] J. J. McMANUS, *Protein Self-Assembly*, Springer, 2019.
- [194] J. J. McMANUS, P. CHARBONNEAU, E. ZACCARELLI, AND N. ASHERIE, *The physics of protein self-assembly*, Current opinion in colloid & interface science, 22 (2016), pp. 73–79.
- [195] W. G. McMILLAN JR AND J. E. MAYER, *The statistical thermodynamics of multicomponent systems*, The Journal of Chemical Physics, 13 (1945), pp. 276–305.
- [196] A. MCPHERSON AND B. CUDNEY, *Optimization of crystallization conditions for biological macromolecules*, Acta Crystallographica Section F: Structural Biology Communications, 70 (2014), pp. 1445–1467.
- [197] R. MEHVAR, *Modulation of the pharmacokinetics and pharmacodynamics of proteins by polyethylene glycol conjugation*, (2000).
- [198] E. J. MEIJER AND F. EL AZHAR, *Novel procedure to determine coexistence lines by computer simulation. application to hard-core yukawa model for charge-stabilized colloids*, The Journal of chemical physics, 106 (1997), pp. 4678–4683.
- [199] M. MINSKY, *Microscopy apparatus us patent 3013467*, USP Office, Ed. US, 658 (1961).
- [200] A. MOHRAZ AND M. J. SOLOMON, *Gelation and internal dynamics of colloidal rod aggregates*, Journal of colloid and interface science, 300 (2006), pp. 155–162.
- [201] A. MOURCHID AND P. LEVITZ, *Long-term gelation of laponite aqueous dispersions*, Physical Review E, 57 (1998), p. R4887.
- [202] D. P. MYATT, L. HATTER, S. E. ROGERS, A. E. TERRY, AND L. A. CLIFTON, *Monomeric green fluorescent protein as a protein standard for small angle scattering*, Biomedical Spectroscopy and Imaging, 6 (2017), pp. 123–134.
- [203] M. H. NADA, *Baoj microbiology scanning electron microscopy*, 2015.
- [204] N. NAKAJIMA AND Y. IKADA, *Mechanism of amide formation by carbodiimide for bioconjugation in aqueous media*, Bioconjugate chemistry, 6 (1995), pp. 123–130.
- [205] S. NGARIZE, A. ADAMS, AND N. HOWELL, *A comparative study of heat and high pressure induced gels of whey and egg albumen proteins and their binary mixtures*, Food Hydrocolloids, 19 (2005), pp. 984–996.
- [206] T. NICOLAI AND S. COCARD, *Light scattering study of the dispersion of laponite*, Langmuir, 16 (2000), pp. 8189–8193.
- [207] M. G. NORO AND D. FRENKEL, *Extended corresponding-states behavior for particles with variable range attractions*, The Journal of Chemical Physics, 113 (2000), pp. 2941–2944.

- [208] NOVAGEN, *pet system manual*.
<https://research.fredhutch.org/content/dam/stripe/hahn/methods/biochem/pet.pdf>.
- [209] H. NYQUIST, *Certain factors affecting telegraph speed*, Transactions of the American Institute of Electrical Engineers, 43 (1924), pp. 412–422.
- [210] ———, *Certain topics in telegraph transmission theory*, Transactions of the American Institute of Electrical Engineers, 47 (1928), pp. 617–644.
- [211] H. OHSHIMA, *A simple expression for henry’s function for the retardation effect in electrophoresis of spherical colloidal particles*, Journal of Colloid and Interface Science, 168 (1994), pp. 269–271.
- [212] H. V. OLPHEN ET AL., *An introduction to clay colloid chemistry, for clay technologists, geologists, and soil scientists*, no. 2nd edition, 1977.
- [213] L. ONSAGER, *Theories of concentrated electrolytes*, Chemical Reviews, 13 (1933), pp. 73–89.
- [214] ———, *The effects of shape on the interaction of colloidal particles*, Annals of the New York Academy of Sciences, 51 (1949), pp. 627–659.
- [215] H. OTSUKA, Y. NAGASAKI, AND K. KATAOKA, *Pegylated nanoparticles for biological and pharmaceutical applications*, Advanced drug delivery reviews, 64 (2012), pp. 246–255.
- [216] K. PAL AND I. BANERJEE, *Polymeric gels: characterization, properties and biomedical applications*, Woodhead Publishing, 2018.
- [217] T. PALBERG, *Crystallization kinetics of repulsive colloidal spheres*, Journal of Physics: Condensed Matter, 11 (1999), p. R323.
- [218] ———, *Crystallization kinetics of colloidal model suspensions: recent achievements and new perspectives*, Journal of Physics: Condensed Matter, 26 (2014), p. 333101.
- [219] T. PALBERG, E. BARTSCH, R. BEYER, M. HOFMANN, N. LORENZ, J. MARQUIS, R. NIU, AND T. OKUBO, *To make a glass—avoid the crystal*, Journal of Statistical Mechanics: Theory and Experiment, 2016 (2016), p. 074007.
- [220] A. PAREDES, *Microscopy | transmission electron microscopy*, in Encyclopedia of Food Microbiology (Second Edition), C. A. Batt and M. L. Tortorello, eds., Academic Press, Oxford, second edition ed., 2014, pp. 711–720.
- [221] G. PARISI AND F. ZAMPONI, *Mean-field theory of hard sphere glasses and jamming*, Reviews of Modern Physics, 82 (2010), p. 789.

- [222] C. PATHMAMANOCHARAN, *Preparation of monodisperse polyisobutene grafted silica dispersion*, Colloids and surfaces, 34 (1988), pp. 81–88.
- [223] S. PAULIN AND B. J. ACKERSON, *Observation of a phase transition in the sedimentation velocity of hard spheres*, Physical review letters, 64 (1990), p. 2663.
- [224] J. PAWLEY, *Handbook of biological confocal microscopy*, vol. 236, Springer Science & Business Media, 2006.
- [225] J. A. PELESKO, *Self assembly: the science of things that put themselves together*, Chapman and Hall/CRC, 2007.
- [226] J. K. PERCUS AND G. J. YEVICK, *Analysis of classical statistical mechanics by means of collective coordinates*, Physical Review, 110 (1958), p. 1.
- [227] J. PERRIN, *Mouvement brownien et réalité moléculaire*, (1909).
- [228] T. PETERS JR, *All about albumin: biochemistry, genetics, and medical applications*, Academic press, 1995.
- [229] K. N. PHAM, A. M. PUERTAS, J. BERGENHOLTZ, S. U. EGELHAAF, A. MOUSSAID, P. N. PUSEY, A. B. SCHOFIELD, M. E. CATES, M. FUCHS, AND W. C. POON, *Multiple glassy states in a simple model system*, Science, 296 (2002), pp. 104–106.
- [230] S.-E. PHAN, W. B. RUSSEL, Z. CHENG, J. ZHU, P. M. CHAIKIN, J. H. DUNSMUIR, AND R. H. OTTEWILL, *Phase transition, equation of state, and limiting shear viscosities of hard sphere dispersions*, Physical Review E, 54 (1996), p. 6633.
- [231] R. PIAZZA, *Interactions and phase transitions in protein solutions*, Current opinion in colloid & interface science, 5 (2000), pp. 38–43.
- [232] —, *Settled and unsettled issues in particle settling*, Reports on Progress in Physics, 77 (2014), p. 056602.
- [233] W. POON, *Crystallization of globular proteins*, Physical Review E, 55 (1997), p. 3762.
- [234] —, *The physics of a model colloid–polymer mixture*, Journal of Physics: Condensed Matter, 14 (2002), p. R859.
- [235] W. C. POON, *Colloidal glasses*, Mrs bulletin, 29 (2004), pp. 96–99.
- [236] W. C. POON, L. STARRS, S. MEEKER, A. MOUSSAID, R. M. EVANS, P. PUSEY, AND M. ROBINS, *Delayed sedimentation of transient gels in colloid–polymer mixtures: dark-field observation, rheology and dynamic light scattering studies*, Faraday Discussions, 112 (1999), pp. 143–154.

-
- [237] W. C. POON, E. R. WEEKS, AND C. P. ROYALL, *On measuring colloidal volume fractions*, *Soft matter*, 8 (2012), pp. 21–30.
- [238] F. G. PRENDERGAST AND K. G. MANN, *Chemical and physical properties of aequorin and the green fluorescent protein isolated from aequorea forskalea*, *Biochemistry*, 17 (1978), pp. 3448–3453.
- [239] N. PUECH, E. GRELET, P. POULIN, C. BLANC, AND P. VAN DER SCHOOT, *Nematic droplets in aqueous dispersions of carbon nanotubes*, *Physical Review E*, 82 (2010), p. 020702.
- [240] P. PUSEY, *The effect of polydispersity on the crystallization of hard spherical colloids*, *Journal de physique*, 48 (1987), pp. 709–712.
- [241] P. N. PUSEY AND W. VAN MEGEN, *Phase behaviour of concentrated suspensions of nearly hard colloidal spheres*, *Nature*, 320 (1986), pp. 340–342.
- [242] L. QU, C. WU, AND L. ZOU, *3d dense separated convolution module for volumetric medical image analysis*, *Applied Sciences*, 10 (2020), p. 485.
- [243] M. QUINN, N. GNAN, S. JAMES, A. NINARELLO, F. SCIORTINO, E. ZACCARELLI, AND J. MCMANUS, *How fluorescent labelling alters the solution behaviour of proteins*, *Physical Chemistry Chemical Physics*, 17 (2015), pp. 31177–31187.
- [244] J. RAYA, J. HIRSCHINGER, S. OVARLEZ, F. GIULIERI, A.-M. CHAZE, AND F. DELAMARE, *Insertion of indigo molecules in the sepiolite structure as evidenced by 1 h–29si heteronuclear correlation spectroscopy*, *Physical chemistry chemical physics*, 12 (2010), pp. 14508–14514.
- [245] L. REIMER, *Transmission electron microscopy: physics of image formation and microanalysis*, vol. 36, Springer, 2013.
- [246] H. REISS AND R. K. BOWLES, *Some fundamental statistical mechanical relations concerning physical clusters of interest to nucleation theory*, *The Journal of chemical physics*, 111 (1999), pp. 7501–7504.
- [247] D. RICKWOOD, *Centrifugation: a practical approach*, no. 543.083 RIC 1984. CIMMYT, 1984.
- [248] I. RIOS DE ANDA, *Self-assembly of multiple soft matter systems*, PhD thesis, University of Bristol, 2019.
- [249] F. ROOSEN-RUNGE, B. S. HECK, F. ZHANG, O. KOHLBACHER, AND F. SCHREIBER, *Interplay of ph and binding of multivalent metal ions: charge inversion and reentrant condensation in protein solutions*, *The Journal of Physical Chemistry B*, 117 (2013), pp. 5777–5787.

- [250] P. W. ROUW, A. WOUTERSEN, B. ACKERSON, AND C. DE KRUIF, *Adhesive hard sphere dispersions: V. observation of spinodal decomposition in a colloidal dispersion*, Physica A: Statistical Mechanics and its Applications, 156 (1989), pp. 876–898.
- [251] C. ROYALL, M. LEUNISSEN, AND A. VAN BLAADEREN, *A new colloidal model system to study long-range interactions quantitatively in real space*, Journal of Physics: Condensed Matter, 15 (2003), p. S3581.
- [252] C. ROYALL, R. VAN ROIJ, AND A. VAN BLAADEREN, *Extended sedimentation profiles in charged colloids: the gravitational length, entropy, and electrostatics*, Journal of Physics: Condensed Matter, 17 (2005), p. 2315.
- [253] C. P. ROYALL, *The behaviour of silica in matt water-based lacquers*, PhD thesis, University of Cambridge, 2000.
- [254] C. P. ROYALL, *Hunting mermaids in real space: Known knowns, known unknowns and unknown unknowns*, Soft Matter, 14 (2018), pp. 4020–4028.
- [255] C. P. ROYALL, J. EGGERS, A. FURUKAWA, AND H. TANAKA, *Probing colloidal gels at multiple length scales: The role of hydrodynamics*, Physical review letters, 114 (2015), p. 258302.
- [256] C. P. ROYALL, M. A. FAERS, S. L. FUSSELL, AND J. E. HALLETT, *Real space analysis of colloidal gels: Triumphs, challenges and future directions*, Journal of Physics: Condensed Matter, 33 (2021), p. 453002.
- [257] C. P. ROYALL, M. E. LEUNISSEN, A.-P. HYNINEN, M. DIJKSTRA, AND A. VAN BLAADEREN, *Re-entrant melting and freezing in a model system of charged colloids*, The Journal of chemical physics, 124 (2006), p. 244706.
- [258] C. P. ROYALL, W. C. POON, AND E. R. WEEKS, *In search of colloidal hard spheres*, Soft Matter, 9 (2013), pp. 17–27.
- [259] C. P. ROYALL AND S. R. WILLIAMS, *The role of local structure in dynamical arrest*, Physics Reports, 560 (2015), pp. 1–75.
- [260] C. P. ROYALL, S. R. WILLIAMS, AND H. TANAKA, *Vitrification and gelation in sticky spheres*, The Journal of chemical physics, 148 (2018), p. 044501.
- [261] E. RUIZ-HITZKY, *Molecular access to intracrystalline tunnels of sepiolite basis of a presentation given at materials discussion no. 3, 24–26 september 2000, university of cambridge, uk.*, Journal of Materials Chemistry, 11 (2001), pp. 86–91.
- [262] W. B. RUSSEL, W. RUSSEL, D. A. SAVILLE, AND W. R. SCHOWALTER, *Colloidal dispersions*, Cambridge university press, 1991.

- [263] J. RUSSO, A. C. MAGGS, D. BONN, AND H. TANAKA, *The interplay of sedimentation and crystallization in hard-sphere suspensions*, *Soft Matter*, 9 (2013), pp. 7369–7383.
- [264] G. SANDI, R. WINANS, S. SEIFERT, AND K. CARRADO, *In situ saxs studies of the structural changes of sepiolite clay and sepiolite- carbon composites with temperature*, *Chemistry of materials*, 14 (2002), pp. 739–742.
- [265] J. SANTAREN, J. SANZ, AND E. RUIZ-HITZKY, *Structural fluorine in sepiolite*, *Clays and Clay Minerals*, 38 (1990), pp. 63–68.
- [266] S. SAVENKO AND M. DIJKSTRA, *Phase behavior of a suspension of colloidal hard rods and nonadsorbing polymer*, *The Journal of chemical physics*, 124 (2006), p. 234902.
- [267] K. SCHÄTZEL AND B. J. ACKERSON, *Density fluctuations during crystallization of colloids*, *Physical Review E*, 48 (1993), p. 3766.
- [268] L. SCHERMELLEH, R. HEINTZMANN, AND H. LEONHARDT, *A guide to super-resolution fluorescence microscopy*, *Journal of Cell Biology*, 190 (2010), pp. 165–175.
- [269] T. SCHILLING, S. DOROSZ, H. J. SCHÖPE, AND G. OPLETAL, *Crystallization in suspensions of hard spheres: a monte carlo and molecular dynamics simulation study*, *Journal of Physics: Condensed Matter*, 23 (2011), p. 194120.
- [270] R. SCHLEIF, *Regulation of the l-arabinose operon of escherichia coli*, *Trends in genetics*, 16 (2000), pp. 559–565.
- [271] A. C. SCHLOSS, D. M. WILLIAMS, AND L. J. REGAN, *Protein-based hydrogels for tissue engineering*, *Protein-Based Engineered Nanostructures*, (2016), pp. 167–177.
- [272] J. W. SCHMELZER, *On the determination of the kinetic pre-factor in classical nucleation theory*, *Journal of non-crystalline solids*, 356 (2010), pp. 2901–2907.
- [273] W. SCHUMANN, *Plasmids current research and future trends*, 2008.
- [274] R. P. SEAR, *Nucleation: theory and applications to protein solutions and colloidal suspensions*, *Journal of Physics: Condensed Matter*, 19 (2007), p. 033101.
- [275] H. SEDGWICK, S. EGELHAAF, AND W. POON, *Clusters and gels in systems of sticky particles*, *Journal of Physics: Condensed Matter*, 16 (2004), p. S4913.
- [276] S. SEIFFERT, E. KUMACHEVA, O. OKAY, M. ANTHAMATTEN, M. CHAU, P. Y. DANKERS, B. W. GREENLAND, W. HAYES, P. LI, R. LIU, ET AL., *Supramolecular polymer networks and gels*, vol. 268, Springer, 2015.

- [277] H. SENFF AND W. RICHTERING, *Temperature sensitive microgel suspensions: Colloidal phase behavior and rheology of soft spheres*, The Journal of chemical physics, 111 (1999), pp. 1705–1711.
- [278] G. SETH ROBERTS, T. A. WOOD, W. J. FRITH, AND P. BARTLETT, *Direct measurement of the effective charge in nonpolar suspensions by optical tracking of single particles*, The Journal of chemical physics, 126 (2007), p. 194503.
- [279] A. SHAKEEL, F. R. LUPI, D. GABRIELE, N. BALDINO, AND B. DE CINDIO, *Bigels: A unique class of materials for drug delivery applications*, Soft Materials, 16 (2018), pp. 77–93.
- [280] C. E. SHANNON, *Communication in the presence of noise*, Proceedings of the IRE, 37 (1949), pp. 10–21.
- [281] P. SHARMA, *Self-assembly of colloidal particles*, Resonance, 23 (2018), pp. 263–275.
- [282] D. J. SHAW, *Introduction to colloid and surface chemistry*, Butterworths, 1980.
- [283] O. SHIMOMURA, F. H. JOHNSON, AND Y. SAIGA, *Extraction, purification and properties of aequorin, a bioluminescent protein from the luminous hydromedusan, aequorea*, Journal of cellular and comparative physiology, 59 (1962), pp. 223–239.
- [284] A. SINGER, E. G. HUERTOS, AND E. GALAN, *Developments in Palygorskite-sepiolite Research: A new outlook on these nanomaterials*, vol. 3, Elsevier, 2011.
- [285] C. SINN, A. HEYMANN, A. STIPP, AND T. PALBERG, *Solidification kinetics of hard-sphere colloidal suspensions*, Trends in Colloid and Interface Science XV, (2001), pp. 266–275.
- [286] M. SKOGE, A. DONEV, F. H. STILLINGER, AND S. TORQUATO, *Packing hyperspheres in high-dimensional euclidean spaces*, Physical Review E, 74 (2006), p. 041127.
- [287] D. A. SKOOG, D. M. WEST, F. J. HOLLER, AND S. R. CROUCH, *Fundamentals of analytical chemistry*, Cengage learning, 2013.
- [288] T. SLUCKIN, D. DUNMUR, AND H. STEGEMEYER, *Crystals that flow*, Taylor & Francis London, 2004.
- [289] C. SMITS, W. BRIELS, J. DHONT, AND H. LEKKERKERKER, *Influence of the stabilizing coating on the rate of crystallization of colloidal systems*, Trends in Colloid and Interface Science III, (1989), pp. 287–292.
- [290] M. J. SOLOMON AND P. T. SPICER, *Microstructural regimes of colloidal rod suspensions, gels, and glasses*, Soft Matter, 6 (2010), pp. 1391–1400.
- [291] B. SRI, V. ASHOK, AND C. ARKENDU, *As a review on hydrogels as drug delivery in the pharmaceutical field*, Int J Pharm Chem Sci, 1 (2012), pp. 642–61.

- [292] S. V. I. (SVI), *Huygens professional*.
<https://svi.nl/Huygens-Professional>.
- [293] G. SWIEGERS, *Assemblies and self-assembly*, ChemInform, 35 (2004).
- [294] T. TADROS, *General principles of colloid stability and the role of surface forces*, 2007.
- [295] ———, *Electrostatic and steric stabilization of colloidal dispersions*, Electrical phenomena at interfaces and biointerfaces, (2012), pp. 153–172.
- [296] J. TAFFS AND C. PATRICK ROYALL, *The role of fivefold symmetry in suppressing crystallization*, Nature communications, 7 (2016), pp. 1–7.
- [297] J. TAFFS, S. R. WILLIAMS, H. TANAKA, AND C. P. ROYALL, *Structure and kinetics in the freezing of nearly hard spheres*, Soft Matter, 9 (2013), pp. 297–305.
- [298] P. TAN, N. XU, AND L. XU, *Visualizing kinetic pathways of homogeneous nucleation in colloidal crystallization*, Nature Physics, 10 (2014), pp. 73–79.
- [299] P. R. TEN WOLDE, *Numerical study of pathways for homogeneous nucleation*, PhD thesis, University of Amsterdam, 1998.
- [300] K. TERAOKA AND J. W. MAYS, *On-line measurement of molecular weight and radius of gyration of polystyrene in a good solvent and in a theta solvent measured with a two-angle light scattering detector*, European polymer journal, 40 (2004), pp. 1623–1627.
- [301] I. TERAOKA, *Polymer solutions: an introduction to physical properties*, (2002).
- [302] G. TIAN, G. HAN, F. WANG, AND J. LIANG, *Sepiolite nanomaterials: structure, properties and functional applications*, in Nanomaterials from Clay Minerals, Elsevier, 2019, pp. 135–201.
- [303] S. TIBBITS, *Design to self-assembly*, Architectural Design, 82 (2012), pp. 68–73.
- [304] J. A. TITUS, R. HAUGLAND, S. O. SHARROW, AND D. M. SEGAL, *Texas red, a hydrophilic, red-emitting flourophore for use with flourescein in dual parameter flow microfluorometric and fluorescence microscopic studies*, Journal of immunological methods, 50 (1982), pp. 193–204.
- [305] S. TORQUATO AND F. STILLINGER, *Exactly solvable disordered sphere-packing model in arbitrary-dimensional euclidean spaces*, Physical Review E, 73 (2006), p. 031106.
- [306] E. TRIZAC, L. BOCQUET, AND M. AUBOUY, *Simple approach for charge renormalization in highly charged macroions*, Physical review letters, 89 (2002), p. 248301.

- [307] E. TRIZAC AND Y. LEVIN, *Renormalized jellium model for charge-stabilized colloidal suspensions*, Physical Review E, 69 (2004), p. 031403.
- [308] R. TUINIER, J. DHONT, AND C. DE KRUIF, *Depletion-induced phase separation of aggregated whey protein colloids by an exocellular polysaccharide*, Langmuir, 16 (2000), pp. 1497–1507.
- [309] R. TUINIER, P. SMITH, W. POON, S. EGELHAAF, D. G. AARTS, H. LEKKERKERKER, AND G. J. FLEER, *Phase diagram for a mixture of colloids and polymers with equal size*, EPL (Europhysics Letters), 82 (2008), p. 68002.
- [310] E. URRUTIA BANUELOS, C. CONTRERAS ABURTO, AND A. MALDONADO ARCE, *A common neighbor analysis of crystallization kinetics and excess entropy of charged spherical colloids*, The Journal of Chemical Physics, 144 (2016), p. 094504.
- [311] O. VAN, *Clay colloid chemistry for clay technologists, geologists, and soil scientists*, Science, 143 (1977).
- [312] S. VAN DER WALT, J. L. SCHÖNBERGER, J. NUNEZ-IGLESIAS, F. BOULOGNE, J. D. WARNER, N. YAGER, E. GOUILLART, AND T. YU, *scikit-image: image processing in python*, PeerJ, 2 (2014), p. e453.
- [313] J. H. VAN'T HOFF, *Die rolle des osmotischen druckes in der analogie zwischen lösungen und gasen*, Zeitschrift für physikalische Chemie, 1 (1887), pp. 481–508.
- [314] F. VARRATO, L. DI MICHELE, M. BELUSHKIN, N. DORSAZ, S. H. NATHAN, E. EISER, AND G. FOFFI, *Arrested demixing opens route to bigels*, Proceedings of the National Academy of Sciences, 109 (2012), pp. 19155–19160.
- [315] K. P. VELIKOV, C. G. CHRISTOVA, R. P. DULLENS, AND A. VAN BLAADEREN, *Layer-by-layer growth of binary colloidal crystals*, Science, 296 (2002), pp. 106–109.
- [316] F. L. VERSO, R. VINK, D. PINI, AND L. REATTO, *Critical behavior in colloid-polymer mixtures: Theory and simulation*, Physical Review E, 73 (2006), p. 061407.
- [317] E. J. W. VERWEY AND J. T. G. OVERBEEK, *Theory of the stability of lyophobic colloids*, Journal of Colloid Science, 10 (1955), pp. 224–225.
- [318] G. VICIDOMINI, P. BIANCHINI, AND A. DIASPRO, *Sted super-resolved microscopy*, Nature methods, 15 (2018), pp. 173–182.
- [319] G. VLIEGENTHART AND H. N. LEKKERKERKER, *Predicting the gas–liquid critical point from the second virial coefficient*, The Journal of Chemical Physics, 112 (2000), pp. 5364–5369.

-
- [320] T. VO-DINH, *Protein nanotechnology: protocols, instrumentation, and applications*, vol. 300, Springer Science & Business Media, 2005.
- [321] A. VRIJ, *Polymers at interfaces and the interactions in colloidal dispersions*, in *Colloid and Surface Science*, Elsevier, 1977, pp. 471–483.
- [322] M. WERTHEIM, *Exact solution of the percus-yevick integral equation for hard spheres*, *Physical Review Letters*, 10 (1963), p. 321.
- [323] G. M. WHITESIDES AND B. GRZYBOWSKI, *Self-assembly at all scales*, *Science*, 295 (2002), pp. 2418–2421.
- [324] G. M. WILKINS, P. T. SPICER, AND M. J. SOLOMON, *Colloidal system to explore structural and dynamical transitions in rod networks, gels, and glasses*, *Langmuir*, 25 (2009), pp. 8951–8959.
- [325] I. WILLIAMS, *Colloids in optically defined confinement*, PhD thesis, University of Bristol, 2013.
- [326] S. R. WILLIAMS, *Topological classification of clusters in condensed phases*, arXiv preprint arXiv:0705.0203, (2007).
- [327] T. WILSON ET AL., *Confocal microscopy*, vol. 426, Academic press London, 1990.
- [328] C. WOHLFARTH, *Dielectric constant of cis-decahydronaphthalene*, in *Supplement to IV/6*, Springer, 2008, pp. 465–465.
- [329] G. WOLBERG, *Sampling, reconstruction, and antialiasing*, (2004).
- [330] P. R. T. WOLDE AND D. FRENKEL, *Enhancement of protein crystal nucleation by critical density fluctuations*, *Science*, 277 (1997), pp. 1975–1978.
- [331] N. H. WOOD, *Hard sphere nucleation rates*, PhD thesis, University of Bristol, 2019.
- [332] P. WOOLSTON AND J. S. VAN DUIJNEVELDT, *Isotropic-nematic phase transition of polydisperse clay rods*, *The Journal of chemical physics*, 142 (2015), p. 184901.
- [333] H. WU, R. ZHANG, W. ZHANG, J. HONG, Y. XIANG, AND W. XU, *Rapid 3-dimensional shape determination of globular proteins by mobility capillary electrophoresis and native mass spectrometry*, *Chemical science*, 11 (2020), pp. 4758–4765.
- [334] Z. XU, L. WANG, F. FANG, Y. FU, AND Z. YIN, *A review on colloidal self-assembly and their applications*, *Current Nanoscience*, 12 (2016), pp. 725–746.

- [335] X. YANG, A. LI, D. LI, Y. GUO, AND L. SUN, *Applications of mixed polysaccharide-protein systems in fabricating multi-structures of binary food gels—a review*, Trends in Food Science & Technology, 109 (2021), pp. 197–210.
- [336] Y. YANG, *Locate nano particles in 3d volumetric confocal images*, 2020.
- [337] N. YASARAWAN AND J. S. VAN DUIJNEVELDT, *Arrested phase separation of colloidal rod–sphere mixtures*, Soft Matter, 6 (2010), pp. 353–362.
- [338] A. YETHIRAJ, *Tunable colloids: control of colloidal phase transitions with tunable interactions*, Soft Matter, 3 (2007), pp. 1099–1115.
- [339] A. YETHIRAJ AND A. VAN BLAADEREN, *A colloidal model system with an interaction tunable from hard sphere to soft and dipolar*, nature, 421 (2003), pp. 513–517.
- [340] Q. YING AND B. CHU, *Overlap concentration of macromolecules in solution*, Macromolecules, 20 (1987), pp. 362–366.
- [341] E. ZACCARELLI, *Colloidal gels: equilibrium and non-equilibrium routes*, Journal of Physics: Condensed Matter, 19 (2007), p. 323101.
- [342] E. ZACCARELLI, G. FOFFI, K. A. DAWSON, S. BULDYREV, F. SCIORTINO, AND P. TARTAGLIA, *Confirmation of anomalous dynamical arrest in attractive colloids: A molecular dynamics study*, Physical Review E, 66 (2002), p. 041402.
- [343] C. K. ZÉBERG-MIKKELSEN, A. BAYLAUCQ, M. BARROUHO, AND C. BONED, *The effect of stereoisomerism on dynamic viscosity: A study of cis-decalin and trans-decalin versus pressure and temperature*, Physical Chemistry Chemical Physics, 5 (2003), pp. 1547–1551.
- [344] F. ZHANG, M. W. SKODA, R. M. JACOBS, R. A. MARTIN, C. M. MARTIN, AND F. SCHREIBER, *Protein interactions studied by saxs: effect of ionic strength and protein concentration for bsa in aqueous solutions*, The Journal of Physical Chemistry B, 111 (2007), pp. 251–259.
- [345] F. ZHANG, S. WEGGLER, M. J. ZILLER, L. IANESELLI, B. S. HECK, A. HILDEBRANDT, O. KOHLBACHER, M. W. SKODA, R. M. JACOBS, AND F. SCHREIBER, *Universality of protein reentrant condensation in solution induced by multivalent metal ions*, Proteins: Structure, Function, and Bioinformatics, 78 (2010), pp. 3450–3457.
- [346] I. ZHANG, R. PINCHAIPAT, N. B. WILDING, M. A. FAERS, P. BARTLETT, R. EVANS, AND C. P. ROYALL, *Composition inversion in mixtures of binary colloids and polymer*, The Journal of Chemical Physics, 148 (2018), p. 184902.

- [347] J. ZHANG, *Protein-protein interactions in salt solutions*, Protein-protein interactions-computational and experimental tools, 1 (2012).
- [348] Z. ZHANG, *Phase behaviour of suspensions of colloidal spheres, discs and rods*, PhD thesis, University of Bristol, 2006.
- [349] Z. ZHANG AND J. S. VAN DUIJNEVELDT, *Isotropic-nematic phase transition of nonaqueous suspensions of natural clay rods*, The Journal of chemical physics, 124 (2006), p. 154910.
- [350] J. ZHAO AND X. LIU, *Electron microscopic methods (tem, sem and energy dispersal spectroscopy)*, (2022).
- [351] F. ZIESE, G. MARET, AND U. GASSER, *Heterogeneous nucleation and crystal growth on curved surfaces observed by real-space imaging*, Journal of Physics: Condensed Matter, 25 (2013), p. 375105.
- [352] R. ZIFF, *Kinetics of aggregation and gelation ed f family and dp landau*, 1984.
- [353] H. ZOCHER, *Spontaneous structure formation in sols; a new kind of anisotropic liquid media*, Z Anorg Allg Chem, 147 (1925), pp. 91–110.

